POLITECNICO
MILANO 1863

School of Industrial and Information Engineering

Department of Chemistry, Materials and Chemical Engineering Giulio Natta
Doctoral Program in Materials Engineering

Rational Design of 3D Printed Drug Delivery Systems based on Structure–Process–Performance Correlations

Supervisors
Prof. Francesco Briatico Vangosa
Prof.ssa Alice Melocchi

PhD Candidate
Arianna Chiappa

Tutor
Prof.ssa Chiara Bertarelli

Academic Year 2024/2025 - Cycle XXXVIII

Abstract

In the last decades, 3D printing (3DP) emerged as a popular technology, being increasingly applied in several industrial sectors and bringing innovation and digitization to production. Pharmaceutical applications of 3DP have also been proposed. The possibility of personalizing the dosage forms in terms of type and quantity of the drug conveyed, release performance and design is one of the main advantages that makes 3DP interesting. Literature is rich in feasibility articles in which the fabrication of the desired system is given priority, postponing a more in-depth investigation on structure-process-performance correlations. This doctoral dissertation aimed to investigate how constituent material formulation, processing parameters, and structural design collectively govern the performance of 3D-printed drug delivery systems, with the overarching goal of defining a practical framework for the rational design of personalized dosage forms with tailored release profiles. Through three case studies, i) gastroretentive expandable devices for metformin oral administration, ii) reservoir-like vaginal rings for local antibiotic delivery and iii) multicomponent hydrogel-based gummies for pediatric oral delivery, the work explored properties–process–performance correlations across different materials, geometries, and administration routes. Taken together, the findings demonstrate that a structured, correlation-driven approach can effectively replace purely empirical, trial-and-error strategies, providing a robust basis for predictive design and process optimization in pharmaceutical 3D printing. The thesis shows that the integration of advanced rheological and mechanical characterizations with the device design allows the control of both material processability and final biopharmaceutical performance, laying a foundation for the future implementation of 3D printing in personalized manufacturing.

Key words

Pharmaceutical 3D printing, Property-process-performance correlations, Rheological and mechanical characterization, Gastroretentive expandable devices, Reservoir-like vaginal rings, Multicomponent hydrogel-based gummies, alginate-hydrogel, k-carragenan hydrogel.

Abstract in Italiano

Negli ultimi decenni, la stampa 3D (3DP) è emersa come una tecnologia popolare, trovando sempre più applicazione in diversi settori industriali e portando innovazione attraverso la digitalizzazione nella produzione. L'applicazione della stampa 3D è stata proposta anche in campo farmaceutico in virtù della possibilità offerta da questa tecnologia di personalizzare le forme di dosaggio in termini di tipo e quantità di farmaco veicolato, prestazioni di rilascio e design. La letteratura è ricca di articoli sulla fattibilità di forme di rilascio prodotte con questa tecnologia, ma in questi lavori priorità viene data alla fabbricazione del sistema desiderato e alla sua efficienza, rimandando un'indagine più approfondita sulle correlazioni struttura-processo-prestazione. Questa tesi di dottorato si è proposta di studiare come la formulazione del materiale costituente, i parametri di processo e il design del prodotto governino collettivamente le prestazioni dei sistemi di somministrazione dei farmaci stampati in 3D, con l'obiettivo generale di definire un quadro per la progettazione razionale di forme di dosaggio con profili di rilascio personalizzato. Attraverso tre casi di studio il lavoro ha esplorato le correlazioni proprietà-processo-prestazione prendendo in considerazione diversi materiali, geometrie e vie di somministrazione. I Casi di studio sono consistiti nello studio di i) Dispositivi espandibili gastroritentivi per la somministrazione orale di metformina, ii) anelli vaginali di tipo "reservoir" per la somministrazione locale di antibiotici, iii) Caramelle gommose multicomponenti a base di idrogeli per la somministrazione orale pediatrica. Nel loro insieme, i risultati dimostrano che un approccio strutturato e guidato dalle correlazioni può sostituire efficacemente le strategie puramente empiriche basate su tentativi ed errori, fornendo una base robusta per la progettazione predittiva e l'ottimizzazione dei processi nella stampa 3D farmaceutica. La tesi dimostra come l'integrazione di caratterizzazioni reologiche e meccaniche con la geometria del dispositivo permetta un controllo dimostra che sia della processabilità del materiale sia delle prestazioni biofarmaceutiche finali, gettando le fondamenta per la futura implementazione della stampa 3D nella produzione personalizzata.

Preface

This doctoral dissertation is aimed to investigate how material properties, printing parameters, and resulting micro- and macro structures would affect the performance of 3D printed drug delivery systems, with the goal of investigating structure-properties–performance correlations for designing pharmaceutical products with different release profiles. The work focuses on three case studies: *I)* gastroretentive expandable devices for personalized oral delivery of metformin, *ii)* reservoir-like vaginal rings containing highly loaded alginate hydrogels for prolonged local antibiotic administration, and *iii)* multicomponent gummies for paediatric oral delivery. The thesis is organized as follows: introductory chapter presenting the state of the art; a section describing the purpose of the work, including the rationale and research questions; the three case studies and the final evaluations and conclusions. The first two case studies are presented more concisely and critically, as three related articles have already been published and are attached in the appendix, whereas the third case study is discussed in greater detail and in a more discursive manner, since a publishable manuscript is still in drafting. Overall, the case studies aim to establish reproducible correlations between formulation, printing parameters, structural features, and functional performance, providing the basis for practical guidelines for the rational design of new drug delivery systems. A concluding chapter discusses how the research findings contribute to advancing both academic knowledge and practical applications in the field. The appendix includes the three published articles as already mentioned above and details regarding the research period abroad at Glatt GmbH, located in Binzen, Germany.

The doctoral scholarship was co-financed by PNRR (Piano Nazionale di Ripresa e Resilienza) resources.

Funded by the European Union NextGenerationEU

Italiadomani PIANO NAZIONALE DI RIPRESA E RESILIENZA

POLITECNICO MILANO 1863

MUR

The original manuscript was reviewed with the assistance of AI-based tools to optimize academic English proficiency.

List of documents attached

1. Marco Uboldi, **Arianna Chiappa**, Margherita Rossi, Francesco Briatico-Vangosa, Alice Melocchi, Lucia Zema; *Development of a multi-component gastroretentive expandable drug delivery system (GREDDS) for personalized administration of metformin;* Expert Opinion on Drug Delivery, 2023, DOI**:** 10.1080/17425247.2023.2294884
2. **Arianna Chiappa**, Alice Fusari, Marco Uboldi, Paola Petrini, Alice Melocchi, Francesco Briatico Vangosa, Lucia Zema; *3D printed reservoir-like vaginal rings for antibiotic delivery;* International Journal of Pharmaceutics, 2025, DOI: 10.1016/j.ijpharm.2025.125217
3. **Arianna Chiappa**, Alice Fusari, Marco Uboldi, Fabiana Cavarzan, Paola Petrini, Lucia Zema, Alice Melocchi, Francesco Briatico Vangosa; *Formulation-Dependent Extrudability of Highly Filled Alginate System for Vaginal Drug Delivery;* Gels, 2025, DOI: 10.3390/gels11070510
4. **Appendix** regarding the foreign research Glatt Pharmaceutical Services GmbH & Co. KG.

Contents

1. Introduction

1.1 3D Printing in the pharmaceutical field

In the last years, 3D printing (3DP) has emerged as one of the most popular technologies and is increasingly applied in multiple industrial sectors, fundamentally changing the concept of traditional manufacturing. Indeed, while conventional industrial production focused on mass-manufacturing of identical products, 3DP enables cost-effective customization. The success of 3DP can be traced back to the 1980s, when several patents were filed on the topic in different countries such as Germany, France, and United States (US Patent No. US5121329A, 1989); (US Patent No. US6508980B1, 1989). Thanks to this technology, an object can be manufactured starting from its electronic model, generated using a computer-aided design (CAD) software, and by sequential layering of the starting materials. For this reason, 3DP is also referred to as additive manufacturing (AM), and differs from the most common subtractive processes, in which an item is obtained by gradual removal of material from a solid block. The key innovation of AM lies in their ability to produce complex geometries that are often unachievable through subtractive methods (Leong, 2003).
From the very beginning, numerous processes have been grouped under the definition of 3DP. Currently, the most accredited classification of AM techniques is that proposed by the American Society for Testing and Materials (ASTM), which identifies seven main domains according to the additive process employed (ISO/ASTM 52900, 2026). These are: extrusion, powder solidification, direct energy deposition, photopolymerization, and lamination of layers.

From automotive and architecture, starting from 2000, 3DP has started to be applied also in the medical field, mainly for the fabrication of dental prostheses and implants (Gerstle, 2014), (Murphy, 2014), (Starosolski, 2014). For these applications, the customization potential is crucial, allowing the resulting piece to perfectly adapt to the anatomical characteristics of the subject involved. To maximize personalization, electronic models can be generated starting from virtual images previously collected from a single patient (*e.g.* tomography), to achieve the maximum degree of anatomical correspondence of the printed part (Rengier, 2010).
More recently, approximately from 2013, 3DP started to be tested also by drug delivery scientists. In fact, the shift toward personalized, patient-specific medicine has introduced new challenges and opportunities for designing intelligent therapeutic systems capable of dynamically adapting to individual needs. Drug delivery technologies have progressively moved away from the standard paradigm “one-size-fits-all” formulations, embracing modular,

customizable, and multifunctional approaches aiming at maximizing therapeutic efficacy, improving patient compliance, and minimizing the chances of side effects (Aina, 2025). The number of pharmaceutical applications of 3DP, particularly at the research level, have been increased after the FDA approval of Spritam, the first commercial dosage form obtained using the powder-based binder jet method.

This interest was prompted by the new possibilities offered by 3DP in drug delivery. Indeed, it enables personalization of the final product in terms of drug type and dose, release performance, excipient composition, and design based on patients' characteristics and needs.

However, the high flexibility that characterizes 3DP also introduces critical challenges in term of process reproducibility and reliability. Ensuring that the overall quality of the printed product is consistent and reproducible, regardless of the specific printer used or the production batch, is a mandatory requirement from the pharmaceutical field but also a complex task given the intrinsic variability of AM. This variability requires the implementation of advanced process controls, such as Process Analytical Technologies (PATs), to monitor critical quality attributes of the dosage form under production in real-time. Therefore, a systematic and profound investigation into the correlations between the constituent material formulation, the process parameters, and the resulting product, in terms of key quality attributes, is essential to reliably predict and control the performance of the resulting medicine.

Among the various 3DP techniques, semisolid-extrusion (SSE) and fused deposition modeling (FDM) are among most exploited processes due to their simplicity and versatility (Seoane-Viaño, 2021) (Penumakala, 2020), (Pereira, 2020). Both rely on an extrusion process, in which the material is deposited layer by layer and solidifies to form the final object (Seoane-Viaño, 2021) (Figure 1.1).

For FDM, feedstock is typically represented by a thermoplastic polymer in the form of either a filament manufactured by hot-melt extrusion (HME) or granules. For SSE, the starting material could be a gel, paste or hydrogel liquid precursor, which can be extruded at low temperatures, enabling the fabrication of delicate formulations.

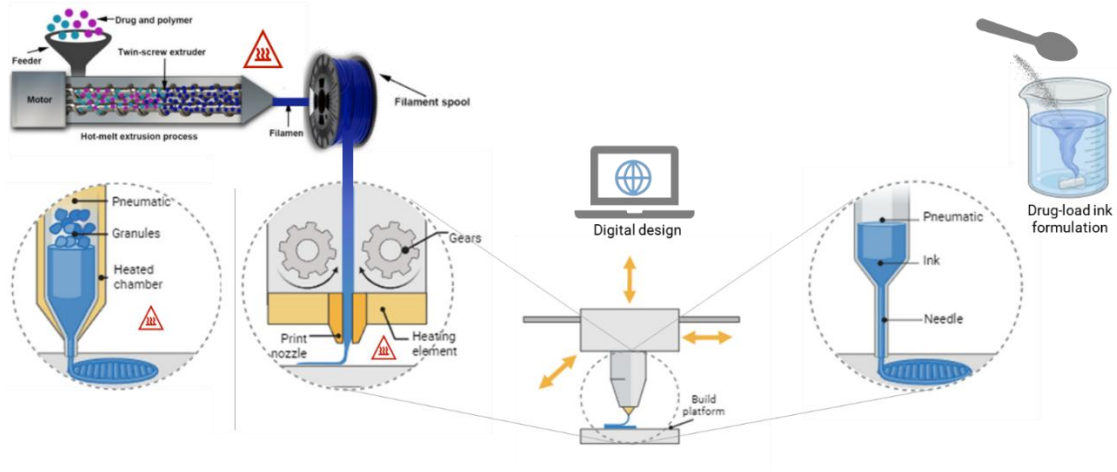

Figure 1.1: Common extrusion process in FDM and SSE 3D printing (figure adapted with Biorender from (Tambe, 2021)).

FDM started to be applied in pharmaceutics for many different reasons: low equipment cost, solvent-free process, ability to create solid dispersions, and reduction of microbial load due to the high processing temperatures (Azad, 2020) (Dumpa, 2021) (Parulski, 2021). Therefore, several research groups have tested FDM for the fabrication of controlled-release drug delivery systems (DDSs) for different administration routes, including gastroretentive devices, pulsatile systems, and prolonged-release matrices (Melocchi, 2021). Initially, filaments used were commercially available, based on polylactic acid (PLA) and polyvinyl alcohol (PVA). Later, researchers focused on manufacturing filaments based on pharmaceutical-grade polymers (Fanous, 2021) (Gültekin, 2019) (Kempin, 2018) (Melocchi, 2016) (Pietrzak, 2015).

SSE allows rapid printing of semisolid formulation at low temperatures. The gelation mechanism of the starting material, which could be by physical, chemical, or radiation cross-linking, allows it to cure rapidly at low or room temperature and with or without post-processing (Korelc, 2024). In pharmaceutical applications, SSE is particularly advantageous for producing soft and chewable drug products and is well-suited for formulations containing thermosensitive drugs. The use of disposable syringes and pre-filled cartridges also promotes compliance with critical quality requirements demanded by regulatory agencies, representing a real opportunity to introduce 3D printing into clinical practice (Rodríguez-Maciñeiras, 2025). Indeed, SSE was tested in hospital settings to produce on-demand, personalized DDSs. Chewable dosage forms with various flavours and colour profiles were manufactured directly in the hospital pharmacy and administered to children with a rare metabolic disorder (Rodríguez-Pombo, 2024).

Key factors influencing DDS performance include material composition, mechanical properties, geometry, AM process employed and processing conditions. In this respect,

understanding the structure–process–performance (SPP) relationships are essential for rational design. Indeed, the performance of a DDS depends not only on its composition but also on the structure, both at a material and device scale, which are determined a priori during the design stage and by selection of appropriate printing parameters and are also affected by the complex chemical-physical phenomena occurring during the 3DP operation. Achieving the desired performance requires integration of formulation, process parameters, and structural design principles, which guide the studies presented in this thesis (Bellinger, 2016) (Kirtane, 2018).

1.2 Drug delivery systems

The European Pharmacopoeia defines immediate release (or conventional release) dosage forms as preparations in which drug release is not deliberately modified- by formulation or manufacturing design. In other words, the dissolution profile is mainly governed by the intrinsic properties of the active substance. On the other hand, modified release systems are preparations in which the rate, time and/or site of the release of active substance is different from that attained by an immediate release dosage form administered by the same route (Figure 1.2). This deliberate modification is achieved by special formulation, design and/or manufacturing approach (Farmacopea Ufficiale della Repubblica Italiana, 2008). More specifically, modified-release drug delivery systems can be designed for a broad range of therapeutic targets, including systemic (*e.g.* oral, intramuscular, subcutaneous) and local routes (*e.g.* transdermal, vaginal, ocular, nasal or pulmonary) (Kumar, 2025).
Moreover, drug products can be classified into single-unit systems, in which the drug is contained in a single device (*e.g.,* a tablet, an intravaginal ring, an implant), and multiple-unit systems, in which the active substance is distributed among many smaller sub-units (*e.g.* pellets, granules, microspheres). These are administered collectively within a larger unit.

1.3 Requirements and rationale for modified release

Modified release systems offer multiple clinical and practical advantages across different administration routes, depending on the release profile they can achieve. Overall, this could imply improve patient compliance, optimized drug exposure, enhanced bioavailability, reduced side effects and administered dose, as well as lower overall cost of therapy (Bruschi, 2025). Consequently, the development of a modified release system should be guided by whether it will be safer, better tolerated, more effective, and advantageous in terms of cost/benefit ratio.

In this framework, the release can be modified along three dimensions:

- **Rate**. The dissolution and release rate can be accelerated to achieve rapid onset of action (fast release systems *e.g.,* fast-dissolving films for pain relief) or decelerated to maintain constant drug levels over prolonged periods (prolonged release systems) and reduce dosing frequency to minimize plasma concentration oscillations, thereby reducing side effects and improving adherence in chronic therapies (Figure 1.2). Advanced systems can even follow zero-order kinetics, ensuring time-independent, constant release rates which are sought both for systemic delivery (e.g. oral or injectable formulations) and for long-acting local systems such as intravaginal rings (Fu, 2010).
- **Time**. Pulsatile systems introduce a latency phase before drug release. This is clinically useful in chronotherapy, where drugs need to be active at specific times of day to match disease activity (e.g., nighttime dosing for morning symptom relief in arthritis or asthma). Lag-time control can be implemented in oral tablets, depot injectables, implants, or stimuli-responsive systems that trigger release in response to physiological cues (pH, temperature, enzymes) (Maroni, 2013)**.**
- **Site.** Targeted delivery aims to concentrate the drug at the anatomical or cellular site where it is needed, whether by physiological retention (*e.g.,* gastroretentive or mucoadhesive systems), active targeting (*e.g.,* ligand-decorated nanocarriers recognizing tumour receptors), or stimuli-responsive release triggered by local microenvironmental conditions (acidic pH in tumours, elevated enzymes in inflamed tissues). This spatial control not only enhances efficacy but also reduces systemic side effects by sparing non-target tissues (Davis, 2008).

In a broader perspective, modified release DDS can be engineered to:

- Achieve spatially controlled drug release. By designing formulations that concentrate the therapeutic agent at the target site—whether a specific region of the gastrointestinal tract, the vaginal mucosa, the lung epithelium, the ocular surface, or tumour microenvironment—it is possible to maximize local efficacy while minimizing systemic exposure and off-target toxicity. Site-specific delivery is particularly valuable when the disease is localized or when the drug acts preferentially at a defined anatomical site (Zheng, 2025);
- Address intrinsic drug limitations. Many active substances suffer from poor solubility, chemical instability in biological fluids (e.g., degradation in gastric acid), or unfavourable pharmacokinetic properties. Modified release technologies can protect labile molecules, enhance dissolution of poorly soluble compounds, and modulate absorption profiles to overcome these challenges (Lane, 2003);

- Optimize therapeutic performance. When constant plasma or tissue concentrations are required - for example in chronic conditions - controlled release allows sustained drug availability over extended periods. Conversely, for diseases requiring time-dependent therapy (chronotherapy), release profiles can be programmed to match circadian rhythms or disease-specific temporal patterns (Ezike, 2023).

The goal of these strategies is to deliver the correct amount of drug, at the right site, at the appropriate rate, and at the desired time. The rationale for selecting a specific modification depends on the physicochemical and pharmacokinetic properties of the drug, the pathophysiology of the disease, and patient-centric factors such as convenience and adherence (Colombo, 2015).

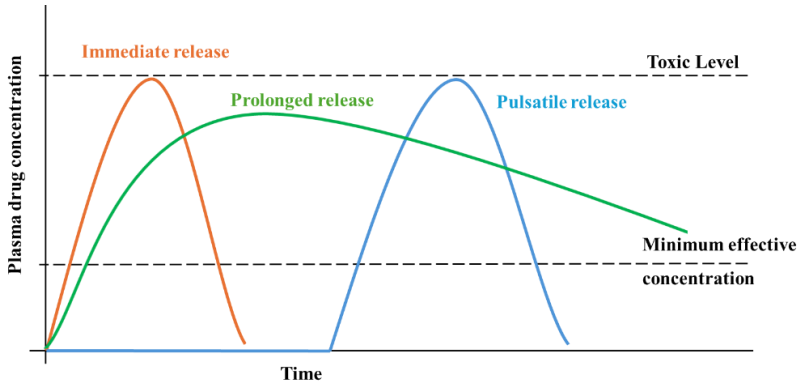

Figure 1.2: release kinetics: immediate (orange), prolonged (green), pulsatile (blue).

1.4 Focus on prolonged release

Prolonged release systems are designed to maintain drug levels within the therapeutic window for extended periods of times, reducing fluctuations associated with the repeated administration of immediate-release dosage forms. This generally leads to better therapeutic outcomes, lower incidence of side effects, smaller total doses, reduced dosing frequency and improved patient compliance. These advantages are relevant both for systemic therapies (e.g. oral prolonged-release tablets) and for long-acting local treatments such as intravaginal rings, which can sustain drug exposure at the mucosal site for days or months.

Having these aspects in mind, a prolonged release form can be considered acceptable if:

- The drug of interest is considered effective and safe. In this respect, it must not cause side effects when the patient is subjected to a certain concentration regimen for a specific period;
- The drug does not require the presence of peaks and troughs nor wash-out periods for optimal action;
- The desired effect can be achieved using a smaller total dose in the case of prolonged release forms compared to a corresponding conventional form;
- It is not possible to prolong the duration of action simply through an increase in the administered strength of the active ingredient.

Merely increasing the administered dose of an immediate-release product extends the time during which concentrations remain above the minimum effective concentration but also increases the risk of exceeding the minimum toxic concentration and leaving the therapeutic window. Prolonged-release systems instead aim to control the input rate, decoupling duration of action from peak concentrations.

Prolonged release systems controlled by diffusion can be matrix systems or reservoir systems.

1.4.1 Matrix Systems

Two types of matrices can be recognized:

- **Hydrophilic Matrices.** Hydrophilic polymer particles are interspersed with drug particles. When the polymer is placed in contact with biological fluids at body temperature, it undergoes a glass transition and passes from a solid, rigid state to a gel.
- **Inert Matrices.** Inert polymers particles, which are insoluble, non-swellable (i.e., does not undergo a glassy-rubbery transition) when exposed to biological fluids, non-degradable, and generally hydrophobic (*e.g.* ethyl cellulose) are interspersed with drug in the particulate state. Thus, matrixes which do not undergo alteration when exposed to biological fluids and are eliminated from the body substantially unaltered after having released the active substance.

Having a matrix in which the active substance is dispersed means that aqueous fluids need to enter from the outside, to meet the active substance and to solubilize it, allowing it to be released. In general, in an inert matrix, diffusion can occur through the bulk polymer (as in homogeneous systems) or through the porosity present in the drug delivery system structure (as in heterogeneous systems).

In fact, inert matrices can be distinguished into two types:

a) **Homogeneous matrices.** These are non-porous matrices. The drug, in molecular or particulate form, is interspersed in the polymer, which constitutes a continuous phase. The drug must be soluble in the polymer. Release occurs by diffusion of the drug molecules through the polymer structure. When the drug migrates from matrix, it leaves pores that are not interconnected (Figure 1.3 a).
b) **Heterogeneous matrices**. These are porous matrices. The drug in particulate form is interspersed with polymer particles. Release occurs by dissolution and subsequent diffusion of the drug molecules in the solvent that fills the preexisting interconnected pores and channels network (Figure 1.3 b).

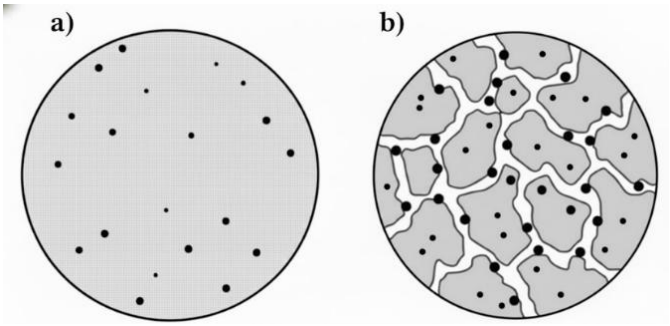

Figure 1.3: schematic representation of homogeneous matrix (a) and heterogeneous one (b) (Adapted form (David, 2025)).

Heterogeneous matrices have release rates compatible with oral administration. Their mechanism of operation involves the biological fluid entering the matrix and dissolving the active substance particles that are on the internal pore surfaces. When the active substance dissolves, new pores form in the matrix, in addition to those initially present. Therefore, more biological fluids will enter the matrix porosities and further dissolve the active substance. Once dissolved the active substance will leave the matrix by spontaneous diffusion according to the concentration gradient.

Conversely, in homogeneous matrices the polymer has no discontinuities: the molecules or particles of the active substance are in a structure that does not communicate with the outside. In this case the active substance molecules must diffuse through the (solid) polymeric matrix, driven by the concentration gradient with the outer environment. This type of process is rather low, and these homogeneous (membrane) matrices are not considered for the oral route because the release times would be too long.

1.4.2 Reservoir Systems

Reservoir systems differ from matrix systems because they consist of two parts: a core containing the drug, surrounded by an insoluble porous or non-porous membrane/barrier (in the latter case defined as homogeneous) that exerts diffusive control over drug release, consisting in a spontaneous diffusion guided by the concentration gradient.
Two types of reservoir DDSs are described in the literature, depending on the membrane they are made of:

- Systems with a homogeneous membrane. The drug present in the core as such (solid – in crystalline powder form, and most commonly in pellet or table form –or liquid, in suspension or solution) must be soluble in the membrane to cross it. The outer film must obviously be insoluble in aqueous fluids but must be permeable to all molecular species.
- Systems with a porous membrane. These have actual pores, or at least free spaces between the polymer chains, defined as voids. The drug present in the core as a solid must be dissolved in the release medium that fills the pores or intermolecular voids and then diffuse through it from the core to the outer environment. A latency time will be present due to the time required for biological fluids to permeate the system and dissolve the active substance. This time might not be significant, as, compared to the hours-long duration of the pharmaceutical form, the latency time might only last a few minutes, making it practically negligible.

From a mechanistic standpoint, prolonged-release DDS are often based on diffusion-controlled designs. In these systems, mass transport is governed by concentration gradients across the barrier and can frequently be described by Fick's laws of diffusion, considering parameters such as diffusion coefficient, partitioning into the polymer and system geometry. Several mathematical models have been proposed in the literature to describe drug release kinetics under these conditions (Paarakh, 2023). Classical mechanistic models include the Higuchi equation, which describes diffusion-controlled release from rigid, non-swelling matrices; zero-order kinetics, representing the ideal case of constant release rate typically observed in reservoir-type systems; first-order kinetics, where the release rate is proportional to the amount of drug remaining in the system; and the Hixson–Crowell model, which accounts for changes in surface area during dissolution or erosion (Costa, 2001). More flexible empirical functions, such as the Weibull model, are also widely used to fit a broad range of release profiles without assuming a specific mechanism. In polymer-based devices, including oral matrices and intravaginal rings, empirical models such as the Korsmeyer–Peppas equation are commonly

used to interpret release data and to distinguish between Fickian diffusion, anomalous transport and zero-order-like profiles. Depending on the microstructure, three idealized situations can be identified:

-diffusion through a homogeneous film (Figure 1.4a),

-diffusion through pores (Figure 1.4b),

-diffusion through polymer chains undergoing glass transition and forming a swollen gel layer (Figure 1.4c).

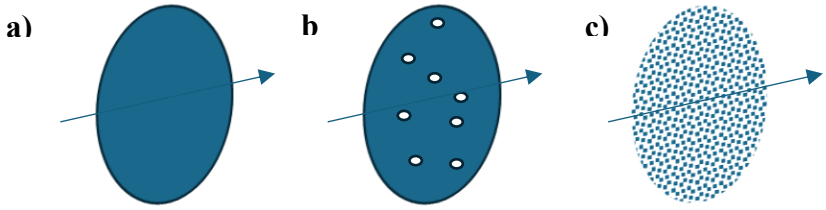

Figure 1.4: illustration of drug diffusion through homogeneous film (a), film with pores (b), and polymer chains undergoing glass-rubbery transitions (c).

In the first case, diffusion across a continuous film can be described by a biological application of Fick's first law. The mass transport across a membrane can be described starting from a mass balance on the drug contained in the reservoir. The rate of mass loss (Eq.1) is proportional to the flux J across the membrane surface S:

$$\frac{dM}{dt} = -J * S \qquad \text{(Eq. 1)}$$

The flux can be expressed through Fick's first law, which relates J to the concentration gradient $\mathrm{d}C/\mathrm{d}x$ across the membrane:

$$J = -D * K * \frac{dC}{dx} \qquad \text{(Eq. 2)}$$

The proportionality constant is the diffusion coefficient D, which depends on temperature, medium viscosity and drug–polymer interactions: small molecules, with sufficient affinity for the polymer

(partition coefficient, K, favouring the membrane), generally diffuse more easily.

$$\frac{dM}{dt} = -D * K * S * \frac{dC}{dx} \qquad \text{(Eq. 3)}$$

For a planar membrane of area S and thickness h, the mass release rate $\mathrm{d}M/\mathrm{d}t$ can be expressed as a function of D, K and the concentration difference between donor and receiver compartments.

In sink conditions, where the concentration in the receiver compartment is less than 1/5 of the concentration in the donor compartment C, this equation simplifies and the driving force is essentially the drug solubility at the inner interface (Eq. 4).

$$\frac{dM}{dt} = -D * S * K * \frac{C}{h} \qquad \text{(Eq. 4)}$$

For porous membranes, the same formalism applies to the continuous polymer phase, while drug transport predominantly occurs through the pore network filled with biological fluid; in this case, the key geometric parameter is the pore size distribution, typically much larger than molecular dimensions, so that diffusion is mainly controlled by tortuosity and porosity. In swellable systems, such as many hydrophilic matrices and elastomeric rings, solvent penetration, polymer relaxation and drug diffusion are coupled: the formation and growth of the hydrated layer modulate the effective diffusion path over time. In these systems, release profiles are often described using semi-empirical models such as the Korsmeyer–Peppas equation (Eq. 5), where the release exponent *n* allows discrimination between Fickian diffusion, zero-order-like behaviour and anomalous transport. (Dash, 2010):

$$\frac{dM}{dt} = n * M_{\infty} * k_{KP} * t^{n-1} \qquad \text{(Eq. 5)}$$

Where:

- M = drug mass released at time t;
- M_{∞} = mass released at equilibrium;
- k_{KP} = Korsmeyer-Peppas kinetic constant;
- n = release factor.

To determine the mechanism of drug release, first 60% of the drug release data must be using the Korsmeyer-Peppas model. The release factor gives information about the release mechanism; in particular, $n < 0.45$ indicates Fickian diffusion, $n = 1$ is associated to zero-order release, and n between 0.45 and 1, non-Fickian diffusion occurs (Altun, 2021) (Wu, 2019).

2. Aim of the work

Several review papers available in the recent literature are focused on 3DP application in the field of DDS, but most of them are mainly feasibility studies, in which prototype fabrication and relevant characterization in terms of pharmaceutical performance are prioritized over detailed analysis of structure-behaviour correlations (Parulski, 2021). Only a limited number of publications deeply address how printing conditions may affect the properties of the resulting drug products. Consequently, the so-called trial-and-error approach remains the most used, despite being costly and time-consuming (Penumakala, 2020). In this respect, the aim of this project was to investigate the correlations between constituent material formulation, process parameters, the resulting structure of DDSs, and their performance, in order to support the development of new drug products. The experimental work focuses on selected case studies chosen for their relevance in terms of release profiles, administration routes and therapeutic targets: *i)* gastroretentive expandable devices (GREDDS) for oral delivery of metformin, *ii)* 3D-printed reservoir-like vaginal rings highly filled alginate hydrogels for prolonged local antibiotic administration, and *iii)* 3D-printed multi-component gummies for oral administration in the paediatric population. For each system, a stepwise, reverse-engineering-like approach is adopted to explore the correlation between formulation, structure and performance of the printed materials. The formulations under investigation are checked from both physical and mechanical perspectives to identify features that may most significantly affect processability and product robustness. The influence of design at both the constituent and device scales on the performance of the DDSs is thoroughly evaluated. Parameters such as geometry, infill percentage, and mechanical behaviour under physiological conditions are assessed. Even if carried out through a set of rationally selected case studies, this analysis aims at validating a roadmap to ensure that the resulting prototypes can achieve the desired key quality attributes, which differ depending on the targeted DDS (*e.g.* a prolonged release gastroretentive device, a reservoir intravaginal ring, a vaginal hydrogel or a paediatric oral gummy). This approach is particularly critical in the pharmaceutical field, where predicting DDS behaviour prior to *in vivo* studies has both ethical and economic implications. Taken together, the above-mentioned case studies are designed not only to explore different therapeutic targets and routes of administration but primarily to identify and establish reproducible correlations between material formulation, 3D printing parameters, structural features, and functional performance. The insights gained from these studies aim to form the basis of a practical 3D printing guideline, which can be applied to the rational design of new DDSs.

3. Properties-Process-Performance correlations in GREDDS

The paper "Development of a multi-component gastroretentive expandable drug delivery system (GREDDS) for personalized administration of metformin" (First attached paper) details the innovative design and preliminary feasibility assessment of a novel oral dosage form. The primary objective was to engineer a system capable of providing controlled and personalized release of metformin, a widely used antidiabetic drug, over an extended period (intended to cover 24–48 hours) within the upper gastrointestinal tract. The therapeutic efficacy of metformin strongly depends on its residence time in the upper gastrointestinal tract, where its absorption predominantly occurs. Therefore, maintaining the dosage form in this region for a prolonged period is essential to ensure effective uptake. In parallel, a sustained release profile is required to provide continuous drug availability over 24–48 hours, since conventional immediate-release formulations exhibit low bioavailability (approximately 56%) and necessitate frequent dosing.

The GREDDS was conceived as a dual-component platform to maximize design versatility. It comprised a drug-loaded core and a 3D-printed umbrella-like skeleton that were manufactured separately and subsequently assembled (Figure 3.1). The core, engineered to combine high drug loading with controlled release, was produced by melt casting a low-molecular-weight poly(ε-caprolactone) (PCL) matrix, whose behaviour was finely tuned by incorporating hydrophilic excipients such as PEG 4000, PEG 8000, or PEO to modulate drug release and polymer degradation kinetics.

The umbrella-like skeleton was specifically designed to ensure gastric retention by mechanical interference with the pylorus, while still being foldable into standard hard gelatine capsules for oral administration. After capsule dissolution, the arms rapidly re-expand to an open configuration (diameter 35.7 mm, larger than the pyloric orifice), a requirement met by selecting a rubbery thermoplastic polyurethane (TPU) as structural material and exploiting fused-filament 3D printing to precisely control arm geometry, thickness, and infill orientation. Three TPU grades (TPU 7, 8, and 9), differing in hardness, were investigated to tailor the mechanical response and optimize the balance between foldability, rapid deployment, and in situ mechanical robustness. In this prototyping phase, 3D printing was crucial to rapidly and cost-effectively manufacture multiple design iterations, avoiding the need for several dedicated, high-cost injection-moulding tools and enabling straightforward adjustment of dimensions,

thicknesses, and overall geometry to refine the mechanical performance of the skeleton. This flexible fabrication strategy also enabled a systematic investigation of the relationships between the properties of the starting TPU grades and the behaviour of the printed device, in terms of forces sustained during gastric retention, and viscoelastic response, ultimately addressing the key question of how reliably the performance of a 3D-printed TPU structure can be predicted from its material characteristics.

The dual-component GREDDS design imposes strict yet balanced assembly requirements to ensure both functionality and reliability. A key aspect is the elastic deformability of the TPU ring at the base of the umbrella-like skeleton, which must expand sufficiently to accommodate insertion of the PCL core stem without permanent deformation, cracking, or excessive friction, while providing a secure fit post-assembly. Dimensional tolerances must allow stable housing of the core, with mechanical strength to withstand manual folding into the hard gelatine capsule, and reproducible recovery of the unfolded shape after gastric fluid exposure.

For safe evacuation of the exhausted system, the design prioritizes a controlled transition: after PCL core degradation, the residual skeleton's resistance drops markedly below gastric contractile thresholds (1.9–3 N), as confirmed by a funnel tests, enabling spontaneous pyloric passage via normal motility without fragmentation into hazardous pieces. Viscoelastic relaxation and mass loss further facilitate this elimination phase, fulfilling core GRDDS safety objectives.

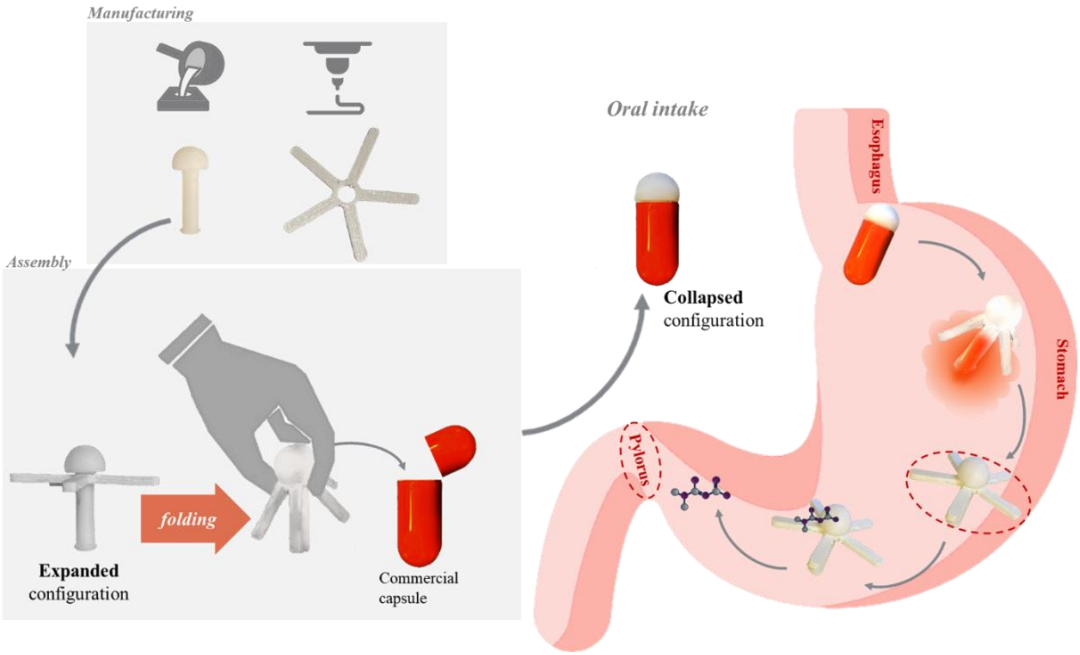

Figure 3.1: Schematic representation of the GREDDS: melt-cast PCL-based core and 3D-printed TPU umbrella-like skeleton, manually folded into a capsule, which subsequently unfolds in the stomach to achieve gastric retention enabling prolonged drug release.

3.1 Structure-Properties-Process-Performance Correlations

The experimental investigations allowed to establish a set of correlations linking the material composition, fabrication process, and final performance.

1. Core composition and performance

For the core, the main design requirements were: *i*) to load at least 500 mg of metformin in a volume compatible with size AAel capsules, and *ii*) to achieve a controlled release over at least 24–48 h, with tunability of the release rate via formulation. The core's performance, evaluated through mass-loss and release testing, highlighted the strong influence of composition on the time profile. The degradation rate in accelerated basic conditions, and the release rate in simulated acidic media were inversely proportional to the PCL content and could be effectively increased by incorporating soluble adjuvants such as PEG 4000, PEG 8000 or PEO, which acted as pore-forming and swelling agents. Formulations with 50% metformin and appropriate levels of hydrophilic polymers enabled faster mass loss and drug liberation, while PCL-rich matrices (75% PCL) supported much longer release, up to several days, confirming the possibility of tailoring the release window by adjusting core composition. Analysis with the Korsmeyer–Peppas model further linked composition to mechanism, showing diffusion-controlled release ($n \approx 0.5$) for PCL-rich matrices with 50% metformin and increasingly non-Fickian behaviour ($0.5 < n < 1$) upon addition of higher fractions of PEG or PEO.

2. TPU melt properties and 3D printing

The manufacturing of the skeleton via FDM required precise control over the highly viscous TPU melt. Optimal printing conditions involved setting retraction values (the parameter that pulls the filament back into the extruder during non-printing movements) and low printing speeds to mitigate the “stringing effect” (filament extruded during non-printing movements, forming web-like strands that compromise surface quality) and ensuring that the infill was consistently oriented along the arms of the umbrella-like skeleton to maximize bending stiffness during folding.

In this framework, tensile tests carried out on both the TPU filament and printed dumbbell showed comparable stress–strain responses, once the actual cross-sectional area of the printed specimens was accounted for. This evidence indicates that the printing process does not introduce significant changes in the intrinsic mechanical behaviour of the material, and

that the effective section can be used as a reliable link between material properties and structural response. Consequently, once robust methods for controlling or measuring the effective cross-section are established, a rational design of the skeleton geometry – or of any alternative geometry – becomes feasible to ensure that the mechanical requirements of the gastroretentive system are met.

3. TPU properties and structure design and performance

The maximum resistance to simulated gastric contractions, measured via the funnel test, increased with both TPU stiffness and arm thickness. This confirms that mechanical performance can be rationally tuned through material selection and geometric design - demonstrating that filament-level properties are as critical as final structural geometry for accurately predicting overall system performance. Only prototypes with 2 mm thick arms achieved sufficient strength, registering peak forces up to 4 N (in the 'UP' position when core-oriented opposite to funnel advancement direction), which exceeds the theoretical threshold for gastric retention (1.9–3 N).

During mechanical characterization, the TPUs exhibited clearly viscoelastic behaviour. This implies that, during storage in the collapsed state inside hard-gelatine capsules, stress relaxation is expected to occur in the folded arms, potentially slowing down and partially hindering deployment once the capsule shell dissolves, with the risk that the structure may not fully open within the typical gastric emptying time. Predicting its long-term mechanical stability and unfolding capability is an essential design requirement.

This aspect was addressed by applying the Time–Temperature Superposition (TTS) principle to stress-relaxation experiments on TPU filaments, enabling extrapolation of relaxation behaviour from short-term tests at elevated temperatures to long storage times at 25 °C. This principle is fundamental in polymer science for characterizing viscoelastic materials like TPUs, where the mechanical response is dependent on both the timescale of the applied stress or strain and the temperature. TTS mathematically assesses that changing the temperature is kinetically equivalent to changing the time scale of the measurement. Specifically, increasing the temperature accelerates molecular motion, meaning a measurement taken at a short time at a high temperature is mechanically equivalent to a measurement taken at a longer time at a lower reference temperature (T_0) (Williams, 1955) (Ferry, 1980).

This allows for the construction of a Master Curve for a viscoelastic property, such as the stress relaxation modulus E, by shifting individual isothermal curves horizontally along the logarithmic time axis until they align with the curve measured at the chosen reference temperature, T_0 (Figure 3.2).

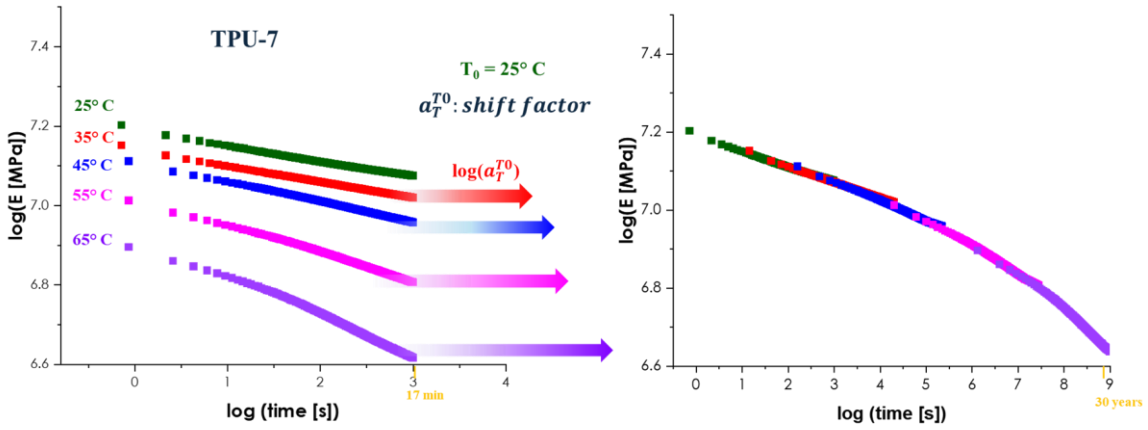

Figure 3.2: logarithmic trend of modules of TPU-7 during time at different temperatures.

The required amount of horizontal displacement for a given temperature T is quantified by the shift factor, $a_T^{T_0}$ (Table 3.1).

Table 3.1: logarithms of shift factors.

T [°C]	**Log($a_T^{T_0}$) TPU-7**	**Log($a_T^{T_0}$) TPU-8**	**Log($a_T^{T_0}$) TPU-9**
35	1.3	0.8	1.1
45	2.05	2.7	2.1
55	4.15	3.9	3.4
65	6.44	5.0	4.8

The time reduced t* at a generic temperature T is related to the time t at the reference temperature T_0 by the shift factor $a_T^{T_0}$ as follows in the equation (Eq. 6):

$$t^* = \frac{t}{a_T^{T_0}} \qquad \text{(Eq. 6)}$$

Knowing the resulting displacement factors, it is possible to identify the conditioning time at 55°C to emulate periods of 18 months of storage at 25°C, thus providing an

experimentally sound basis for assessing whether the folded skeleton maintains sufficient elastic recovery to ensure deployment after long-term storage (Table 3.2).

Table 3.2: Reduced exposure times at 55 °C equivalent to 18 months of storage at 25 °C for each TPU grade.

T [°C]	t* TPU-7	t* TPU-8	t* TPU-9
55	56 min	99 min	314 min

Crucially, after the drug-containing core was exhausted and fully degraded, the maximum force required to push the remaining skeleton through the funnel dropped to ≈0.3 N, well below gastric contractile forces, supporting the intended transition from a “retentive” to a “passing” configuration as a built-in safety feature of the design.

4. Properties-Process-Performance correlations in 3D Printed Reservoir-Like Vaginal Rings

The works "3D Printed Reservoir-Like Vaginal Rings for Personalized Antibiotic Delivery" and "Formulation-Dependent Extrudability of Highly Filled Alginate System for Vaginal Drug Delivery" (Second and Third attached papers) detail the design, manufacturing, and comprehensive characterization of novel 3D printed reservoir-like Vaginal Rings (VRs) intended for personalized and prolonged administration of metronidazole (MTZ), the first-line treatment against bacterial vaginosis. This addresses key requirements: *i*) high MTZ loading (up to 50 vol%) despite low solubility to enable >48 h local release; *ii*) extrudability of precursors for point-of-care filling; *iii*) tuneable mechanics/stability in vaginal pH ~4.5; and *iv*) geometry-controlled zero-order kinetics via open surface area (OSA) overcoming poor compliance/dosing of current suppositories/semisolids (23–29% recurrence).

The dual-component system - a soft, FDM-printed TPE shell filled with in situ-crosslinking ALG hydrogel - decouples structure from formulation for customization. The ALG precursor, via internal $CaCO_3$/GDL gelation, remains liquid/extrudable ~1.5 h post-activation, allowing extemporaneous filling of the TPE ring after personalized therapeutic formulation of the precursor. Manufacturing workflow for 3D printed reservoir-like vaginal rings is shown in figure 4.1.

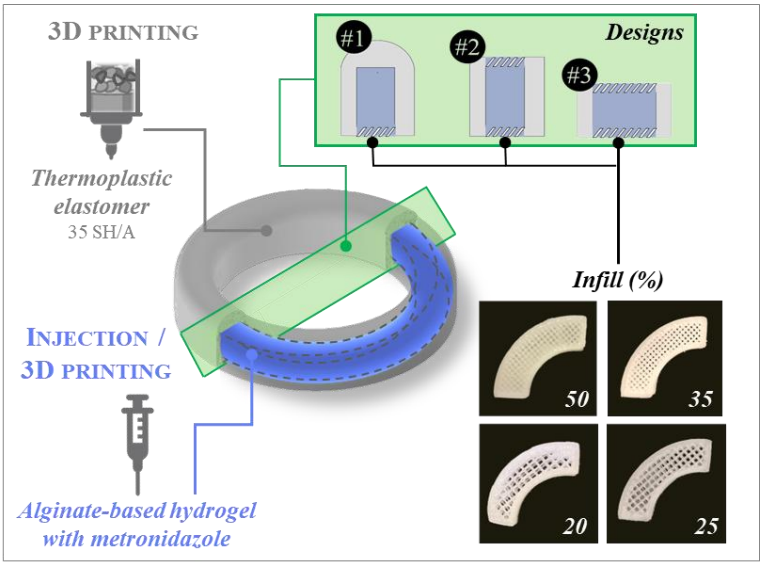

Figure 4.1: Manufacturing workflow for 3D printed reservoir-like vaginal rings (VRs).

4.1 Structure-Properties-Process-Performance Correlations

The experimental investigations established precise correlations linking material properties, processing conditions, and functional performance for the TPE shell and ALG hydrogel components. Successful development depends on the precise manufacturing and the rheological control of both the TPE shell and the highly filled hydrogel precursor.

1. TPE Shell: Rheology and FDM Printability

The TPE shell requires defect-free FDM printing of compliant rings with tuneable OSA. The outer TPE shell was manufactured using FDM at 190°C. The TPE material, selected for its compliance and biocompatibility, exhibits shear-thinning behaviour (viscosity decreases with increasing shear rate), which is advantageous for the FDM process, ensuring easier flow through the 0.5 mm nozzle. Rheological analysis revealed the TPE exhibits a solid-like behaviour (G'>G") at low frequencies, which transitions to G'<G" (viscous liquid behaviour) at higher frequencies and temperatures. This viscoelastic behaviour is desirable: the TPE maintains its shape once deposited (solid-like at rest) but allows sufficient macromolecular inter-diffusion between layers (viscous-like during deposition) to ensure proper adhesion and defect-free final parts. Processing at 470 kPa balances flow and prevents *die swell*, with an 80°C bed aiding adhesion, allowing quarters of rings – considered in the research instead of full ring to save time and material - to print in 50 min with RSD <5% in weight and dimensions.

2. Hydrogel Precursor: Composition and Extrudability

The study rigorously investigated extrudability (the material's ability to flow through a small opening under pressure) which is significantly challenged by the incorporation of high solid volume fractions (up to 50%) of MTZ particles. The addition of MTZ powder, exceeding the saturation concentration, resulted in a substantial non-linear increase in the viscosity (over 40 times for 2% ALG). For the highest MTZ loads, the system shifted from purely non-linear viscous to plastic behaviour, exhibiting a yield stress. The presence of a yield stress is beneficial in 3D printing as it prevents dripping but necessitates higher extrusion pressure. The flow curves of the MTZ suspensions were fitted using the Cross' model and, where yielding occurred, the Herschel-Bulkley model. A key challenge was predicting extrudability at the high shear rates typical of extrusion (100 s^{-1} to 10,000 s^{-1}) through the filling system nozzle during ring filling. A 3D bioprinter was used as a capillary rheometer to estimate the apparent shear viscosity at these higher rates, showing that the Cross and Herschel Bulkley model can

extrapolate the precursor viscosity even at high shear rates. Therefore, the rheological characterization may constitute a valuable tool in the extrusion process design.

3. Hydrogel: Mechanics and Stability

The composition of the inner hydrogel directly governed its mechanical behaviour, a key property for retention and dissolution in the vaginal environment. The MTZ filler particles acted as a stiffening agent within the crosslinked alginate network. Increasing the MTZ volume fraction significantly increased the hydrogel's overall storage modulus (G') and consistency. This indicates a successful transition from a soft, easily deformable liquid dispersion to a stiff, self-standing hydrogel simply by modifying the amount of filler added. Crucially, while the un-filled hydrogels maintain stability for extended periods, the presence of the MTZ filler directly influences long-term structural integrity. As the MTZ dissolves, it creates cavities that progressively weaken the hydrogel matrix, accelerating its eventual fragmentation and mass loss. This mass loss (and corresponding MTZ release) is faster for formulations with lower ALG content or higher MTZ content. Thus, the final stability is a compromise between the mechanical strength offered by the ALG network and the dissolution-induced weakening caused by the high drug load.

4. Release Kinetics: Geometry and Load Control

The primary goal of achieving customizable drug delivery was accomplished by establishing a definitive link between the geometry of the system and the resulting release kinetic. The release rate of MTZ was fundamentally governed by the drug's limited solubility (approx. 10 mg/mL), which dictates the formation and thickness of a saturated gel layer through which the drug must diffuse. The MTZ drug load primarily controls the duration of this release process; a higher load necessitates a longer time for dissolution. However, the release kinetics resulted could be strongly affected by the ring openings geometry, namely the Open Surface Area (OSA), defined by the total area of the openings and the infill percentage of the internal shell wall. The studies demonstrated that the MTZ release rate is linearly proportional to the OSA/Volume ratio. By designing three different VR structures (Design #1, #2, #3) with varying OSA values, the release rate could be tuned. Specifically, structures with greater width (Design #3) effectively minimized the impact of the internal diffusive path, helping to maintain a constant release rate for longer periods. This geometrical control enables therapy personalization without changing the chemical composition of the hydrogel, offering a distinct advantage over traditional monolithic systems.

5. Properties-Process-Performance Correlations in 3D Printed Hydrogel Gummies

4.1 Introduction

The present work aims to develop an innovative chewable drug delivery system based on hydrogel formulations suitable for 3D printing. In recent years, increasing attention has been directed toward the development of personalized, accessible, and patient-friendly drug delivery systems, particularly for paediatric populations and individuals experiencing swallowing difficulties. Among the various dosage forms explored, chewable preparations such as medicated gummies have gained notable interest due to their pleasant taste, soft texture, and attractive appearance, which can improve patient compliance and reduce the psychological barriers often associated with medication intake (Herrada-Manchón, 2020) (Rodríguez Pombo, 2022).

Despite these advantages, most commercially available gummies are characterized by high contents of simple sugars and typically rely on gelatine as a gelling agent. This composition raises nutritional and ethical concerns, especially given the growing adoption of vegan diets and the demand for formulations with low glycaemic impact. Moreover, high sugar levels make these products unsuitable for individuals at risk of obesity or diabetes, conditions that remain among the leading global health challenges. Beyond dietary considerations, gelatine-based gummies display limited thermal stability, as they tend to soften and deform at temperatures above 35 °C, posing difficulties for transport and storage in warmer climates (Rycerz, 2019), (Čižauskaitė, 2019), (Ganatra, 2024).

Recent advances in material science and 3D printing technologies have created new opportunities for the design of personalized DDS. Hydrogel-based 3D printing has emerged as a promising platform, enabling the fabrication of drug-loaded structures with tuneable shapes, doses, and release profiles. Hydrogels -three-dimensional polymer networks with high water content, biocompatibility, and biodegradability -have long been investigated for biomedical applications such as tissue engineering, wound healing, biosensing, and controlled drug release. Their exceptional water retention capacity makes them highly suitable for physiological environments; however, their limited mechanical strength and processing challenges have restricted their broader implementation (Niu, 2023), (Chyzy, 2020), (Chai, 2017).

In this context, the integration of 3D printing into the pharmaceutical and food sectors represents a transformative step toward patient-centric dosage form design. This technology enables the additive manufacturing of customized, easy-to-swallow products without the need for molds or manual operations, while supporting the incorporation of multiple active pharmaceutical ingredients within a single construct. Furthermore, the adoption of a rational design approach -combining material selection, formulation engineering, and process optimization- can ensure reproducibility, structural stability, and predictable drug release behaviour. Such a systematic strategy is particularly valuable for the development of health-oriented gummy formulations, enabling the production of visually appealing, vegan, and sugar-reduced dosage forms. This approach holds great promise for paediatric drug delivery, where treatment adherence can be enhanced by transforming medication intake into a more engaging and enjoyable experience. The study systematically explores and combines natural polymers to obtain printable hydrogels optimized for drug incorporation, filament extrusion, and geometrical fidelity after deposition. In particular, the gelling agent κ-carrageenan (KC) and the thickening agent xanthan gum (XG) were investigated because they combine natural, safe food-grade polymers with tuneable structure and functionality, making them very attractive for drug delivery and edible systems.

KC is a high-molecular-weight polysaccharide composed of 1,3-linked β-D-galactopyranose and 1,4-linked 3,6-anhydro-α-D-galactopyranose units (Figure 5.1), typically extracted from red seaweeds such as *Chondrus, Eucheuma, Gigartina, and Hypnea* (Geonzon, 2020).

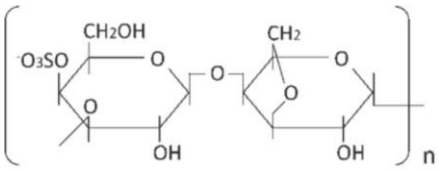

Figure 5.1: κ-Carrageenan chemical structure.

XG, instead, is a polysaccharide produced by the bacterium *Xanthomonas campestris* (Nsengiyumva, 2022). XG comprises a β-1,4-linked glucan backbone with charged trisaccharide side chains (β-D-mannopyranosyl-(1,4)-α-D-glucopyranosyl-(1,2)-β-D-mannopyranosyl-6-O-acetate) on alternating backbone residues, like depicted in Figure5.2.

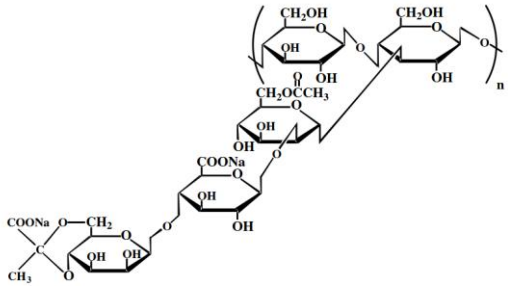

Figure 5.2: Chemical structure of xanthan gum.

Various theories have been proposed to describe the gelation mechanism of KC, most of which depict it as a coil-to-helix transition followed by helix aggregation into a three-dimensional network, a process strongly influenced by temperature changes (Geonzon, 2019).

The rheological, mechanical, and functional properties of these materials were evaluated to guide polymer selection and optimize the printing process, while in vitro drug release studies were performed to correlate structural features with release performance. The resulting system represents a novel concept that merges health benefits, functional performance, and visual appeal. In addition to allowing dose personalization, it also supports nutritional adaptability (vegan, gluten-free, low-sugar) and embraces a patient-centred design philosophy. Ultimately, this research contributes to bridging the gap between pharmaceutical technology and user-oriented design, providing a versatile platform for the future of personalized paediatric medicine.

5.2 Materials

κ-Carrageenan (KC; CAS = 37288-59-8) and Xanthan Gum (XG; CAS = 98112-77-7) were purchased from Special Ingredients (I); Naproxen (NPX)-containing granules (50% of NPX) and pellets (10% of NPX) manufactured during the research period carried out at Glatt GmbH, Germany (see Appendix for detailed information on the granule and pellet formulations).

5.3 Methods

5.3.1 Hydrogel formulation

KC and XG, were weighed (E50S/3, Gibertini, I) and dissolved in deionized water under magnetic stirring (25°C for15 minutes at 300 rpm, IKA RCT, IKA-Werke GmbH & Co. KG, D). Different combinations of KC and XG were tested as highlighted in Table 5.1. The content of KC ranged from 1% to 3% w/v (calculated as the ratio between the polymer powder weight and the volume of the resulting solution), while that of XG from 0% to 0.75% w/V.

Table 5.1: inks composition and relevant formulation codes.

KC [% w/V] \ XG [%w/V]	0	0.5	0.75
1	K1	K1X0.5	K1X0.75
1.5	K1.5	K1.5X0.5	K1.5X0.75
2	K2	K2X0.5	K2X0.75
3	K3	K3X0.5	K3X0.75

To avoid water evaporation, which could have led to a change in the solution concentration, the beaker containing the solution was kept closed using a crystallization vessel as a cover. For preparing drug-containing formulations, either NPX-containing granules or pellets were added to selected solutions (ranging from 5 to 10% w/w for granules and from 10 to 35% w/w for pellets), during the heating step. The selection of pellet and granule concentrations in the gummy formulation was guided by both pharmacological and technological considerations.

For the pellets, which contain 10% Naproxen, a high concentration of 35% w/w was chosen because it allows approaching the target paediatric dose of Naproxen of 120 mg for a 12 kg child. Concentrations higher than 35% are impractical, as excessive pellet loading would occupy too much volume and prevent proper embedding by the hydrogel matrix. A lower concentration of 10% w/w was included to provide an additional point for evaluating the influence of pellet loading on the mechanical and rheological properties of the hydrogels.

For the granules, which contain 50% w/w Naproxen, the target dose can be achieved with a 5% w/w incorporation. To explore the effect of particle loading on the formulation, a second concentration of 10% w/w was selected, which represents the maximum amount that still allows for a homogeneous mixture within the hydrogel matrix. This approach ensures that both types of particles are studied over a range of concentrations that are pharmaceutically relevant and technically feasible.

The formulations were poured in cubic and cylindrical molds and let cool for the tests on hydrogels or they were poured in a 5mL syringe when still hot to perform tests on the liquid formulation precursor of hydrogels.

5.3.2 Rheological characterization of liquid precursors

Steady shear tests were performed with Modular Compact Rheometer MCR 502 (Anton Paar GmbH, A) equipped with smooth parallel plate geometry (D = 25 mm), loading the hydrogel liquid precursor formulations. Steady shear test measurements were performed by imposing a shear rate logarithmic ramp from 1 s^{-1} to 100 s^{-1} for each formulation. The test temperature was 55 °C as at this temperature no sol-gel transition could occur for the considered systems. (Stojkov, 2021).

Viscosity curves could be fitted using Cross model (Eq. 7) for the inks:

$$\frac{\eta - \eta_\infty}{\eta - \eta_0} = \frac{1}{1+(k\dot{\gamma})^n} \qquad \text{(Eq. 7)}$$

Where η is the viscosity, $\dot{\gamma}$ is the shear rate, η_0 is the zero-shear viscosity plateau, η_∞ is the plateau viscosity at infinite shear rate, here assumed to be zero, *k* is the relaxation time and *n* is the power index (n=1 Newtonian behaviour, n < 1 shear thinning fluid, n > 1 shear thickening one). Although the Cross model can describe the entire flow curve, including the low- and high-shear Newtonian plateaus, the rheological relevant region for these hydrogel formulations is the intermediate shear rate range, where the systems exhibit shear-thinning behaviour. In this central region, the Power Law model provided a quality of fit comparable to that of the Cross model, while involving fewer parameters and a more straightforward interpretation of the consistency index and flow behaviour index. For this reason, and to ensure consistency and direct comparability across all formulations (including pellet- and granule-loaded systems), the Power Law model was selected to describe their flow behaviour (Eq. 8).

$$\eta = k * \dot{\gamma}^{n-1} \qquad \text{(Eq. 8)}$$

5.3.3 Investigation of the Hydrogel formation

Oscillatory Temperature sweep tests were performed with Modular Compact Rheometer MCR 502 (Anton Paar GmbH, A) equipped with smooth parallel plate geometry (D = 50 mm). The 50 mm geometry was selected for the oscillatory tests to improve the measurement sensitivity at so low strain amplitude value during a stage in which the material was still weakly structured and therefore generated a low torque. Shear strain amplitude and frequency were kept constant: 0.05% and 1 Hz respectively, while cooling liquid precursors formulations from 55 to 23°C at a constant cooling rate of – 3°C/min, to trigger the gelation.

For placebo inks a gap of 1 mm was set, while for samples containing either granules or pellets, a gap 5 times higher than the average diameter of the multi-particulate systems was employed (gap = 1.25 mm).

The nominal sol-gel transition point was estimated by the cross over point (G'=G'') (Stojkov, 2021).

5.3.4 Rheological characterization of hydrogels

The viscoelastic characterizations of the hydrogel formulations were performed with a Modular Compact Rheometer MCR 502 (Anton Paar GmbH, A) equipped with profiled measuring plate geometry (D = 25 mm). All characterizations were carried out at room temperature. Hydrogel samples were prepared the day before, by pouring about 5 mL of the hot precursor formulations in a cylindrical mold (D = 25 mm), obtaining cylindric samples about 1.5 mm in height. Strain amplitude sweep tests were conducted in oscillatory regime, with the shear strain ranging from 0.1% to 100%, with a constant frequency of 1 Hz. The limit strain of LVE region is the strain amplitude at which G' and G'' start depending on the applied strain, so that the curve starts deviating from a constant value. The shear strain amplitude at G' and G'' intersection represents the flow point (γF), where the viscous behaviour of the material becomes dominant.

Frequency sweep tests were conducted in oscillatory regime, in an angular frequency range from 0.1 rad/s to 100 rad/s. Logarithmic spacing between frequencies was adopted, and data were acquired at each frequency after the attainment of steady state. The angular frequency range was scanned from higher to lower frequencies and then in the opposite direction. Shear strain amplitude of 0.05%, in the LVE region of every hydrogel was adopted. Frequency sweeps were used to investigate the behaviour and the inner structure of KC and XG, as well as on the long-term stability of the formulations. Once the effects of hydrogel formulation and filling on its mechanical behaviour have been assessed, it may be interesting to interpret them in terms of gel structure. This can be carried out by applying the Weak Gel Theory to the complex modulus, G*, vs. frequency data (Eq.9) (Rahman, 2020) (Gabriele, 2001):

$$\log(G^*) = \log\left(\sqrt{G'^2 + G''^2}\right) = \log(A_f) + \frac{1}{z} * \log(\omega) \qquad \text{(Eq. 9)}$$

Where A_f *represents* the gel strength and z the degree of interaction between different units composing the hydrogel.

5.3.5 Printability

All the 3D printing experiments were carried out using a BIO X Bioprinter (Cellink, US) equipped with a syringe pump printhead able to guarantee a constant flow rate of the ink through the nozzle.

As suggested from *Theus et al.*, the ink printability was evaluated using four different parameters (Theus, 2020). The first two indices assess the printability of a filament, whereas the other two evaluate the fidelity of a grid structure.

- **Spreading ratio (*SR*)**: it describes the spread of the deposited ink with respect to the dimension of the nozzle (Eq. 10), which ideally has to be equal to 1 which ideally has to be equal to 1 when the diameter of the printed filament is equal to the diameter of the nozzle.

$$SR = \frac{diameter\ of\ printed\ filament}{diameter\ of\ the\ nozzle} \qquad \text{(Eq. 10)}$$

- **Uniformity factor (*U*):** it describes if the filament is printed uniformly or not. In this case the standard deviation of the spreading ratio, can be used;

- **Pore coefficient (P_r)**: it is 3D printed pore geometry index (Eq. 11), meaning a pore with a square geometry. While $P_r < 1$ suggests roundish pores, $P_r = 1$ identifies square pores (i.e. the ideal situation) and $P_r > 1$ refers to irregularly shaped pores (Merli, 2022) .

$$P_r = \frac{(Pore\ perimeter)^2}{16 \cdot (Pore\ area)} \qquad \text{(Eq. 11)}$$

- **Perimeter coefficient (P_e):** it evaluates the printing accuracy of the perimeter of a square. P_e, calculated as in Eq. 12, less than 1 suggests roundish corners of the grid and in contrary P_e greater than 1 indicates an irregular external perimeter.

$$P_e = \frac{1}{\left[\left|\frac{1}{2}\times\left(\frac{Ł_x}{L_x}+\frac{Ł_y}{L_y}\right)-1\right|+1\right]\times\left[1+\frac{1}{2}\times\left(\frac{SD_x}{L_x}+\frac{SD_y}{L_y}\right)\right.} \qquad \text{(Eq. 12)}$$

$Ł_x$ and $Ł_y$ are the mean lengths of the printed edges, SD_x and SD_y are their standard deviations and L_x and L_y are the theoretical lengths of the geometry along the horizontal and vertical axes, respectively (Sardelli, 2021). To evaluate all the above detailed parameters, grids (Figure 1) were printed setting the printing parameters detailed in Table 5.1 for all the investigated inks.

Table 5.1: printing parameters set.

Printing parameter	**Value**
Printhead Temperature	55 °C
Print bed Temperature	23 °C
Printing speed	10 mm/s
Nozzle diameter	• 0.84 mm (for placebo and granules-containing formulations) • 1.46 mm (for pellets-containing formulations)
Flow rate	• 5.55 µL/s (for placebo and granules-containing formulations) • 16.74 µL/s (for pellets-containing formulations)

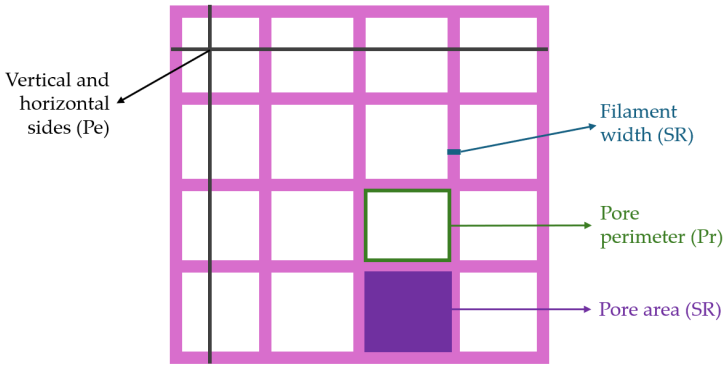

Figure 5.1: outline of the grids to be printed, highlighting the measures taken to evaluate printability parameters.

Images of the printed grids were acquired using an iPhone 16 Pro Max camera (48 MP, maximum resolution 8064 × 6048 pixels). All images were obtained with the same illumination (through a light box) and positioning the lens of the camera at a fixed distance from the filament, ensuring no parallaxes and consistent magnification. The spatial scale was defined by placing millimetre graph paper next to the printed construct in each image, allowing the conversion of pixel dimensions into physical units by analysing the acquired images through the software ImageJ (Fiji contributors, USA, 2010).

After the preliminary tests, 3D printing of increasingly complex geometries was approached:

- Cylinder (d = 25 mm, h = 4 mm) which was first printed using a concentric infill pattern with 100% infill density, to ensure optimal layer adhesion and to produce samples suitable for dissolution testing and rheological characterization of the hydrogel.

- Elephant (Figure 5.2)

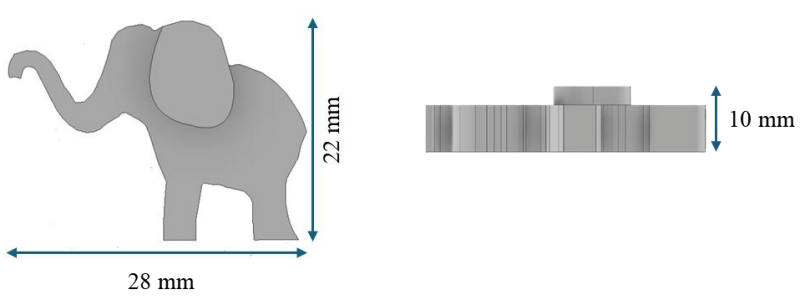

Figure 5.2: elephant CAD.

5.3.6 Release performance

NPX release from hydrogel-based gummies (n=5) were investigated using a USP dissolution apparatus II (Agilent 708-DS, US-MA; 800 mL of deionized water kept at 37 ± 0.5 ◦C, paddle rotating at 100 rpm) (Geever, 2008). The latter related to a peristaltic pump (Agilent, US-MA) and with a UV spectrometer, for automatic collection of fluids at pre-defined time points and absorbance measurements (λ max = 270 nm). The amount of NPX released over time was calculated from a purposely built calibration curve in the 0.0025-0.25 mg/mL range (y = 4.1461x, R^2 = 0.9999, figure 5.3).

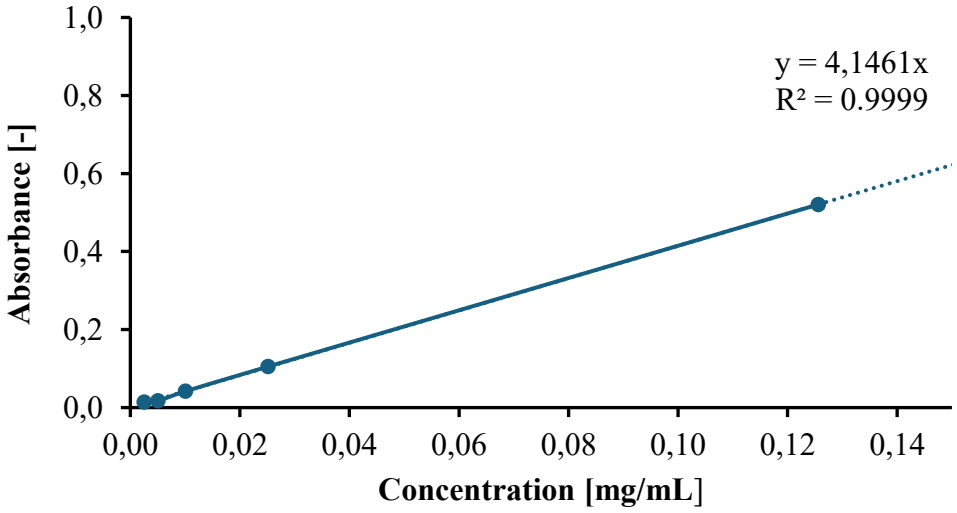

Figure 5.3: experimental calibration curve of Naproxen.

5.4 Research strategy

Given the extensive combinatorial space of precursor solutions and inks achievable by varying natural polymers and drug loadings, preliminary screening was essential to prioritize formulations for detailed characterization. Key criteria included ease of solution preparation, printability, rheological properties, and stability of the final hydrogels, which collectively guided the selection of optimal candidates for the drug delivery system (DDS). This streamlined screening workflow is illustrated in the flowchart (Figure 5.4).

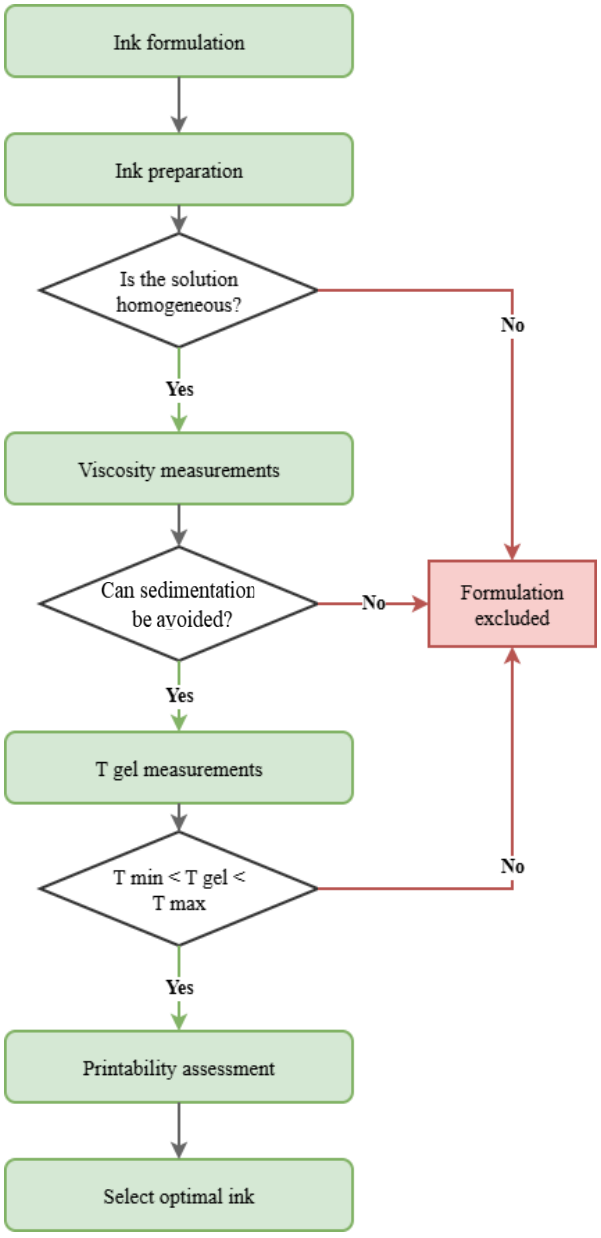

Figure 5.4: Screening process flowchart. The main parameters belonging to the research strategy are solution homogeneity, viscosity and gelation temperature of the hydrogel.

This approach enabled a stepwise elimination of less promising candidates according to specific evaluation parameters considered fundamental for a 3D printable hydrogel. The first parameter considered in the screening process was ink homogeneity. A well-prepared ink must appear clear and free of visible aggregates, as the presence of undissolved particles would indicate incomplete polymer dissolution, an issue that can compromise print quality and reproducibility. Establishing a minimum viscosity threshold is critical to prevent the sedimentation of suspended particulate matter, such as drug-loaded pellets, during both the ink preparation and printing phases. Consequently, formulations displaying insufficient viscosity were excluded from the study. Regarding phase stability, the primary objective is to delay phenomena such as precipitation or flotation – driven by density difference between the solid phase and the dispersant liquid – beyond the timeframe required for ink handling and printing. This stability is essential to maintain the homogeneous particle distribution within the final dosage form and to prevent nozzle clogging (Höfer, 2018). It is assumed that the time between loading the ink into the cartridge and the end of the printing process is approximately one hour. Since the typical filling height of the syringe ranges between 3 and 4 cm, the maximum acceptable sedimentation velocity is estimated at 0.01 mm/s. Using Stoke's equation, the minimum value of viscosity the ink should have to obtain a maximum sedimentation velocity of 0.01 mm/s is 1.7 Pa s. The sol-gel transition temperature (T_{gel}) constitutes a pivotal parameter within the material screening strategy. The T_{gel} must fall within a defined operational window that aligns with both the hardware specifications of the 3D printing platform and the rheological requirements for handling. An excessively high gelation point would complicate the fluid handling process, inducing premature solidification, whereas T_{gel} too low could compromise the post-extrusion shape fidelity and structural stability.

Given the process of interest, and the related 3D printing tools, specific thermal boundaries were established:

- **Upper Critical Limit:** 50°C. This value was 5°C lower than formulation and mixing temperature to prevent premature gelation during ink transfer into the printing cartridge. This threshold also meets the hardware constraints, i.e. a printhead's maximum temperature of approximately 65°C.
- **Lower Critical Limit:** 28°C. The value was 5°C higher than the laboratory temperature, so that the extruded ink remains in a solid state under typical storage and usage conditions (room temperature).

5.5 Results

5.5.1 Screening: Viscosity and Sedimentation

According to Stokes' law, the minimum viscosity required to maintain sedimentation velocity below this limit is 1.7 Pa·s. Therefore, flow curves derived from steady shear tests were analysed to verify compliance with these criteria. Besides this, the shear-thinning behaviour desirable for extrusion-based 3D printing was checked.

Representative curves for the systems of interest are depicted in Figure 5.5.

a)

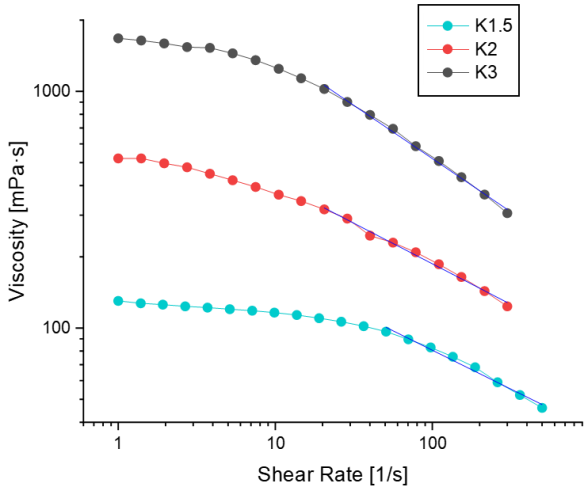

b)

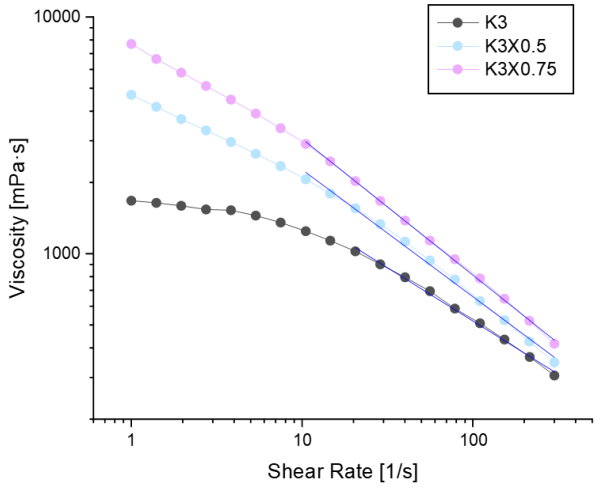

c)

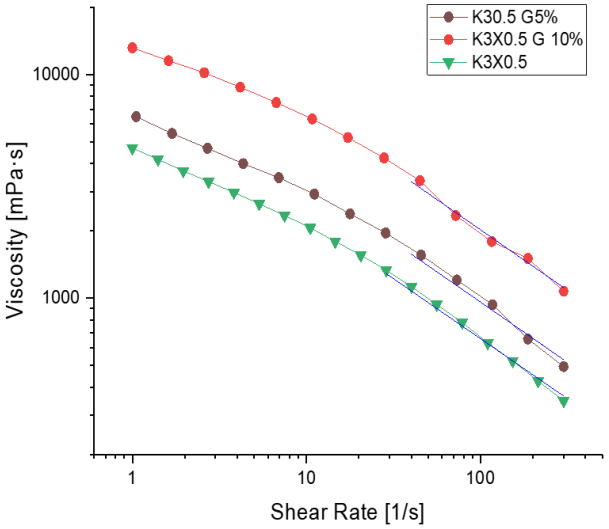

Figure 5.5: Example of flow curves for different precursor solution formulations: (a) effect of KC concentration, (b) effect of XG concentration, (c) effect of granule concentration fitted with power law.

To gain deeper insight into the rheological behaviour of the solutions, flow curves are fitted considering the Cross and Power Law models. The Cross model proved suitable for KC solutions, which exhibit a distinct Newtonian plateau at the lowest shear rates investigated. However, formulations containing additional components, such as XG, acting as a thickener, or fillers, lacked a discernible zero-shear viscosity plateau within experimental range. For this reason, for the sake of data comparison, the power law model is used to fit all flow curves. Consequently, to ensure comparative uniformity across all datasets, the Power Law model was adopted as the standard fitting equation. For pure KC solutions, the fitting was restricted to the shear-thinning region, excluding the initial Newtonian plateau.

The regression parameters, presented in Figure 5.6 and Figure 5.7 reveal that both KC and XG significantly modulate the rheological profile. The consistency index *k* exhibits a not clear correlation with KC concentration; the addition of XG induces a further increase in *k*, confirming its efficacy as a thickening agent for the precursor solution. Conversely, the flow behaviour index (n) decreases as KC concentration rises, indicating enhanced shear-thinning beneficial for the extrusion process. Notably, the impact of XG is more pronounced at lower KC concentrations. At higher KC levels, the influence of XG content diminishes, suggesting a saturation effect wherein the structural contribution of the carrageenan network becomes the dominant factor governing the rheological response.

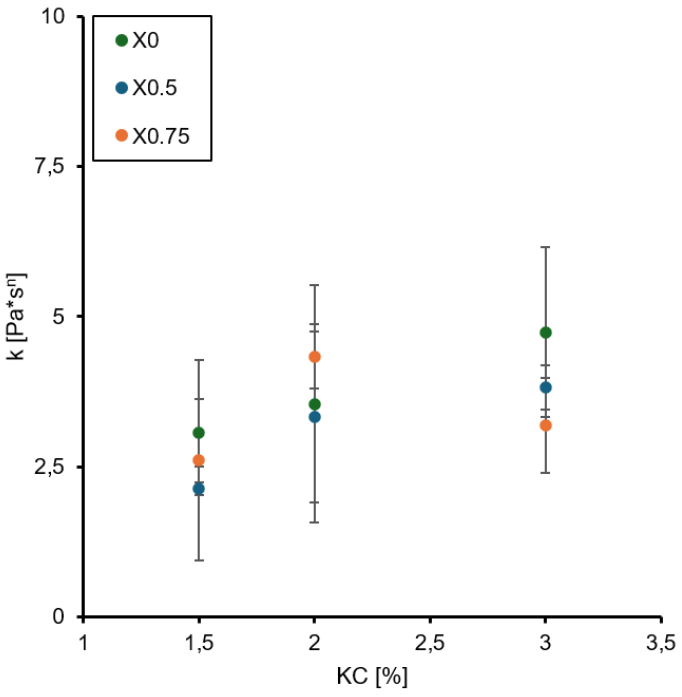

Figure 5.6: Consistency index for different precursor solutions (KC, KC+XG).

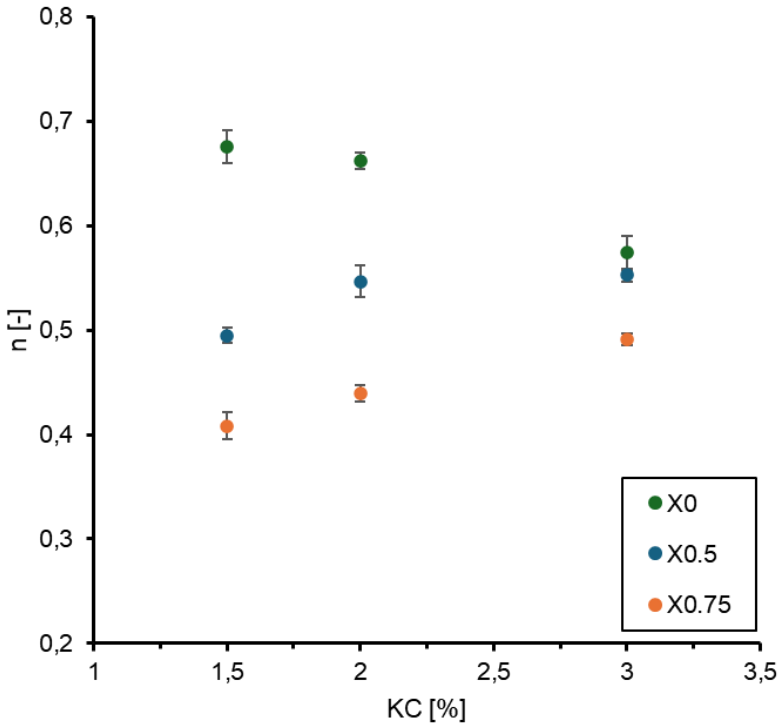

Figure 5.7: Power law index, n, for different precursor solutions (KC, KC+XG).

In accordance with the screening strategy, a minimum viscosity threshold of 1.7 Pa·s was established to inhibit particle sedimentation. Theoretically, compliance with this threshold should be assessed against the zero-shear viscosity of the precursor formulation. However, given that systems deviating from the Cross-model behaviour did not exhibit a distinct Newtonian plateau, the direct determination of the zero-shear viscosity was precluded. Consequently, the apparent viscosity measured at a low shear rate of 0.1 s^{-1} was adopted as a representative proxy for the ink's rheological state under quasi-static (resting) conditions. The experimental results, presented in Figure 5.8, demonstrate the necessity of incorporating XG to achieve the viscosity levels required for phase stability.

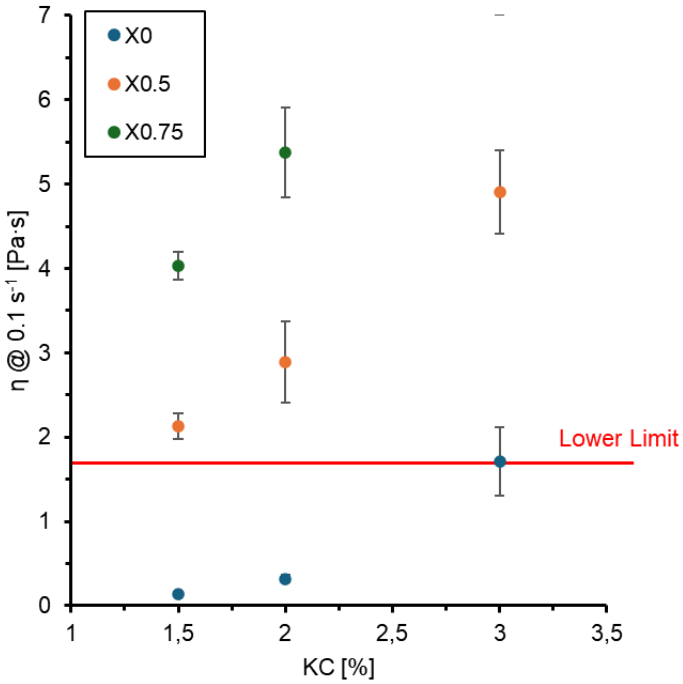

Figure 5.8: Minimum viscosity of unfilled precursor solutions, compared to the viscosity limit for filler sedimentation.

Formulations consisting solely of KC were excluded from subsequent analyses due to their failure to meet the minimum viscosity threshold required for phase stability.

To provide a comprehensive rheological profile, the characterization was extended to precursor solutions loaded with solid particulates (granules or pellets), utilizing the Power Law model for data fitting (Eq 6). Consistent with theoretical expectations for suspension rheology, the incorporation of a solid phase induced a marked increase in viscosity. Accordingly, the consistency index *k* exhibited a significant positive correlation with filler loading, following a trend that appears independent of the specific filler type (Figure 5.9). Conversely, the flow behaviour index *n* depended also on the particulate nature: granules induced a slight increase in *n*, indicating a reduction in shear-thinning, whereas pellets caused a marginal – and statistically negligible – decrease (Figure 5.10). This discrepancy suggests potential variations in the physicochemical interactions between the biopolymer matrix (XG/KC) and the respective fillers. An alternative hypothesis concerns the mechanical stability of the dispersed phase under high-shear conditions: granules may undergo partial disaggregation during flow, unlike the mechanically stable pellets.

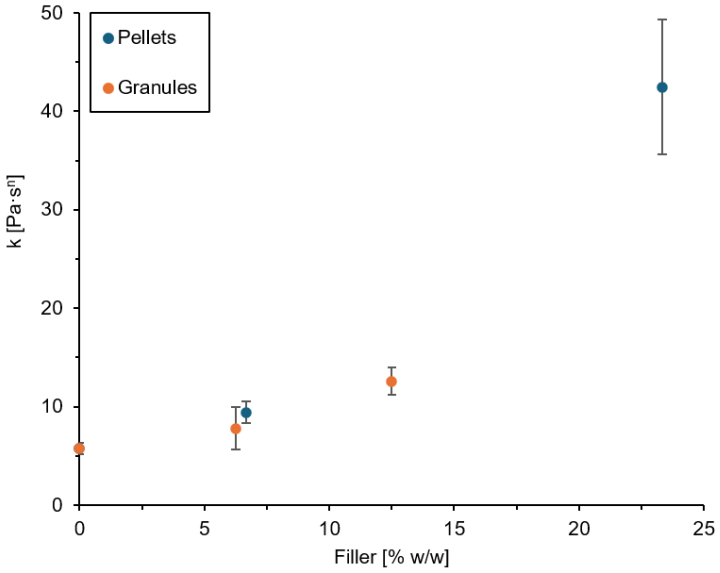

Figure 5.9: Consistency index for filler-loaded formulations (precursor solution: K3X0.5).

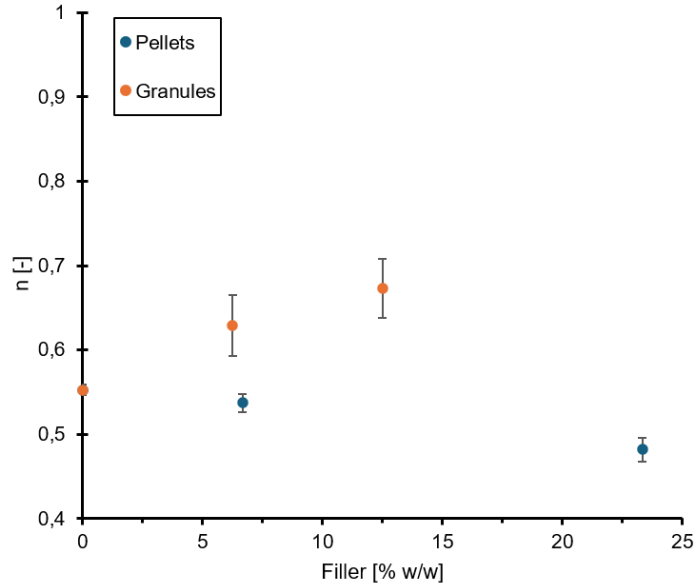

Figure 5.10: Power index for filler-loaded formulations (precursor solution: K3X0.5).

5.5.2 Gelation temperature control

To verify compliance of the formulations with the thermal boundaries previously described, temperature sweep tests were conducted. Temperature sweep tests were therefore performed for multiple purposes: to determine the gelation temperature, essential for setting printing parameters and selecting appropriate preparation conditions for the precursor solution, and to compare this temperature with technological limits during the screening process. Figure 5.11

reports an example of G' and G'' dependence on temperature and the intersection between the two curves is defined as gelation temperature.

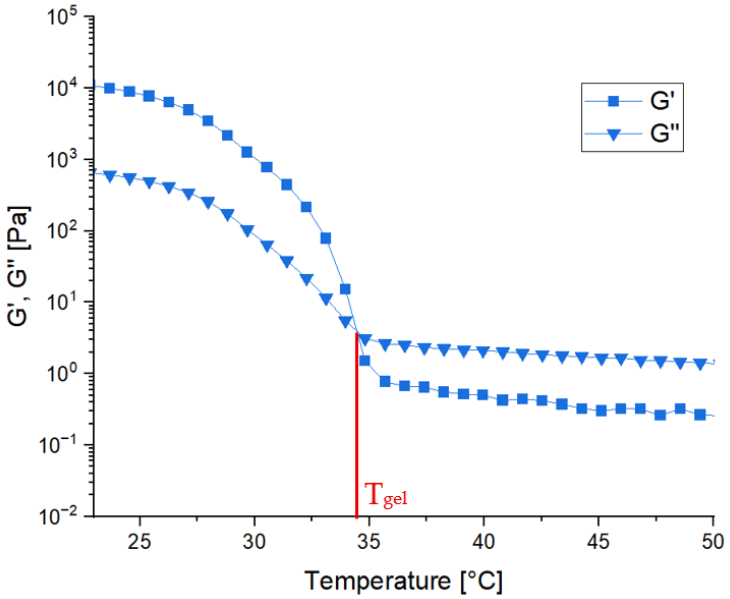

Figure 5.11: G' and G'' trends during temperature ramp test for K2 formulation with crossed each other in the T_{gel} point.

As illustrated in Figure 5.12, show an increase of the T_{gel} of KC hydrogels at increasing biopolymer concentrations.

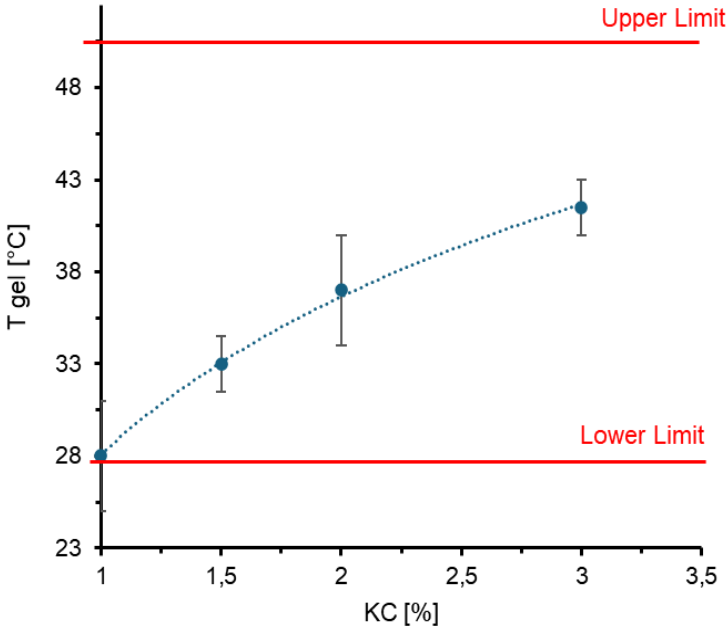

Figure 5.12: KC inks gelation temperature and comparison with limits imposed in the screening process.

Specifically, the data exhibits a logarithmic dependency, mathematically described by equation 14.

$$T_{gel}[°C] = 28.5 * \log[\mathrm{KC}(\%)] + 28.1 \qquad (R^2 = 0.998) \quad \text{(Eq. 14)}$$

This regression model serves a dual purpose: quantifying the observed trend and providing a predictive tool to estimate the gelation temperature of untested formulations within the investigated range.

Furthermore, the analysis reveals that precursor solutions containing 1% w/w KC exhibit a T_{gel} perilously close to the screening lower limit (28°C);considering the relatively high standard deviation observed in the experimental data—which implies a significant risk of falling below the stability threshold—a conservative decision was made to exclude all K1 formulations from subsequent investigations.

As for XG, its presence and concentrations did not affect the sol-gel transition point, as illustrated in Figure 5.13, confirming that this component acts simply as a thickener in the formulation.

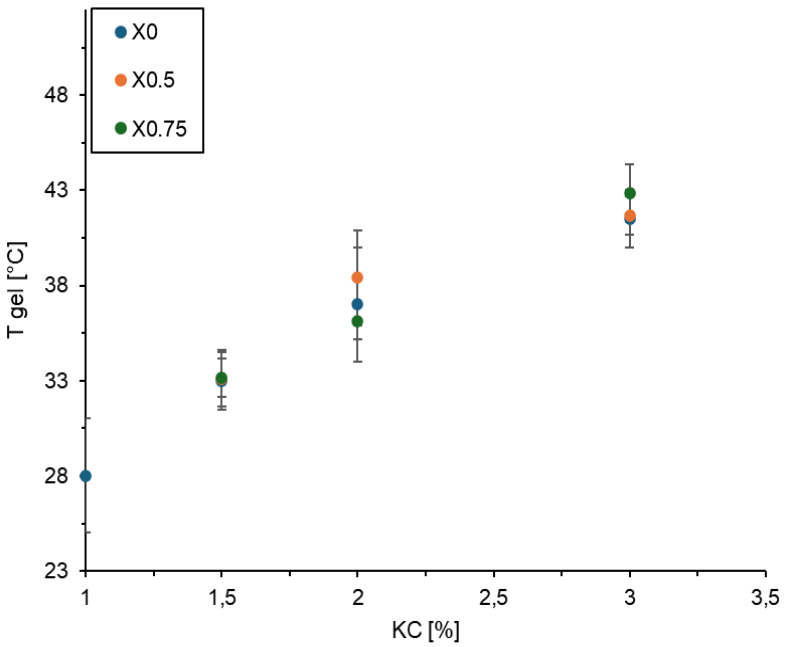

Figure 5.13 - T_{gel} for different unfilled formulations

The determination of the gelation temperature T_{gel} in particle-loaded hydrogels presents a distinct rheological challenge. In these composite systems, the classical sol-gel transition criterion—defined by the crossover of the G' and G"—is inapplicable. Specifically, G' remains

consistently higher than G" throughout the testing frequency range, indicating that the dispersion exhibits solid like behaviour even prior to the thermal gelation of the polymer matrix. At the test frequency and initial temperature, the material behaves like a solid. This could suggest the presence of an uninvestigated yield stress. Although the moduli magnitudes converge at elevated temperatures (where the matrix is in the sol state), they do not intersect. Upon cooling, the onset of gelation is identified as the knee point where the two moduli begin to diverge sharply, characterized by a rapid escalation in G' (Figure 5.14).

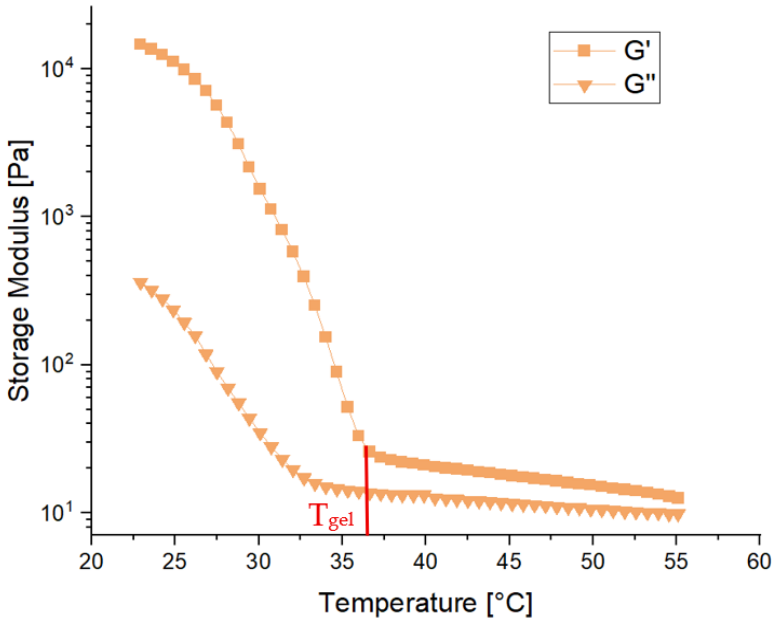

Figure 5.14: Dynamic mechanical response to temperature variation for 10% w/w filled K2X0.5 formulation.

While this method entails a degree of semi-empirical interpretation compared to the crossover method, the results indicate that the apparent gelation temperature is not affected by the presence of pellets or granules (

Figure5.15).

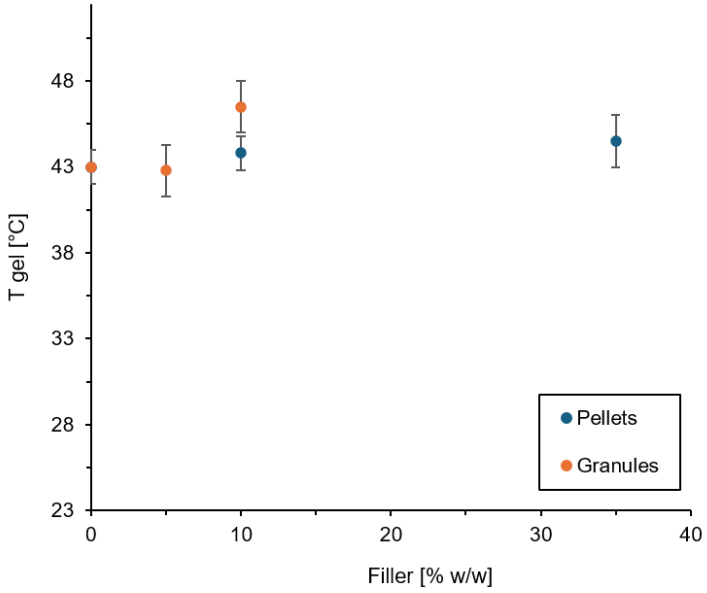

Figure 5.15: Gelation temperature dependence on filler type and content for K3X0.5 formulations.

5.5.3 Formulation effects on hydrogel performances

Following the preliminary screening phase the selected candidate formulations (Table 5.3) underwent a comprehensive rheological and mechanical characterization.

Table 5.3: selected formulations

KC [% w/V] \ **XG [%w/V]**	**0.5**	**0.75**
1.5	K1.5X0.5	K1.5X0.75
2	K2X0.5	
3	K3X0.5	

The primary objective of this advanced analysis was to elucidate the intrinsic material properties and correlate them with both processability (printability) and the final performance of the construction.

Frequency sweep tests were conducted to assess stability, mechanical stiffness, and the degree of the internal network connectivity for both unloaded and filled hydrogel systems. Given the

frequency-independent nature of the materials, manifested by the negligible slopes of the G' and G" curves within the linear viscoelastic region as shown in figure 5.16, a reference frequency of 1 Hz was selected for comparative analysis.

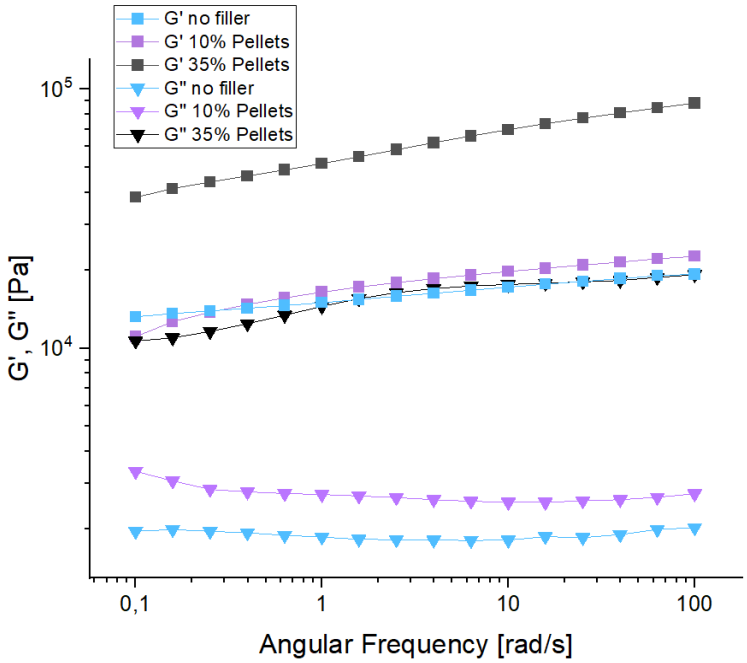

Figure 5.16: Effect of filler content on G' and G'' moduli for K3X0.5 hydrogels in frequency sweeps.

Conversely, the influence of XG appears marginal, confirming that its role is limited to the control of precursor viscosity. The only effect is observed in the stiffest hydrogel formulations, where the addition of XG correlates with a slight reduction in moduli magnitude, accompanied by an improvement in data reproducibility (reduced standard deviation).

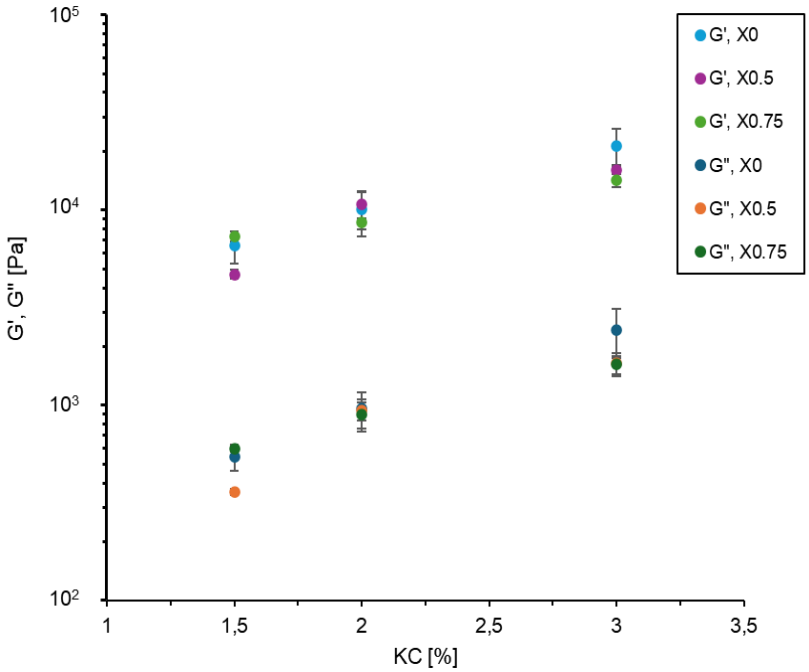

Figure 5.17: Effect of hydrogel formulation in G' and G'' moduli at fixed frequency and shear strain amplitude.

The incorporation of solid fillers (pellets or granules) induces a complex, concentration-dependent modulation of viscoelastic properties. Initially, the addition of the dispersed phase reduces the moduli, suggesting a localized disruption of the biopolymer network (network destructuring effect).

However, this trend reverses at higher filler loadings. Specifically, formulations containing high concentrations of pellets exhibit a substantial increase in both storage and loss moduli. This shift indicates a transition in the rheological mechanism: at elevated solid fractions, the stiffness of the rigid filler particles seems to become the dominant factor, overcoming the matrix-disruption effect and leading to a marked reinforcement of the system (as illustrated in 5.18).

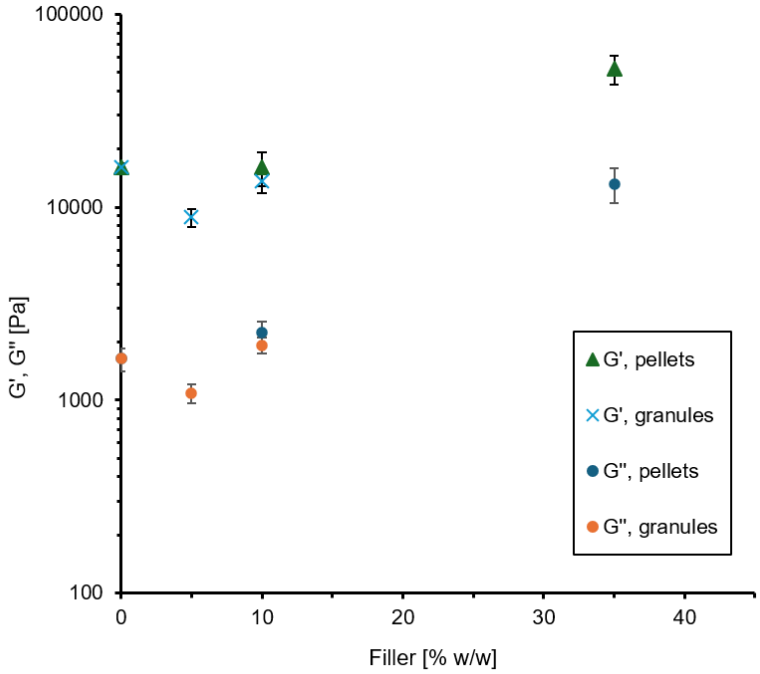

Figure 5.18: Effect of fillers in storage and loss moduli at fixed frequency and shear strain amplitude for K3X0.5 hydrogels.

To provide some microstructural insight of the macroscopic mechanical behaviour, the frequency-dependent complex modulus (G*) data were analysed using the Weak Gel Model (WGM). This theoretical framework is particularly appropriate for physical gels like KC, which can be approximated as a cooperative arrangement of flow units engaged in strand formation.

By fitting the experimental data to the weak gel constitutive equation (see *2.4 Rheological characterization of hydrogels*), two critical parameters were derived: the network strength (A_f) and the interaction factor (z). These indices allow for a quantitative comparison of the internal architecture across different formulations.

As illustrated in Figures 5.19 and 5.20, the dependence of the weak gel model parameters of KC concentration confirms that the gel viscoelastic behaviour is controlled by the KC matrix. An increase in biopolymer concentration causes a marked rise in A_f and a concurrent decrease in z. This inverse trend indicates the formation of a denser, more interconnected network structure characterized by reduced relaxation potential. Conversely, the addition of XG exerted no statistically significant impact on either parameter, as evidenced by the overlapping error bars associated with batch-to-batch variability.

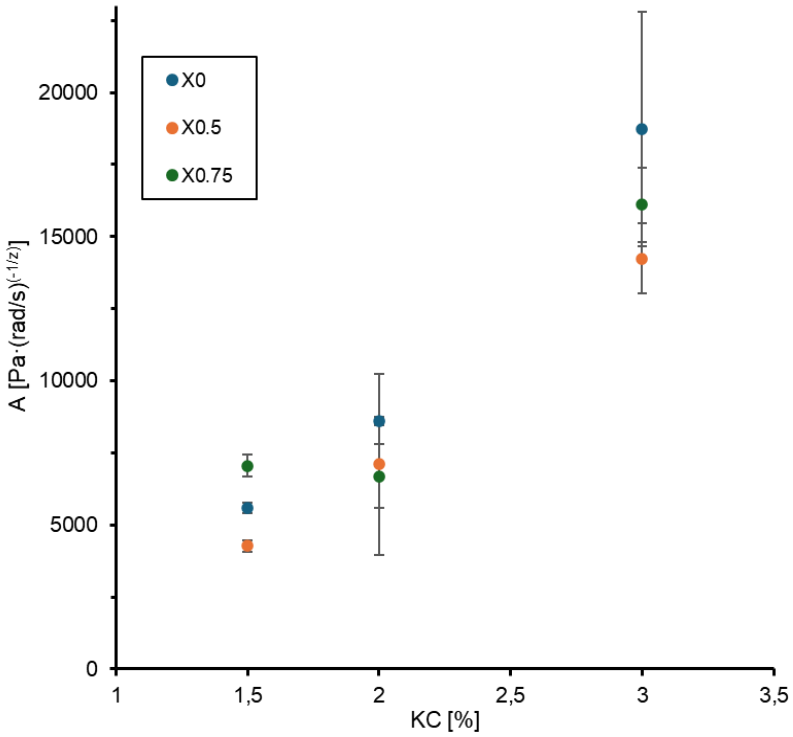

Figure 5.19: Gel strength, A_f, for different unfilled hydrogel formulations.

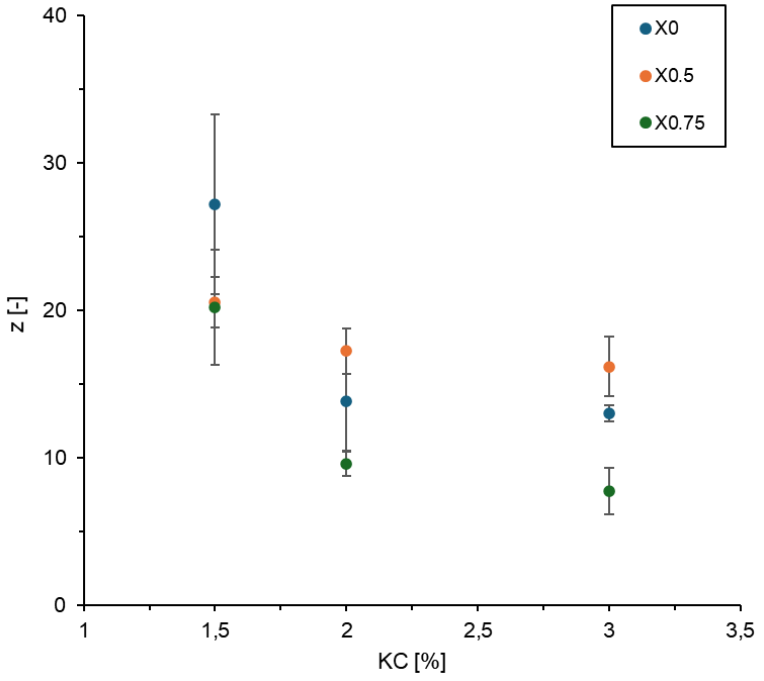

Figure 5.20: Degree of interaction, z, for different unfilled hydrogel formulations.

In the composite systems (Figures 5.21 and 5.22), the gel strength mirrored the non-monotonic behaviour previously observed for the storage and loss moduli. However, the interaction factor displayed a distinct, monotonic decrease with the filler loading.

Crucially, when comparing equivalent volume percentages of granules and pellets, the derived structural parameters were practically identical. This strongly suggests that the modification of the rheological response is governed fundamentally by the volumetric fraction of the dispersed phase, rather than by the specific geometry or type of the filler particles.

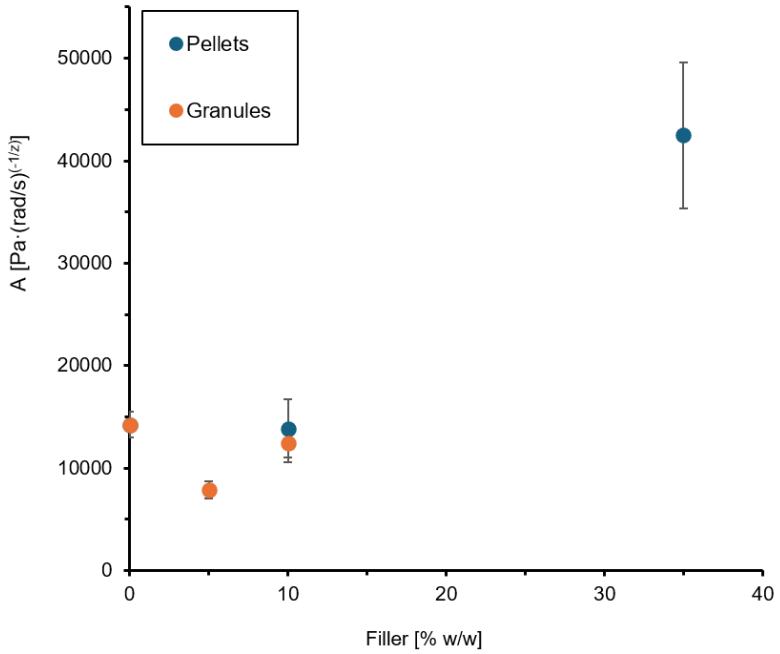

Figure 5.21: Gel strength, A_f, dependence on filler content for K3X0.5 formulations.

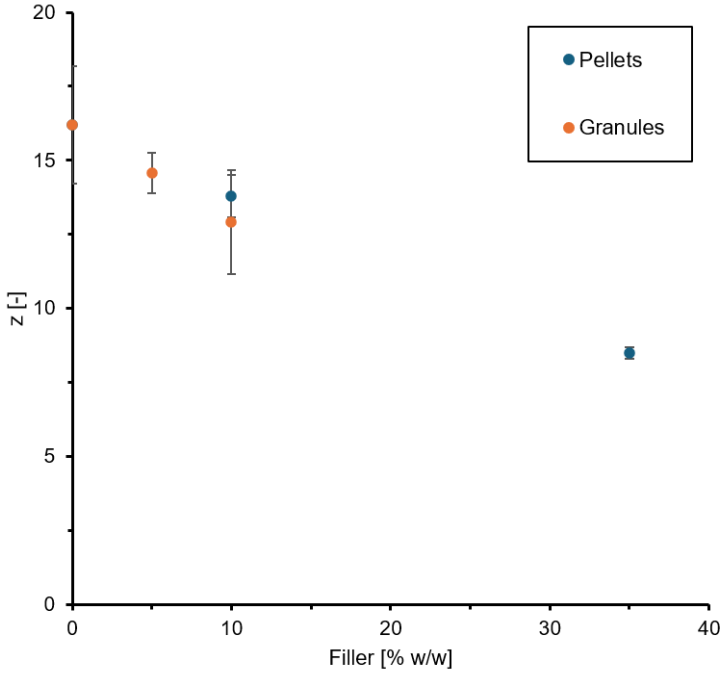

Figure 5.22: Degree of interaction, z, dependence on filler type and content for K3X0.5 formulation.

5.5.4 Printability and shape fidelity

Following the rheological and mechanical characterization, the printability of the candidate inks was quantitatively assessed using the shape fidelity indices defined in Equations 10-12: spreading ratio (SR), uniformity factor (U), pore coefficient (Pr), and perimeter coefficient (C).

The spreading ratio displayed a clear inverse dependency on the ink's viscosity. As illustrated in Figure 5.23, an increase in the concentration of both gelling agents, KC and viscosity enhancers, XG, resulted in a marked reduction of the SR value. This trend confirms that higher viscosities effectively mitigate post-extrusion filament spreading, enhancing dimensional accuracy. However, to demonstrate this hypothesis, a systematic study including a calibration curve with standards would be necessary.

The uniformity factor (U) exhibited a positive correlation with the polymer content. Higher concentrations of rheological modifiers led to a significant reduction in the standard deviation of the spreading ratio, indicating improved consistency along the printed filament length.

A detailed comparison of formulations K1.5X0.5, K1.5X0.75, and K2X0.5 reveals a distinct hierarchical influence of the components. Specifically, the variation in XG exerted a more pronounced effect on filament uniformity than the variation in the KC. This observation is statistically corroborated by the analysis of the error bars (Figure 5.23), where formulations with higher XG content showed reduced variability, pointing to the critical role of the thickener in stabilizing the extrusion flow.

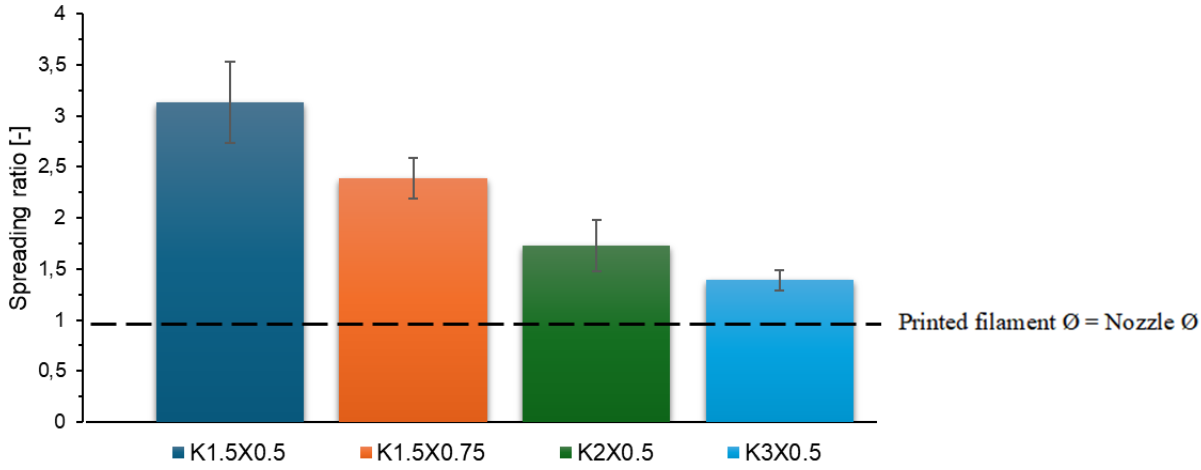

Figure 5.23: Spreading ratio, SR, of the selected best four inks. Error bars are taken as representative of the printed filament uniformity (standard deviation).

Based on the comparative analysis, formulation K3X0.5, exhibiting the lowest spreading ratio and superior filament uniformity, as observed by the lower error bar, was selected as the

benchmark matrix for assessing the impact of the dispersed phase (Figure 5.24). Subsequently, granules and pellets were introduced at varying volumetric fractions to quantify their influence on shape fidelity and extrusion consistency.

At low filler concentrations, the printability remained statistically unchanged compared to the unfilled ink. Neither the spreading ratio nor the uniformity factor displayed significant variation, suggesting that the matrix rheology remains dominant in this regime.

Conversely, at higher loadings the two filler types induced distinct printability defects, likely driven by different physical mechanisms:

- In the case of granules filled inks, a marked increase in the spreading ratio was observed. This phenomenon is attributed to the partial solubility of the granules within the aqueous phase. We speculate that the partial disaggregation and dissolution of the granules foster the release of soluble species that which in their turn induce a localized reduction in bulk viscosity, thereby promoting post-deposition filament slumping (spreading).
- As for pellets filled inks, high pellet concentration primarily compromised filament homogeneity as observed in the increased dimensional variance. This behaviour is consistent with the presence of inert solid inclusions, which perturb the laminar flow profile within the nozzle and disrupt the homogeneity of the extruded strand.

Notably, for pellet-loaded inks, the reduction in printability appears to reach a saturation point: the spreading and uniformity for the 10% and 35% formulations were statistically indistinguishable (overlapping error bars), indicating that beyond a certain threshold, further filler addition does not exacerbate the loss of fidelity.

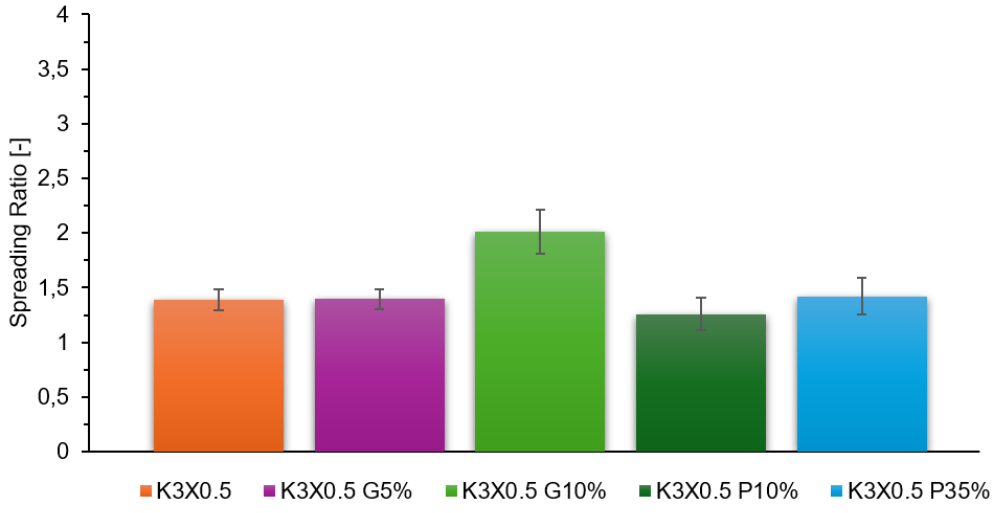

Figure 5.24: Spreading ratio, SR, of K3X0.5 filled ink. Error bars are taken as representative of the printed filament uniformity (standard deviation).

Following the assessment of filament definition, the Pore Coefficient (Pr) and Perimeter Coefficient (C) were evaluated. For the optimized library of base inks, the printed scaffolds demonstrated excellent capability to reproduce the desired geometry. Image analysis confirmed that both indices approximated the ideal value of 1. Interestingly, a subtle yet consistent discrepancy was observed between the two metrics: the internal pore geometry exhibited superior accuracy compared to the external perimeter (Figures 5.25 and 5.26). This is likely an artifact of the deposition path planning. Since the fabrication protocol typically begins with the definition of the outer shell outline, perimeter deposition coincides with the extrusion initiation phase, which is likely more susceptible to transient flow instabilities and trigger irregularities. Conversely, by the time the printhead moves to build the internal structure, the extrusion flow has achieved a steady-state regime, resulting in higher deposition precision.

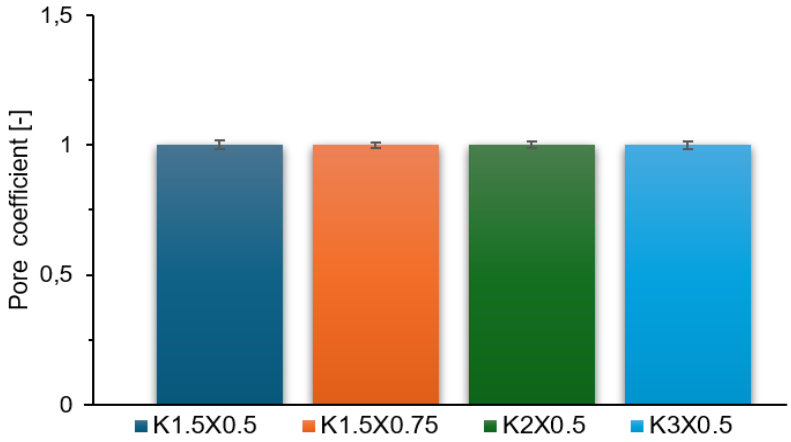

Figure 5.25: Internal geometry fidelity, assessed by pore coefficient parameter for unfilled inks.

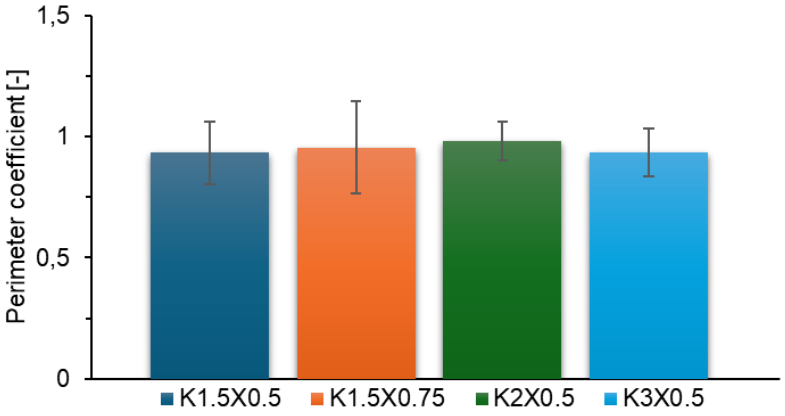

Figure 5.26: External geometry fidelity, assessed by perimeter coefficient parameter for unfilled inks.

Regarding the filler-loaded formulations, all tested inks exhibited high shape fidelity, satisfying the set printability criteria. To maintain methodological consistency with the previous characterization phases, formulation K3X0.5 was considered as the reference matrix for comparative analysis. The measure of geometric fidelity (Pr and C) for the filled inks mirrored the trends observed in the unfilled hydrogels. No statistically significant deviations were recorded across the various filler concentrations, indicating that the inclusion of granules or pellets does not compromise the precision and stability of the printed constructs.

Furthermore, the discrepancy between internal and external accuracy persisted in the loaded systems: the external perimeter consistently displayed slightly lower fidelity compared to the internal geometry (Figures 5.27 and 5.28). This confirms that the loss accuracy is not formulation-dependent, but rather a process artifact associated with flow instability during the extrusion start-up phase.

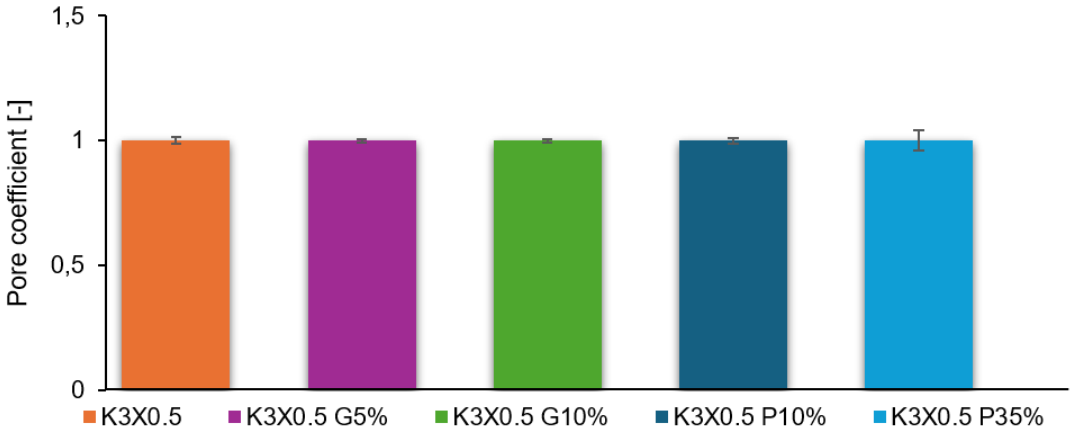

Figure 5.27: pore coefficient parameter for filler-loaded inks (base ink: K3X0.5).

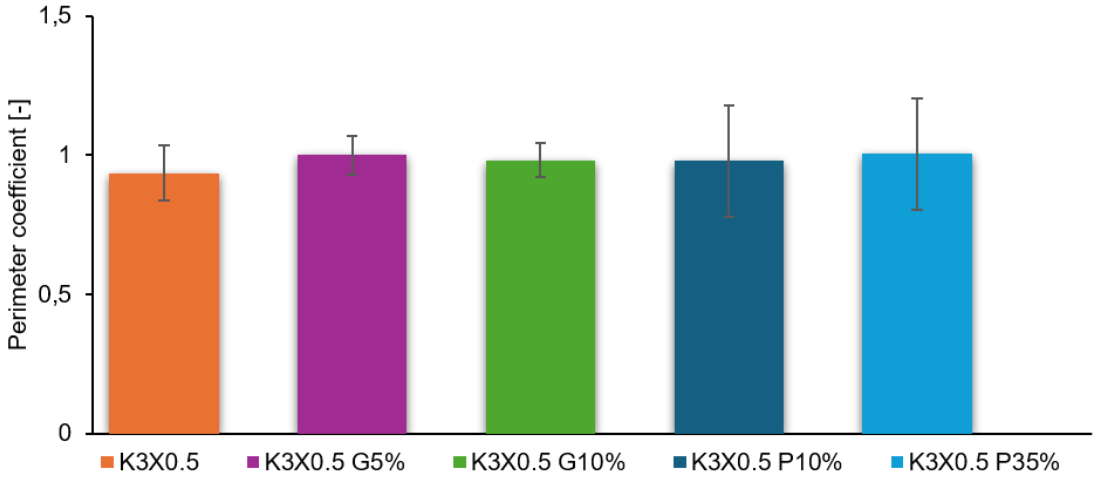

Figure 5.28: perimeter coefficient parameter for filler-loaded inks (base ink: K3X0.5).

Among the quantitative indices evaluated, the spreading ratio and its standard deviation emerged as the most discriminative parameter for the evaluation of printing results. Consequently, this quality index was adopted as the primary selection criterion. Based on this analysis, formulation K3X0.5, which exhibited the most favourable spreading behaviour (minimal post-extrusion deformation), was identified as the optimal candidate. Accordingly, this formulation alone was taken into consideration in the production of 3D printed objects.

5.5.5 3D Printing trials and results

To validate the prediction from the printability indexes, cylindrical constructs were printed using two distinct formulations, as depicted in Figure 5.29. The ink selected were K1.5X0.5 and pellet loaded (35%) K3X0.5, as example of poor printability and a better property of Spreading ratio.

Particularly in figure 5.29: panel (a) displays a construct printed using the K1.5X0.5 formulation with the addition of a coloured tracer to highlight the contours. This specimen exhibits suboptimal shape fidelity, characterized by a noticeable loss of geometric definition, particularly at the high-curvature regions (rounded corners) and evidence of structural sagging.

The panel (b) shows a cylinder fabricated with the K3X0.5 formulation loaded with 35% (w/w) pellets. In stark contrast to the previous sample, this construct demonstrates superior dimensional stability and high shape retention, effectively maintaining sharp features and vertical integrity despite the high solid loading.

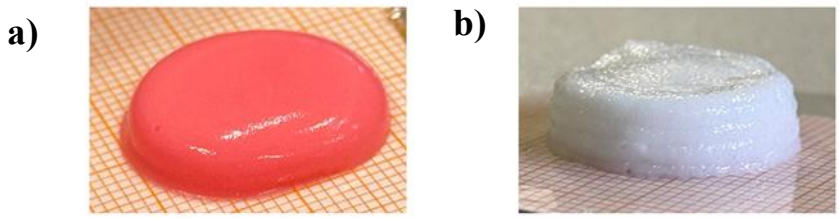

Figure 5.29: (a) K1.5X0.5; (b) K3X0.5 with 35% of pellets.

To further assess the suitability of the optimized matrix for fabricating complex, free-form geometries, a proof-of-concept demonstrator (an elephant-shaped model) was fabricated. Figure 5.30 depicts the resulting construct, printed using the K3X0.5 formulation doped with a food-grade dye to enhance feature visualization. The successful printing of this artifact confirms the material's capability to retain high shape fidelity, even when dealing with varying curvatures and intricate features.

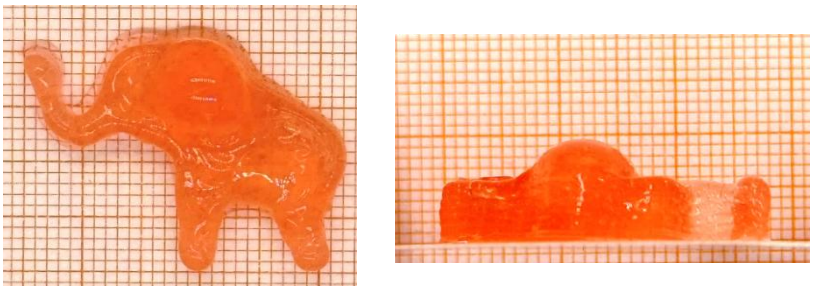

Figure 5.30: up and front view of printed elephant using K3X0.5 formulation.

5.6 Characterization of the gummies as Drug Delivery Systems

Dissolution tests and drug release

In vitro dissolution assays were conducted to evaluate the release kinetics of the active pharmaceutical ingredient, NPX. The test was performed first on granules and pellets as such and in a quantity equal to that estimated to be contained in a hydrogel sample, as reference. Subsequently, two basic gummy-formulations, both filled with granules and pellets, were tested with better and worse printability (K3X0.5 and K1.5X0.5) to compare how much the formulation impacted the performance of the drug delivery system. The dissolution curves, presented in Figure 5.31, demonstrate that both the fillers alone and the filled hydrogel dosage forms (excepting K3X0.5 P35%) exhibit a release complying with the standard requirements for Immediate Release (IR, >80% release at 30 min) formulations. However, a distinct modulation of the kinetics is observed during the initial phase of the process. While the fillers display a pronounced burst release, embedding these particles within the hydrogel network results in a measurable retardation of the initial NPX release rate. This phenomenon is attributed to the presence of the polymeric matrix, which acts as a diffusive barrier, increasing the path length for drug transport. Regarding the comparison between the two filler types, the observed variations in release performance are ascribed to their differences in composition, the specific drug loading capacity, and the distinct manufacturing techniques employed for drug incorporation in each carrier system. While the samples loaded with granules demonstrated to satisfy the immediate release kinetics requirements even with increasing carrageenan concentration (cold-shaded curves in figure 5.31), the systems loaded with pellets showed a slow-release profile which in the case of the K3X0.5 P35% formulation goes beyond the IR requirements (warm-shaded curves in figure 5.31).

In fact, compliance with the immediate release criteria was achieved only with the K1.5X0.5 P35% matrix.

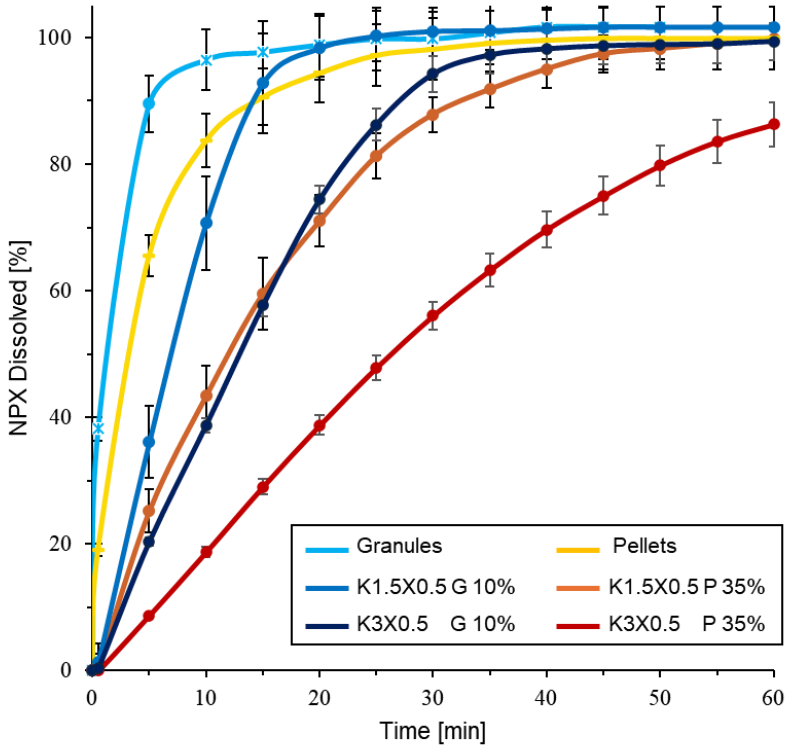

Figure 5.31: NPX dissolution profiles.

This difference in kinetics might be explained by the microstructural properties of the hydrogel network. The K1.5X0.5 formulation, characterized by a lower shear modulus, possesses a lower crosslinking density. According to rubber elasticity theory, this corresponds to a larger average mesh size, which minimizes steric hindrance and facilitates the rapid diffusion of the drug molecules. In contrast, the K3X0.5 formulation exhibits a higher modulus, indicative of a denser polymer network with reduced pore dimensions. This tighter mesh imposes a significant restriction on molecular mobility (hindered diffusion), thereby retarding the elution process.

A similar structural rationale explains the systematic delay observed in pellet-loaded systems compared to granule-loaded ones. As previously established by rheological characterization, hydrogels containing 35% w/w pellets exhibit a higher bulk crosslinking density compared to those with 10% w/w granules. Consequently, the pellet-loaded matrix presents a more tortuous and restrictive diffusive path, leading to the observed reduction in release kinetics.

5.7 Conclusions

The aim of this case of study is to determine structure-properties-performance correlations in a 3D-printed, hydrogel-based gummy designed to incorporate different types of fillers containing active pharmaceutical ingredients.

KC, a natural polymer, was selected as gelling agent due to a gelation temperature low enough to ease the ink handling and printing. The temperature-dependent gelation is expected to enable the formation of the 3D-printed gummy by exploiting the thermal difference between the printhead and the print bed, ensuring proper shape retention. In extrusion-based 3D printing, high viscosity is essential to prevent filament bulging and to ensure precise adherence to the programmed path. For this reason, XG was added to the hydrogel as a thickening agent.

Various formulations can be developed by combining different amounts of gelling and thickening agents to create the base hydrogel, which serves as a matrix for incorporating drug fillers. To identify the most suitable hydrogel for this purpose, a screening process was carried out involving visual inspection, rheological analysis and 3D printing evaluations based on a rational setting of specific requirements, which are related to the ink processing and printing.

At first, the maximum amount of KC was defined based on the ink homogeneity requirement. Viscosity was identified as a critical rheological parameter for the 3D printable filled hydrogel, essential to prevent filler sedimentation during ink formulation and ensure shape retention after printing. Steady shear tests confirmed that all formulations exhibit shear-thinning behaviour, favourable for the extrusion process in 3D printing. Rheological tests revealed that both KC and XG significantly influence viscosity: higher polymer content increases consistency and enhances shear-thinning properties. The presence of fillers further increases viscosity, primarily dependent on filler size and concentration. Formulations with viscosity below a minimum threshold imposed to limit sedimentation were excluded, further reducing the number of design parameters.

As XG shows a thermotropic gelation mechanism, temperature sweep tests were conducted to determine gel transition temperature, T_{gel}, a key parameter for both ink preparation and 3D printing. A strong correlation was observed between κ-carrageenan concentration and T_{gel}, indeed Xanthan gum and drug fillers had minimal influence on gelation temperature. An empirical equation has been proposed to predict the gelation behaviour across untested

formulations. Based on these findings, only formulations with gelation temperatures within the defined processing range (28–50 °C) were selected for further investigation.

κ-Carrageenan and xanthan gum hydrogels were further investigated to assess the effect of formulation on their performance in terms of printing process and as gummies.

Among the formulations remaining after the screening process, the four with the shortest pouring times were selected for printability assessment, to identify the most adequate ink for the 3D printing process. Several parameters were considered to assess printability, but only spreading ratio and its standard deviation (i.e. uniformity factor) resulted significant. Increasing concentrations of gelling and thickening agents improved filament uniformity and reduced spreading, with the thickener having a greater impact on consistency, which seem to indicate solution viscosity as the parameter governing the shape retention. The K3X0.5 formulation demonstrated the best balance of low spreading and high filament uniformity and was therefore selected as the reference one. Adding low filler amounts to this formulation had minimal effect on printability; however, higher granule content increased spreading probably due to their disaggregation and partial solubility, while pellets caused slight irregularities in filament surface aspect without statistically significant differences at varying concentrations.

Final printing trials on cylindrical and elephant-shaped samples were conducted after having optimized the elephant shape through CAD design and adjusting operating variables such as the speed.

Among the formulations tested, the hydrogel K3X0.5 demonstrated the best balance between printability and drug release kinetics, while filler incorporation with granules provided improved cohesion. Additionally, granules contain a higher Naproxen load, allowing for easier modulation of drug content across a wider range by varying their concentration.

This study presents several limitations that should be addressed in future work. Organoleptic properties such as taste and sweetness were not evaluated, although these are crucial for patient compliance, especially in paediatric formulations. Further investigation is needed to determine the optimal type and concentration of sweeteners and flavouring agents, and to assess their impact on the hydrogel's mechanical and release properties. Long-term stability and packaging conditions were also not examined, which are essential to guarantee product shelf-life and effectiveness over time. Moreover, regulatory considerations were beyond the scope of this work but will be critical for product validation, market approval, and clinical implementation. Finally, exploring the feasibility of on-site production of personalized hydrogel gummies in

hospitals or pharmacies could offer significant benefits for rapid patient-specific treatments, representing an important direction for future research.

Building on the understanding and characterization established in this study, a promising future improvement would be the integration of machine learning techniques. Machine learning could efficiently explore a broader formulation space, thus predicting the effects of varying key parameters, accelerating the optimization process and enabling the design of customized hydrogels with tailored properties.

6. Final evaluations and Conclusions

This doctoral dissertation set out to investigate how constituent material formulation, processing parameters, and structural design collectively govern the performance of 3D-printed drug delivery systems, with the overarching goal of defining a practical framework for the rational design of personalized dosage forms with tailored release profiles. Through three complementary case studies *i)* gastroretentive expandable devices for metformin administration, *ii)* reservoir-like vaginal rings for local antibiotic delivery and *iii)* multicomponent hydrogel-based gummies for paediatric oral delivery, the work systematically explored properties–process–performance correlations across different materials, geometries, and administration routes. Taken together, the findings demonstrate that a structured, correlation-driven approach can effectively replace purely empirical, trial-and-error strategies, providing a robust basis for predictive design and process optimization in pharmaceutical 3D printing.

6.1 Summary of main findings by case study

In the first case study, a dual component gastroretentive expandable drug delivery system (GREDDS) was developed for the prolonged and personalized release of metformin within the upper gastrointestinal tract. The system combined a melt-cast poly(ε-caprolactone) (PCL)-based core, capable of loading high metformin doses, with a 3D-printed thermoplastic polyurethane (TPU) umbrella-like skeleton engineered to ensure gastric retention via mechanical interference with the pylorus. The results showed that the degradation and drug release profiles of the core could be finely tuned by adjusting PCL content and the fraction of hydrophilic excipients such as PEG 4000, PEG 8000, or PEO, enabling transition from faster mass loss and liberation to multi-day release windows as PCL content increased. Korsmeyer–Peppas analysis further linked formulation to mechanism, evidencing diffusion-controlled release for PCL-rich matrices and increasingly anomalous transport upon higher hydrophile loading, thus confirming that composition can be used as a rational lever to modulate release kinetics.

For the GREDDS skeleton, the investigation established a clear connection between filament-level TPU properties, fused-filament fabrication conditions, and macroscopic mechanical performance. Tensile tests on filaments and printed specimens demonstrated that, once the effective cross-sectional area is properly accounted for, the intrinsic stress–strain behaviour of

TPU is largely preserved through the printing process, enabling reliable translation of material data into structural design parameters. By varying TPU grade and arm thickness, the maximum resistance to simulated gastric contractions in funnel tests could be rationally tuned, with 2 mm thick arms made from stiffer grades reaching peak forces up to about 4 N, thus safely exceeding the theoretical threshold for gastric retention of 1.9–3 N. At the same time, controlled viscoelastic relaxation, quantified through Time–Temperature Superposition (TTS) and master curves constructed from stress-relaxation experiments, allowed prediction of long-term mechanical stability in the folded state and identification of conditioning protocols at elevated temperature equivalent to up to 18 months of storage at 25 °C. Importantly, after complete degradation of the PCL core, the residual skeleton exhibited a drastic drop in maximum funnel force to approximately 0.3 N, well below gastric contractile forces, ensuring safe transition from a retentive to a passable configuration as an intrinsic safety feature of the design.

The second case study focused on dual-component reservoir-like vaginal rings, designed for prolonged and customizable local delivery of metronidazole (MTZ) to treat bacterial vaginosis. Here, a compliant thermoplastic elastomer (TPE) shell, manufactured by FDM, was combined with an in-situ crosslinking alginate hydrogel precursor highly loaded with MTZ, allowing decoupled optimization of structural and functional, formulation-related, performance. Rheological characterization of the TPE demonstrated shear-thinning behaviour and a favourable viscoelastic profile, with solid-like behaviour at low frequencies and more viscous-like response at higher frequencies and temperatures, which together supported defect-free printing, layer adhesion, and stable ring geometry. Controlled processing parameters—such as nozzle pressure, printing temperature and bed temperature—enabled reproducible fabrication of quarters of the ring with low variability in mass and dimensions, thereby providing a robust platform for precisely tuning the open surface area, which was shown to control the release kinetics. The work established quantitative links between composition, rheology, extrudability, mechanical stability and release performance at high MTZ loadings. The incorporation of MTZ powder above solubility limits produced a marked, non-linear increase in viscosity and, for the highest drug loads, a transition towards yield-stress, Bingham-like behaviour, beneficial to prevent dripping but requiring higher extrusion pressures. By fitting flow curves with Cross and Herschel–Bulkley models and using a 3D bioprinter as a capillary rheometer, it was possible to reliably extrapolate apparent viscosity at the high shear rates relevant to ring filling, thus enabling predictive assessment of extrudability from rheological data alone. After gelation, MTZ particles acted as stiffening fillers that increased the storage modulus, but their gradual dissolution generated cavities that accelerated fragmentation, especially in formulations with

lower alginate content or higher MTZ volume fractions, revealing a critical trade-off between mechanical robustness and release duration. Drug release studies finally showed that the MTZ release rate was linearly proportional to the OSA/volume ratio and primarily governed by the limited solubility of MTZ and the geometry-controlled thickness of the saturated layer through which diffusion occurred. By varying ring design, it was possible to maintain nearly constant release rates over extended periods simply by changing OSA, without altering hydrogel composition, demonstrating the potential of geometry-based personalization.

The third case study addressed the development of 3D-printed hydrogel-based gummies as chewable dosage forms for paediatric oral delivery, designed to combine immediate or fast release with improved acceptability, vegan composition and reduced sugar content. The core of this work was the formulation and systematic screening of κcarrageenan (KC)/xanthan gum (XG) inks, with and without Naproxen-containing granules or pellets, to establish correlations between solution rheology, gelation temperature, printability metrics, hydrogel mechanics and drug release performance. Steady-shear rheology showed that both KC and XG critically modulated viscosity and shear-thinning behaviour, with KC concentration exerting a dominant effect and XG acting as a powerful thickener, particularly at lower KC contents. A minimum apparent viscosity threshold of 1.7 Pa·s at low shear rates was set to prevent sedimentation of suspended multi-particulate fillers within the typical printing time and syringe filling height, and this criterion, combined with Stokes-law-based estimates of sedimentation velocity, was used to exclude formulations with insufficient phase stability from further investigation. Temperature-sweep tests allowed definition of an operational window for gelation temperature compatible with printhead and bed constraints and led to the derivation of a predictive logarithmic relationship between KC content and T_{gel}, ensuring that selected formulations gelled above room temperature but below the maximum process temperature.

On the hydrogel side, oscillatory rheology and the application of weak-gel theory to the relevant experimental results revealed how KC concentration predominantly controlled the magnitude of storage and loss moduli, while XG played a subtler role, slightly reducing moduli in the stiffest systems and improving reproducibility. The addition of solid fillers (granules or pellets) induced a non-monotonic evolution of viscoelastic properties, initially weakening the network and then reinforcing it at high loading, where the mechanical contribution of the rigid particulate phase became dominant. Printability tests using a bioprinter equipped with a syringe-pump head and structured image analysis provided a set of quantitative indices—spreading ratio, uniformity factor, pore coefficient and perimeter coefficient—that linked ink

formulation and printing conditions to filament quality and grid fidelity. Finally, dissolution studies on both cast and printed hydrogels loaded with Naproxen granules or pellets revealed distinct release behaviours: granule-loaded gummies supported faster, more immediate release, while pellet-containing systems provided more prolonged profiles, thereby offering a modular means to tailor kinetics within the same family of dosage forms.

6.2 General considerations for a 3D-printing design framework

Beyond the specific outcomes of each case study, the work contributes a transversal, correlation-based framework for designing 3D-printed drug delivery systems that can be generalized across materials and routes of administration. First, it demonstrates that systematic rheological characterization – through models such as Cross, Herschel–Bulkley and Power Law, and complemented by mechanical tests on the material in the solid state (e.g. stress-relaxation tests and the application of time temperature superposition) – provides a powerful predictive handle on both processability (e.g. extrudability, filament/stringing behaviour, sedimentation stability) and performance-relevant microstructure (e.g. gel strength, weak-gel parameters), reducing reliance on empirical printing trials. Second, it shows that geometric design parameters, such as arm thickness and infill orientation in gastroretentive skeletons, ring open surface area and shell thickness in vaginal rings, or nozzle diameter and infill patterns in hydrogel gummies, can be tightly linked to in vitro mechanical and release metrics through appropriately chosen test methods (funnel tests, oscillatory rheology, dissolution), enabling targeted tuning of device behaviour.

Third, the thesis highlights the importance of modular, dual-component and multicomponent architectures that decouple structural and formulation roles, thereby widening the design space and facilitating personalization. In the GREDDS and vaginal ring systems, this decoupling enabled independent optimization of mechanical retention and drug release, while in the gummies it allowed combination of a common hydrogel matrix with different multi-particulate drug releasing fillers to diversify release profiles. Across all case studies, the adoption of project-engineering, requirement-driven strategies – starting from explicit functional targets (e.g. residence time, release duration, mechanical requirements, extrudability windows) and working to identify suitable material formulations and printing parameters—proved effective in translating structure–process–performance correlations into practical design rules.

6.3 Practical implications for personalized drug delivery

From a practical standpoint, the outcomes of this research underscore the potential of 3D printing as an enabling tool for truly personalized drug delivery solutions across diverse clinical scenarios. The gastroretentive expandable drug delivery system concept suggests that once suitable material–geometry combinations are identified, it is possible to tailor metformin dose and release duration within the same platform by modifying core composition and, in perspective, skeleton dimensions, offering individualized therapy for chronic metabolic diseases while potentially improving adherence by reducing dosing frequency. The reservoir-like vaginal rings demonstrate that, by decoupling shell geometry from hydrogel composition, it is feasible to adjust OSA and hence release rate without reformulating the drug-loaded reservoir, which is particularly attractive for adapting local antibiotic regimens to different disease severities or recurrence risks. The hydrogel gummies exemplify how 3D printing can converge nutritional and pharmaceutical design, enabling visually appealing, vegan, low-sugar, and dose-flexible dosage forms that are especially suitable for paediatric patients or individuals with swallowing difficulties.

Moreover, the methodologies adopted in this work are compatible with point-of-care or near-patient manufacturing scenarios, where semisolid extrusion (SSE) and fused deposition modeling (FDM) can be integrated into hospital or community pharmacy workflows, as already suggested in emerging clinical studies on 3D-printed paediatric dosage forms. The emphasis on quantitative, model-based correlations and on reproducible process windows also supports future integration of these approaches into quality-by-design frameworks and advanced process control strategies, which are essential prerequisites for regulatory acceptance of 3D-printed medicinal products. In this sense, the thesis provides both scientific insight and practical tools that can inform the transition of 3D-printed drug delivery systems from laboratory feasibility to clinically and industrially viable solutions.

6.4 Limitations

Despite these advances, several limitations must be acknowledged. First, the experimental work was primarily confined to in vitro characterization, including mechanical testing, rheology, physic-chemical analysis and dissolution experiments, without extending to in vivo pharmacokinetic or pharmacodynamic evaluations. As a result, the translation of the observed release and retention profiles into actual therapeutic outcomes—such as bioavailability

improvement for metformin, clinical cure and recurrence rates for bacterial vaginosis, or adherence gains in paediatric patients—remains to be demonstrated.

Second, while the thesis systematically explored a rationally selected subset of formulations and geometries, the overall design space of printable materials, process conditions and structural configurations is considerably larger; further optimization and validation would be required to broaden applicability to other drugs or dosing regimens.

Third, scale-up and long-term stability considerations were only partially addressed. For example, the TTS-based assessment of TPU viscoelastic relaxation provided a sound basis for predicting mechanical stability over extended storage, but comprehensive stability studies on complete assembled systems, including potential interactions between components and real-world environmental fluctuations, were beyond the scope of this work. Similarly, the manufacturing approaches, while scalable in principle, were implemented on laboratory-scale FDM and SSE platforms; issues such as continuous production, automation, in-line monitoring and regulatory compliance under GMP conditions remain to be fully resolved. Lastly, aspects that are critical for patient acceptance, such as the sensory and organoleptic characteristics of gummies or the user experience associated with ring insertion and wear, were not experimentally investigated and should be carefully considered in future translational studies.

6.5 Future perspectives and Conclusions

Building on the structure–process–performance correlations established in this work, several directions for future research can be envisaged. A priority is the *in vivo* validation of the most promising prototypes, for example through preclinical and clinical studies assessing gastroretentive residence time and metformin pharmacokinetics for GREDDS, vaginal pharmacokinetics and clinical outcomes for antibiotic rings, and bioavailability and acceptability for paediatric gummies. Such studies would not only confirm the therapeutic relevance of the in vitro findings but also help refine design criteria by linking structural and process parameters to meaningful clinical endpoints. A second avenue is the expansion of the material and drug space, leveraging the same correlation-based strategies to accommodate additional APIs, including poorly soluble, biologic or thermosensitive molecules, and to explore alternative polymers and crosslinking mechanisms tailored to specific stability and release requirements.

In parallel, the wealth of experimental data generated on rheology, printability, mechanical behaviour and release could be harnessed to develop data-driven or machine-learning models,

capable of predicting process windows and performance outcomes from formulation and design inputs, thereby further reducing experimental burden and accelerating development. At the manufacturing level, integrating these models into digital workflows, potentially connected to hospital or industrial 3D-printing units, could support real-time adaptation of dosage form geometry and composition to individual patient needs while maintaining stringent quality standards. Finally, given the regulatory and ethical challenges associated with personalized 3D-printed medicines, future work should also address standardization of characterization protocols, establishment of design spaces under quality-by-design paradigms, and dialogue with regulatory agencies to define appropriate pathways for approval and post-marketing surveillance.

In conclusion, this dissertation demonstrates that a structured, correlation-driven approach to materials, process and structural design can provide a solid foundation for the rational development of 3D-printed drug delivery systems. By spanning multiple administration routes, dosage forms and therapeutic contexts, the three case studies collectively validate the central hypothesis that understanding and exploiting properties–process–performance relationships is key to unlocking the full potential of pharmaceutical 3D printing in the era of personalized medicine.

7. References

Aina, Morenikeji; Baillon, Fabien; Sescousse, Romain; Sanchez-Ballester, Noelia M.; Begu, Sylvie; Soulairol, Ian; Sauceau, Martial. (2025). From conception to consumption: Applications of semi-solid extrusion 3D printing in oral drug delivery. *International Journal of Pharmaceutics*, 674, 125436. doi:10.1016/j.ijpharm.2025.125436

Altun, Esra; Yuca, Esra; Ekren, Nazmi; Kalaskar, Deepak M.; Ficai, Dan; Dolete, Georgiana; Ficai, Anton. (2021). Kinetic Release Studies of Antibiotic Patches for Local Transdermal Delivery. *Pharmaceutics*, 13(5), 613. doi:10.3390/pharmaceutics13050613

Azad, Mohammad A.; Olawuni, Deborah; Kimbell, Georgia; Badruddoza, Abu Zayed Md; Hossain, Md. Shahadat; Sultana, Tasnim. (2020). Polymers for Extrusion-Based 3D Printing of Pharmaceuticals: A Holistic Materials–Process Perspective. *Pharmaceutics*, 12(2), 124. doi:10.3390/pharmaceutics12020124

Bellinger, Andrew M.; Jafari, Mousa; Grant, Tyler M.; Zhang, Shiyi; Slater, Hannah C.; Wenger, Edward A.; Mo, Stacy; Lee, Young-Ah Lucy; Mazdiyasni, Hormoz; Kogan, Lawrence; Barman, Ross; Cleveland, Cody; Booth, Lucas; Bensel, Taylor; Minahan, Daniel; Hurowitz, Haley M.; Tai, Tammy; Daily, Johanna; Nikolic, Boris; Wood, Lowell; Eckhoff, Philip A.; Langer, Robert; Traverso, Giovanni. (2016). Oral, ultra–long-lasting drug delivery: Application toward malaria elimination goals. *Science Translational Medicine*, 8(365), 365ra157. doi:10.1126/scitranslmed.aag2374

Bruschi, Marcos Luciano. (2025). *Strategies to Modify the Drug Release from Pharmaceutical Systems.* Woodhead Publishing.

Chai, Qinyuan; Jiao, Yang; Yu, Xinjun. (2017). Hydrogels for Biomedical Applications: Their Characteristics and the Mechanisms behind Them. *Gels*, 3(1), 6. doi:10.3390/gels3010006

Čižauskaitė, Gabija; Jakubaitytė, Rūta; Žilius, Mindaugas; Jurevičiūtė, Inga; Ivanauskas, Lukas; Jakštas, Vidas. (2019). Natural Ingredients-Based Gummy Bear Composition Designed According to Texture Analysis and Sensory Evaluation In Vivo. *Molecules*, 24(7), 1442. doi:10.3390/molecules24071442

Colombo, Francesco A. (2015). *Principi di tecnologie farmaceutiche.* CEA Editrice.

Costa, Sousa Lobo.(2001). Modeling and comparison of dissolution profiles. *Eur J Pharm Sci,*13(2):123-33. doi: 10.1016/s0928-0987(01)00095-1.

Crump, Scott S. (1989). *US Patent No. US5121329A.*

Dash, Priyabrata N.; Murthy, P. N.; Nath, L. K. (2010). Kinetic modeling on drug release from controlled systems. *Acta Poloniae Pharmaceutica – Drug Research*, 67(3), 217–223.

David, Reinhard; Nandhakumar, Gurusamy. (2025). Magnetic microspheres: Pioneering advancements in precision drug delivery and beyond. *World Journal of Pharmaceutical Research*, 14(5), 198–217. doi:10.20959/wjpr20255-35671

Davis, Mark E.; Chen, Zhen; Shin, David M. (2008). Nanoparticle therapeutics: an emerging treatment modality for cancer. *Nature Reviews Drug Discovery*, 7, 771–782. doi:10.1038/nrd2614

Dumpa, Nagireddy; Butreddy, Anilkumar; Komanduri, Naga Venkata Krishna; Bandari, Siva; Repka, Michael A. (2021). 3D printing in personalized drug delivery: An overview of hot-melt

extrusion-based fused deposition modeling. *International Journal of Pharmaceutics*, 600, 120501. doi:10.1016/j.ijpharm.2021.120501

Ezike, Tochukwu C.; Ugwu, Ogechukwu; Eze, Chidimma; Ogbuefi, Ugochukwu; Okafor, Chinenye. (2023). Advances in drug delivery systems, challenges and future directions. *Heliyon*, 9(7), e17488. doi:10.1016/j.heliyon.2023.e17488

Fanous, Marina; Bitar, May; Gold, Shira; Khalil, George; Khalil, Rami; Khalil, Youssef; Khalil, Hadi; Khalil, Samer. (2021). Development of immediate release 3D-printed dosage forms for a poorly water-soluble drug by fused deposition modeling: Study of morphology, solid state and dissolution. *International Journal of Pharmaceutics*, 598, 120417. doi:10.1016/j.ijpharm.2021.120417

Farmacopea Ufficiale della Repubblica Italiana. (2008). Roma: Zecca dello stato.

Ferry, John D. (1980). *Viscoelastic properties of polymers.* JOHN WILEY & SONS.

Fu, Yao; Kao, Wei-Jen. (2010). Drug release kinetics and transport mechanisms of non-degradable and degradable polymeric delivery systems. *Expert Opinion on Drug Delivery*, 7(4), 429–444. doi:10.1517/17425241003602259

Gabriele, Domenico; De Cindio, Bernardo; D'Antona, Paola. (2001). A weak gel model for foods. *Rheologica Acta*, 40, 120–127. doi:10.1007/s003970000139

Ganatra, Laxmi J.; Patel, Dhruv; Patel, Riddhi; Patel, Jignesh; Patel, Bhavesh; Patel, Dharmesh. (2024). Drug-loaded vegan gummies for personalized dosing of simethicone: A feasibility study of semi-solid extrusion-based 3D printing of pectin-based low-calorie drug gummies. *International Journal of Pharmaceutics*, 635, 123777. doi:10.1016/j.ijpharm.2024.123777

Geever, Liam M.; Devine, Declan M.; Nugent, Michael J. D.; Kennedy, James E.; Lyons, John G.; Higginbotham, Catherine L. (2008). Characterisation and controlled drug release from novel drug-loaded hydrogels. *European Journal of Pharmaceutics and Biopharmaceutics*, 69(3), 1147–1159. doi:10.1016/j.ejpb.2007.12.021

Geonzon, Francis B.; Raghavan, Srinivasa R. (2020). Gelation mechanism and network structure in gels of carrageenans and their mixtures viewed at different length scales – A review. *Food Hydrocolloids*, 101, 106039. doi:10.1016/j.foodhyd.2020.106039

Geonzon, Rhea G.; Raghavan, Srinivasa R. (2019). Network structure and gelation mechanism of kappa and iota carrageenan elucidated by multiple particle tracking. *Food Hydrocolloids*, 90, 173–180. doi:10.1016/j.foodhyd.2019.01.062

Gerstle, Travis L.; Ibrahim, Ahmed M. S.; Kim, Paul S.; Lee, Brian T.; Lin, Samuel J. (2014). A Plastic Surgery Application in Evolution. *Plastic and Reconstructive Surgery – Ideas and Innovations*, 133(2), 446–451.

Gültekin, Hasan E.; Tort, Selin; Acartürk, Füsun. (2019). An effective technology for the development of immediate release solid dosage forms containing low-dose drug: Fused deposition modeling 3D printing. *Pharmaceutical Research*, 36, 128. doi:10.1007/s11095-019-2620-2

Herrada-Manchón, Héctor; Goyanes, Alvaro; Basit, Abdul W.; Gaisford, Simon. (2020). 3D printed gummies: Personalized drug dosage in a safe and appealing way. *International Journal of Pharmaceutics*, 588, 119687. doi:10.1016/j.ijpharm.2020.119687

Höfer, Reinhard M. (2018). Sedimentation of inertialess particles in Stokes flows. *Communications in Mathematical Physics*, 360, 55–101. doi:10.1007/s00220-018-3131-y

ISO/ASTM 52900. (2026). Retrieved from https://www.iso.org/obp/ui/#iso:std:iso-astm:52900:dis:ed-2:v1:en

Kempin, Wolfgang; Domínguez-Robles, Juan; Fuenmayor, Eder; Stirling, Richard; Thakur, Rahul R. S.; Goyanes, Alvaro; Basit, Abdul W.; Gaisford, Simon. (2018). Immediate release 3D-printed tablets produced via fused deposition modeling of a thermo-sensitive drug. *Pharmaceutical Research*, 35, 124. doi:10.1007/s11095-018-2397-y

Kirtane, Ameya R.; Abouzid, Omar; Minahan, Daniel; Bensel, Taylor; Hill, Alison L.; Selinger, Christian; Bershteyn, Anna; Craig, Morgan; Mo, Shirley S.; Mazdiyasni, Hormoz; Cleveland, Cody; Rogner, Jaimie; Lee, Young-Ah Lucy; Booth, Lucas; Javid, Farhad; Wu, Sarah J.; Grant, Tyler; Bellinger, Andrew M.; Nikolic, Boris; Hayward, Alison; Wood, Lowell; Eckhoff, Philip A.; Nowak, Martin A.; Langer, Robert; Traverso, Giovanni. (2018). Development of an oral once-weekly drug delivery system for HIV antiretroviral therapy. *Nature Communications*, 9, 2. doi:10.1038/s41467-017-02294-6

Korelc, Karin; Seme-Lipej, Barbara; Kocbek, Petra; Kristl, Julijana. (2024). Towards personalized drug delivery via semi-solid extrusion: Exploring poly(vinyl alcohol-co-vinyl acetate) copolymers for hydrochlorothiazide-loaded films. *European Journal of Pharmaceutical Sciences*, 194, 106645. doi:10.1016/j.ejps.2024.106645

Kumar, Akash; Sandhu, Lovepreet Kaur; Duggal, Sanjiv. (2025). A Comprehensive Review on Controlled Release Drug Delivery System. *International Journal of Research Publication and Reviews*, 6(5), 13787–13795.

Lane, Majella E.; Maria, José. (2003). *Modified-release drug delivery technology.* . New York: Marcel Dekker.

Leong, Kam Fai; Cheah, Ching Kit; Chua, Chee Kai. (2003). Solid freeform fabrication of three-dimensional scaffolds for engineering replacement tissues and organs. *Biomaterials*, 24(13), 2363–2378. doi:10.1016/S0142-9612(03)00030-9

Maroni, Alessandra; Zema, Lucia; Del Curto, Barbara; Foppoli, Anastasia; Gazzaniga, Andrea. (2013). Film coatings for oral pulsatile release. *International Journal of Pharmaceutics*, 457(1), 177–183. doi:10.1016/j.ijpharm.2013.03.010

Melocchi, Alice; Parietti, Federico; Maroni, Alessandra; Foppoli, Anastasia; Gazzaniga, Andrea; Zema, Lucia. (2016). Hot-melt extruded filaments based on pharmaceutical grade polymers for 3D printing by fused deposition modeling. *International Journal of Pharmaceutics*, 509(1–2), 255–263. doi:10.1016/j.ijpharm.2016.05.036

Melocchi, Alice; Uboldi, Marta; Maroni, Alessandra; Foppoli, Anastasia; Palugan, Laura; Zema, Lucia; Gazzaniga, Andrea. (2021). The Chronotopic™ system for pulsatile and colonic delivery of active molecules in the era of precision medicine: Feasibility by 3D printing via fused deposition modeling (FDM). *Pharmaceutics*, 13(5), 759. doi:10.3390/pharmaceutics13050759

Merli, Marta; Bianchi, Federica; Di Giuseppe, Davide; Pugliese, Roberto; Vozzi, Giovanni; Ahluwalia, Arti. (2022). Pectin-based bioinks for 3D models of neural tissue produced by a pH-controlled kinetics. *Frontiers in Bioengineering and Biotechnology*, 10, 1032542. doi:10.3389/fbioe.2022.1032542

Murphy, Sean V.; Atala, Anthony. (2014). 3D bioprinting of tissues and organs. *Nature Biotechnology*, 32, 773–785. doi:10.1038/nbt.2958

Niu, Meng; Zhang, Zhen; Li, Yuxin; Wang, Xiaoyu; Li, Meng. (2023). Investigation of 3D printing of children starch gummies with precise and special shape based on change of model parameters. *Journal of Food Engineering*, 352, 111568. doi:10.1016/j.jfoodeng.2023.111568

Nsengiyumva, Emmanuel M.; Agyemang, Paul; Ofori, Isaac; Zhang, Xiaoying; Zhang, Hong. (2022). Xanthan gum in aqueous solutions: Fundamentals and applications. *International Journal of Biological Macromolecules*, 209, 583–604. doi:10.1016/j.ijbiomac.2022.06.189

Paarakh, Mukesh P.; Jose, Paul A.; Setty, Chandrashekhar; Peterchristoper, Gnanaraj. (2023). Release kinetics – concepts and applications. *International Journal of Pharmacy Research & Technology (IJPRT)*, 8(1), 12–20. doi:10.31838/ijprt/08.01.02

Parulski, Oliver J.; Jannin, Vincent; Goyanes, Alvaro. (2021). Challenges of fused deposition modeling 3D printing in pharmaceutical applications: Where are we now? *Advanced Drug Delivery Reviews*, 176, 113810. doi:10.1016/j.addr.2021.113810

Penumakala, Praveen K.; Santo, Loredana; Kandasubramanian, Balasubramanian. (2020). A critical review on the fused deposition modeling of thermoplastic polymer composites. *Composites Part B: Engineering*, 201, 108336. doi:10.1016/j.compositesb.2020.108336

Pereira, Gabriela F.; Figueiredo, Susana; Fernandes, Ana I.; Pinto, João F. (2020). Polymer selection for hot-melt extrusion coupled to fused deposition modelling in pharmaceutics. *Pharmaceutics*, 12(8), 795. doi:10.3390/pharmaceutics12080795

Pietrzak, Katarzyna; Isreb, Abdullah; Alhnan, Mohamed A. (2015). A flexible-dose dispenser for immediate and extended release 3D printed tablets. *European Journal of Pharmaceutics and Biopharmaceutics*, 96, 380–387. doi:10.1016/j.ejpb.2015.07.027

Rahman, J. M. H.; Nordin, M. N.; Zainal, N. H.; Ahmad, M. I.; Jusoh, M. (2020). Rheological and mechanical properties of edible gel materials for 3D food printing technology. *Heliyon*, 6(11), e05859. doi:10.1016/j.heliyon.2020.e05859

Rengier, Fabian; Mehndiratta, Anurag; von Tengg-Kobligk, Henning; Zechmann, Christoph M.; Unterhinninghofen, Roland; Kauczor, Hans-Ulrich; Giesel, Frederik L. (2010). 3D printing based on imaging data: review of medical applications. *International Journal of Computer Assisted Radiology and Surgery*, 5, 335–341. doi:10.1007/s11548-010-0476-x

Rodríguez-Maciñeiras, Xela; Barcia-López, Cristina; López-Iglesias, Marta; Tomé-Miguéns, Marta; Martínez-Pérez, Laura; Lado-Tomé, Marta; Goyanes, Alvaro. (2025). Advancing medication compounding: Use of a pharmaceutical 3D printer to auto-fill minoxidil capsules for dispensing to patients in a community pharmacy. *International Journal of Pharmaceutics*, 646, 125251. doi:10.1016/j.ijpharm.2025.125251

Rodríguez-Pombo, Lucía; Ares-López, Ana; López-Iglesias, Marta; Gómez-Lado, Noelia; Barcia, Elena; Tomé, Marta; Goyanes, Alvaro. (2022). Innovations in Chewable Formulations: The Novelty and Applications of 3D Printing in Drug Product Design. *Pharmaceutics*, 14(8), 1732. doi:10.3390/pharmaceutics14081732

Rodríguez-Pombo, Lucía; López-Iglesias, Marta; Paredes-López, Marta; Martínez-Pérez, Laura; Lado-Tomé, Marta; Goyanes, Alvaro. (2024). Paediatric clinical study of 3D-printed personalised medicines for rare metabolic disorders. *International Journal of Pharmaceutics*, 642, 124140. doi:10.1016/j.ijpharm.2024.124140

Rycerz, Karolina; Stepien, Karolina A.; Czapiewska, Magdalena; Arafat, Basit; Goyanes, Alvaro; Basit, Abdul W.; Gaisford, Simon. (2019). Embedded 3D printing of novel bespoke soft dosage form concept for pediatrics. *Pharmaceutics*, 11(12), 630. doi:10.3390/pharmaceutics11120630

Sardelli, Maria; Tognato, Riccardo; Vozzi, Giovanni; Ahluwalia, Arti; Tonda-Turo, Caterina; Zanetti, Marco; Visai, Livia; Ricotti, Leonardo. (2021). Reactive printing of engineered alginate inks. *Soft Matter*, 17, 8105–8117. doi:10.1039/D1SM00604E

Seoane-Viaño, Iria; Januskaite, Patricija; Alvarez-Lorenzo, Carmen; Basit, Abdul W.; Goyanes, Alvaro. (2021). Semi-solid extrusion 3D printing in drug delivery and biomedicine: Personalised solutions for healthcare challenges. *Journal of Controlled Release*, 332, 367–389. doi:10.1016/j.jconrel.2021.02.027

Starosolski, Zbigniew A.; Hollister, Scott J.; Wheeler, Matthew B.; Johnson, Kevin M.; Shih, Andrew. (2014). Application of 3-D printing (rapid prototyping) for creating physical models of pediatric orthopedic disorders. *Pediatric Radiology*, 44, 216–221. doi:10.1007/s00247-013-2800-1

Stojkov, Goran; Niyazov, Zafar; Niyazov, Zoran. (2021). Relationship between Structure and Rheology of Hydrogels for Various Applications. *Gels*, 7(4), 255. doi:10.3390/gels7040255

Tambe, Srushti; Jaiswal, Deepak; Sharma, Pankaj; Sharma, Shubham; Singh, Gurmeet; Singh, Gurvinder. (2021). Hot-melt extrusion: Highlighting recent advances in pharmaceutical applications. *Journal of Drug Delivery Science and Technology*, 63, 102452. doi:10.1016/j.jddst.2021.102452

Theus, Alexander S.; Sarker, Mahmudul; Chen, Xiongbiao. (2020). Bioprintability: Physiomechanical and biological requirements of materials for 3D bioprinting processes. *Polymers*, 12(10), 2262. doi:10.3390/polym12102262

Williams, Malcolm L.; Ferry, John D.; Landel, Robert F. (1955). The temperature dependence of relaxation mechanisms in amorphous polymers and other glass-forming liquids. *Journal of the American Chemical Society*, 77(14), 3701–3707. doi:10.1021/ja01619a008

Wu, Iren Yeeling; Balakrishnan, Saravanan; Babu, Suresh; Basu, Anirban. (2019). Interpreting non-linear drug diffusion data: Utilizing Korsmeyer–Peppas model to study drug release from liposomes. *European Journal of Pharmaceutical Sciences*, 138, 105026. doi:10.1016/j.ejps.2019.105026

Yoo, E. M. (1989). *US Patent No. US6508980B1.*

Zheng, Jian-Yuan; Yang, Li-Hua; Wang, Rui; Li, Xiao-Feng. (2025). Targeted polymeric drug delivery systems with stimuli-responsive release capabilities: Status and future perspectives. *Nanomedicine*, 20(18), 2609–2612. doi:10.1080/17435889.2025.2541570

Expert Opinion on Drug Delivery

ISSN: (Print) (Online) Journal homepage: https://www.tandfonline.com/loi/iedd20

Development of a multi-component gastroretentive expandable drug delivery system (GREDDS) for personalized administration of metformin

Marco Uboldi, Arianna Chiappa, Margherita Rossi, Francesco Briatico-Vangosa, Alice Melocchi & Lucia Zema

To cite this article: Marco Uboldi, Arianna Chiappa, Margherita Rossi, Francesco Briatico-Vangosa, Alice Melocchi & Lucia Zema (13 Dec 2023): Development of a multi-component gastroretentive expandable drug delivery system (GREDDS) for personalized administration of metformin, Expert Opinion on Drug Delivery, DOI: 10.1080/17425247.2023.2294884

To link to this article: https://doi.org/10.1080/17425247.2023.2294884

Published online: 13 Dec 2023.

EXPERT OPINION ON DRUG DELIVERY
https://doi.org/10.1080/17425247.2023.2294884

Taylor & Francis
Taylor & Francis Group

ORIGINAL RESEARCH

Development of a multi-component gastroretentive expandable drug delivery system (GREDDS) for personalized administration of metformin

Marco Uboldi[a], Arianna Chiappa[b], Margherita Rossi[b], Francesco Briatico-Vangosa[b], Alice Melocchi[a] and Lucia Zema[a]

[a]Sezione di Tecnologia e Legislazione Farmaceutiche "Maria Edvige Sangalli", Dipartimento di Scienze Farmaceutiche, Università degli Studi di Milano, Milano, Italy; [b]Dipartimento di Chimica, Materiali e Ingegneria Chimica "G. Natta", Politecnico di Milano, Milano, Italy

ABSTRACT

Objectives: Efficacy and compliance of type II diabetes treatment would greatly benefit from dosage forms providing controlled release of metformin in the upper gastrointestinal tract. In this respect, the feasibility of a new system ensuring stomach-retention and personalized release of this drug at its absorption window for multiple days was investigated.

Methods: The system proposed comprised of a drug-containing core and a viscoelastic umbrella-like skeleton, which were manufactured by melt-casting and 3D printing. Prototypes, alone or upon assembly and insertion into commercially-available capsules, were characterized for key parameters: thermo-mechanical properties, accelerated stability, degradation, drug release, deployment performance, and resistance to simulated gastric contractions.

Results: Each part of the system was successfully manufactured using purposely-selected materials and the performance of final prototypes matched the desired one. This included: *i)* easy folding of the skeleton against the core in the collapsed administered shape, *ii)* rapid recovery of the cumbersome configuration at the target site, even upon storage, and *iii)* prolonged release of metformin.

Conclusions: Composition, geometry, and performance of the system developed in this work were deemed acceptable for stomach-retention and prolonged as well as customizable release of metformin in its absorption window, laying promising bases for further development steps.

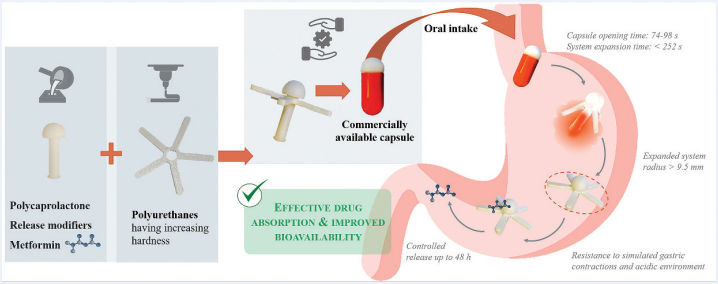

ARTICLE HISTORY
Received 7 August 2023
Accepted 11 December 2023

KEYWORDS
3D printing; fused deposition modeling; prolonged release; viscoelastic behavior; oral administration; diabetes

1. Introduction

Interest in gastroretentive drug delivery systems (GRDDSs) can be dated back to the late '80s [1–3]. At that time, researchers investigated a variety of formulation strategies for developing orally administered dosage forms able to control drug release and to remain into the stomach for long times (generally ≥8 h), despite physiological contractions and presence of food. Over years, GRDDSs were shown a promising solution for providing effective concentrations of different active ingredients, either to exert a local action in the gastric environment (e.g., for treating inflammatory diseases as well as for *Helicobacter pylori* eradication) or to improve their systemic absorption [4,5]. In the latter case, they were used to increase the bioavailability of *i)* weakly acidic molecules, which are poorly soluble in basic pHs, and of *ii)* drugs that are primarily absorbed into the stomach or in the first portion of the small intestine. Moreover, the ability of GRDDSs to prolong drug release over several days following a single oral intake allowed to enhance therapy adherence, especially when dealing with patients treated with multiple drugs at high quantities and/or with short half-life [6,7]. Indeed, their administration resulted in a simplification of the therapeutic regimen, reducing the number of units taken throughout the day.

Although GRDDSs are well-known to provide high patient compliance and improved bioavailability, in the past years

CONTACT Alice Melocchi alice.melocchi@unimi.it Sezione di Tecnologia e Legislazione Farmaceutiche "Maria Edvige Sangalli", Dipartimento di Scienze Farmaceutiche, Università degli Studi di Milano, via G. Colombo 71, Milano 20133, Italy; Francesco Briatico-Vangosa francesco.briatico@polimi.it Dipartimento di Chimica, Materiali e Ingegneria Chimica "G. Natta", Politecnico di Milano, Milano 20133, Italy

their attainment has represented a major challenge for scientists, probably because technological advancements were needed to ease their manufacturing. Indeed, GRDDSs have recently gained renewed attention within the research community, due to the availability of new materials and the advent of easy-to-access as well as versatile manufacturing techniques, such as 3D and 4D printing [8–13]. In this respect, systems with increased complexity were designed not only for conveyance of small molecules but also for delivering biologics *via* the oral route, taking advantage of physical modes typical of transdermal applications (e.g., piercing, jetting, ultrasound) [14–22]. The star-shaped drug delivery platform named Lyndra LYNX, which is already under clinical evaluation, represents one of the main examples of the so-called next generation GRDDSs [23]. Indeed, it was designed to reduce dosing frequency from once a week to once a month, and to have broad applicability across multiple therapeutic areas [24–28]. Illnesses that result hard-to-treat and are considered socially and economically impactful – such as altered psychiatric conditions, dyslipidemia, opioid use disorder, pregnancy prevention, malaria eradication, and HIV – are among the pathologies that this platform would help managing. Moreover, the implementation of GRDDSs like the Lyndra LYNX platform into medical practice could lead to major reduction of overall healthcare expenses. By way of example, they would reduce the strength of the active ingredient administered, by avoiding its undesired loss associated with release outside the absorption window and enable more efficient use of available resources [5,17].

In the last decades, prolonged retention within the stomach was attained taking advantage of high-density-, floatation-, adhesion/anchoring- and expansion-based formulation approaches, pursued either alone or in combination [1,29–33]. High-density GRDDSs are generally formulated to contain inert materials to increase the weight/volume ratio of the final product. Being responsible for device settling below the level of the pylorus, such materials are intended to decrease likelihood of elimination during gastric emptying. Conversely, low density floating systems would remain on top of the stomach content, thus prolonging their residence time. For mucoadhesive dosage forms, long-lasting retention is enabled by the presence of a component ensuring their adhesion to the epithelial surface of the target organ. Finally, expansion-based systems (GREDDSs) are actively or passively able to modify their size after swallowing. Once within the gastric environment, they gain a spatial encumbrance greater than the average dimensions of the open pylorus. However, for oral intake by swallowing, they need to present a collapsed shape, from both the functional perspective and the patient's psychological point of view. Thus, they are often delivered into commercially-available hard capsules. With respect to the expansion that GREDDSs must undergo once within the target organ, most of them assume the configuration responsible for retention following either swelling or unfolding processes. While in the former case the desired volume increase is triggered by absorption of water/biological fluids, various unfolding approaches have been investigated over years, especially to ensure transition from the collapsed to the expanded shape in the shortest possible time. Such strategies mainly involved mechanical/elastic deployment, shape memory effect, and superelasticity [5,34,35]. By way of example, the unique superelastic behavior of nitinol was used for manufacturing a necklace-like device able to convey high drug dosages covering multiple weeks of treatment [36,37]. In the same way, by using shape memory polymers as feedstock material for 3D printing, the novel concept of 4D printing was preliminarily tested for the production of systems intended for retention within various hollow muscular organs [38–44].

Type II diabetes is one of the most widespread pathologies in high-income countries, generating major healthcare expenses if not well-managed [45]. Metformin hydrochloride generally represents the first-line drug for newly diagnosed diabetic patients, because of its high efficacy, safety, tolerability, and limited cost [46–51]. Indeed, it not only prevents rise in blood glucose by decreasing insulin resistance, but also reduces glycated hemoglobin without incurring hypoglycemic episodes. Moreover, metformin is able to provide other extra-glycemic effects that would be beneficial for people suffering from diabetes. Indeed, it protects against cardiovascular risk, which generally increases over time if hyperglycemia is not well-controlled, and favors loss of body weight. Currently, metformin is mainly formulated in immediate release (IR) dosage forms for oral consumption. However, drug bioavailability resulting from this administration mode is about 56%, because part of the active ingredient is lost, being not properly available where it is mostly absorbed, i.e., in the upper gastrointestinal tract [42–57]. Therefore, controlled release of metformin at its absorption window could be highly beneficial. However, its high water solubility (300 mg/mL) as well as short half-life (40 min) could pose major challenges toward this target [11,58–60]. As a consequence, patients are currently forced to assume the drug several times through the day (generally 500–1000 mg taken twice a day), which often leads to nausea, diarrhea, loss of appetite and lactic acidosis due to the burst effect resulting from each administration [61–64]. In addition, during chronic therapy, metformin receptors become less responsive, thus requiring an increase in the administered quantity to maintain the beneficial effects. In this respect, metformin-containing dosage forms ensuring its prolonged release in the upper gastrointestinal tract would represent a major step forward in the current treatment of diabetes [60]. Besides increasing therapy effectiveness and possibly limiting the risk of patient hospitalization for uncontrolled symptoms, the therapeutic approach involving the use of GRDDSs would have a major impact on the costs associated with diabetes, which in Europe were estimated to be around € 2850 for each subject yearly [65–70].

Based on these premises, the aim of the present work was to design and to preliminarily evaluate the feasibility of a GREDDS with improved potential in the treatment of type II diabetes, being conceived for prolonged release of personalized doses of metformin in the upper gastrointestinal tract. With respect to other stomach-retentive devices already described in the scientific literature, the system here proposed comprised two different components: one responsible for retention into the target organ and the other one for controlled release of different doses of metformin, calculated to be compatible with the current needs of type II diabetes

patients. Only upon assembly of these parts, the final GREDDS could be attained. This peculiar configuration allowed us to take the most from the combined use of design, formulation, and manufacturing strategies. Moreover, it made it possible to deal with the system components individually and in parallel, thus simplifying and speeding up the experimental campaign, while increasing the flexibility of the GREDDS under investigation. Indeed, any of the above-mentioned parts might be fine-tuned independently and, in a wider perspective, be used for the development of other devices, following a lego-style assembly approach.

2. Materials and methods

2.1. Materials

Metformin (d_{50} = 54 µm and d_{90} = 349 µm; Methapharmaceutical, ES); polycaprolactone (PCL; average Mw 14,000, Sigma Aldrich, D); polyethylene glycol (PEG) 4000 (A.C.E.F., I); PEG 8000 (Clariant, I); polyethylene oxide (PEO; Sentry Polyox WSR N10 LEO NF, Colorcon, UK); polyurethane-based (TPU) filaments (nominal diameter = 1.75 mm) (Flexmark 7, 8, and 9 identified as TPU 7, TPU 8, and TPU 9; TreeD Filaments, I); poly-lactic acid (PLA) filament (TreeD filaments, I); hard-gelatin capsules DB caps size AAel (capacity = 0.97 mL, internal body diameter = 9.39 ± 0.06 mm, body length = 19.05 ± 0.46 mm, overall closed length = 22.6 ± 0.03 mm) and size 00el (capacity = 1.02 mL, external body diameter = 8.18 mm, body length = 22.20 ± 0.46 mm, overall closed length = 25.3 ± 0.03 mm) (Capsugel, I); silicon RPRO 30 base A and hardener B (Reschimica, I).

2.2. Methods

2.2.1. Manufacturing

3D printing by fused deposition modeling (FDM) was employed for manufacturing GREDDS components and testing samples (i.e., placebo cores and dumbbell specimens) to be used for either screening or development purposes, as described in the Results and Discussion Section. FDM was carried out by means of a Kloner3D 240 twin printer (Kloner3D, I) equipped with 0.5 mm nozzles. PLA and TPU 7, 8 and 9 filaments were printed as received. The main operating conditions set to 3D print different filaments are reported in Table 1.

Silicon-casting was employed for the fabrication of negative molds. These were composed of two halves and were subsequently used to melt-cast drug-containing cores starting from the formulations reported in Table 2. A previously weighed (Analytical balance, Gibertini, I) mass of drug and excipients were mixed in a mortar following the method of progressive dilutions and heated in a beaker up to 110 °C, under continuous mixing. The resulting molten formulations were poured into the silicon molds, which were then closed with manual clamps. After 30 min cooling at room temperature, the resulting drug-containing cores were manually removed from the molds.

All the specimens were characterized for weight (n = 6; Analytical balance, Gibertini, I), dimensions (n = 6; MiniTest FH7200 equipped with FH4 probe, diameter of the sphere = 1.5 mm, ElektroPhysik, D; caliper, Mitutoyo, J) and were also photographed (V4K Ultra High Definition USB Document Camera, IPEVO, US-CA; GoPro Hero Session, US-CA; Optical microscope 5X magnification, Olympus BX 60, J). These data were used to evaluate, in an indirect way, the reproducibility of the manufacturing processes employed.

Table 1. Printing parameters set for the different filaments in use.

	TPU 7	TPU 8	TPU 9	PLA
Nozzle temperature (°C)	215	220	220	220
Build plate temperature (°C)		40		
Fan speed (%)	0	0	50	100
Printing speed (mm/s)	15	30	30	70
Retraction (mm)	0	0	4.2	2.2
Number of perimeters		1		2
Layer height (mm)		0.2		0.15
Infill (%)		100		100
Infill type		Rectilinear		

Table 2. Composition (% by weight) of the GREDDS cores.

Metformin	PCL	PEG 4000	PEG 8000	PEO
50	50			
25	75			
50	40	10		
50	40		10	
50	40			10
50	25	25		
50	25		25	

2.2.2. Characterization

DSC analyses were performed by a DSC Q100 (TA Instruments, US-DE), using nitrogen as a purge gas (70 mL/min). Indium was employed as a calibration standard. Samples of about 10 mg underwent 3 subsequent heating/cooling cycles from 0 to 250 °C (rate 10 °C/min).

SEM microphotographs were acquired by a Phenom XL SEM (Thermo Scientific, US-MA). Images of the top of the cores and of their cross-section (attained by cutting the samples on a plane perpendicular to the core axis) were taken.

Tensile tests (n = 3) were carried out on TPU filaments (gauge length L_0 = 25 mm) and on dumbbell specimens (L_0 = 27.5 mm) immediately after production, after drying or after being immersed for 15 days either in water or in HCl 0.1 N. During immersion, samples were checked for weight (Analytical balance, Gibertini, I) at pre-determined times. Independently of the treatment undergone, specimens were kept at a constant temperature of 23 °C prior any mechanical characterization. Before testing, dimensions of the different prototypes were assessed (micrometer IP65 0–25 mm Mitutoyo, J). More into detail, diameter of the filaments was measured at 3 different points along their length, while thickness and width of the cross-section of dumbbell prototypes were evaluated at 3 points along their gauge length. Out of the measurements an average cross-section area (A_0) was calculated.

The experiments were performed at strain rates of 0.0017, 0.017, and 0.17 s^{-1}. Since specimen slippage was unavoidable, results were considered valid up to a 300% sample deformation. In all cases, pneumatic grips closing at a pressure of 3 $\frac{kgf}{cm^2}$

were employed to reduce slippage, which especially occurred at the highest stretch level. From the measured force (F) and displacement (ΔL), nominal stress (σ) and nominal strain (ε) were calculated as follows:

$$\sigma = \frac{F}{A_0} \tag{1}$$

$$\varepsilon = \frac{\Delta L}{L_0} \tag{2}$$

Results were represented as stress *versus* strain curves.

Two different dynamometers were employed for tensile testing: *i)* a Hounsfield Dynamometer (Hounsfield, UK), equipped with a mechanical extensometer and a 5 kN load cell and *ii)* an Instron 5697 dynamometer (Instron, US-MA) provided with a 10 kN load cell. In the latter case, a non-contact method based on a video-extensometer system was employed to measure sample deformation. To this end, 5 lines (5 mm distant from each other) were drawn on the specimen and their motion was recorded with a 10 M pixel camera (UI 5490 SE uEye, D). The resulting movie was divided into frames, which were processed by a specific image analysis software (ImageJ, US-CA) to determine the local displacement (ΔL).

Besides the tensile characterization, cyclic tests entailing loading and unloading stages were performed on TPU filaments, using the Instron dynamometer equipped with the video-extensometer system. The cycle consisted in a stretching phase (up to 200% deformation) followed by unloading and was repeated at least 3 consecutive times on the same specimen. Loading/unloading phases were carried out either at a constant strain rate of 0.17 s^{-1}, or by setting a strain rate of 0.17 s^{-1} for loading and 0.017 s^{-1} for unloading.

Stress relaxation experiments required that a static tensile strain (ε_0) was quasi-instantaneously applied to the sample and maintained constant while measuring the stress (σ) evolution over time. These analyses were performed by means of a RSA3 Dynamic Mechanical Analyzer (TA Instrument, US-DE). Nominal tensile strains (ε_0) equal to 1, 2, 3, 4, 5, and 10% were applied to TPU filaments (L_0 = 12.5 mm). The experiments were carried out at several constant temperatures (i.e., from 25 to 75 °C with 10 °C temperature steps) and at ε_0 values equal to 5 and 10%. From the measurements collected, the time evolution of the relaxation modulus, $E(\varepsilon_0, t)$, was determined as:

$$E(\varepsilon_0, t) = \frac{\sigma(t)}{\varepsilon_0} \tag{3}$$

By relying on the time-temperature reduction scheme, values measured at different temperatures and at $\varepsilon_0 = 10\%$ were superimposed to build a master curve for the relaxation modulus at the reference temperature T_0 = 25 °C [71]. The application of the reduction scheme allowed to determine a shift factor ($a_T^{T_0}$) defined as follows:

$$a_T^{25} = \frac{t}{t^*} \tag{4}$$

where t and t* represent the time at which the relaxation modulus assumed the same value at a generic temperature T and at 25 °C, respectively. This quantity allowed for estimating the temperature effect in speeding up the viscoelastic time-dependent phenomena and was particularly useful for designing accelerated testing procedures.

Funnel tests were performed (n = 3) using an experimental set-up adapted from the literature [24,27]. The RSA3 Dynamic Mechanical Analyzer was operated in compression-mode to force a prototype of the GREDDS under development into a funnel (45° angle, cylindrical opening of 20 mm in diameter) connected to the lower plate of the instrument (Figure 1). Both umbrella-like skeletons as such and assembled with PCL-based cores were evaluated. In the latter case, the specimen was positioned so that the core was oriented either in the advancing direction (i.e., named as the down position) or in the opposite one (i.e., named as the up position), as sketched in Figure 1. Moreover, umbrella-like skeletons were tested *i)* immediately after manufacturing, *ii)* after 4 h upon insertion into hard-gelatin capsules, to resemble extemporaneous preparation of the system to be administered, and *iii)* following storage at 55 °C for pre-defined time periods, thus accelerating any changes that might occur after long-term storage at room temperature.

The sample under evaluation was manually positioned at the center of the funnel, in contact with its wall, and pushed down at a constant rate of 0.1 mm/s for 250 s, while measuring the force opposed to the movement of the piston. The data collected were represented as force *versus* displacement curves. Here different zones can be recognized: *i)* at low displacements (i.e., up to about 12 mm), the arms of the umbrella-like skeleton slip against the converging surface of the funnel, reaching the limit of its narrow zone, *ii)* the arms stopped at that position, while the connection ring was pushed into the narrow section, *iii)* the peak force was reached and the arms folded as well as entered the narrow section of the funnel, sliding along the almost vertical wall of the latter. Out of the observed motion/deformation mechanism and based on previous literature data, the maximum force required for samples to pass through the funnel represented the ability of the system to resist gastric contractions and was used to compare different samples.

Opening tests were performed on prototypes (n = 6) folded into hard-gelatin capsules. These were immersed into a 250 mL crystallizer filled with 200 mL of HCl 0.1 N and kept at 37 °C. Their behavior upon contact with the media was recorded using a camera (UI1490LE-M-GL Ueye camera, IDS imaging, D; Computar MACRO 10× lenses, J) and monitored with a stopwatch (digital stopwatch, Wokex, I). From the recording, the opening time of the capsules as well as the deployment time of the folded prototypes contained were determined. In order to estimate the degree of recovery of the initial unfolded geometry, specimens were photographed from above before and after the experiment (V4K Ultra High Definition USB Document Camera, IPEVO, US-CA). Image J software was employed to measure, on the images acquired, the diameter of the circumference surrounding the projection of the umbrella-like skeleton on the observation plane (Figure 2). The closer the radius of the unfolded prototype was to its original value before folding, the closer its shape would be to the original planar one.

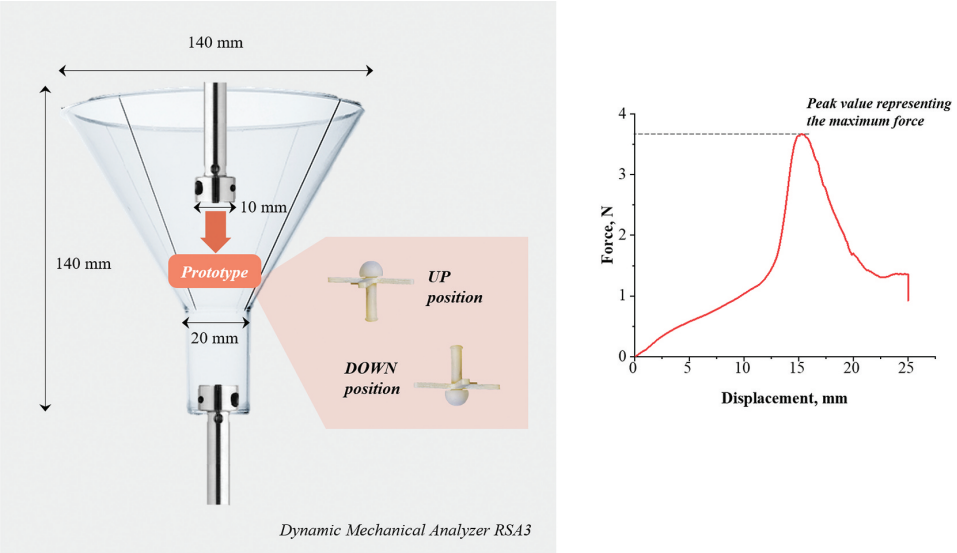

Figure 1. Outline of the funnel experiment set-up together with an example of the resulting curve.

Samples were tested immediately after manufacturing and upon storage of the umbrella-like skeleton at 55 °C for increasing times (up to 18 h depending on the TPU grade) that corresponded to 18 months' storage at room temperature, according to the time-temperature reduction scheme.

Mass-loss tests were performed on PCL-based drug containing cores ($n = 3$). These were kept at 25 °C in unstirred conditions, using NaOH 5 M (pH = 14) as the aqueous medium to accelerate polymer degradation, as already reported in the literature [72–74]. Samples were immersed into 20 mL of this solution and withdrawn at pre-determined time points (i.e., 0.5, 1, 3, 6, 24, 48, 72 h and 5 as well as 7 days). After removal, they were washed 3 times with distilled water and let to dry for 8 h at 40 °C (WVR oven, I). Once completely dry, the specimens were checked for weight (Analytical balance, Gibertini, I) and the percentage of mass loss (m_l) was calculated as:

$$m_l(\%) = \frac{m_d - m_0}{m_0} \times 100 \quad (5)$$

where m_d and m_0 represent the mass of the sample after drying and before starting the experiment, respectively.

Release tests were carried out on PCL-based drug containing cores either alone or inserted into umbrella-like skeletons ($n = 3$), using a USP38 dissolution apparatus 2 (800 mL HCl 0.1

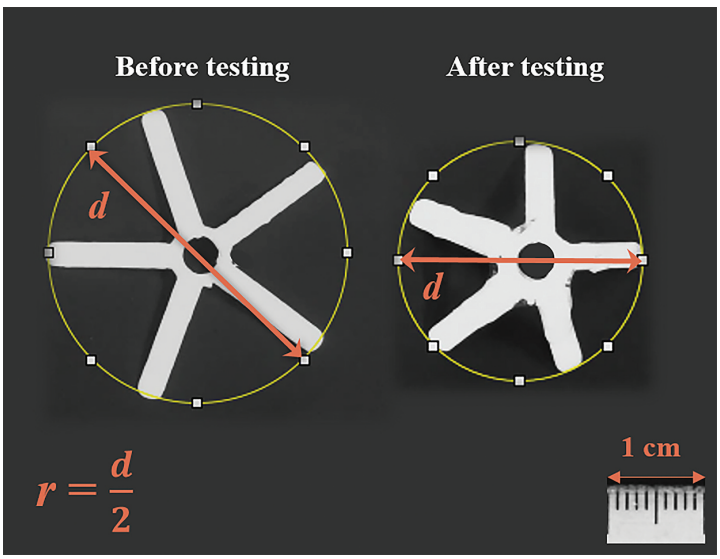

Figure 2. Photographs taken from above on a TPU-based umbrella-like skeleton before the experiment and at the end of the opening test, even if not fully deployed, highlighting the procedure for determining its radius.

N, kept at 37 ± 0.5 °C; 50 rpm) (Distek, CH). Fluid samples were withdrawn at specific time points and assayed spectrophotometrically (λ = 237 nm). The drug concentrations were determined using a calibration curve purposely built in the 0.01–1 mg/mL range ($R^2 = 1.000$). In addition, the resulting data were analyzed using the Korsmeyer-Peppas model:

$$\frac{M_t}{M_\infty} = K \cdot t^n \quad (6)$$

where $\frac{M_t}{M_\infty}$ represents the fraction of drug released at time *t*, while K is the kinetic constant (dimension of time^{-n}) and n the diffusional exponent (dimensionless). Both K and *n* depend on structural and geometric characteristics of the system. Data were fitted up to $\frac{M_t}{M_\infty} = 0.6$

3. Results and discussion

3.1. Design concept

The main features envisaged for the new GREDDS to be developed were:

- simplicity of administration and operation, as well as ease of disposal once exhausted, which would increase patients' compliance and safety;
- sufficiently prolonged retention within the stomach and controlled release;
- flexibility in terms of metformin dosing and release rate, to meet different therapeutic needs of subjects suffering from type II diabetes.

To fulfill the above-mentioned requirements, the system was designed to be composed of: a central core and an umbrella-like skeleton entailing 5 arms joined together, responsible for drug release and retention performance, respectively. The choice of decoupling the release-controlling part from that ensuring retention was quite new in the field and was intended to increase the versatility of the system. This way, the key aspects of each component could be assessed independently and in parallel, thus making the research efforts more effective.

The core entailed a hemispherical-shaped end, purposely designed to fit the body of a commercially available capsule and to act as the respective cap. This choice allowed not only to have the final system resemble the shape of a capsule, being more acceptable from the patients' perspective, but also to maximize the volume of the core so as the strength of metformin that could be loaded. Indeed, the drug quantity conveyed in this system was intended to fulfill the actual therapeutic needs of subjects suffering from type II diabetes.

By inserting the core, from its smaller end, into the central ring of the umbrella-like skeleton, the two parts were assembled in an expanded configuration, suitable for retention of the system into the stomach. By folding the arms of the umbrella-like skeleton against the core, a collapsed shape was attained, which was able to fit within the body of the selected capsule. This way, locking and oral administration of the assembled system would be possible. In Figure 3, final electronic models of the various components of the GREDDS, either as such or upon assembly, are reported together with photographs of the actual prototypes.

Following the form-fit-function approach, the individual components of the GREDDS were designed by taking into account the characteristics necessary for proper interaction with each other and to guarantee effective working mechanism of the assembled device. It was therefore fundamental to identify, at an early stage of development, the key quality parameters for each part, taking into account how shape, dimensions, and performance might differ from predetermined values without impairing function. As a result, the selection of appropriate materials for the different components of the GREDDS played a pivotal role.

3.2. Core

3.2.1. Design

The core of the GREDDS was designed *i)* to convey personalized doses of metformin, in order to better address the needs of specific diabetic patients, who might become less responsive to the drug over time, and *ii)* to release such doses in a controlled way. In addition, the amount of the active ingredient contained needed to be compatible with, at least, one day of treatment. Indeed, as previously discussed, the current therapeutic regimen for type II diabetes entails the use of 500–1000 mg of metformin. The latter is administered multiple times through the day *via* IR tablets, leading to a drug bioavailability of approximately 50%. Better results could be attained by resorting to GREDDSs able to continuously release the selected active ingredient at the appropriate absorption site, thus reducing the chances of drug loss. This way, not only the overall dose of metformin taken daily could be reduced, but also the number of relevant administrations. As a result, a 500 mg dosage strength could become compatible with a 24–48 h treatment. For this reason, the above-mentioned metformin amount was chosen as the first target for the GREDDS under investigation. However, such a high dose occupies a major volume, posing serious challenges for the development of a prolonged-release matrix, which needs to be formulated with specific adjuvants to ensure the expected performance. Dimensions of AAel DB capsules were set at the highest limit for the system in its collapsed shape to maximize drug load as well as formulation space, while still ensuring easy swallowing of the device. This allowed for clear definition of overall length and diameter of the system, and also guided the design of the cap-shaped end of the drug containing core (Figure 3).

3.2.2. Manufacturing

The quite high drug load to be conveyed into the core along with the need for prolonged release steered the choice toward a high-density system to be produced by hot-processing starting from a matrix-forming polymer capable to ensure controlled release over 24 h, even at low concentrations [75–79]. To this target, resorting to either inert or hydrophilic swellable/soluble polymers traditionally employed in the formulation of oral products did not seem appropriate. On the other hand, excipients typical of other administration routes and especially proposed for long-term

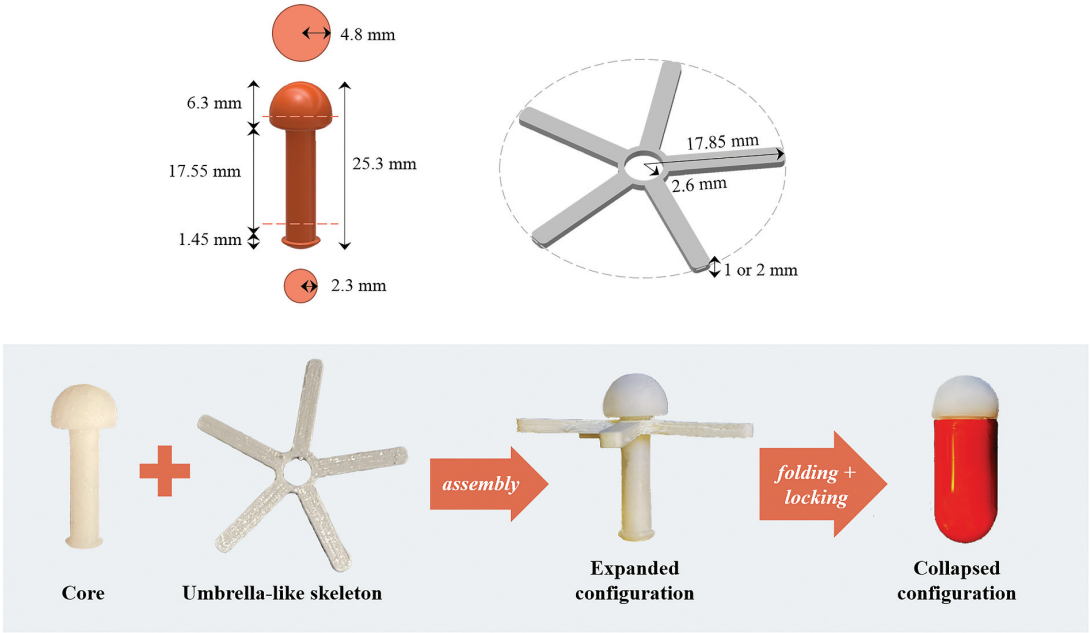

Figure 3. Electronic models and resulting photographs of the main components of the GREDDS, as such, upon assembly and after insertion into a commercially available capsule body.

applications were considered. In this respect, PCL was selected as an interesting matrix-forming polymer for a variety of reasons. Besides having been tested for the manufacturing of prolonged-release inserts/implants, its biocompatibility, mechanical properties as well as biodegradability profile in physiological conditions (upon hydrolysis of their ester linkages) have already been deepened [80–85]. In addition, degradation and release rate from PCL-based matrices could be fine-tuned through the use of appropriate additives [25,86–88]. Focusing on core manufacturing, this polymer could easily undergo hot-processing, in view of its melting point of 60°C as well as of a glass transition temperature of about −60°C [89–91]. Finally, PCL potential outside the field of implantable systems has been recently demonstrated. Indeed, it was proposed for the fabrication of controlled-release systems to be orally administered, even resorting to novel manufacturing approaches (e.g., injection molding, 3D printing, electrospinning) [24,25,27,92–95].

A relatively low molecular weight PCL (i.e., 14,000 Da) was preferred for this study. Indeed, higher grades would imply excessively long degradation times, ranging from 3 weeks to 3 years, which would not be compatible with the 2 days treatment targeted for the GREDDS under development [96–98]. The PCL-based drug-containing cores were produced by melt-casting, which was easy to perform at the lab-scale and allowed to contain the starting investments in manufacturing equipment. This strategy is fundamental during R&D stages of a new system, because the experiments are mainly aimed at attaining prototypes for preliminary validation studies. Therefore, melt-casting started to be employed by many researchers, with promising results also toward the possibility of using the data collected in subsequent scale-up phases, entailing for instance other hot-processing techniques more suitable for large-scale production (e.g., hot melt extrusion, injection molding) [27,99].

Very preliminary attempts toward the use of 3D printing for prototyping activities were poorly successful, probably due to the limited viscosity of the PCL-based melt. Indeed, the low viscosity was responsible for uncontrolled dripping of the material from the 3D printer nozzle and for unsuitable cooling, despite the tentative changes to modify retraction-associated parameters to control such a phenomenon. As a consequence, the first printed layers were not able to withstand the weight of the subsequent ones, as required when an object is built layer-by-layer. However, FDM was essential for printing PLA-based prototypes of the core and for fine-tuning their details. Indeed, such FDM prints were used as templates for the manufacturing of negative silicon-based molds, which were then employed in melt-casting of actual drug-containing cores.

A range of PCL-based formulations were prepared, not only for testing increased drug loads, but also for fine-tuning the performance of the core, by adding a variety of adjuvants at different concentrations. Polymers freely-soluble in water were selected because, due to their high hydrophilicity, were expected to enhance the degradation rate of the PCL-based samples and to speed up drug release. These included PEGs with diverse molecular weights and PEO, which is well-known to increase about 50% in volume prior to solubilization, thus having the potential to create major discontinuities into the PCL structure. As far as metformin is concerned, relevant HCl salt was selected because it is water soluble and has a melting point around 222–226 °C. As a consequence, it should remain suspended into the polymeric melt, as also confirmed by DSC (data not shown).

Despite the manual procedure for relevant manufacturing, all the melt-casted cores pointed out reproducible weight (1010 mg, CV ≤ 10%) and dimensions analogous to the nominal ones. To better appreciate the microstructure, SEM photomicrographs of the prototypes obtained were also acquired. By way of example, images relevant to samples of different compositions, taken both on their external surface and on the relevant cross-section, are collected in Figure 4.

As expected, the hot-processing technique employed resulted in all the specimens exhibiting a relatively compact structure, irrespective of their composition. Indeed, a limited number of pores were visible, appearing as little dark holes into the gray polymeric matrix. No major differences were highlighted when comparing different areas (i.e., outside versus inside). Moreover, metformin particles turned out clearly visible and homogeneously distributed inside the polymeric structure. Indeed, drug white crystals emerged on the external surface of the items, thus being immediately available for interaction with aqueous fluids. Interestingly, the number of such crystals seemed higher on the surface of the sample corresponding to the junction between the two halves of the mold. Although the prototypes appeared quite smooth when inspected visually, a certain surface roughness was noticed by looking at the SEM photomicrographs, which highlighted repetitions of small steps of material. This was consistent with the fabrication mode of PCL-based parts. Indeed, the cores were manufactured using silicon molds that were cast starting from previously printed PLA-based templates. Therefore, their layer-by-layer structure was first transferred to the mold and then to the molten material during melt-casting of the drug-containing samples.

3.2.3. Performance

Mass loss analysis of cores based on neat PCL and loaded with either 25 or 50% of metformin were first carried out (Figure 5a). Then PCL-based prototypes containing 50% of the drug and either 10 or 25% of soluble adjuvants instead of PCL were tested (Figure 5b). In particular, PEO was loaded at 10% only, due to the high viscosity and poor homogeneity of the resulting melt when dealing with higher concentrations. Based on the existing literature, the mass loss experiment involved the use of basic pH fluids to speed up PCL degradation and to better highlight the contribution of the different release modifiers [72–74]. This strategy was deemed particularly cost-effective, thus suitable for a feasibility study. In fact, resorting to the use of enzymes for the same purpose would have been more challenging, introducing major source of variabilities in the experimental set-up and thus in the associated outcomes. Indeed, type, concentration, extraction source and specific working conditions (e.g., pH, temperature) for each enzyme considered would have been crucial [100,101]. Moreover, the scientific literature indicated that the effect of efficient enzymes toward PCL degradation (e.g., lipases) would start to be relevant after a relatively long interaction time [100,102–105]. By way of example, it is reported that lipases can degrade PCL to oligomers and monomers within 3–4 weeks, while in normal conditions no degradation would be visible for 9 weeks [80,96,101,106,107]. Based on these considerations, the use of enzyme-containing media could be expected to have a major impact on the final elimination of the exhausted GREDDS and was avoided for assessing the release performance at this stage because, for our system, the latter was planned to correspond to only a few days of treatment.

While the weight of neat PCL-based prototypes remained practically unchanged over 7 days (mass loss < 0.8%), samples containing 50% of metformin loose approximately half of their initial weight after 2 days of testing. The rate of mass loss increased over time, probably due to a rise in the surface area of PCL exposed to degradation (i.e., cleavage of the polymer ester linkages), which was caused by the dissolution of the soluble drug. Indeed, by remaining suspended into the polymeric matrix, the metformin particles acted as pore formers.

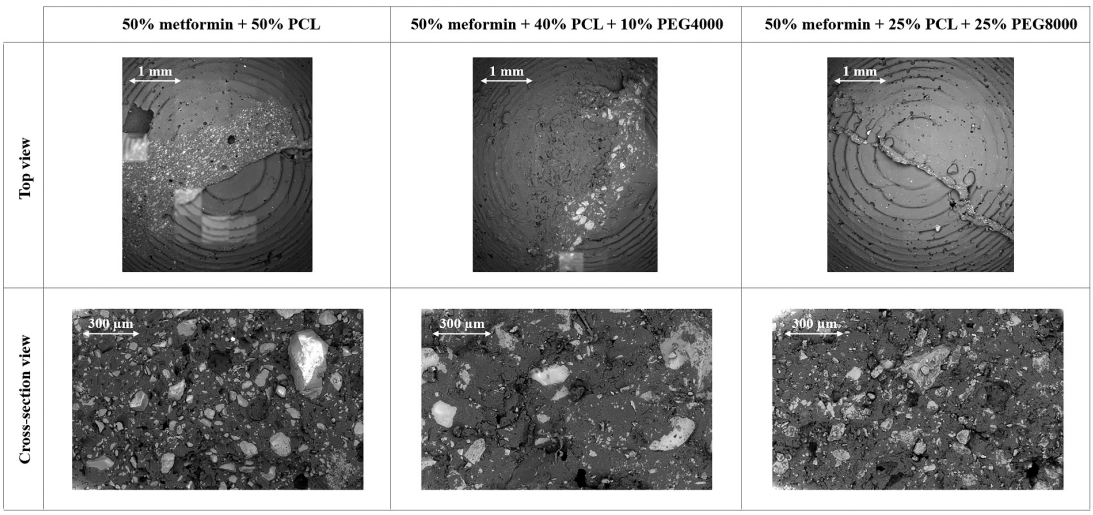

Figure 4. SEM photomicrographs (top and cross-section view) of different PCL-based cores.

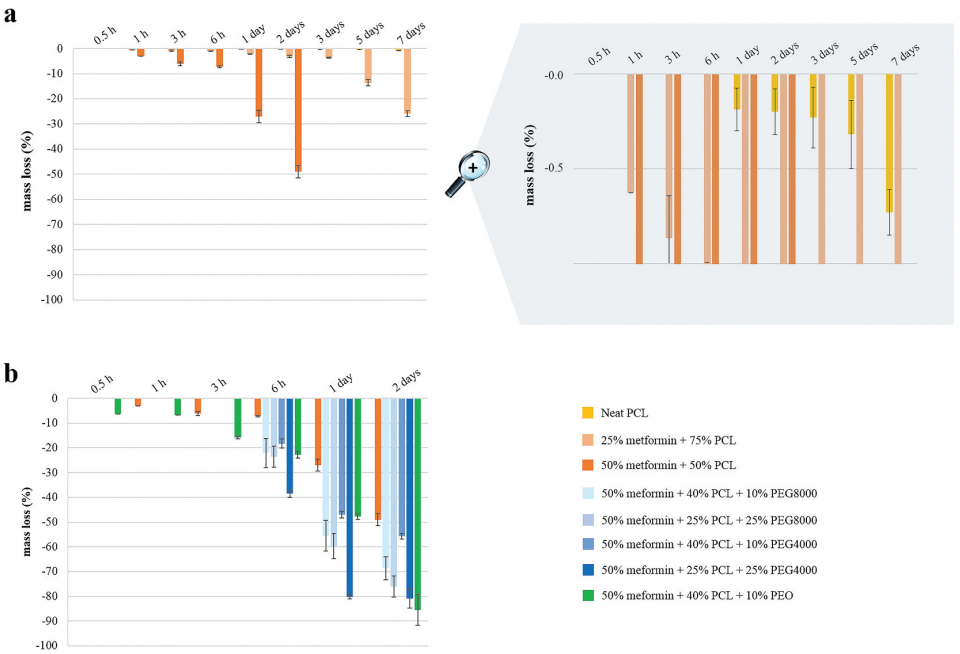

Figure 5. Mass loss data relevant to specimens a) based on neat PCL and loaded with either 25 and 50% of metformin or b) containing 50% of the drug and different amounts of soluble adjuvants.

Focusing on the behavior of specimens containing soluble adjuvants, mass loss turned out even faster, in agreement with preliminarily literature findings in this respect [25,86–88,98,108–110]. More into detail, mass loss data increased in the PEO > PEG8000 > PEG4000 order. The higher the amount of excipient added, so as the lower the PCL content, the higher the rate of mass loss. Interestingly, the action of PEO turned out visible after 2 days, probably because relevant swelling needed a certain time to become effective.

Consistent results in terms of release rate were observed for metformin-containing PCL cores. In this case, *in vitro* testing took place in enzyme-free acidic media according to targeted biological environment (Figure 6). As expected, a particularly slow release, even exceeding the desired timeframe of 2 days, was pointed out by cores based on neat PCL. More into detail, the lowest release rate was observed with samples having the highest polymer content, so as the lowest drug dose (i.e., 25%). Indeed, they lasted for about 14 days. On the other hand, release duration was reduced to 6 days when dealing with cores containing 50% of metformin, which was further proven to act as a soluble pore-former. Overall, drug delivery turned out faster when the PCL content within the matrix was decreased. Moreover, the possibility of fine-tuning the system performance according to the characteristics and the amount of the adjuvant employed was demonstrated.

The release data collected were also analyzed using the Korsmeyer-Peppas model, which is widely employed for describing drug release from polymeric systems and has been recently applied to deepen the performance of PCL-based matrices [111–114]. Indeed, this power law was demonstrated useful when the release mechanism is unknown or when more than one phenomenon would occur concomitantly (e.g., diffusion of water into the matrix as well as swelling and dissolution of the latter). The values of the n exponent, well-known for providing information on the drug release mechanism (i.e., Fickian diffusion *versus* non-Fickian one), were calculated for all the drug-containing cores under evaluation and are summarized in Table 3. Cores made with PCL and containing 50% metformin were the only characterized by *a n* value of 0.500 and a narrow 95%-confidence-interval, thus indicating a diffusion-controlled release mechanism. The behavior of samples of analogous composition but with reduced drug content (i.e., 25% of metformin) was quite similar ($n = 0.514$). Conversely, all the other prototypes clearly exhibited a non-Fickian diffusion mechanism (i.e., $0.5 < n < 1$). Interestingly, although specimens containing 50% of the selected drug combined with 25% of different PEGs pointed out mean *n* values closer to 0.5, their 95% confidence interval turned out very wide.

After 6 months' storage (25 ± 5°C, 55 ± 5% RH), drug-containing cores were further tested for release. The resulting profiles turned out analogous to those previously discussed, which was deemed particularly promising toward stability of the DDS under investigation.

Overall, the data collected supported the feasibility and the application potential of the drug-containing core of the novel GREDDS under development. More into detail, interesting relations among size, shape, composition (i.e., type and amount of adjuvants as well as strength of metformin conveyed) and degradation as well as release performance of this part were highlighted. In a further development step, this preliminary information will necessarily be supplemented and supported by stability and safety data collected in the physiological environment.

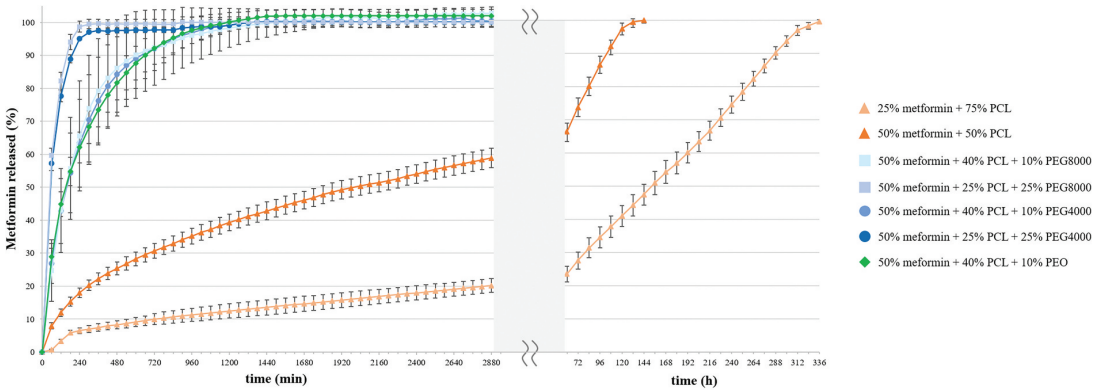

Figure 6. Release profiles relevant to different PCL-based cores.

Table 3. Fitting parameters relevant to the Korsmeyer-Peppas model.

	n	n LoConf*	n UpConf**	R^{2***}
25% metformin + 75% PCL	0.514	0.487	0.541	0.939
50% metformin + 50% PCL	0.500	0.494	0.506	0.997
50% meformin + 40% PCL + 10% PEG8000	0.802	0.720	0.883	0.992
50% meformin + 25% PCL + 25% PEG8000	0.562	0.198	0.926	0.997
50% meformin + 40% PCL + 10% PEG4000	0.684	0.632	0.736	0.996
50% meformin + 25% PCL + 25% PEG4000	0.510	0.256	0.763	0.998
50% meformin + 40% PCL + 10% PEO	0.593	0.549	0.637	0.994

*95% Lower confidence limit of exponent n.
**95% Upper confidence limit of exponent n.
***Regression correlation coefficient.

3.3. Umbrella-like skeleton

3.3.1. Design

In the actual configuration of the GREDDS, the umbrella-like skeleton was responsible for the attainment of collapsed and expanded shapes, ensuring administration and retention, respectively. To this aim, it was conceived as a set of flexible arms joined through a central ring (Figure 3). The latter would not only connect the above-mentioned arms and enable folding and unfolding, but also ensure proper assembly of the final system, allowing for correct positioning of the core. In addition, the dimensions of the arms were such that, upon folding, they would completely fill the space left by the core in the capsule body.

The expanded configuration of the umbrella-like skeleton was designed to be inscribed within a circumference of 35.7 mm in diameter. This choice was made to avoid passage of the umbrella-like skeleton in the expanded configuration through the pylorus. Indeed, when open, the diameter of such sphincter could reach 22.1 mm but more commonly is reported to be in the 13–17 mm range [17,29]. Focusing on the arms, two different thicknesses were initially considered (i.e., 1 and 2 mm), to evaluate the influence of this parameter on the umbrella-like skeleton behavior. Notably, the dimensions of the skeleton arms could impact on the encumbrance of the device when in the folded configuration. These thicknesses were selected because they did not impair the possibility for the system to be housed in commercially-available capsule bodies. Besides size requirements, the mechanical behavior of this component was fundamental for the final performance of the GREDDS, as it should be able to fulfill many different needs. As long as the GREDDS remains in the stomach, it should resist gastric contractions while maintaining its cumbersome shape and without representing a potential hazard for the physiological environment. From the administration point of view, the collapsed configuration had *i)* to be easily achieved by folding the arms without breaking or damaging them and *ii)* to be maintained inside the body of a standard capsule over the product shelf-life. At any time during this period, upon administration of the GREDDS, the arms were expected to undergo an immediate elastic deployment following capsule dissolution in the stomach environment. Even if the unfolding process of the umbrella-like skeleton does not occur instantaneously, it should take place fast enough to ensure the recovery of a sufficient fraction of its initial diameter, thus preventing early elimination of the system from the open pylorus. Such folding/unfolding requirements imply that the material behavior should be elastic up to high deformations (i.e., hyperelastic) or, at most, viscoelastic with a relatively low relaxation time. In this respect, no or very limited permanent deformations should result from the folding phase.

3.3.2. Manufacturing

Considering the peculiar deployment performance envisaged for the umbrella-like skeleton, excipients commonly employed in the manufacturing of DDSs would not guarantee its correct functioning. Therefore, the research of a compliant material was broadened to the medical device field, in order to include thermoplastic elastomers composed of soft and hard segment. Among those, TPU was deemed as particularly promising in view

of its hyperelastic (i.e., non-linear elastic) mechanical response and stability in a variety of challenging environments (i.e., extreme pH values, various solvents, and different temperature conditions) [115–118]. In addition, preliminary research findings suggested the suitability of this material for pharmaceutical applications and particularly for the formulation of DDSs intended for oral administration [24,27,119–127]. As a further advantage, filaments based on TPUs with different mechanical characteristics are already available, favoring the use of FDM for manufacturing the umbrella-like skeleton. This technique was deemed interesting due to its capability to deliver complex shapes and to ensure their modification in real-time [75,128–130].

The FDM process required a range of preliminary trials to identify the best conditions for printing this GREDDS component. First, TPUs with different nominal hardness (i.e., ranging from a very soft 70 Shore A for TPU 7 to a relatively hard 95 Shore A for TPU 9) were selected. Since their viscosity remained particularly low at the appropriate processing temperature, speed and retraction distance were set to high values to avoid early flow of the material from the nozzle. Indeed, the latter resulted in the so-called stringing effect, which occurred when the printer-head oozed some melted polymer during its travel across an open space to reach the next point. When these strings solidified, they resembled a cobweb, affecting the appearance and the performance of the final item. Not only was the printing speed maintained low, but also the motion of the printer-head was enhanced by manually acting on the G-code to reduce undesired travels across the part under construction and relevant distances, thus resulting in a reduced fabrication time. Moreover, as the different arms of the umbrella-like skeleton needed to be considered as a single part, their G-code was modified accordingly. In particular, the angle of the infill was adjusted to have it always oriented in the axial direction of the arm (i.e., the radial direction of the circle circumscribing the umbrella-like skeleton). In other words, the infill pattern resembled spokes of a wheel surrounding the central ring. This strategy was pursued to have all the arms printed (thus in principle behave) in the same way and to increase their resistance toward any tractions they might undergo during folding in the collapsed shape. For the same purpose, the perimeters of each arm and those of the central ring were not just partially superimposed, as happened in standard printing settings, but were completely overlapped to ensure a strong anchoring. Indeed, quality, and reproducibility of the common area between the arms and the ring walls was the most critical to be controlled. Moreover, for correct folding and unfolding of the umbrella-like skeleton, a solid connection between these zones was required, as they would receive the most stress.

By identifying appropriate 3D printing conditions, the resulting prototypes pointed out good weight reproducibility (240 mg, CV ≤ 5% and 460 mg, CV ≤ 4% for system having 1 and 2 mm thick arms, respectively) and dimensions analogous to the nominal ones even in the most challenging areas, i.e., arms (CV ≤ 10%).

Aiming at predicting the mechanical performance of the umbrella arms, a preliminary investigation was performed, focusing on the thermo-mechanical behavior of TPUs characterized by different nominal hardness. The experimental campaign started from uniaxial tensile experiments carried out on filaments. As the thermo-mechanical history applied to the polymer during 3D printing may affect the properties of the final item, printed dumbbell specimens were also tested. These samples represent the geometry of choice for preliminary trials and, being relatively easy to fabricate, they were 3D printed in conditions similar to those used for the umbrella-like skeleton. In Figure 7, the results of tensile tests attained from filaments and 3D printed dumbbells are summarized. As expected, TPU 9 always had a stiffer behavior than TPU 8 and 7 (Figure 7b). However, major differences were observed between filaments and printed specimens, which may be ascribed either to a different material behavior upon processing or to a misestimation of the effective area of the samples. To separate these two effects, dumbbell specimens were cut, observing their cross-section with an optical microscope. As visible from the photograph reported in Figure 7a, the presence of pores/discontinuities was highlighted, and these could markedly reduce the resistant surface with respect to the nominal one. Therefore, an effective cross-section area was calculated for all the printed samples and used to correct the tensile test data. The stress–strain curve following this adjustment correlated very well with those relevant to TPU 7 and 8 filaments, confirming that the printing process did not affect the properties of the starting material. As for TPU 9, a slight effect of processing could not be excluded. Indeed, at relatively high strain levels, the corrected curves relevant to dumbbell specimens did not perfectly overlap to those of filaments. Overall, 3D printing seemed to have only a small effect on the selected TPUs, which allowed for further investigation of the material behavior using just filaments as screening samples.

Stress–strain curves resulting from tensile tests performed at different strain rates (i.e., 0.0017, 0.017, and 0.17 s^{-1}) and from samples immersed either in distilled water or in HCl 0.1 N are reported in Figure 8a,b, respectively. The former conditions allowed for estimating the viscoelastic behavior (here intended as strain rate dependence) of the different TPU grades considered, which turned out negligible for TPU 7 and limited for TPU 8 and 9. On the other hand, exposure to different aqueous media, even for relatively long times, did not markedly affect the response of any TPUs, which might be especially promising considering the targeted application. Overall, the data pointed out good reproducibility, especially at lower ε values.

In order to gather information regarding the suitability of the TPUs under investigation for 3D printing the umbrella-like skeletons, two aspects were mainly investigated: *i)* the ability of TPU filaments to recover the applied strain in cyclic tests, which would highlight any possible non-recoverable bending, and *ii)* their stress relaxation over time at fixed deformation. This would occur when maintaining the system within a capsule for relatively long times and would provide an indication of the rate of the subsequent unfolding.

Focusing on the results of loading-unloading tests, a residual strain of limited entity was observed after a first cycle carried out up to 200% (Figure 9a). Such a residual strain

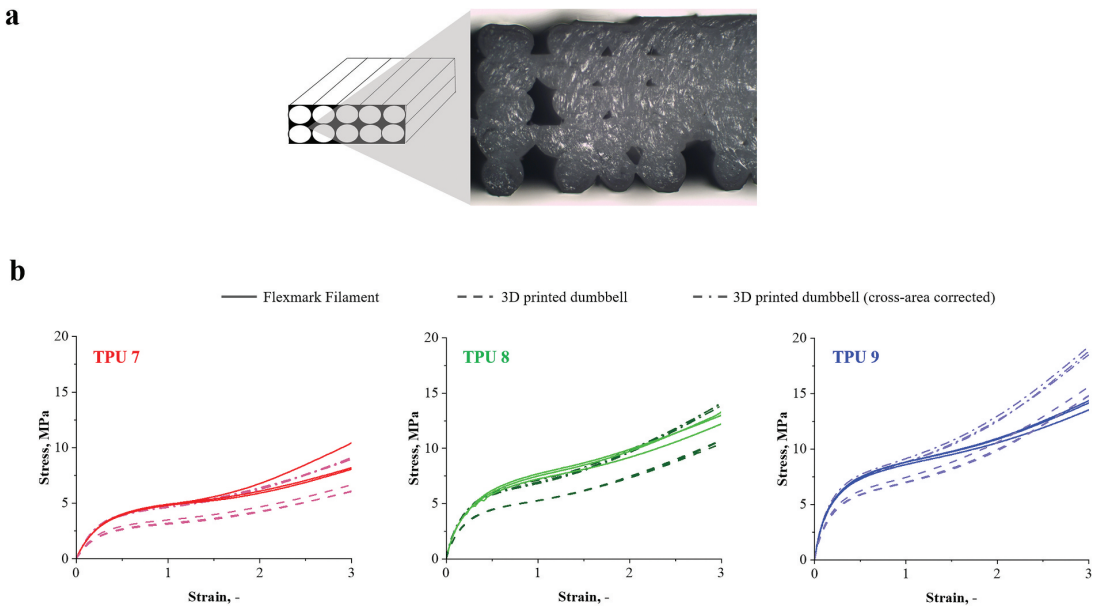

Figure 7. a) outline and photomicrograph of the cross-section of a printed TPU 7-based dumbbell and b) stress–strain curves relevant to various TPU filaments and resulting printed specimens. In the latter case, the stress values were also corrected for the actual cross-area (*i.e.*, by excluding voids).

increased with stiffness of the considered TPU. After this first cycle, the residual strain did not present any major changes. From the second cycle on, all the materials showed a lower value of stress at the same strain with respect to what was previously highlighted. This suggests that the unfolding might be incomplete and that the ability of the umbrella-like skeleton to sustain loads during gastric contractions could be reduced after repeated folding/unfolding.

To better understand the stability of the umbrella-like skeleton, intended as the impact of maintaining this part folded within a capsule for relatively long times, a viscoelastic characterization was deemed fundamental.

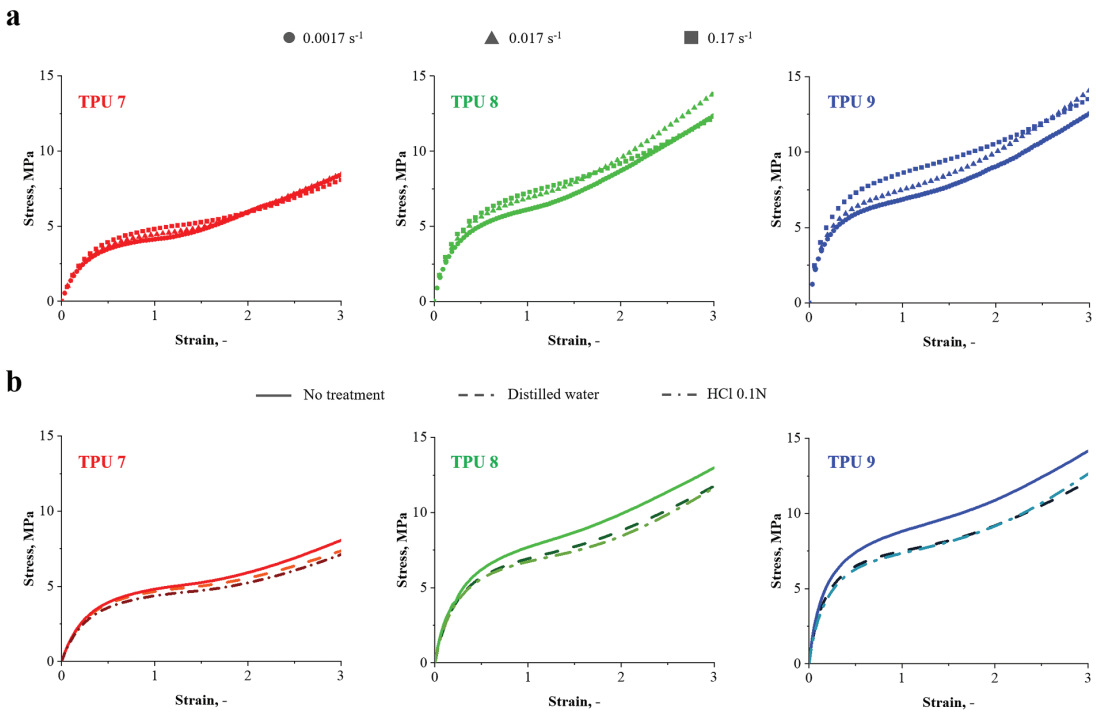

Figure 8. Stress–strain curves relevant to various TPU filaments tested a) at increasing strain rates and b) upon exposure to diverse environmental conditions.

Indeed, deployment of the skeleton should take place even after prolonged storage, during which the system will be subjected to an imposed constant strain. In this respect, the stress relaxation phenomena might affect its unfolding performance upon removal of the external constraint represented by the capsule body. When tested at different strains (i.e., 1, 2, 3, 4, 5, and 10%), the relaxation modulus of all the TPU filaments decreased monotonously with respect to the applied strain. By way of example, data relevant to samples tested at 25 °C are reported in Figure 9b. As expected, the relaxation modulus determined in fixed time and applied strain conditions increased with the TPU hardness. Moreover, for each TPU grade investigated, the relaxation modulus at fixed time decreased by applying higher strain, indicating a non-linear viscoelastic behavior in a deformation range of interest for the umbrella-like skeleton. Finally, the relaxation occurred faster for TPU 9 and could not be disregarded for any TPUs. To speed up the above-mentioned phenomenon, the investigation was deepened by taking into account different temperatures. In these experiments, only the most severe strain (i.e., equal to 10%) was applied. Relying on the time-temperature reduction scheme and shifting the results along the logarithmic time axis, the relaxation modulus master curve was built (Figure 9c). The trend of the latter not only confirmed that TPU 9 relaxed faster than TPU 8 and 7, but also highlighted a certain stress relaxation. This has to be accounted for when considering the possible effects of long-term storage of the umbrella-like skeleton within a capsule. To this end, stress relaxation of folded samples was accelerated by conditioning them at 55 °C for 56, 99, and 314 min for TPU 7, 8, and 9. These times were calculated based on the time-temperature

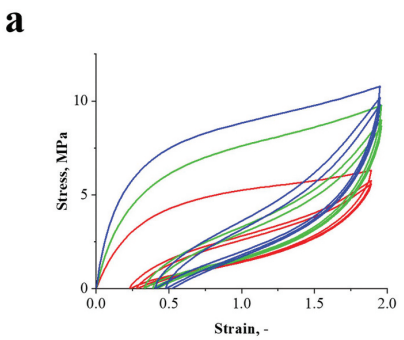

		Cycle		
		1st	2nd	3rd
TPU 7	σ_{max}	6.31	5.75	5.59
	ε_{max}	1.89	1.89	1.89
TPU 8	σ_{max}	9.31	8.55	8.22
	ε_{max}	1.94	1.94	1.94
TPU 9	σ_{max}	11.21	10.44	10.08
	ε_{max}	1.89	1.89	1.89

$\text{Log}(a_T^{T_0})$ values, $T_0 = 25°C$

	Temperature, °C			
	35	45	55	65
TPU 7	1.30	1.05	2.10	1.82
TPU 8	0.77	1.95	1.20	1.1
TPU 9	1.10	1.00	1.30	1.39

Figure 9. a) loading-unloading stress–strain curves, b) relaxation modulus at different temperature conditions and at increasing strain values *versus* log-time curves and c) resulting master curves (shift factors details in table) relevant to various TPU filaments.

reduction scheme to be representative of 18 months' storage at 25 °C, thus allowing to preliminary assess the stability of the system over time.

3.3.3. Performance

The unfolding capability of the TPU component of the GREDDS under development needed to be evaluated, as it would be responsible for the gastric retention ability of the entire system. Unfolding rate and efficiency of umbrella-like skeletons with arms of different thickness were assessed by measuring: *i)* the time needed for complete deployment following contact with HCl 0.1 N, and *ii)* their ability to regain the initial diameter. In this respect, samples were tested either immediately after folding and insertion within a capsule or following storage under the accelerated conditions previously defined (corresponding to 18 months' storage at ambient conditions) (Figure 10). For simplicity reasons, experiments were performed on umbrella-like skeletons without the drug-containing cores, after having verified that the presence of the latter did not affect the unfolding mechanism. The specimens tested immediately after insertion into the capsules showed the desired deployment, regardless of the arm thickness. Indeed, they reached dimensions similar to those measured before folding (diameter of 36.00 ± 1.02 mm and 35.96 ± 1.22 mm for skeletons provided with 1 and 2mm-thick arms, respectively) (Figure 10a). In terms of kinetics, all the TPU-based specimens did not unfold instantaneously. However, the deployment time was always lower than 70 s from the capsule opening (Figure 10b). Since this value was lower than the time required for capsule dissolution (74–98 s), it was deemed acceptable. More into detail, unfolding times decreased with increasing TPU modulus. This may be explained by an active action of the arms. Indeed, the latter probably fostered the opening of the capsule by breaking and moving apart its walls, with the action of stiffer arms being more effective. Focusing on the storage impact, a small tendency toward a reduction in the dimensions of the deployed umbrella-like skeleton was observed and resulted less evident for samples provided with 2 mm thick arms. Nevertheless, the diameter values attained were always greater than those reported for the open pylorus, thus in principle not affecting the retention performance of the samples. With respect to the opening time, it generally increased with storage, with no major differences between umbrella-like skeletons having 1 or 2 mm-thick arms.

Further information on the functionality of the umbrella-like skeleton was gathered taking advantage of the funnel test. According to the literature, this experiment would provide the maximum resistance a GRDDS would oppose to forces that are expected to push it through a predefined rigid funnel restriction, intended to roughly mimic the gastric sphincter [24,27]. Indeed, data already published suggested that only systems capable of withstanding forces from 1.9 to 3 N might be compatible with gastric retention [24,131]. The funnel experiment was thus carried out on assembled systems (i.e., PCL-based cores inserted into the TPU-based umbrella-like skeletons). The latter were either conveyed in a capsule for a limited period (identified as $t = 0$), thus accounting for the time needed for the extemporaneous preparation of the GREDDS before relevant administration, or upon storage (Figure 11). This was done to preliminarily estimate stability of the system response over

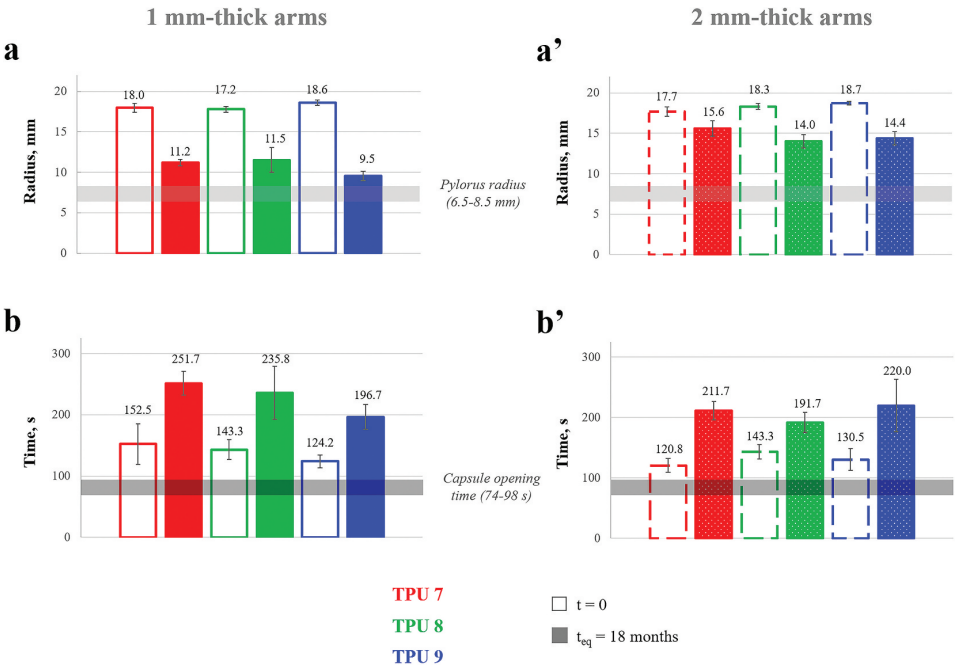

Figure 10. Radius (a, a') and opening time (b, b') data relevant to 1 and 2mm-thick umbrella-like skeletons based on various TPUs, tested upon insertion into commercially-available capsules and at increasing storage times.

time. As before described, storage was performed by keeping the umbrella-like skeletons at 55 °C for a certain time, which was calculated to be equivalent to 18 months' storage at 25 °C (t_{eq} = 18 months). Since previous tests highlighted a reduction in force at fixed deformation after a loading-unloading cycle, folding was also performed immediately after manufacturing. The experiments were repeated on assembled systems differing for the position of the hemispherical-shaped end of the core while passing through the funnel (see Figure 1). Indeed, it would not be possible to predict the direction in which the system would approach the pylorus in vivo.

The results of the funnel tests underlined that the higher the modulus of the TPU used for printing the umbrella-like skeleton, the higher the force required to push it. Moreover, the force data turned out greater when dealing with samples in the up position. Indeed, in such a position, the top part of the core acted as a physical obstacle, thus hindering undesired folding of the TPU-based arms. However, prototypes having 1 mm-thick arms reached, in the best-case scenario (i.e., umbrella-like skeletons based on TPU 9 and tested in the up position), peak values of about 0.5 N only. Alternatively, for samples entailing arms of 2 mm in thickness, force peaks up to 4 N were registered, thanks to an increased arm stiffness through the rise of its momentum of inertia. Specimens tested after storage always pointed out lower force data. This behavior could be associated with a limited recovery of the unfolded shape upon long-term maintenance within the capsule. Indeed, these umbrella-like skeletons were characterized by a truncated cone shape, which made expulsion from the funnel easier, especially when they were tested in the down position.

3.4. Ongoing work

Based on the data collected so far, preliminary trials were performed on assembled systems (*i.e.* having the drug-containing core inserted into the umbrella-like skeleton, with the latter folded and conveyed within a commercially available capsule body). As expected, not only was the opening performance of the GREDDS prototypes analogous to that observed with screening samples, but also their release profiles were superimposed to those attained when dealing with the cores alone. Funnel tests were also carried out on assembled devices subjected to release experiments. Samples were withdrawn at specific time points and tested, in order to rule out possible impact of contact with the acidic media over time. Interestingly, the maximum forces attained turned out comparable to the values previously discussed. Only when the PCL-based cores were exhausted and completely degraded, the maximum forces required to push the umbrella-like skeletons out of the funnel were markedly reduced (≤0.3 N). This result was considered particularly promising toward possible spontaneous elimination of the system from the stomach at the end release.

The overall behavior pointed out by assembled prototypes supported the suitability of the approach followed in this work, *i.e.* dealing with individual components of the device in parallel for simplifying and speeding up further experiments.

3.5. Future perspectives

The present study was intended to be part of a wider work, in the perspective of which the feasibility evaluation here described represented the first step. Indeed, the relations found between material properties, composition and performance of each component of the GREDDS under investigation were preparatory for further experiments and intended to guide the next research steps. These will be mainly aimed at increasing the resistance of the umbrella-like skeleton toward the funnel experiments, for instance *i)* fine-tuning the dimensional details of this component by means of a rational design process, and *ii)* identifying alternative materials for its manufacturing (e.g., different grades of thermoplastic polyurethanes or other thermoplastic elastomers). At the same time, the formulation of the drug-containing core will be optimized to perfectly match the expected 2 days-lasting release. Finally, great attention will be paid at finding novel design/composition strategies that will favor removal of the system from the stomach when required. By way of example, a new configuration of the umbrella like-skeleton is currently under evaluation, involving the presence of segments that could be degraded in the gastric environment. This is expected to occur only after complete release of metformin from the core, which would make the exhausted GREDDS smaller than the pylorus, thus favoring its spontaneous elimination from the gastrointestinal tract. In parallel, the resulting prototypes

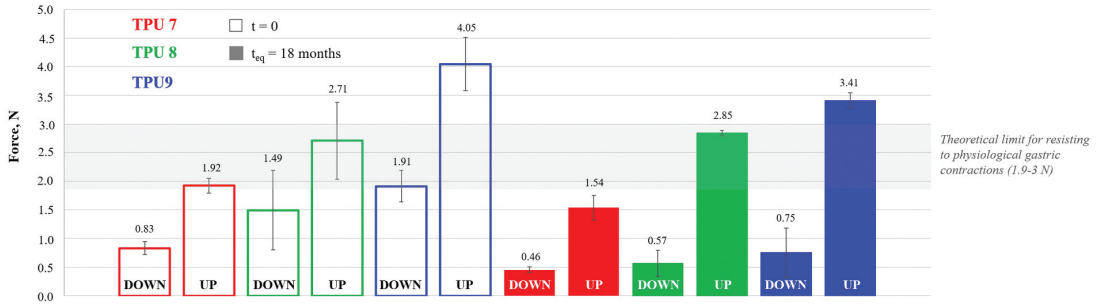

Figure 11. Maximum forces registered during the funnel test relevant to assembled GREDDS entailing umbrella-like skeletons (2 mm-thick arms) based on various TPUs and tested at increasing storage times.

will be deeply assessed for safety and reproducibility of their overall performance, for instance planning *in vitro* tests relying on the use of simulating gastric fluids differing for type and quantity of enzymes, as well as *ex vivo* and *in vivo* experiments.

4. Conclusions

Following a renovated interest for GRDDSs, especially in view of the suitability of such systems for therapy personalization and the possibility of using innovative technologies and materials for their manufacturing, a novel metformin-containing expandable device for the treatment of type II diabetes was designed and its feasibility was preliminarily demonstrated. The system proposed was intended to guarantee prolonged release of the drug at its absorption window, in order to cover one or more days of treatment with a single oral administration. It was conceived to include a drug-containing core based on PCL, ensuring controlled release, and a TPU umbrella-like skeleton. The latter was responsible for the achievement of the collapsed shape for oral intake and of the expanded one for gastric retention. Each of these parts was thoroughly characterized for key quality parameters: thermo-mechanical properties, resistance to simulated gastric contractions, stability, interaction with aqueous fluids, release as well as folding/unfolding performance. Thanks to the work performed, important links have been identified between composition and size/shape of each of the above-mentioned components, which supported the feasibility and will be fundamental in the development of the final GREDDS.

Author contributions

M Uboldi: Conceptualization, Software, Investigation, Writing – Original Draft
A Chiappa: Investigation, Data Curation, Writing – Original Draft, Validation
M Rossi: Investigation, Data Curation
F Briatico-Vangosa: Methodology, Formal analysis, Resources, Writing – Review & Editing
A Melocchi: Conceptualization, Writing – Original Draft, Writing – Review & Editing, Supervision
L Zema: Resources, Writing – Review & Editing, Supervision, Project administration

Funding

This paper was not funded.

Declaration of interest

The authors have no relevant affiliations or financial involvement with any organization or entity with a financial interest in or financial conflict with the subject matter or materials discussed in the manuscript. This includes employment, consultancies, honoraria, stock ownership or options, expert testimony, grants or patents received or pending, or royalties.

Reviewer disclosures

Peer reviewers on this manuscript have no relevant financial or other relationships to disclose

ORCID

Alice Melocchi http://orcid.org/0000-0001-5602-3314

References

1. Lopes CM, Bettencourt C, Rossi A, et al. Overview on gastroretentive drug delivery systems for improving drug bioavailability. Int J Pharm. 2016;510(1):144–158. doi: 10.1016/j.ijpharm.2016.05.016
2. Kumar M, Kaushik D. An overview on various approaches and recent patents on gastroretentive drug delivery systems. Recent Pat Drug Deliv Formul. 2018;12(2):84–92. doi: 10.2174/1872211312666180308150218
3. Pinto JF. Site-specific drug delivery systems within the gastro-intestinal tract: from the mouth to the colon. Int J Pharm. 2010;395(1–2):44–52. doi: 10.1016/j.ijpharm.2010.05.003
4. Streubel A, Siepmann J, Bodmeier R. Gastroretentive drug delivery systems. Expert Opin Drug Deliv. 2006;3(2):217–233. doi: 10.1517/17425247.3.2.217
5. Baride KS, Chemate SZ, Borkar GS, et al. An overview of the gastroretentive drug delivery system. Int J Pharm Sci Rev Res. 2023;80(2):104–115. doi: 10.47583/ijpsrr.2023.v80i02.016
6. Uboldi M, Melocchi A, Moutaharrik S, et al. Administration strategies and smart devices for drug release in specific sites of the upper GI tract. J Control Release. 2022;348:537–552. doi: 10.1016/j.jconrel.2022.06.005
7. Awasthi R, Kulkarni GT. Decades of research in drug targeting to the upper gastrointestinal tract using gastroretention technologies: where do we stand? Drug Deliv. 2016;23(2):378–394. doi: 10.3109/10717544.2014.936535
8. Dhiman S, Philip N, Singh TG, et al. An insight on novel approaches & perspectives for gastro-retentive drug delivery systems. Current Drug Deliv. 2023;20(6):708–729. doi: 10.2174/1567201819666220819200236
9. Melocchi A, Uboldi M, Cerea M, et al. A graphical review on the escalation of fused deposition modeling (FDM) 3D printing in the pharmaceutical field. J Pharm Sci. 2020;109(10):2943–2957. doi: 10.1016/j.xphs.2020.07.011
10. Tripathi J, Thapa P, Maharjan R, et al. Current state and future perspectives on gastroretentive drug delivery systems. Pharmaceutics. 2019;11(4):193. doi: 10.3390/pharmaceutics11040193
11. Vrettos NN, Roberts CJ, Zhu Z. Gastroretentive technologies in tandem with controlled-release strategies: a potent answer to oral drug bioavailability and patient compliance implications. Pharmaceutics. 2021;13(10):1591. doi: 10.3390/pharmaceutics13101591
12. Pal R, Pandey P, Nogai L, et al. The future perspectives and novel approach on gastro retentive drug delivery system (GRDDS) with currrent state. J Popul Ther Clin Pharmacol. 2023;30(17):594–613. doi: 10.53555/jptcp.v30i17.2852
13. Sambre TK, Mehta T, Sambre TT. Saga of gastroretentive drug delivery system: emerging concepts, recent advances and technological progress. Int J Pharm Sci Res. 2023;14(5):2030–2059.
14. Abramson A, Caffarel-Salvador E, Khang M, et al. An ingestible self-orienting system for oral delivery of macromolecules. Science. 2019;363(6427):611–615. doi: 10.1126/science.aau2277
15. Abramson A, Frederiksen MR, Vegge A, et al. Oral delivery of systemic monoclonal antibodies, peptides and small molecules using gastric auto-injectors. Nat Biotechnol. 2021;40(1):103–109. doi: 10.1038/s41587-021-01024-0
16. Abramson A, Kirtane AR, Shi Y, et al. Oral mRNA delivery using capsule-mediated gastrointestinal tissue injections. Matter. 2022;5(3):975–987. doi: 10.1016/j.matt.2021.12.022
17. Altreuter DH, Kirtane AR, Grant T, et al. Changing the pill: developments toward the promise of an ultra-long-acting gastroretentive dosage form. Expert Opin Drug Deliv. 2018;15(12):1189–1198. doi: 10.1080/17425247.2018.1544615
18. Byrne J, Huang HW, McRae JC, et al. Devices for drug delivery in the gastrointestinal tract: a review of systems physically interacting with the mucosa for enhanced delivery. Adv Drug Deliv Rev. 2021;177:113926. doi: 10.1016/j.addr.2021.113926

19. Caffarel-Salvador E, Abramson A, Langer R, et al. Oral delivery of biologics using drug-device combinations. Curr Opin Pharmacol. 2017;36:8–13. doi: 10.1016/j.coph.2017.07.003
20. Chu JN, Traverso G. Foundations of gastrointestinal-based drug delivery and future developments. Nat Rev Gastroenterol Hepatol. 2022;19(4):219–238. doi: 10.1038/s41575-021-00539-w
21. Kirtane AR, Tang C, Freitas D, et al. Challenges and opportunities in the development of mucosal mRNA vaccines. Curr Opin Immunol. 2023;85:102388. doi: 10.1016/j.coi.2023.102388
22. Subramanian DA, Langer R, Traverso G. Mucus interaction to improve gastrointestinal retention and pharmacokinetics of orally administered nano-drug delivery systems. J Nanobiotechnology. 2022;20(1):362. doi: 10.1186/s12951-022-01539-x
23. Lyndra therapeutics [cited 2023 Nov 30] https://lyndra.com/
24. Bellinger AM, Jafari M, Grant TM, et al. Oral, ultra-long-lasting drug delivery: Application toward malaria elimination goals. Sci Transl Med. 2016;8(865):365ra157. doi: 10.1126/scitranslmed.aag2374
25. Hayward A, Bensel T, Mazdiyasni H, et al. Scalable gastric resident systems for veterinary application. Sci Rep. 2018;8(1):11816. doi: 10.1038/s41598-018-30212-3
26. Kanasty R, Low S, Bhise N, et al. A pharmaceutical answer to nonadherence: once weekly oral memantine for Alzheimer's disease. J Control Release. 2019;303:34–41. doi: 10.1016/j.jconrel.2019.03.022
27. Kirtane AR, Abouzid O, Minahan D, et al. Development of an oral once-weekly drug delivery system for HIV antiretroviral therapy. Nat Commun. 2018;9(1):2. doi: 10.1038/s41467-017-02294-6
28. Kirtane AR, Hua T, Hayward A, et al. A once-a-month oral contraceptive. Sci Transl Med. 2019;11(521):eaay2602. doi: 10.1126/scitranslmed.aay2602
29. Klausner EA, Lavy E, Friedman M, et al. Expandable gastroretentive dosage forms. J Control Release. 2003;90(2):143–162. doi: 10.1016/S0168-3659(03)00203-7
30. Pawar VK, Kansal S, Garg G, et al. Gastroretentive dosage forms: a review with special emphasis on floating drug delivery systems. Drug Deliv. 2011;18(2):97–110. doi: 10.3109/10717544.2010.520354
31. Pawar VK, Kansal S, Asthana S, et al. Industrial perspective of gastroretentive drug delivery systems: physicochemical, biopharmaceutical, technological and regulatory consideration. Expert Opin Drug Deliv. 2012;9(5):551–565. doi: 10.1517/17425247.2012.677431
32. Prinderre P, Sauzet C, Fuxen C. Advances in gastro retentive drug-delivery systems. Expert Opin Drug Deliv. 2011;8(9):1189–1203. doi: 10.1517/17425247.2011.592828
33. Chaudhari S, Walde S, Purohit A. A review on floating drug delivery systems. Int J Pharm Sci Res. 2023;81(1):37–41. doi: 10.47583/ijpsrr.2023.v81i01.008
34. Mahmoud DB, Schulz-Siegmund M. Utilizing 4D printing to design smart gastroretentive, esophageal, and intravesical drug delivery systems. Adv Health Mat. 2022;12(19):2202631. doi: 10.1002/adhm.202202631
35. Melocchi A, Uboldi M, Cerea M, et al. Shape memory materials and 4D printing in pharmaceutics. Adv Drug Deliv Rev. 2021a;173:216–237. doi: 10.1016/j.addr.2021.03.013
36. Verma M, Vishwanath K, Eweje F, et al. A gastric resident drug delivery system for prolonged gram-level dosing of tuberculosis treatment. Sci Transl Med. 2019;11(483):eaau6267. doi: 10.1126/scitranslmed.aau6267
37. Verma M, Chu JN, Salama JA, et al. Sa1527 development of a long-acting direct-acting antiviral system for Hepatitis C Virus treatment in a swine model. Gastroenterol. 2020;158(6):S–1321. doi: 10.1016/S0016-5085(20)33972-X
38. Inverardi N, Scalet G, Melocchi A, et al. Experimental and computational analysis of a pharmaceutical-grade shape memory polymer applied to the development of gastroretentive drug delivery systems. J Mech Behav Biomed Mater. 2021;124:104814. doi: 10.1016/j.jmbbm.2021.104814
39. Melocchi A, Inverardi N, Uboldi M, et al. Retentive device for intravesical drug delivery based on water-induced shape memory response of poly(vinil alcohol): design concept and 4D printing feasibility. Int J Pharm. 2019a;559:299–311. doi: 10.1016/j.ijpharm.2019.01.045
40. Melocchi A, Uboldi M, Inverardi N, et al. Expandable drug delivery system for gastric retention based on shape memory polymers: development via 4D printing and extrusion. Int J Pharm. 2019b;571:118700. doi: 10.1016/j.ijpharm.2019.118700
41. Uboldi M, Melocchi A, Moutaharrik S, et al. Dataset on a small-scale film-coating process developed for self-expanding 4D printed drug delivery devices. Coatings. 2021;11(10):1252. doi: 10.3390/coatings11101252
42. Uboldi M, Pasini C, Pandini S, et al. Expandable drug delivery systems based on shape memory polymers: impact of film coating on mechanical properties and release and recovery performance. Pharmaceutics. 2022;14(12):2814. doi: 10.3390/pharmaceutics14122814
43. Uboldi M, Perrotta C, Moscheni C, et al. Insights into the safety and versatility of 4D printed intravesical drug delivery systems. Pharmaceutics. 2023;15(3):757. doi: 10.3390/pharmaceutics15030757
44. Uboldi M, Gelain A, Buratti G, et al. Development of 4D printed intravesical drug delivery systems: scale-up of film-coating. J D Deliv Sci Technol. 2023;87:104875. doi: 10.1016/j.jddst.2023.104875
45. Hatipoglu BA. Rekindling hope for remission: current impact of diabetes for our world's future health and economy. Endocrinol Metab Clin N Am. 2023;52(1):1–12. doi: 10.1016/j.ecl.2022.06.006
46. Baker C, Retzik-Stahr C, Singh V, et al. Should metformin remain the first-line therapy for treatment of type 2 diabetes? Ther Adv Endocrinol Metab. 2021;12:2042018820980225. doi: 10.1177/2042018820980225
47. Buse JB, DeFronzo RA, Rosenstock J, et al. The primary glucose-lowering effect of metformin resides in the gut, not the circulation: results from short-term pharmacokinetic and 12-week dose-ranging studies. Diabetes Care. 2016;39(2):198–205. doi: 10.2337/dc15-0488
48. Garber AJ, Duncan TG, Goodman AM, et al. Efficacy of metformin in type II diabetes: results of a double-blind, placebo-controlled, dose-response trial fn1. Am J Med. 1997;103(6):491–497. doi: 10.1016/S0002-9343(97)00254-4
49. Corcoran C, Jacobs TF. Metformin. Treasure Island (FL): StatPearls Publishing; 2023.
50. Sanchez-Rangel E, Inzucchi SE. Metformin: clinical use in type 2 diabetes. Diabetologia. 2017;60(9):1586–1593. doi: 10.1007/s00125-017-4336-x
51. Sheehan MT. Current therapeutic options in type 2 diabetes mellitus: a practical approach. Clin Med Res. 2003;1(3):189–200. doi: 10.3121/cmr.1.3.189
52. Boldhane SP, Kuchekar BS. Gastroretentive drug delivery of metformin hydrochloride: formulation and in vitro evaluation using 32 full factorial design. Current Drug Deliv. 2009;6(5):477–485. doi: 10.2174/156720109789941641
53. Hoffman A, Stepensky D, Lavy E, et al. Pharmacokinetic and pharmacodynamic aspects of gastroretentive dosage forms. Int J Pharm. 2004;277(1–2):141–153. doi: 10.1016/j.ijpharm.2003.09.047
54. Kim JH, Song SH, Joo SH, et al. Formulation of a gastroretentive in situ oral gel containing metformin HCl based on DoE. Pharmaceutics. 2022;14(9):1777. doi: 10.3390/pharmaceutics14091777
55. Pawar R, Jagdale S, Randive D. Development of floating gastroretentive drug delivery system based on a novel excipient for metformin hydrochloride using mixture design. Int J Pharm Pharm Sci. 2020;12(10):62–71. doi: 10.22159/ijpps.2020v12i10.38678
56. Kumar A, Sharma AK, Dutt R. A review of gastro-retentive drug delivery systems for antidiabetics and its present status. Res J Pharm Technol. 2021;14(1):538–546. doi: 10.5958/0974-360X.2021.00098.6
57. Upadhyay P, Pandit JK, Upadhyay S, et al. Studies on formulation and optimization of gastro retentive multi-particulates of Glibenclamide and metformin hydrochloride for the treatment of type II diabetes mellitus using gelucire: a review. J Pharm Sci Res. 2010;2(6):351–354.

58. Jeong YS, Jusko WJ. Meta-assessment of metformin absorption and disposition pharmacokinetics in nine species. Pharmaceuticals. 2021;14(6):545. doi: 10.3390/ph14060545
59. Scheen AJ. Clinical pharmacokinetics of metformin. Clin Pharmacokinet. 1996;30(5):359–371. doi: 10.2165/00003088-199630050-00003
60. Stepensky D, Friedman M, Srour W, et al. Preclinical evaluation of pharmacokinetic-pharmacodynamic rationale for oral CR metformin formulation. J Control Release. 2001;71(1):107–115. doi: 10.1016/S0168-3659(00)00374-6
61. Aroda VR, Ratner RE. Metformin and type 2 diabetes prevention. Diabetes Spectr. 2018;31(4):336–342. doi: 10.2337/ds18-0020
62. Blough B, Moreland A, Mora A Jr. Metformin-induced lactic acidosis with emphasis on the anion gap. Proc (Bayl Univ Med Cent). 2015;28(1):31–33. doi: 10.1080/08998280.2015.11929178
63. Nasri H, Rafieian-Kopaei M. Metformin: current knowledge. J Res Med Sci. 2014;19(7):658–664. doi: 10.12659/MSMBR.889344
64. Rojas LBA, Gomes MB. Metformin: an old but still the best treatment for type 2 diabetes. Diabetol Metab Syndr. 2013;5(1):6. doi: 10.1186/1758-5996-5-6
65. Hemels M, Jensen RCØ, Toumi M, et al. Relative effectiveness management of type II diabetes in europe: can the agencies' demands be met? Value Health. 2010;13:A55. doi: 10.1016/S1098-3015(10)72253-1
66. Diabetes in Europe [cited 2023 Nov 30] https://www.mepinterestgroupdiabetes.eu/wp-content/uploads/2021/11/IDF-Atlas-Factsheet-2021_EUR.pdf
67. IDF Diabetes Atlas [cited 2023 Nov 30] https://diabetesatlas.org/data/en/indicators/17/
68. Jönsson B. Revealing the cost of type II diabetes in Europe. Diabetologia. 2002;45(7):S5–S12. doi: 10.1007/s00125-002-0858-x
69. Völzke H, Ittermann T, Schmidt CO, et al. Prevalence trends in lifestyle-related risk factors. Dtsch Arztebl Int. 2015;112(11):185–192. doi: 10.3238/arztebl.2015.0185
70. Zhuo X, Zhang P, Hoerger TJ. Lifetime direct medical costs of treating type 2 diabetes and diabetic complications. Am J Prev Med. 2013;45(3):253–261. doi: 10.1016/j.amepre.2013.04.017
71. Ferry JD. Viscoelastic properties of polymers. (NY) (NY): John Wiley & Sons; 1980.
72. Daskalakis E, Hassan MH, Omar AM, et al. Accelerated degradation of poly-ε-caprolactone composite scaffolds for large bone defects. Polymers. 2023;15(3):670. doi: 10.3390/polym15030670
73. Lee SH, Lee JH, Cho YS. Analysis of degradation rate for dimensionless surface area of well-interconnected PCL scaffold via in-vitro accelerated degradation experiment. Tissue Eng Regen Med. 2014;11(6):446–452. doi: 10.1007/s13770-014-0067-y
74. Zhou ZX, Chen YR, Zhang JY, et al. Facile strategy on hydrophilic modification of poly(ε-caprolactone) scaffolds for assisting tissue-engineered meniscus constructs in vitro. Front Pharmacol. 2020;11:471. doi: 10.3389/fphar.2020.00471
75. Dumpa N, Butreddy A, Wang H, et al. 3D printing in personalized drug delivery: an overview of hot-melt extrusion-based fused deposition modeling. Int J Pharm. 2021;600:120501. doi: 10.1016/j.ijpharm.2021.120501
76. Kallakunta VR, Sarabu S, Bandari S, et al. An update on the contribution of hot-melt extrusion technology to novel drug delivery in the twenty-first century: part I. Expert Opin Drug Deliv. 2019;16(5):539–550. doi: 10.1080/17425247.2019.1609448
77. Sarabu S, Bandari S, Kallakunta VR, et al. An update on the contribution of hot-melt extrusion technology to novel drug delivery in the twenty-first century: part II. Expert Opin Drug Deliv. 2019;16(6):567–582. doi: 10.1080/17425247.2019.1614912
78. Simões MF, Pinto RMA, Simões S. Hot-melt extrusion in the pharmaceutical industry: toward filing a new drug application. Drug Discov Today. 2019;24(9):1749–1768. doi: 10.1016/j.drudis.2019.05.013
79. Zema L, Loreti G, Melocchi A, et al. Injection molding and its application to drug delivery. J Control Release. 2012;159(3):324–331. doi: 10.1016/j.jconrel.2012.01.001
80. Dash TK, Konkimalla VB. Poly-ε-caprolactone based formulations for drug delivery and tissue engineering: a review. J Control Release. 2012;158(1):15–33. doi: 10.1016/j.jconrel.2011.09.064
81. Elbjorn M, Provencio J, Phillips P, et al. An innovative polymeric platform for controlled and localized drug delivery. Pharmaceutics. 2023;15(7):1795. doi: 10.3390/pharmaceutics15071795
82. Henderson B. Polycaprolactones: properties, applications, and selected research. London (UK): Nova Science Publishers; 2017.
83. Malikmammadov E, Tanir TE, Kiziltay A, et al. PCL and PCL-based materials in biomedical applications. J Biomater Sci Polym Ed. 2018;29(7–9):863–893. doi: 10.1080/09205063.2017.1394711
84. Mohamed R, Yusoh K. A review on the recent research of polycaprolactone (PCL). Adv Mat Res. 2015;1134:249–255. doi: 10.4028/www.scientific.net/AMR.1134.249
85. Mondal D, Griffith MV, Venkatraman SS. Polycaprolactone-based biomaterials for tissue engineering and drug delivery: Current scenario and challenges. Int J Polym Mater. 2016;65(5):255–265. doi: 10.1080/00914037.2015.1103241
86. Faglie A, Emerine R, Chou S-F. Effects of poloxamers as excipients on the physicomechanical properties, cellular biocompatibility, and in vitro drug release of electrospun polycaprolactone (PCL. Fibers Polyms. 2023;15(14):2997. doi: 10.3390/polym15142997
87. Douglas P, Jones AG, Walker D. Analysis of in vitro drug dissolution from PCL melt extrusion. Chem Eng J. 2010;164(2–3):359–370. doi: 10.1016/j.cej.2010.03.077
88. Guastaferro M, Baldino M, Cardea S, et al. Supercritical processing of PCL and PCL-PEG blends to produce improved PCL-based porous scaffolds. J Supercrit Fluids. 2022;186:105611. doi: 10.1016/j.supflu.2022.105611
89. Dalton M, Ebrahimi F, Xu H, et al. The influence of the molecular weight of poly(ethylene oxide) on the hydrolytic degradation and physical properties of polycaprolactone binary blends. Macromol. 2023;3(3):431–450. doi: 10.3390/macromol3030026
90. Douglas P, Albadarin AB, Sajjia M, et al. Effect of poly ethylene glycol on the mechanical and thermal properties of bioactive poly(ε-caprolactone) melt extrudates for pharmaceutical applications. Int J Pharm. 2016;500(1–2):179–186. doi: 10.1016/j.ijpharm.2016.01.036
91. Homaeigohar S, Boccaccini AR. Nature-derived and synthetic additives to poly(ε-caprolactone) nanofibrous systems for biomedicine; an updated overview. Front Chem. 2022;19:809676. doi: 10.3389/fchem.2021.809676
92. Bezerra GSN, De Lima GG, Colbert DM, et al. Micro-injection moulding of PEO/PCL blend–based matrices for extended oral delivery of fenbendazole. Pharmaceutics. 2023;15(3):900. doi: 10.3390/pharmaceutics15030900
93. Bezerra GSN, de Lima TADM, Colbert DM, et al. Formulation and evaluation of fenbendazole extended-release extrudes processed by hot-melt extrusion. Polymers. 2022;14(19):4188. doi: 10.3390/polym14194188
94. Berger V, Green Buzhor M, Evstafeva D, et al. 3D printing of a controlled urea delivery device for the prevention of tooth decay. Int J Pharm. 2023;631:122528. doi: 10.1016/j.ijpharm.2022.122528
95. Vlachou M, Siamidi A, Anagnostopoulou D, et al. Tuning the release of the pineal hormone melatonin via poly(ε-caprolactone)-based copolymers matrix tablets.J. Drug Deliv Sci Technol. 2023;79:04051. doi: 10.1016/j.jddst.2022.104051
96. Bartnikowski M, Dargaville TR, Ivanovski S, et al. Degradation mechanisms of polycaprolactone in the context of chemistry, geometry and environment. Prog Polym Sci. 2019;96:1–20. doi: 10.1016/j.progpolymsci.2019.05.004
97. Evonik Leading Beyond Chemistry [cited 2023 Nov 30]. https://healthcare.evonik.com/en/medical-devices/bioresorbable-polymers/standard-polymers
98. Sun H, Mei L, Song C, et al. The in vivo degradation, absorption and excretion of PCL-based implant. Biomaterials. 2006;27(9):1735–1740. doi: 10.1016/j.biomaterials.2005.09.019
99. Balguri SP, Adelli GR, Tatke A, et al. Melt-cast noninvasive ocular inserts for posterior segment drug delivery. J Pharm Sci. 2017;106(12):3515–3523. doi: 10.1016/j.xphs.2017.07.017

100. Blackwell CJ, Haernvall K, Guebitz GM, et al. Enzymatic degradation of star poly(ε-caprolactone) with different central units. Polymers. 2018;10(11):1266. doi: 10.3390/polym10111266
101. Castilla-Cortázar I, Más-Estellés J, Meseguer-Dueñas JM, et al. Hydrolytic and enzymatic degradation of a poly(ε-caprolactone) network. Polym Degrad Stab. 2012;97(8):1241–1248. doi: 10.1016/j.polymdegradstab.2012.05.038
102. Gan Z, Liang Q, Zhang J, et al. Enzymatic degradation of poly(ε-caprolactone) film in phosphate buffer solution containing lipases. Polym Degrad Stab. 1997;56(2):209–213. doi: 10.1016/S0141-3910(96)00208-X
103. Pastorino L, Pioli F, Zilli M, et al. Lipase-catalyzed degradation of poly(ε-caprolactone). Enzyme Microb Technol. 2004;35(4):321–326. doi: 10.1016/j.enzmictec.2004.05.005
104. Liu M, Zhang T, Long L, et al. Efficient enzymatic degradation of poly (3-caprolactone) by an engineered bifunctional lipase-cutinase. Polym Degrad Stab. 2019;160:120–125. doi: 10.1016/j.polymdegradstab.2018.12.020
105. Woodruff MA, Hutmacher DW. The return of a forgotten polymer–polycaprolactone in the 21st century. Prog Polym Sci. 2010;35(10):1217–1256. doi: 10.1016/j.progpolymsci.2010.04.002
106. Chen DR, Bei JZ, Wang SG. Polycaprolactone microparticles and their biodegradation. Polym Degrad Stab. 2000;67(3):455–459. doi: 10.1016/S0141-3910(99)00145-7
107. Hoshino A, Isono Y. Degradation of aliphatic polyester films by commercially available lipases with special reference to rapid and complete degradation of poly(L-lactide) film by lipase PL derived from Alcaligenes sp. Biodegradation. 2002;13(2):141–147. doi: 10.1023/A:1020450326301
108. Cheng L, Lei L, Guo S. In vitro and in vivo evaluation of praziquantel loaded implants based on PEG/PCL blends. Int J Pharm. 2010;387(1–2):129–138. doi: 10.1016/j.ijpharm.2009.12.010
109. Dalton M, Ebrahimi F, Xu H, et al. The influence of the molecular weight of poly(ethylene oxide) on the hydrolytic degradation and physical properties of polycaprolactone binary blends. Macromol. 2023;3(3):431–450. doi: 10.3390/macromol3030026
110. Jiang Y, Mao K, Cai X, et al. Poly(ethyl glycol) assisting water sorption enhancement of poly(ε-caprolactone) blend for drug delivery. J Appl Polym Sci. 2011;122(4):2309–2316. doi: 10.1002/app.34382
111. Chang HI, Williamson MR, Perrie Y, et al. Precipitation casting of drug-loaded microporous PCL matrices: incorporation of progesterone by co-dissolution. J Control Release. 2005;106(3):263–272. doi: 10.1016/j.jconrel.2005.05.013
112. Asvadi NH, Dang NTT, Davis-Poynter N, et al. Evaluation of microporous polycaprolactone matrices for controlled delivery of antiviral microbicides to the female genital tract. J Mater Sci Mater Med. 2013;24(12):2719–2727.
113. Dang NTT, Turner MS, Coombes AGA. Development of intra-vaginal matrices from polycaprolactone for sustained release of antimicrobial agents. J Biomater Appl. 2013;28(1):74–83. doi: 10.1177/0885328212437393
114. Wong BS, Teoh SH, Kang L. Polycaprolactone scaffold as targeted drug delivery system and cell attachment scaffold for postsurgical care of limb salvage. Drug Deliv Transl Res. 2012;2(4):272–283. doi: 10.1007/s13346-012-0096-9
115. Chattopadhyay DK, Webster DC. Thermal stability and flame retardancy of polyurethanes. Prog Polym Sci. 2009;34(10):1068–1133. doi: 10.1016/j.progpolymsci.2009.06.002
116. Das A, Mahanwar P. A brief discussion on advances in polyurethane applications. Adv Ind Eng Polym Res. 2020;3(3):93–101. doi: 10.1016/j.aiepr.2020.07.002
117. Petrović ZS, Ferguson J. Polyurethane elastomers. Prog Polym Sci. 1991;16(5):695–836. doi: 10.1016/0079-6700(91)90011-9
118. Xie F, Zhang T, Bryant P, et al. Degradation and stabilization of polyurethane elastomers. Progress Poly Sci. 2019;90:211–268. doi: 10.1016/j.progpolymsci.2018.12.003
119. Cherng JY, Hou TY, Shih MF, et al. Polyurethane-based drug delivery systems. Int J Pharm. 2013;450(1–2):145–162. doi: 10.1016/j.ijpharm.2013.04.063
120. Claeys B, Vervaeck A, Hillewaere XKD, et al. Thermoplastic polyurethanes for the manufacturing of highly dosed oral sustained release matrices via hot melt extrusion and injection molding. Eur J Pharm Biopharm. 2015;90:44–52. doi: 10.1016/j.ejpb.2014.11.003
121. St John KR. The use of polyurethane materials in the surgery of the spine: a review. Spine J. 2014;14(12):3038–3047. doi: 10.1016/j.spinee.2014.08.012
122. Joseph J, Patel RM, Wenham A, et al. Biomedical applications of polyurethane materials and coatings. Trans Inst Met. 2018;96(3):121–129. doi: 10.1080/00202967.2018.1450209
123. Koutsamanis I, Roblegg E, Spoerk M. Controlled delivery via hot-melt extrusion: a focus on non-biodegradable carriers for non-oral applications. J Drug Deliv Sci Technol. 2023;81:104289. doi: 10.1016/j.jddst.2023.104289
124. M'Bengue MS, Mesnard T, Chai F, et al. Evaluation of a medical grade thermoplastic polyurethane for the manufacture of an implantable medical device: the impact of FDM 3D-printing and gamma sterilization. Pharmaceutics. 2023;15(2):456. doi: 10.3390/pharmaceutics15020456
125. Verstraete G, Van Renterghem J, Van Bockstal PJ, et al. Hydrophilic thermoplastic polyurethanes for the manufacturing of highly dosed oral sustained release matrices via hot melt extrusion and injection molding. Int J Pharm. 2016;506(1–2):214–221. doi: 10.1016/j.ijpharm.2016.04.057
126. Verstraete G, Samaro A, Grymonpré W, et al. 3D printing of high drug loaded dosage forms using thermoplastic polyurethanes. Int J Pharm. 2018;536(1):318–325. doi: 10.1016/j.ijpharm.2017.12.002
127. Wendels S, Avérous L. Biobased polyurethanes for biomedical applications. Bioact Mater. 2021;6(4):1083–1106. doi: 10.1016/j.bioactmat.2020.10.002
128. Cailleaux S, Sanchez-Ballester NM, Gueche YA, et al. Fused deposition modeling (FDM), the new asset for the production of tailored medicines. J Control Release. 2021;330:821–841. doi: 10.1016/j.jconrel.2020.10.056
129. Melocchi A, Uboldi M, Briatico-Vangosa F, et al. The chronotopic™ system for pulsatile and colonic delivery of active molecules in the era of precision medicine: feasibility by 3D printing via fused deposition modeling (FDM). Pharmaceutics. 2021;13(5):759. doi: 10.3390/pharmaceutics13050759
130. Parulski C, Jennotte O, Lechanteur A, et al. Challenges of fused deposition modeling 3D printing in pharmaceutical applications: where are we now? Adv Drug Deliv Rev. 2021;175:13810. doi: 10.1016/j.addr.2021.05.020
131. Kong F, Singh RP. A human gastric simulator (HGS) to study food digestion in human stomach. J Food Sci. 2010;75(9):E627–35. doi: 10.1111/j.1750-3841.2010.01856.x

International Journal of Pharmaceutics 671 (2025) 125217

Contents lists available at ScienceDirect

International Journal of Pharmaceutics

journal homepage: www.elsevier.com/locate/ijpharm

3D printed reservoir-like vaginal rings for antibiotic delivery

Arianna Chiappa [a], Alice Fusari [a], Marco Uboldi [b], Paola Petrini [a], Alice Melocchi [b,*], Francesco Briatico Vangosa [a], Lucia Zema [b]

[a] Dipartimento di Chimica, Materiali e Ingegneria Chimica "G. Natta", Politecnico di Milano, Piazza Leonardo da Vinci 32, 20133, Milano, Italy
[b] Sezione di Tecnologia e Legislazione Farmaceutiche "Maria Edvige Sangalli", Dipartimento di Scienze Farmaceutiche, Università degli Studi di Milano, via Giuseppe Colombo 71, 20133, Milano, Italy

ARTICLE INFO

Keywords:
Personalized therapy
Vaginal infections
Hollow vaginal ring
Alginate-based hydrogel
Metronidazole

ABSTRACT

Targeting the development of 3D printed reservoir-like vaginal rings (VRs) intended to fulfill the needs of precision medicine, prototypes ensuring prolonged release of metronidazole (MTZ) were preliminary manufactured and tested. Indeed, this drug represents the first-line therapy against bacterial vaginosis, which would especially benefit from convenient as well as easy dose adjustment and from more than 48 h continuous release, thus avoiding barely tolerated and repeated administrations. Starting from a soft thermoplastic elastomer (TPE), hollow ring structures were successfully printed at 190 °C and then extemporaneously filled with drug-loaded, *in-situ*-crosslinking hydrogel formulations based on alginate (ALG). 3 VR designs, differing in dimensions, number of open surfaces as well as in relevant areas were investigated, together with 9 drug-saturated hydrogel formulations containing extra suspended MTZ particles (20–50 %) and increasing ALG concentrations (2–6 %). Manufacturing of final rings was fine-tuned based on materials thermo-mechanical properties. For comparison purposes, hydrogels with analogous composition were either cast using purposely developed molds or 3D printed mimicking the ring design. VR release performance turned out dependent on the drug solubility and on the surface area available for hydrogel contact with vaginal fluids. Interestingly, this surface resulted correlated to both the outer and inner structure of the system. The data collected would provide an effective asset to increase the versatility of reservoir-like VRs, making them a powerful tool towards therapy customization.

1. Introduction

Vaginal rings (VRs) are flexible, torus-shaped, polymeric devices, which over years were demonstrated well-tolerated among the female population [Boyd et al., 2020; Carson et al., 2021; Johansson, Sitruk-Ware, 2004]. Indeed, they ensure controlled release of drugs to the vagina for treatment and prevention of various clinical conditions. Although suitable for both systemic therapies and local applications, to date they are mainly used for contraceptive purposes [Abdollahpour et al., 2023; Barriga Pooley et al., 2020; Guazzelli et al., 2014; Krovi et al., 2021; Monteiro et al., 2018]. If compared with drug products conveying the same hormonal therapy *via* the oral route, VRs exhibit major advantages. Indeed, they *i)* enable long-lasting systemic delivery of estrogens and progestins, covering ≥ 1 month of therapy without the need for repeated applications, *ii)* avoid daily fluctuations of the drug concentration in the bloodstream and *iii)* do not require any daily action from the patient, thus increasing compliance and limiting misuse (*e.g.* forgetting one or more dosage forms, late initiation of a new cycle) [Roumen, 2007]. In addition, administration through VRs allows to overcome limitations related to gastrointestinal absorption and to hepatic first-pass metabolism, resulting in greater drug bioavailability at lower dosages. In a broader perspective, VR-based contraceptives represented a women's empowering tool: not only were they demonstrated beneficial towards sexual and reproductive health, but also favored socio-economic development of the users. For this reason, starting from the proof-of-concept study published by Mishell and Lumkin in the '70s and focused on a medroxyprogesterone acetate-containing device, several hormone-releasing VRs have been described, which were designed to be worn continuously from 1 week to 1 year [Brache, Faundes, 2010; Carson et al., 2021; Mishell et al., 1970, 1972, Mishell, 1993; Tietz, Klein, 2019]. By way of example, progestin-only and combined progestin-estrogen rings were marketed, such as NuvaRing®, Progering®, Annovera®, Fertiring®, Ornibel® and Femring®. These systems are generally characterized by either matrix- or reservoir-like

* Corresponding author.
E-mail address: alice.melocchi@unimi.it (A. Melocchi).

https://doi.org/10.1016/j.ijpharm.2025.125217
Received 10 December 2024; Received in revised form 8 January 2025; Accepted 11 January 2025
Available online 16 January 2025

structures, in which silicon and ethylenevinyl acetate-based elastomers, eventually in combination with polyurethanes, were the most used ring-forming materials. Hot-processing techniques were the only enough versatile to guarantee the manufacturing, at scale, of VRs with the desired configurations [Casati et al., 2020; Koutsamanis et al., 2023; Patil et al., 2024; Zema et al., 2012]. In matrix-like products manufactured by one-step injection molding (*e.g.* Fertiring®, Progering®), solid crystalline drugs were dispersed throughout the whole device volume. On the other hand, reservoir-like VRs (*e.g.* Nuvaring®, Femring®, Ornibel®), involving a core from which drugs are intended to diffuse through surrounding release-controlling walls, were generally manufactured by rather complex multi-step injection molding and co-extrusion processes. Despite their simplicity of use, development and production of VRs with desired size, mechanical characteristics and release performance over time, to ensure contraception and minimal side effects, was generally a quite long and intricated process. It found its rational in the absorption capacity of the vaginal epithelium and in the ability of selected drugs − mainly highly potent lipophilic (log p > 2) and low molecular weight (< 540 g/mol) active molecules − to diffuse through the ring-forming materials [McBride et al., 2019]. However, most VRs are characterized by an undesired initial burst effect, due to accumulation of the drugs on the ring surface during storage, followed by their release at constant rate.

Based on the benefits VRs provided towards the administration of hormonal therapy, such drug delivery systems (DDSs) have recently been investigated for other purposes, not only at the research level but also in pre-clinical and clinical settings. By way of example, researchers are currently evaluating the possibility of using them for preventing sexual transmission of human immunodeficiency virus (HIV) infections in developing countries [Griffin et al., 2019; Malcolm et al., 2016; Krovi et al., 2021; Rahman, Ahmed, 2016]. To this end, VRs were deemed particularly advantageous from the economic point of view, as they entail reduced dosing frequency and non-invasive self-administration, thus not requiring any physician's intervention for either their administration or removal.

In 2014, with the widespread of 3D printing and particularly following the availability of relatively cheap desktop equipment, scientists working in the pharmaceutical field started approaching this technology, willing to demonstrate its potential for the manufacturing of a range of personalized DDSs [Auel et al., 2025; Deng et al., 2025; Dumpa et al., 2021; Muhindo et al., 2023; Majrashi et al., 2024; Parulski et al., 2021; Zema et al., 2017]. Most of the first published works focused on the oral route and on the feasibility of relatively simple drug products [Alzoubi et al., 2023; Bandari et al., 2021; Melocchi et al., 2020]. However, with the passing of time, the literature was populated by more complex devices (*e.g.* pierced, hollow, multi-component, multi-layered, 4D printed) intended for different administration modes, also including vaginal delivery [Antezana et al., 2023; Gazzaniga et al., 2023; Inverardi et al., 2021; Kumar et al., 2024; Melocchi et al., 2021; Muhindo et al., 2023; Narala et al., 2024; Uboldi et al., 2022a, 2023a,b,2024]. As expected, additive manufacturing based on hot-processing (*e.g.* fused deposition modeling, droplet deposition modeling, direct powder deposition) resulted among the most popular techniques when dealing with vaginal administration, and was mainly employed for printing matrix-like rings starting from relatively hard-polymers (*e.g.* polylactic acid, polycaprolactone, ethylenevinyl acetate) [Algahtani et al., 2024; Fu et al., 2018; Moroni et al., 2023, Tiboni et al., 2021, Xu et al., 2025; Welsh et al., 2019]. The technique was successful in achieving a comprehensive personalization of the VRs, in terms not only of drug load and device microstructure, thus allowing to fine-tune the final release performance, but also of overall ring design, widening the portfolio of printable shapes besides the common torus-like geometry. However, as the drugs needed to be embedded into the molten polymer for manufacturing matrix-like VRs, only thermally stable molecules were used. In this respect, Arany and coworkers made a preliminary step forward: they demonstrated the feasibility of pre-printed void parts of a ring mimicking the commercial Nuvaring® shape, which were filled with different jellified formulations [Arany et al., 2021].

Considering the striking importance of personalized therapy, we investigated the possibility to 3D print a comfortable, versatile reservoir-like VRs for prolonged release of drugs, to be used in case for vaginal inflammation and infections. Indeed, bacterial vaginosis is a widespread pathological condition that profoundly impact the lives and health of 23–29 % of women worldwide, with a prevalent incidence in low-income countries [https://www.who.int/news-room/fact-sheets/detail/bacterial-vaginosis; Kenyon et al., 2013; Muzny and Kardas, 2020]. It is generally treated by oral administration of antibiotics, although there is a high recurrence rate due to the presence of poly-microbial biofilms, which would require local delivery of specifically adjusted drug dosages, matching the specificity of each single condition [Gao et al., 2024; Sousa et al., 2023]. Currently, the local therapy relies on standardized antibiotics-, antifungal- and anti-inflammatory-containing semisolid preparations, for which accurate dosing is hard to achieve, and on vaginal capsules, whose repeated administration might be poorly comfortable for the patient and could exacerbate the condition of distress [Donders et al., 2014; Tomás et al., 2020]. In this respect, VRs would enable longer treatment with a single administration, thus enhancing effectiveness of the therapy and patients' compliance, by also improving the life quality of the women under treatment. As a major novelty with respect to what already available in the literature, the VR here proposed was intended to be composed of a soft material and to be filled with a liquid formulation that will crosslink only inside the ring cavity, finally resulting in a hydrogel. Such a configuration would enable *i)* precise, personalized and extemporaneous filling of the cavity with formulations purposely-developed around the needs of the patient (*i.e.* fine-tuning of the drug dosages or even combinations of different active ingredients), for instance within the hospital pharmacy and following specific indications of the gynecologists, and *ii)* control of drug release based on the design features of the ring combined with the composition characteristics of the filling. In the present work, the proof-of-concept filling was represented by an alginate-based hydrogel containing the first-line drug against bacterial vaginosis, *i.e.* metronidazole.

2. Materials and methods

2.1. Materials

Thermoplastic elastomer (TPE; HTM8510/408 THERMOLAST® M, Shore hardness = 35, KRAIBURG TPE, D); Metronidazole (MTZ; M_w = 171.15 g/mol, nominal true density = 1.45 g/mL, d_{50} = 38 μm and d_{90} = 146 μm, Methapharmaceutical, ES); Sodium alginate (ALG; average M_w = 120000–190000 g/mol, M/G ratio = 1.56, Sigma Aldrich, D); Calcium carbonate ($CaCO_3$; Sigma Aldrich, D); glucono-δ-lactone (GDL; Sigma Aldrich, D); Vagilen suppositories 500 mg (Alfasigma, I).

2.2. Methods

2.2.1. Hydrogel formulation

The different hydrogels representing the filling of the VR cavity were attained by adapting a previously described protocol entailing an internal gelation process (Fig. 1) and following the formulations reported in Table 1 [Guagliano et al., 2023]. Different ALG contents and drug loads were tested, keeping the ratio between $CaCO_3$ and ALG constant.

The protocol employed required the use of *i)* MTZ-saturated solution in distilled water, *ii)* different amounts of ALG and $CaCO_3$, the latter being a source of Ca^{2+}ions, *iii)* extra quantities of MTZ powder and *iv)* a solution of GDL as the acidifying agent (3.6 % w/w in MTZ-saturated solution).

A 1st suspension of $CaCO_3$ in MTZ-saturated ALG solution was prepared under magnetic stirring (300 rpm for about 30 min at 25 °C). Extra MTZ powder and GDL solution were subsequently added (manual

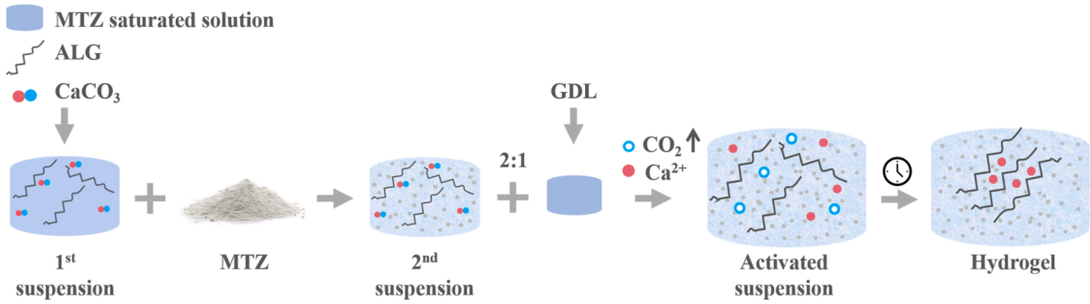

Fig. 1. Outline of the formulation steps pursued to attain the various hydrogels under investigation.

Table 1
Hydrogel formulations investigated.

Formulation code	HA.20	HA.35	HA.50	HB.20	HB.35	HB.50	HC.20	HC.35	HC.50
ALG (%w/w_{tot})	2			4			6		
$CaCO_3$ (%w/V_{tot})	0.17			0.34			0.51		
MTZ powder (%V/V_{tot})	20	35	50	20	35	50	20	35	50
GDL (%w/w_{tot})	1.2								

mixing for 2 min with a glass stirrer), leading to the achievement of the 2nd suspension and of the activated suspension, respectively. Specifically, the solution containing the acidifying agent was added in 1:2 volume ratio with respect to the 1st suspension, so as diluting its components. Since $CaCO_3$ was insoluble in the ALG solution, upon acidification with GDL, Ca^{2+} ions become slowly available, acting as ALG crosslinking agents. This is the reason why the final suspension was called activated. MTZ powder was added in different volume fractions (20, 35, 50 % V/V_{tot}) with respect to the desired final volume of the hydrogel (V_{tot}), also entailing dilution with the acidifying solution. The upper 50 % V/V_{tot} limit for MTZ powder addition was defined to avoid percolation [Wilms et al., 2022]. This way, the hydrogel precursor formulations remained in the liquid state for approximately 1 h and half, while complete crosslinking with the attainment of the final hydrogels required about 4 h.

When still liquid, such precursor formulations were injected into different systems (*i.e.* hollow rings or molds) using a 5 mL syringe equipped with G18 gauge (internal diameter = 0.81 mm) needles. In addition, not less than 1 h but within 2 h from preparation, hydrogels underwent 3D printing.

2.2.2. TPE characterization

The TPE selected for 3D printing the hollow ring was characterized for thermo-mechanical properties.

DSC analyses were carried out by a DSC Q100 (TA Instruments, US-DE), using nitrogen as a purge gas (70 mL/min). Indium was employed as a calibration standard. Samples of about 10 mg underwent subsequent heating/cooling/heating cycles from −40 to 220 °C (rate 10 °C/min).

Melt viscosity curves were built using a twin-screw extruder (Haake™ MiniLab II, Thermo Scientific, Madison, US-WI) as a capillary rheometer. The experiments entailed setting logarithmic steps of the screws rotational speed (from 1 to 350 s^{-1}), while temperatures ranged from 160 to 190 °C.

Dynamic mechanical analyses were performed using a rotational rheometer (MCR 502, Anton Paar, A), working in oscillation mode with a parallel plate configuration (25 mm diameter plates, 1 mm gap). The tests were carried out at 0.1 % shear strain amplitude, with the frequency ranging from 1 to 500 rad/s, and at temperatures between 160 and 190 °C. Under these conditions, the elastic – or storage – modulus (G') and the viscous – or loss – modulus (G''), which describe the viscoelastic response of the material, were measured [Macosko, 1993].

2.2.3. 3D printing

The TPE-based hollow ring was 3D printed using a R-GEN-100 (REGEN-HU, CH) equipped with a thermoplastic cartridge and a stainless steel 0.5 mm nozzle, under the operating conditions reported in Table 2. Details relevant to the various designs of VRs developed are reported in the Results and Discussion Section. For testing different geometrical features, quarters of rings were printed, enabling to save time and material.

The overall open surface area (OSA) of VRs (*i.e.* the area available for contact with fluids) was calculated as follows, starting from the area of a quarter of an annulus (A) and considering the infill % set:

$$OSA = A^*(1 - infill\%)^*n \quad (1)$$

$$A = \frac{1}{4}^*\left(R_o^2 - R_i^2\right)^*\pi \quad (2)$$

where R_o and R_i represented the outer and inner radius of the annulus, respectively, while n was the number of open surfaces ($n = 1$ or 2).

Setting the same parameters reported in Table 2, TPE-based molds resembling a quarter of a ring were also 3D printed and used for the manufacturing of hydrogel samples by casting. While maintaining the internal shape and the relevant volume constant, molds were provided with relatively thinner walls with respect to 3D printed rings, to ease removal of the hydrogels. CAD files for the molds were designed with Autodesk Inventor Professional 2024 software (Autodesk Inc., US-CA) (Fig. 2) and converted into .stl files *via* the printer BioCAM software. All printed items were characterized for weight (analytical balance, Gibertini, I) and dimensions (digital caliper, Mitutoyo, J).

Hydrogel samples were 3D printed using an extrusion-based bioprinter (BIO X, CELLINK, UK) equipped with a 3 mL cartridge and G18

Table 2
Operating parameters set for printing TPE.

Nozzle temperature (°C)	190
Build plate temperature (°C)	80
Pressure (kPa)	470
Fan speed (%)	0
Printing speed (mm/s)	4
Retraction (mm)	0
Number of perimeters	2
Layer height (mm)	0.50
Infill (%)	20–100
Infill type	Rectilinear

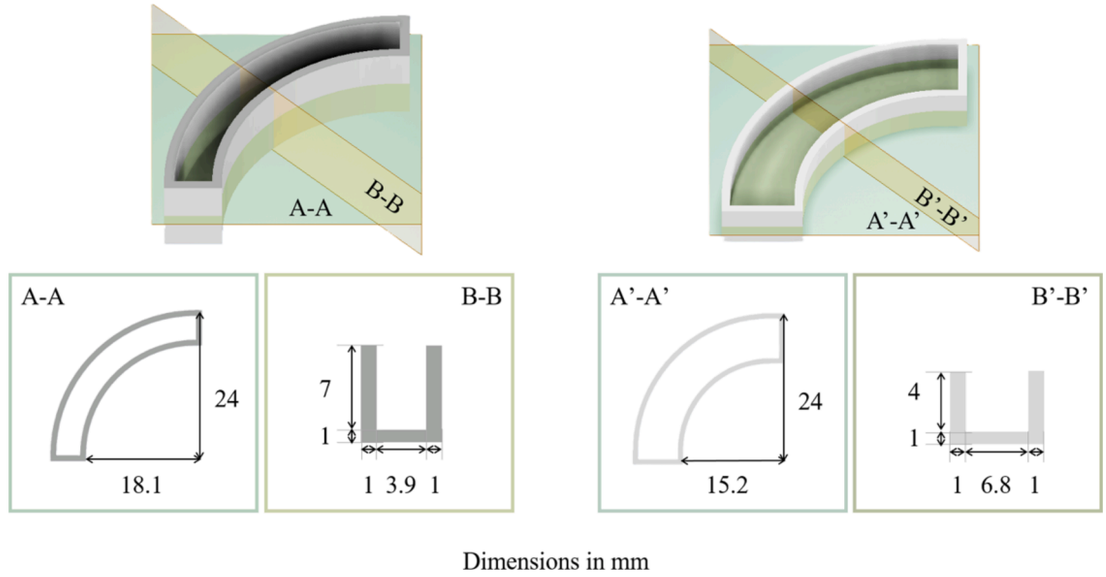

Fig. 2. Outline of horizontal (A-A, A'-A') and vertical (B-B, B'-B') sections, including dimensional details, of the printed molds.

gauge needles. CAD files resembling shape and dimensions of the cavity of the molds previously discussed were saved in .stl format and imported into the printer software (Cellink HeartWare, CELLINK, UK). Operating conditions employed with all the formulations tested are reported in Table 3.

Hydrogel samples either attained by 3D printing or by casting in TPE molds were kept at room temperature in sealed petries until testing, to prevent water evaporation.

2.2.4. Release performance

Drug release from VRs filled with hydrogels as well as from hydrogel samples as such was assessed according to a method already reported in the scientific literature [Boyd et al., 2019]. Specimens were inserted into sinkers to avoid floatation and tested in a USP dissolution apparatus II (Agilent 708-DS, US-MA; 600 mL of acetate buffer pH 4.5 kept at 37 ± 0.5 °C, paddle rotating at 10 rpm) equipped with a pump (Agilent, US-MA) for automatic collection of fluids at pre-defined time points. The pump was connected to a UV spectrometer (Agilent Cary 60 UV–Vis, cuvette with 2 mm path length, US-MA), to ensure automatic absorbance measurements. The amount of MTZ released over time was calculated from a purposely built calibration curve in the concentration range of 0.01-2 mg/mL ($y = 1.2174x$, $R^2 = 0.9997$). The release data were also processed using the Origin Software 2024 (Origin Lab, I) to calculate the release rate at each time point.

Table 3
Operating parameters set for printing the hydrogel formulations.

Gauge inner diameter (mm)	0.81
Gauge temperature (°C)	25
Build plate temperature (°C)	25
Pressure (kPa)	75
Printing speed (mm/s)	4
Retraction (mm)	0
Number of perimeters	1
Layer height (mm)	0.84
Infill (%)	50–100
Infill type	Grid

3. Results

3.1. Design

Results of the research activity focused on the development of the VR design are reported in Fig. 3 and Table 4, respectively. In particular, details relevant to both the horizontal (A-A) and vertical (B-B) sections of the rings are highlighted in the Figure, while the main dimensional features are summarized in the Table. To maintain high compliance, the ring had an external diameter analogous to that of commercially available products (*i.e.* 50 mm). On the other hand, 3 design variants were developed (referred to as #1, #2 and #3). They were all characterized by a constant volume of the internal cavity and differed in the number as well as in the area of the open surfaces located in the top/bottom portions of the ring. The above mentioned area was modified by setting decreasing infill percentages during 3D printing. In this respect, the dimensions of the voids left were such to allow extemporaneous filling of the ring cavity with the hydrogel precursor formulations upon insertion of the syringe needle.

3.2. Thermo-mechanical characterization of TPE

The TPE employed in this work was specifically designed for use within the medical industry, being compatible with both hot melt extrusion and injection molding processes [https://www.kraiburg-tpe.com/en/medical; Markarian 2017]. The polymer was demonstrated biocompatibile according to ISO 10993–4, −5, −10 and −11 and approved for permanent contact with the skin and direct contact with blood. Moreover, it could be sterilized using different methods, such as ethylene oxide gas, superheated steam, γ- as well as β-rays. Current TPE marketed applications mainly entail closures that must reseal after being perforated with a needle (*e.g.* vial stoppers), soft-touch handles and friction grips for medical tools, gaskets and seals. However, given its unique peculiarities, this TPE holds potential for other utilizations in the field, especially for systems in which its soft nature could bring competitive advantages towards patient's compliance. Based on this information, it was selected as an interesting candidate for the manufacturing of the structure of the hollow VR. However, as no data about printability of the chosen TPE were available, the first part of the study focused on relevant thermo-mechanical characterization to assess its processability by additive manufacturing.

Besides being similar to a 3D printer nozzle in terms of geometry, a

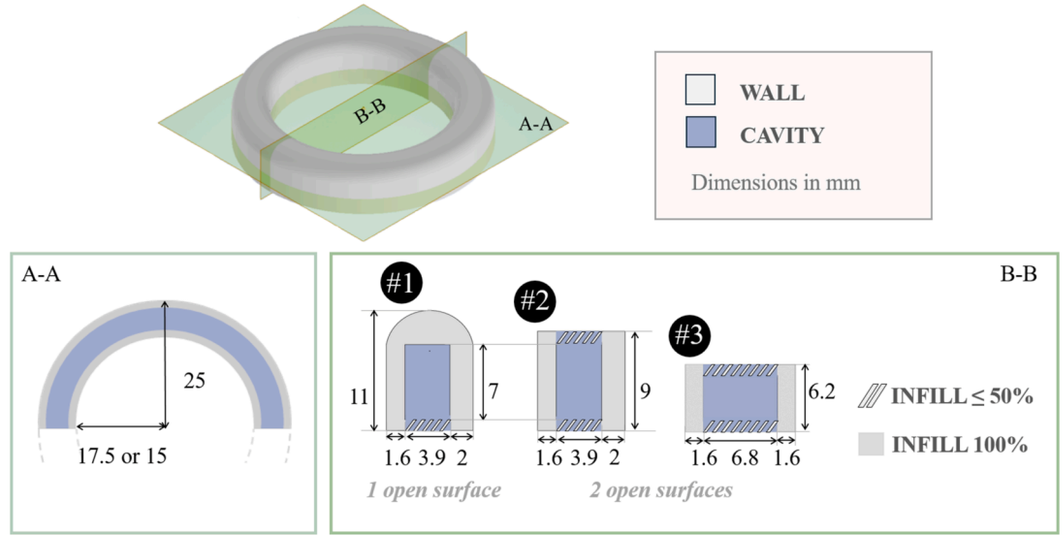

Fig. 3. Outline of horizontal (A-A) and vertical (B-B) sections, including dimensional details, of the 3 VR designs developed.

Table 4
Main features of the VR designs developed.

	Design		
	#1	#2	#3
Internal radius (mm)	17.5		15
Width of the hollow B-B section (mm)	3.9		6.8
Height of the hollow B-B section (mm)	7		4.2
Width of the ring (mm)	7.5	7.5	10
Height of the ring (mm)	11	9	6.2
Thickness of the external ring wall (mm)	2		1.6
Thickness of the internal ring wall (mm)	1.6		
Cavity volume (mL)	3.6		
Number of flat open surfaces on B-B section	1	2	
Thickness of the open surface wall (mm)	1		
Infill of the open surface wall (%)	20, 25, 35, 50		

capillary rheometer has been already demonstrated able to reproduce the Hagen-Poiseuille flow and the shear rate range thermoplastic materials would be subject to during extrusion-based additive manufacturing [Acierno, Piatti 2023]. In fact, a satisfactory correspondence was observed between rheological measurements collected using a standard capillary rheometer and a twin-screw extruder equipped with a recirculation chamber [Casati et al. 2018]. Therefore, this equipment was employed to assess the TPE melt viscosity under different temperatures and shear strain rate conditions. Testing temperatures were set between 160 and 190 °C, with the former being defined based on DSC data showing a TPE melting peak close to 160 °C (data not shown). Moreover, the thermogram did not reveal polymer degradation phenomena up to 220 °C. Final flow curves highlighted a shear thinning behavior for TPE, which would be advantageous for the 3D printing technique employed in this work (Fig. 4a). The processing temperature (*i.e.* 190 °C) was selected considering the viscosity reduction observed at the highest temperature. Indeed, the lower the viscosity the easier the flow through the printer nozzle.

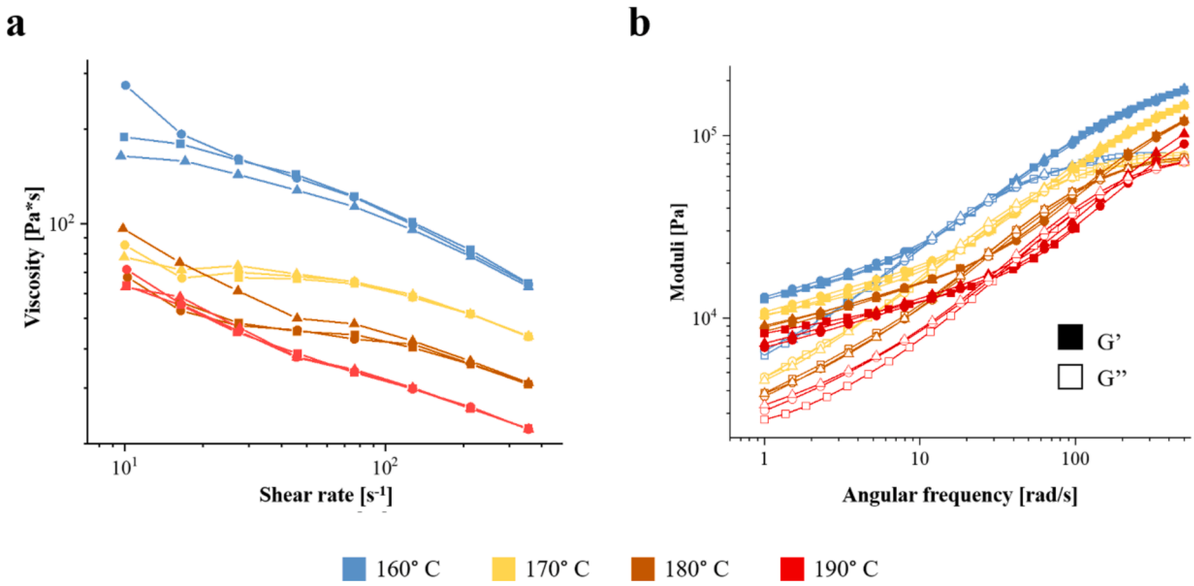

Fig. 4. a) TPE melt viscosity curves attained using the twin-screw extruder as a capillary rheometer together with b) G' and G'' profiles resulting from oscillatory rheometer tests.

At all the temperatures considered, the TPE pointed out a solid like behavior ($G' > G''$) at low frequencies (Fig. 4b). However, there was a range of angular frequencies for which $G' < G''$ and, at higher temperatures, such a range shifted towards lower frequencies. From the 3D printing process perspective, this is the desirable behavior: once deposited, the TPE would not flow further for the time required by the polymer to cool down and to consolidate in the final shape. Nevertheless, a range of intermediate times exist in which TPE macromolecules behave like a very viscous liquid. By ensuring a good degree of interdiffusion between the polymer chains of two subsequent deposited layers, this would result in proper adhesion between them and in a defect-free final part, which can be handled with no risk of damage from layer detachment [Costanzo et al., 2022; Seppala et al., 2017]. Such a behavior would be favored at relatively high temperatures, thus strengthening the choice to work at 190 °C.

3.3. Manufacturing

Following the design step, 3D printing was employed for manufacturing the VRs. For testing purposes, quarter of rings were fabricated, thus speeding up the process and saving materials. Indeed, they represented the minimum unit provided with all the design features to be studied. Quarters were manufactured according to #1, #2 and #3 designs, with all of them entailing a constant inner volume of the cavity corresponding to 0.9 mL, flat open surfaces with ≤ 50 % infill (Fig. 5), and different nominal area available for fluid passage (*i.e.* OSA) (Table 5).

To favor adhesion among the deposited layers, the temperature of the printing bed was increased up to 80 °C, the highest allowed by the equipment. On the other hand, the pressure value set (470 kPa) enabled a continuous flow of TPE throughout the nozzle avoiding any die swell, which would have resulted in an over-extrusion affecting the dimensions of the openings in the VRs. Printed units were reproducible in weight (ranging from 0.8 to 1.50 g depending on the design considered and on the infill % set), with a relative standard deviation (RSD) < 5 %. For resolution purposes, the printing rate was maintained low, resulting in a fabrication time of about 50 min for each ring quarter. The printed parts also pointed out limited variation in width and height compared to the nominal dimensions (Table 6).

Table 5
Open surfaces area relevant to the various VRs designed.

		OSA (mm^2)		
		design #1	**design #2**	**design #3**
Infill (%)	**20**	1.03	2.06	3.42
	25	0.97	1.93	3.20
	35	0.84	1.67	2.78
	50	0.64	1.29	2.14

Using again TPE as feedstock material and setting the same operating conditions above discussed, molds were 3D printed resembling the 3 different ring quarters designs previously shown. Following injection of the precursor formulations (*i.e.* activated suspensions) in such molds and *in situ* crosslinking, hydrogel specimens were obtained by casting. They were characterized by reproducible weight (RSD < 3 %) and dimensions.

Finally, hydrogels with the same shape and dimensions of those obtained by casting were 3D printed (Fig. 6) decreasing the infill % from 100 to 50 %. This way, samples in principle characterized by different surface areas exposed to dissolution fluids were obtained.

Table 6
Dimensional characteristics of the printed VRs.

Width ± standard deviation (mm)			**Height ± standard deviation (mm)**		
#1	**#2**	**#3**	**#1**	**#2**	**#3**
7.74 ± 0.10	7.72 ± 0.10	10.27 ± 0.05	10.90 ± 0.08	9.03 ± 0.20	6.32 ± 0.10

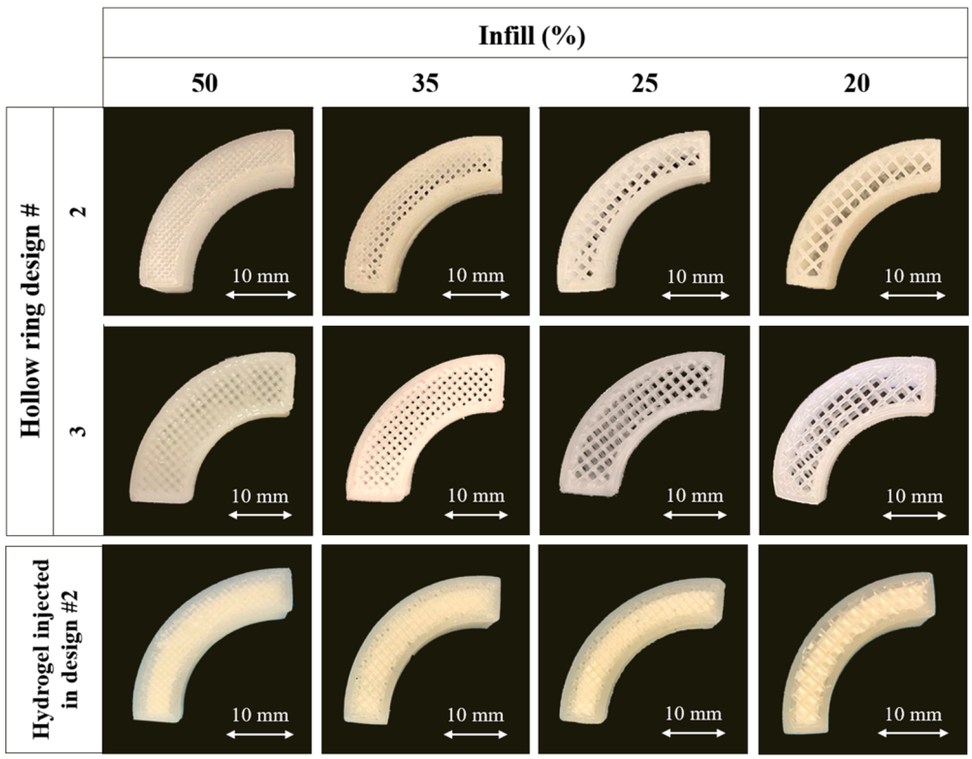

Fig. 5. photos of VR quarters printed starting from different designs and setting decreasing infill %, before and after filling the cavity with a hydrogel formulation.

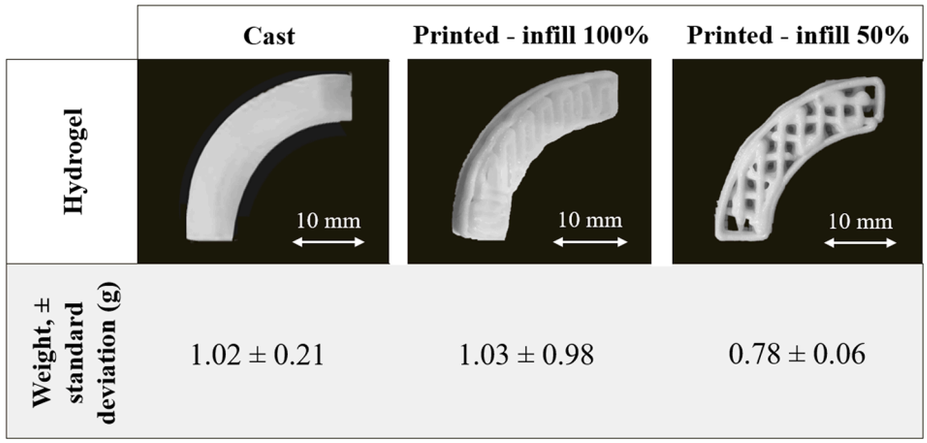

Fig. 6. HB.50 samples either cast or 3D printed setting different infill %.

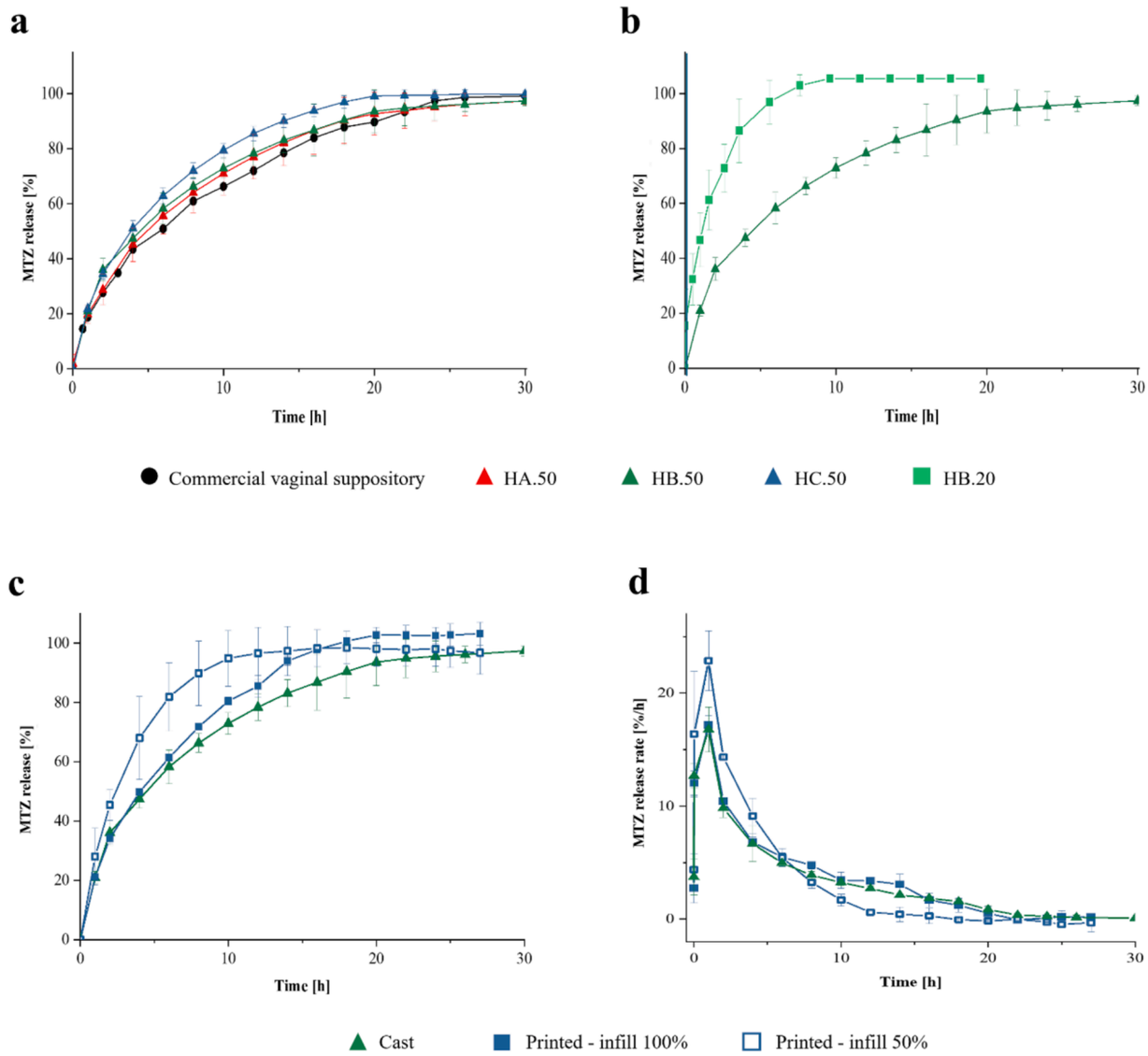

Fig. 7. Release profiles relevant to a) a commercially available vaginal suppository compared to hydrogels with analogous MTZ load and differing in the ALG content; b) hydrogels differing in the MTZ load; c) HB.50 hydrogels either cast or printed with different infill % together with d) relevant release rate curves.

3.4. Release performance

Release performance of samples attained by casting (in design #1 TPE molds) hydrogel precursor formulations having 50 % MTZ load and different ALG contents (HA.50, HB.50 and HC.50) was assessed (Fig. 7a). In this respect, a commercial vaginal suppository containing a comparable amount of the selected drug was taken as a reference. Very similar release profiles were obtained from the various products under investigation and from hydrogels with different ALG concentration. This finding highlighted the major role played by MTZ solubility over the ALG content, which was expected to change the crosslinking degree of the hydrogel. Further confirmation was provided by HB.20 specimens: despite containing almost halved content of MTZ with respect to HB.50 samples, they showed a faster drug release at least in the first 20 h testing (Fig. 7b). Assuming a homogeneous distribution of the drug particles within the hydrogel and considering the MTZ limited solubility (about 10 mg/mL at 25 °C), it is reasonable to foresee the formation of a saturated gel layer between the solvent penetration front (located deeper within the gel) and that of drug dissolution. This layer contains the drug particles that are going through dissolution, and its thickness increases by raising the starting MTZ load. As the layer thickness increased, the rate of drug release slowed down accordingly. Indeed, a faster advancement of the dissolution front was noticed in HB.20 hydrogels immersed in unstirred dissolution medium (data under publication).

By 3D printing the ALG-based formulations, hydrogel samples with different infill were obtained. They were in principle suitable for evaluating the impact of an increase in the area exposed to aqueous fluids and available for MTZ release on the VR performance. Indeed, in a further development stage, the internal cavity of the ring could be provided with microstructural details – for instance manufactured with a promptly soluble polymer – resulting in the formation, upon contact with vaginal fluids, of a gel structure with predefined fluid-exposed surface area. As an example, data relevant to HB hydrogels either attained by casting or 3D printed in the same shape but with different infill % are shown in Fig. 7c. The lower the infill the higher the surface-to-volume ratio. Cast and printed hydrogels with 100 % infill were characterized by almost superimposed release profiles. As no differences were observed in the weight of the samples and being them analogous in volume by design, their comparable behavior could be attributed to a similar density. On the other hand, the amount of drug released from specimens exposing a higher surface area to aqueous fluids, because of the lower infill % set during manufacturing, was higher in the first 10–12 h of testing. Also, the release rate values calculated turned out greater during the first 3–4 h (Fig. 7d). Thereafter, the rate tended to decrease and to match that of relatively higher-density systems, reducing even faster and approaching a zero value when all MTZ was released.

Since the hydrogel release performance was independent on the ALG content, the selection of the precursor formulation for further experiments was based on the extemporaneous filling of VRs. Indeed, the ALG content tuned the viscosity of the activated suspensions, thereby impacting on how difficult was filling the ring cavity by injection and on leakage of the formulation from its openings. The viscosity of activated suspensions containing 50 % of MTZ and 2 (HA.50), 4 (HB.50) or 6 (HC.50) % of ALG, at a shear rate simulating the VRs filling process (*i.e.* 100 s^{-1}), was 1.8, 7.4 and 13.4 Pa*s, respectively. Dealing with HC.50, the viscosity turned out so high that a major pressure had to be applied for filling the ring cavity, often resulting in higher variability of the final sample weight ($\geq$ 10 %). On the other hand, the activated suspension containing the lowest ALG amount (HA.50) was easy to inject but tended to leak out from the VR openings. This phenomenon was even more evident when the ALG formulation contained only 20 % of MTZ (HA.20), thus showing only a 0.2 Pa*s viscosity. Based on these results, the HB formulation with 4 % w/w_{tot} ALG content was selected for further studies.

The release profiles of design #1 VRs, *i.e.* presenting a single pervious surface printed by setting different infill % (corresponding to diverse OSA, as reported in Table 5), which were filled with the HB.50 hydrogel formulation are shown in Fig. 8a. These prototypes still exhibited a prolonged release behavior but lacked in the initial burst, which was observed when testing hydrogel samples as such. In addition, the performance of filled VRs lasted for longer, because the MTZ release was slowed down by the limited area of contact with the incoming fluids. The kinetics tended to the zero order, with the relevant profile becoming linear, as the release was primarily determined by drug diffusion through a gel with constant saturated concentration. Comparing samples printed with either 50 % or 20 % infill allowed to link the decrease in the release rate (highlighted as the slope of the linear profile) with the OSA reduction. This comparison also evidenced a quicker advancement of the dissolution front, separating the exhausted swollen layer (developed from the open surface) from that still containing MTZ particles. This progression was highlighted in the B-B' section of the specimens withdrawn after more than 30 h of testing (Fig. 8a). The performance of systems with greater OSA values, obtained by increasing either the number of flat open surfaces (design #2 *versus* #1) or their width (design #3 *versus* #2), but printed keeping the infill at 35 %, further confirmed these assumptions (Fig. 8b). The B-B' section of specimens partially depleted of MTZ particles in the proximity of both fluid inlet surfaces was again useful for assessing the different movement rate of diffusion and penetration fronts within the systems. The main advantage associated with design #3, with respect to #1 and #2, was the minor impact of a greater diffusive path on the reduction of the release rate over time. This allowed to maintain a constant release rate for longer, which would be in principle useful for widening the portfolio of performances achievable with the VR under development. Given the peculiar structure of the system, the possible contribution of a swelling restricted mechanism on the release behavior of hydrogels conveyed within the VRs was worth investigating [Gazzaniga et al., 1993; Uboldi et al., 2021, 2022b]. This was ruled out by testing rings in which the inner cavity was only half filled with the hydrogel precursor formulation. Doing so, any possible squeezing of the resulting cross-linked hydrogel by the outer ring, acting as a physical constraint, would be reduced. As an example, data relevant to design #2, 35 % infill VRs are reported in Fig. 8c. Interestingly, the amount of MTZ released over time was greater in the presence of an empty volume within the cavity, and thus in the absence of any possible pressure applied by the ring to the hydrogel. Therefore, this result can be mainly attributed to a larger surface available for fluid contact. However, the increased variability pointed out by the release profiles indicated that it is not worth pursuing such a strategy to improve the overall versatility of the system.

Finally, the possibility to 3D printt both the inner hydrogel and the outer ring was tested as an interesting approach to further increase the OSA. In accordance with results previously discussed, the presence of a larger surface area tended to increase the amount of MTZ released at each time point (Fig. 8d). However, also when dealing with hydrogels printed with 50 % infill, thus resulting in the presence of voids, a certain variability in the amount of drug released reappeared. This was mainly associated with the presence of multiple empty spaces, whose simultaneous filling by biological fluids to ensure a consistent prolonged release would be hard to achieve.

Plotting drug release data relevant to the first h of testing as a function of the surface area/volume ratio of the various VRs was helpful in further understating the drug release mechanism (Fig. 9). After initial contact with aqueous fluids, the rate of release from a hydrogel volume with constant surface area (named unitary release rate) rapidly reached a constant and very low value, which was independent of system design and MTZ load.

For this system, the OSA was thereby demonstrated the only parameter to rule on the apparently different release rate observed.

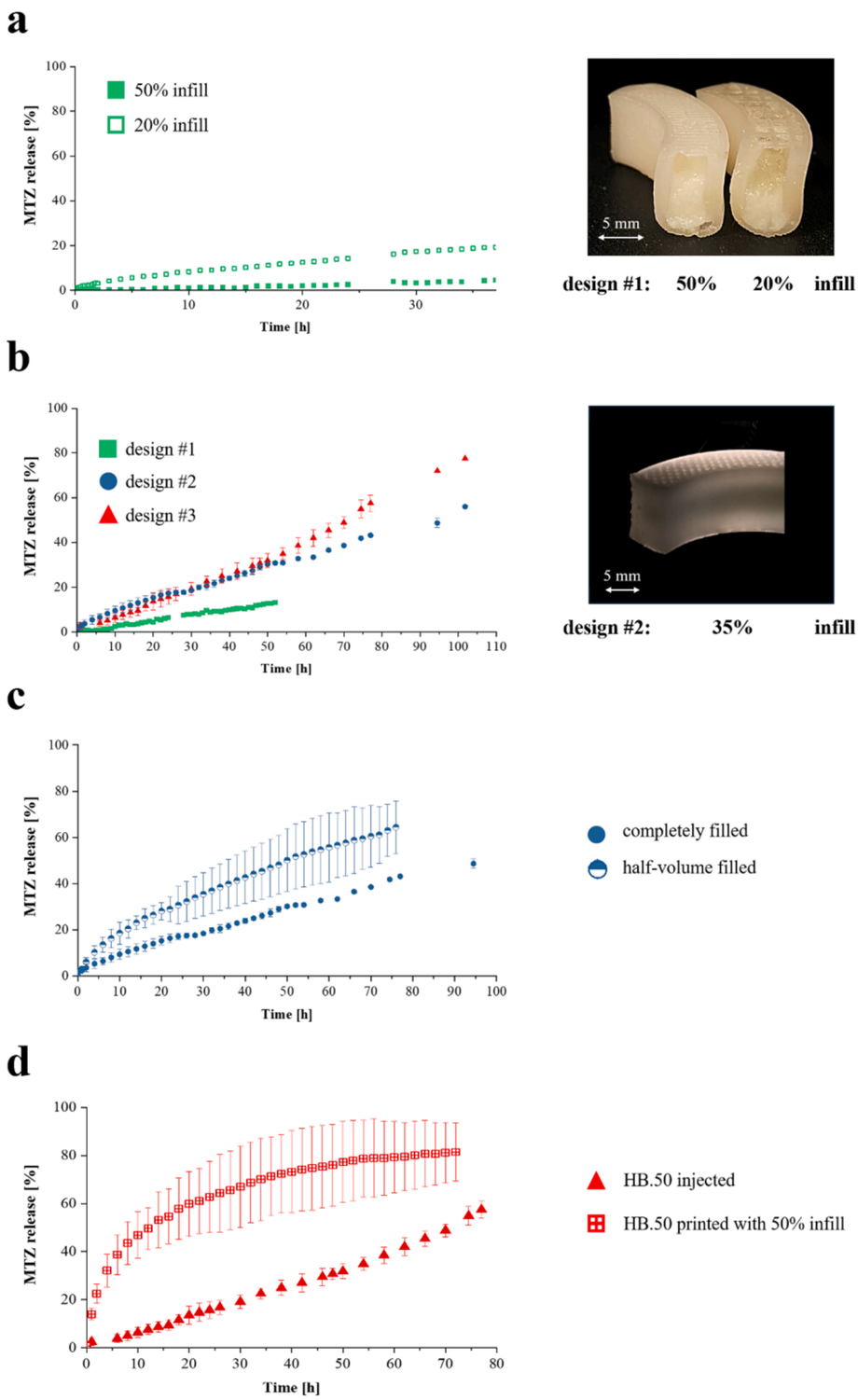

Fig. 8. Release profiles from VRs: a) printed from design #1 by setting different infill %; b) printed from different designs by setting 35% infill; c) printed from design #2 by setting 35% infill and filled either completely or partially with HB.50 hydrogel; d) printed from design #3 by setting 35% infill and completely filled by either injecting or printing by setting 50% infill HB.50 hydrogel. Photos of cut samples withdrawn at the end of the experiment reported aside the corresponding release profiles.

4. Conclusions

In this work, the feasibility of personalized and patient-compliant VRs for the treatment of vaginal inflammation as well as infections was assessed. The system proposed was composed of a 3D printed TPE-based soft hollow ring that can be filled, at the point of care, with *in situ* forming hydrogel formulations. The latter may contain tunable amounts of drugs, in a suspended form, to in principle match the needs of therapies lasting for different time frames. The duration of the release was demonstrated to be controlled by the drug solubility combined with the

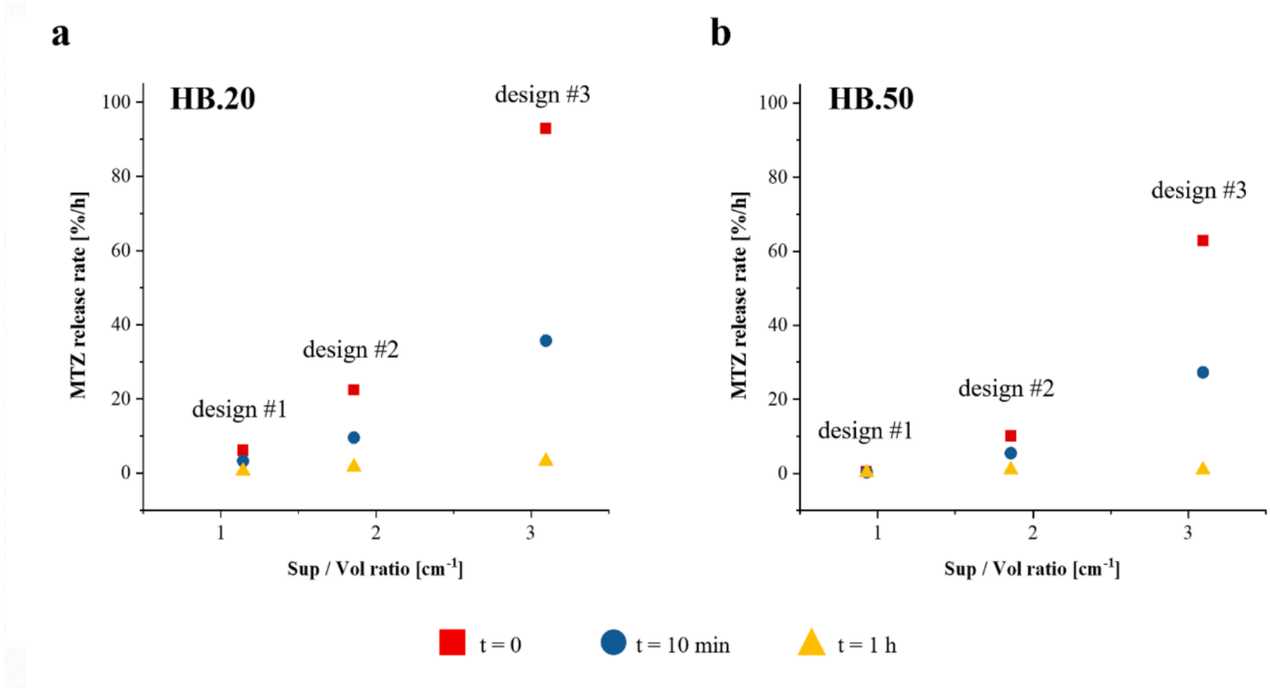

Fig. 9. MTZ release rate values calculated at different times and relevant to VRs printed starting from various designs, by setting 35% infill and filled with a) HB.20 and b) HB.50 hydrogels *versus* surface area/volume ratio.

surface area available for contact with biological fluids. 3D printing was confirmed key in controlling the versatility of the device under development by producing tailored open areas, not only in the top/bottom surfaces of the ring but also in the structure of the inner hydrogel.

Based on these considerations, the VR here described may serve as an advantageous alternative to semisolid preparations and to vaginal suppository, overcoming current dosing challenges and avoiding repeated and uncomfortable administrations.

CRediT authorship contribution statement

Arianna Chiappa: Writing – original draft, Visualization, Methodology, Investigation, Formal analysis. **Alice Fusari:** Writing – review & editing, Writing – original draft, Supervision, Data curation, Conceptualization. **Marco Uboldi:** Software, Investigation. **Paola Petrini:** Writing – review & editing, Resources. **Alice Melocchi:** Writing – review & editing, Writing – original draft, Supervision, Data curation, Conceptualization. **Francesco Briatico Vangosa:** Writing – review & editing, Resources, Project administration, Conceptualization. **Lucia Zema:** Writing – review & editing, Resources, Project administration, Funding acquisition, Conceptualization.

Declaration of competing interest

The authors declare that they have no known competing financial interests or personal relationships that could have appeared to influence the work reported in this paper.

Acknowledgments

The analysis of the VRs release performance was conducted within the MUSA - Multilayered Urban Sustainability Action - project, funded by the European Union - NextGenerationEU, under the National Recovery and Resilience Plan (NRRP) Mission 4 Component 2 Investment Line 1.5: Strenghtening of research structures and creation of R&D "Innovation Ecosystems", set up of "Territorial leaders in R&D".

References

Abdollahpour, S., Ashrafizaveh, A., Azmoude, E., 2023. Effects of the combined contraceptive vaginal ring on female sexual function: a systematic review and meta-analysis. Mal. J. Med. Sci. 30, 21–30. https://doi.org/10.21315/mjms2023.30.1.3.

Acierno, D., Patti, A., 2023. Fused deposition modelling (FDM) of thermoplastic-based filaments: process and rheological properties - an overview. Materials. 16, 7664. https://doi.org/10.3390/ma16247664.

Algahtani, M.S., Ahmad, J., Mohammed, A.A., Ahmad, M.Z., 2024. Extrusion-based 3D printing for development of complex capsular systems for advanced drug delivery. Int. J. Pharm. 663, 124550. https://doi.org/10.1016/j.ijpharm.2024.124550.

Alzoubi, L., Aljabali, A.A.A., Tambuwala, M.M., 2023. Empowering precision medicine: the impact of 3d printing on personalized therapeutic. AAPS PharmSciTech 24, 228. https://doi.org/10.1208/s12249-023-02682-w.

Antezana, P.E., Municoy, S., Ostapchuk, G., Catalano, P.N., Hardy, J.G., Evelson, P.A., Orive, G., Desimone, M.F., 2023. 4D printing: the development of responsive materials using 3D-printing technology. Pharmaceutics. 15, 2743. https://doi.org/10.3390/pharmaceutics15122743.

Arany, P., Papp, I., Zichar, M., Regdon Jr., G., Béres, M., Szalóki, M., Kovács, R., Fehér, P., Ujhelyi, Z., Vecsernyés, M., Bácskay, I., 2021. Manufacturing and examination of vaginal drug delivery system by FDM 3D printing. Pharmaceutics. 13, 1714. https://doi.org/10.3390/pharmaceutics13101714.

Auel, T., Mentrup, A.F.C., Oldfield, L.R., Seidlitz, A., 2025. 3D printing of pharmaceutical dosage forms: recent advances and applications. Adv. Drug Deliv. Rev. 217, 115504. https://doi.org/10.1016/j.addr.2024.115504.

Bandari, S., Nyavanandi, D., Dumpa, N., Repka, M.A., 2021. Coupling hot melt extrusion and fused deposition modeling: critical properties for successful performance. Adv. Drug Deliv. Rev. 172, 52–63. https://doi.org/10.1016/j.addr.2021.02.006.

Barriga Pooley, P., Von Hoveling, A., Galán, G., López Berroa, J., 2020. Analysis and new contraception frontiers with combined vaginal rings. Gynaecol. Endocrinol. 36, 475–478. https://doi.org/10.1080/09513590.2020.1729730.

Boyd, P., Variano, B., Spence, P., McCoy, C.F., Murphy, D.J., Dallal Bashi, Y.H., Malcolm, R.K., 2019. In vitro release testing methods for drug-releasing vaginal rings. J.control. Release. 313, 54–69. https://doi.org/10.1016/j.jconrel.2019.10.015.

Boyd, P., Merkatz, R., Variano, B., Malcolm, R.K., 2020. The ins and outs of drug-releasing vaginal rings: a literature review of expulsions and removals. Expert Opin. Drug Deliv. 17, 1519–1540. https://doi.org/10.1080/17425247.2020.1798927.

Brache, V., Faundes, A., 2010. Contraceptive vaginal rings: a review. Contraception 82, 418–427. https://doi.org/10.1016/j.contraception.2010.04.012.

Carson, L., Merkatz, R., Martinelli, E., Boyd, P., Variano, B., Sallent, T., Malcolm, R.K., 2021. The vaginal microbiota, bacterial biofilms and polymeric drug-releasing vaginal rings. Pharmaceutics. 13, 751. https://doi.org/10.3390/pharmaceutics13050751.

Casati, F., Briatico-Vangosa, F., Baldi, F., Melocchi, A., Maroni, A., Gazzaniga, A., Zema, L., 2018. Assessment of hot-processability and performance of ethylcellulose-based materials for injection-molded prolonged-release systems: An investigational

approach. Int. J. Pharm. 548, 400–407. https://doi.org/10.1016/j.ijpharm.2018.07.015.
Casati, F., Melocchi, A., Moutaharrik, S., Uboldi, M., Foppoli, A., Maroni, A., Zema, L., Neut, C., Siepmann, F., Siepmann, J., Gazzaniga, A., 2020. Injection molded capsules for colon delivery combining time-controlled and enzyme-triggered approaches. Int. J. Mol. Sci. 21, 1917. https://doi.org/10.3390/ijms21061917.
Costanzo, A., Cavallo, D., McIlroy, C., 2022. High-performance co-polyesters for material-extrusion 3D printing: a molecular perspective of weld properties. Addit. Manuf. 49, 102474. https://doi.org/10.1016/j.addma.2021.102474.
Deng, M., Wu, S., Ning, M., 2025. 3D printing for controlled release Pharmaceuticals: current trends and future directions. Int. J. Pharm. 669, 125089. https://doi.org/10.1016/j.ijpharm.2024.125089.
Donders, G.G., Zodzika, J., Rezeberga, D., 2014. Treatment of bacterial vaginosis: what we have and what we miss. Expert Opin. Pharmacother. 15, 645–657. https://doi.org/10.1517/14656566.2014.881800.
Dumpa, N., Butreddy, A., Wang, H., Komanduri, N., Bandari, S., Repka, M.A., 2021. 3D printing in personalized drug delivery: An overview of hot-melt extrusion-based fused deposition modeling. Int. J. Pharm. 600, 120501. https://doi.org/10.1016/j.ijpharm.2021.120501.
Fu, J., Yu, X., Jin, Y., 2018. 3D printing of vaginal rings with personalized shapes for controlled release of progesterone. Int J Pharm. 539, 75–82. https://doi.org/10.1016/j.ijpharm.2018.01.036.
Gao, M., Manos, J., Whiteley, G., Zablotska-Manos, I., 2024. Antibiofilm agents for the treatment and prevention of bacterial vaginosis: a systematic narrative review. J. Infect. Dis. 230, e508–e517. https://doi.org/10.1093/infdis/jiae134.
Gazzaniga, A., Sangalli, M., Conte, U., Caramella, C., Colombo, P., La Manna, A., 1993. On the release mechanism from coated swellable minimatrices. Int. J. Pharm. 91, 167–171. https://doi.org/10.1016/0378-5173(93)90336-E.
Gazzaniga, A., Foppoli, A., Cerea, M., Palugan, L., Cirilli, M., Moutaharrik, S., Melocchi, A., Maroni, A., 2023. Towards 4D printing in pharmaceutics. Int. J. Pharm. X. 5, 10017. https://doi.org/10.1016/j.ijpx.2023.100171.
Griffin, J.B., Ridgeway, K., Montgomery, E., Torjesen, K., Clark, R., Peterson, J., Baggaley, R., van der Straten, A., 2019. Vaginal ring acceptability and related preferences among women in low- and middle-income countries: a systematic review and narrative synthesis. PLoS One 14. https://doi.org/10.1371/journal.pone.0224898.
Guagliano, G., Volpini, C., Camilletti, J., Donnaloja, F., Briatico-Vangosa, F., Visai, L., Petrini, P., 2023. Internally crosslinked alginate-based bioinks for the fabrication of in vitro hepatic tissue models. Biofabrication 15, 3. https://doi.org/10.1088/1758-5090/acd872.
Guazzelli, C.A.F., Barbieri, M., Vieira, C.S., Torloni, M.R., 2014. New developments in vaginal rings for contraception. Curr. Obstet. Gynecol. Rep. 3, 143–149. https://doi.org/10.1007/s13669-014-0080-0.
https://www.kraiburg-tpe.com/en/medical last access on January 7, 2025.
https://www.who.int/news-room/fact-sheets/detail/bacterial-vaginosis, last access on January 7, 2025.
Inverardi, N., Scalet, G., Melocchi, A., Uboldi, M., Maroni, A., Zema, L., Gazzaniga, A., Auricchio, F., Briatico-Vangosa, F., Baldi, F., Pandini, S., 2021. Experimental and computational analysis of a pharmaceutical-grade shape memory polymer applied to the development of gastroretentive drug delivery systems. J. Mech. Behav. Biomed. Mater. 124, 104814. https://doi.org/10.1016/j.jmbbm.2021.104814.
Johansson, E.D.B., Sitruk-Ware, R., 2004. New delivery systems in contraception: vaginal rings. Am. J. Obstet. Gynecol. 190, S54–S59. https://doi.org/10.1016/j.ajog.2004.01.056.
Kenyon, C., Colebunders, R., Crucitti, T., 2013. The global epidemiology of bacterial vaginosis: a systematic review. Am. J. Obstet. Gynecol. 209, 505–523. https://doi.org/10.1016/j.ajog.2013.05.006.
Koutsamanis, I., Roblegg, E., Spoerk, M., 2023. Controlled delivery via hot-melt extrusion: A focus on non-biodegradable carriers for non-oral applications. J. Drug Deliv. Sci. Technol. 81, 104289. https://doi.org/10.1016/j.jddst.2023.104289.
Krovi, S.A., Johnson, L.M., Luecke, E., Achilles, S.L., van der Straten, A., 2021. Advances in long-acting injectables, implants, and vaginal rings for contraception and HIV prevention. Adv. Drug Deliv. Rev. 176, 113849. https://doi.org/10.1016/j.addr.2021.113849.
Kumar, S., Malviya, R., Sridhar, S.B., 2024. 3D printable customized drug delivery system for the vaginal delivery of therapeutics: Unlocking potential prospects for women care. Ann. 3D Print. Med. 16, 100177. https://doi.org/10.1016/j.stlm.2024.100177.
Macosko, C.W., 1993. Rheology principles, measurements and applications. Wiley-VCH.
Majrashi, M.A.A., Yahya, E.B., Mushtaq, R.Y., H.P.S, A.K., Rizg, W.Y., Alissa, M., Alkharobi, H., Badr, M.Y., Hosny, K.M., 2024. Revolutionizing drug delivery: exploring the impact of advanced 3D printing technologies on polymer-based systems. J. Drug Deliv. Sci. Technol. 98, 105839. Doi: 10.1016/j.jddst.2024.105839.
Malcolm, R.K., Boyd, P.J., McCoy, C.F., Murphy, D.J., 2016. Microbicide vaginal rings: technological challenges and clinical development. Adv. Drug Deliv. Rev. 103, 33–56. https://doi.org/10.1016/j.addr.2016.01.015.
Markarian, J., 2017. Overmolding continues to grow & find creative new applications. Plast. Eng. 73, 70–76. https://doi.org/10.1002/j.1941-9635.2017.tb01709.x.
McBride, J.W., Boyd, P., Dias, N., Cameron, D., Offord, R.E., Hartley, O., Kett, V.L., Malcolm, R.K., 2019. Vaginal rings with exposed cores for sustained delivery of the HIV CCR5 inhibitor 5P12-RANTES. J. Control. Release. 298, 1–11, 10.10.1016/j.jconrel.2019.02.003.
Melocchi, A., Uboldi, M., Cerea, M., Foppoli, A., Maroni, A., Moutaharrik, S., Palugan, L., Zema, L., Gazzaniga, A., 2020. A Graphical review on the escalation of fused deposition modeling (FDM) 3D Printing in the pharmaceutical field. J. Pharm. Sci. 109, 2943–2957. https://doi.org/10.1016/j.xphs.2020.07.011.
Melocchi, A., Uboldi, M., Cerea, M., Foppoli, A., Maroni, A., Moutaharrik, S., Palugan, L., Zema, L., Gazzaniga, A., 2021. Shape memory materials and 4D printing in pharmaceutics. Adv. Drug Deliv. Rev. 173, 216–237. https://doi.org/10.1016/j.addr.2021.03.013.
Mishell, D.R., 1993. Vaginal contraceptive rings. Ann. Med. 25, 191–197. https://doi.org/10.3109/07853899309164167.
Mishell, D.R., Talas, M., Parlow, A.F., Moyet, D.L., 1970. Contraception by means of a silastic vaginal ring impregnated with medroxyprogesterone acetate. Am. J. Obstet. Gynecol. 107, 100–107. https://doi.org/10.1016/s0002-9378(16)33897-2.
Mishell, D.R., Lumkin, M., Stone, S., Mishell, D.R., 1972. Inhibition of ovulation with cyclic use of progestogen-impregnated intravaginal devices. Am. J. Obstet. Gynecol. 113, 927–932. https://doi.org/10.1016/0002-9378(72)90658-8.
Monteiro, I., Guazzelli, C.F., Bahamondes, L., 2018. Advances in contraceptive vaginal rings: what does the future hold? Exp. Opin. Pharmacother. 19, 1685–1691. https://doi.org/10.1080/14656566.2018.1519549.
Moroni, S., Bischi, F., Aluigi, A., Campana, R., Tiboni, M., Casettari, L., 2023. 3D printing fabrication of ethylene-vinyl acetate (EVA) based intravaginal rings for antifungal therapy. J. Drug Deliv. Sci. Technol. 84, 104469. https://doi.org/10.1016/j.jddst.2023.104469.
Muhindo, D., Elkanayati, R., Srinivasan, P., Repka, M.A., Ashour, E.A., 2023. Recent advances in the applications of additive manufacturing (3D printing) in drug delivery: a comprehensive review. AAPS PharmSciTech 24, 57. https://doi.org/10.1208/s12249-023-02524-9.
Muzny, C.A., Kardas, P., 2020. A narrative review of current challenges in the diagnosis and management of bacterial vaginosis. Sex. Transm. Dis. 47, 441–446. https://doi.org/10.1097/OLQ.0000000000001178.
Narala, S., Ali Youssef, A.A., Munnangi, S.R., Narala, N., Lakkala, P., Vemula, S.K., Repka, M., 2024. 3D printing in vaginal drug delivery: a revolution in pharmaceutical manufacturing. Expert Opin Drug Deliv. 18, 1–15. https://doi.org/10.1080/17425247.2024.2306139.
Parulski, C., Jennotte, O., Lechanteur, A., Evrard, B., 2021. Challenges of fused deposition modeling 3D printing in pharmaceutical applications: where are we now? Adv. Drug Deliv. Rev. 175, 113810. https://doi.org/10.1016/j.addr.2021.05.020.
Patil, H., Vemula, S.K., Narala, S., Lakkala, P., Munnangi, S.R., Narala, N., Jara, M.O., Williams, R.O., Terefe, H., Repka, M.A., 2024. Hot-Melt Extrusion: from theory to application in pharmaceutical formulation -Where are we now? AAPS PharmSciTech 25, 37. https://doi.org/10.1208/s12249-024-02749-2.
Rahman, S.S., Ahmed, A.B., 2016. Vaginal drug delivery system a promising approach for antiretroviral drug in the prevention of HIV infection: a review. J. Pharm. Sci. Res. 8, 1330–1338. https://doi.org/10.1208/s12248-009-9082-7.
Roumen, F.J.M.E., 2007. The contraceptive vaginal ring compared with the combined oral contraceptive pill: a comprehensive review of randomized controlled trials. Contraception 75, 420–429. https://doi.org/10.1016/j.contraception.2007.01.013.
Seppala, J.E., Hoon, H.S., Hillgartner, K.E., Davis, C.S., Migler, K.B., 2017. Weld formation during material extrusion additive manufacturing. Soft Matter 13, 6761–6769. https://doi.org/10.1039/C7SM00950J.
Sousa, L.G.V., Pereira, S.A., Cerca, N., 2023. Fighting polymicrobial biofilms in bacterial vaginosis. Microb. Biotechnol. 16, 1423–1437. https://doi.org/10.1111/1751-7915.14261.
Tiboni, M., Campana, R., Frangipani, E., Casettari, L., 2021. 3D printed clotrimazole intravaginal ring for the treatment of recurrent vaginal candidiasis. Int. J. Pharm. 596, 120290. https://doi.org/10.1016/j.ijpharm.2021.120290.
Tietz, K., Klein, S., 2019. In vitro methods for evaluating drug release of vaginal ring formulations - A critical review. Pharmaceutics. 11, 538. https://doi.org/10.3390/pharmaceutics11100538.
Tomás, M., Palmeira-de-Oliveira, A., Simões, S., Martinez-de-Oliveira, J., Palmeira-de-Oliveira, R., 2020. Bacterial vaginosis: standard treatments and alternative strategies. Int. J. Pharm. 587, 119659. https://doi.org/10.1016/j.ijpharm.2020.119659.
Uboldi, M., Melocchi, A., Moutaharrik, S., Cerea, M., Gazzaniga, A., Zema, L., 2021. Dataset on a small-scale film-coating process developed for self-expanding 4D printed drug delivery devices. Coatings 11, 1252. https://doi.org/10.3390/coatings11101252.
Uboldi, M., Melocchi, A., Moutaharrik, S., Palugan, L., Cerea, M., Foppoli, A., Maroni, A., Gazzaniga, A., Zema, L., 2022a. Administration strategies and smart devices for drug release in specific sites of the upper GI tract. J. Control. Release 348, 537–552. https://doi.org/10.1016/j.jconrel.2022.06.005.
Uboldi, M., Pasini, C., Pandini, S., Baldi, F., Briatico-Vangosa, F., Inverardi, N., Maroni, A., Moutaharrik, S., Melocchi, A., Gazzaniga, A., Zema, L., 2022b. Expandable drug delivery systems based on shape memory polymers: impact of film coating on mechanical properties and release and recovery performance. Pharmaceutics. 14, 2814. https://doi.org/10.3390/pharmaceutics14122814.
Uboldi, M., Perrotta, C., Moscheni, C., Zecchini, S., Napoli, A., Castiglioni, C., Gazzaniga, A., Melocchi, A., Zema, L., 2023a. Insights into the safety and versatility of 4d printed intravesical drug delivery systems. Pharmaceutics. 15, 757. https://doi.org/10.3390/pharmaceutics15030757.
Uboldi, M., Chiappa, A., Pertile, M., Piazza, A., Tagliabue, S., Foppoli, A., Palugan, L., Gazzaniga, A., Zema, L., Melocchi, A., 2023b. Investigation on the use of fused deposition modeling for the production of IR dosage forms containing Timapiprant. Int. J. Pharm. X 5, 100152. https://doi.org/10.1016/j.ijpx.2022.100152.
Uboldi, M., Chiappa, A., Rossi, M., Briatico-Vangosa, F., Melocchi, A., Zema, L., 2024. Development of a multi-component gastroretentive expandable drug delivery system (GREDDS) for personalized administration of metformin. Expert Opin. Drug Deliv. 21, 131–149. https://doi.org/10.1080/17425247.2023.2294884.

Welsh, N.R., Malcolm, R.K., Devlin, B., Boyd, P., 2019. Dapivirine-releasing vaginal rings produced by plastic freeforming additive manufacturing. Int J Pharm. 572, 118725. https://doi.org/10.1016/j.ijpharm.2019.118725.

Wilms, P., Hinrichs, J., Kohlus, R., 2022. Macroscopic rheology of non-Brownian suspensions at high shear rates: the influence of solid volume fraction and non-Newtonian behaviour of the liquid phase. Rheol. Acta 61, 123–138. https://doi.org/10.1007/s00397-021-01320-1.

Xu, H., Zhang, S., Song, K., Yang, H., Yin, J., Huang, Y., 2025. Droplet-based 3D bioprinting for drug delivery and screening. Adv. Drug Deliv. Rev. 217, 115486. https://doi.org/10.1016/j.addr.2024.115486.

Zema, L., Loreti, G., Melocchi, A., Maroni, A., Gazzaniga, A., 2012. Injection molding and its application to drug delivery. J. Control. Release. 159, 324–331. https://doi.org/10.1016/j.jconrel.2012.01.001.

Zema, L., Melocchi, A., Maroni, A., Gazzaniga, A., 2017. Three-dimensional printing of medicinal products and the challenge of personalized therapy. J. Pharm. Sci. 106, 1697–1705. https://doi.org/10.1016/j.xphs.2017.03.021.

gels

Article

Formulation-Dependent Extrudability of Highly Filled Alginate System for Vaginal Drug Delivery

Arianna Chiappa [1], Alice Fusari [1], Marco Uboldi [2], Fabiana Cavarzan [1], Paola Petrini [1], Lucia Zema [2], Alice Melocchi [2] and Francesco Briatico Vangosa [1,*]

[1] Dipartimento di Chimica, Materiali e Ingegneria Chimica "G. Natta", Politecnico di Milano, Piazza Leonardo da Vinci 32, 20133 Milano, Italy; arianna.chiappa@polimi.it (A.C.); alice.fusari@polimi.it (A.F.); fabiana.cavarzan@polimi.it (F.C.); paola.petrini@polimi.it (P.P.)

[2] PhormulaMi Lab, Sezione di Tecnologia e Legislazione Farmaceutiche "Maria Edvige Sangalli", Dipartimento di Scienze Farmaceutiche, Università degli Studi di Milano, Via Giuseppe Colombo 71, 20133 Milano, Italy; marco.uboldi@unimi.it (M.U.); lucia.zema@unimi.it (L.Z.); alice.melocchi@unimi.it (A.M.)

* Correspondence: francesco.briatico@polimi.it; Tel.: +39-0232902399

Abstract

The incorporation of solid particles as a filler to a hydrogel is a strategy to modulate its properties for specific applications, or even to introduce new functionalities to the hydrogel itself. The efficacy of such a modification depends on the filler content and its interaction with the hydrogel matrix. In drug delivery applications, solid particles can be added to hydrogels to improve drug loading capacity, enable the inclusion of poorly soluble drugs, and modulate release kinetics. This work focuses on the case of alginate (ALG)-based hydrogels, obtained following an internal gelation procedure using $CaCO_3$ as the Ca^{2+} source and containing a high solid volume fraction (up to 50%) of metronidazole (MTZ), a drug with low water solubility, as a potential extrusion-based drug delivery system. The impact of the hydrogel precursor composition (ALG and MTZ content) on the rheological behavior of the filled hydrogel and precursor suspension were investigated, as well as the hydrogel stability and MTZ dissolution. In the absence of solid MTZ, the precursor solutions showed a slightly shear thinning behavior, more accentuated with the increase in ALG concentration. The addition of drugs exceeding the saturation concentration in the precursor suspension resulted in a substantial increase (about one order of magnitude) in the low-shear viscosity and, for the highest MTZ loadings, a yield stress. Despite the significant changes, precursor formulations retained their extrudability, as confirmed by both numerical estimates and experimental validation. MTZ particles did not affect the crosslinking of the precursors to form the hydrogel, but they did control its viscoelastic behavior. In unfilled hydrogels, the ALG concentration controls stability (from 70 h for the lowest concentration to 650 h for the highest) upon immersion in acetate buffer at pH 4.5, determining the MTZ release/hydrogel dissolution behavior. The correlations between composition and material properties offer a basis for building predictive models for fine-tuning their composition of highly filled hydrogel systems.

Keywords: alginate-based hydrogel; high solid powder content hydrogel; rheological characterization; drug delivery

Academic Editor: Nikolaos Bouropoulos

Received: 2 June 2025
Revised: 24 June 2025
Accepted: 25 June 2025
Published: 1 July 2025

Citation: Chiappa, A.; Fusari, A.; Uboldi, M.; Cavarzan, F.; Petrini, P.; Zema, L.; Melocchi, A.; Briatico Vangosa, F. Formulation-Dependent Extrudability of Highly Filled Alginate System for Vaginal Drug Delivery. *Gels* **2025**, *11*, 510. https://doi.org/10.3390/gels11070510

1. Introduction

Hydrogels loaded with a high amount (>20%) of suspended micro- or nanoparticles are also referred to as suspension-based, highly loaded, or particulate-laden hydrogels, and they fall within the category of highly filled materials [1].

Therapeutic agents can be used as fillers in pharmaceutical hydrogel formulations [2]. These systems belong to drug delivery systems (DDSs) and are increasingly emerging as one of the most promising and technologically advanced therapeutic approaches across various clinical scenarios, as they enhance treatment efficacy, including cancer therapies and [3] wound healing [4].

The fillers, especially if in high concentration, modulate the mechanical properties of hydrogels, which enhances local retention, sustains a site-specific drug release [5], and minimizes drug off-target accumulation throughout the body, thus reducing adverse effects associated with systemic exposure [6,7]. The release of drugs can be modulated through multiple mechanisms, including diffusion and swelling, as well as in response to external stimuli such as pH changes, temperature, and the presence of enzymes [8].

Highly filled hydrogels overcome the water solubility issues that are so common for many drugs, making it possible to load poorly water-soluble drugs at a therapeutic dosage in a water-based system: the hydrogel. They are particularly valuable in mucosal, dermal, and implantable drug delivery, where prolonged drug availability and high local concentrations are desirable, and solubility limits often necessitate formulations containing drugs above their saturation concentration [9].

In this context, the use of extrudable hydrogels, soft materials that can pass through a nozzle, are gaining increasing attention for the 3D printing of dosage forms in personalized medicine, and minimally invasive administration, where control of flow is essential [10]. Despite their potential, the formulation of such systems remains challenging: the presence of solid particles significantly influences the mechanical properties of the hydrogel [11] in such a way that upon extrusion through a nozzle the hydrogel may undergo damage.

A strategy to promote highly filled drug delivery systems (HF-DDS) extrudability is by injecting the liquid hydrogel precursors, which are converted in situ into a hydrogel via safe physical or chemical crosslinking [12,13].

To date, a variety of in situ-forming injectable hydrogels have been developed for gene delivery, regenerative medicine, and cell therapy [14–16]. Among the hydrogel-forming polymers that can be exploited for in situ crosslinking, alginate (ALG) represents one of the most investigated [17–20] due to the compatibility of the crosslinking process to the in situ delivery.

A specific mechanism of crosslinking, referred to as internal gelation, can be controlled so that the alginate crosslinking kinetic can be adjusted to be extruded, either by injection or 3D printing, in a viscous liquid form, while progressing to the formation of a shape-defined gel after extrusion [21,22]. One of the challenges of extrusion is selecting an appropriate process timing for the extrusion hydrogel precursor in its liquid phase. Even in this case, however, the addition of a high volumetric fraction of micro- or nanoparticles to the precursor solution increases its viscosity, thus limiting or even suppressing precursor extrudability. This may require increasing the nozzle size and/or the applied pressure to extrude the hydrogel precursor.

Besides the extrudability issue, common to several application fields and technologies, for the specific case of Drug Delivery Systems (DDS), the stability of the hydrogel and the release mechanism and kinetics are of the utmost importance, and this aspect may also be affected by the hydrogel composition and particle volume fraction.

In this work, we propose a systematic investigation of how hydrogel composition and microparticle loading affect hydrogel precursor rheology and filled hydrogel mechanical

properties and stability, with the aim of providing practical tools for optimizing both formulation and device efficiency.

As a case study, the investigation is carried out on an alginate (ALG) hydrogel obtained via internal gelation and filled with metronidazole (MTZ), in view of its use as DDS for the first-line treatment of bacterial vaginosis in the vaginal environment. Indeed, this environment poses a great challenge for drug delivery systems, due to the low pH and the requirements of sustained release. In respect to the first challenge, thanks to its good stability in a pH range from 3 to 10, ALG represents an interesting candidate for the development of hydrogel-based drug delivery systems intended for vaginal delivery [23]. However, the resulting systems could have some drawbacks due to their softness/compliance, and their limited adhesion to the mucosa and therefore relatively short residence time, especially considering that the continuous renewal of fluids might contribute to the removal of the dosage form [24,25]. Furthermore, when MTZ is considered as an active ingredient, its low aqueous solubility of MTZ (12.476 mg/mL) makes it difficult to achieve sustained therapeutic levels. The adoption of a filled hydrogel as DDS would on one hand permit the appropriate dosage of MTZ, and on the other hand would allow modulation of the DDS mechanical and release performance. Finally, control of hydrogel precursor solution rheological behavior would allow its adoption in different dosage scenarios, from dispensing to the preparation of cast or 3D-printed soft drug delivery devices.

2. Results and Discussion

2.1. Metronidazole Particle Size Distribution

The granulometric profile of pristine MTZ was determined to evaluate the particle size distribution of the powder and to rule out the larger particles, which could also be observed by optical microscopy (Figure 1a). Considering that the apparent D90 value of pristine MTZ was equal to 0.497 mm, the risk of clogging phenomena during any extrusion operation, either performed via syringe or using the 3D printer, could not be excluded. For this reason, the material was milled and further sieved. This way, the apparent D90 was reduced to 0.146 mm, thus limiting the risk of clogging (Figure 1b).

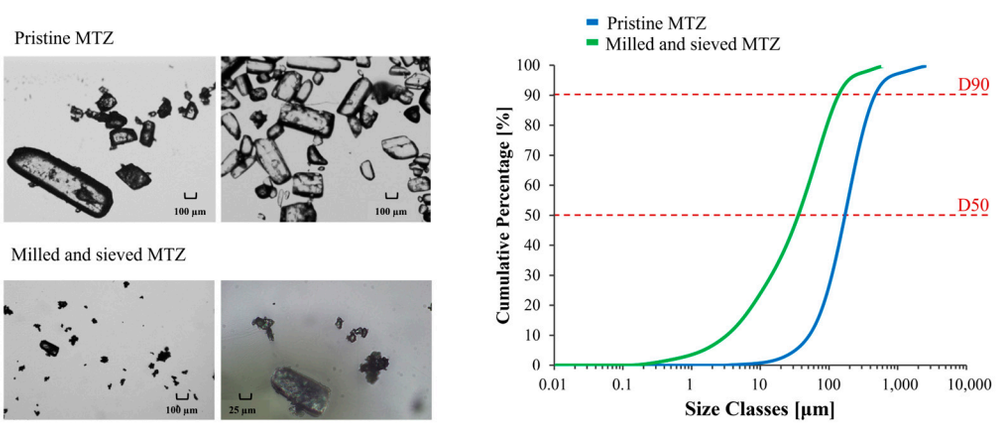

(**a**) (**b**)

Figure 1. Optical micrographs (**a**) and cumulative particle size distribution curves of pristine and milled/sieved MTZ (**b**).

2.2. Solutions and $CaCO_3$ Suspensions Flow Behavior Without MTZ Powder

In steady state shear tests of ALG solutions, prepared either using distilled water or a saturate MTZ solution (Figure 2a), raising the ALG concentration resulted in an increase in the zero-shear viscosity value, η_0, and lowered the shear rate level at which the shear

thinning behavior can be observed. This latter effect was especially noted for solutions containing 4% and 6% ALG. Instead, a quasi-Newtonian behavior was observed for 2% ALG solution.

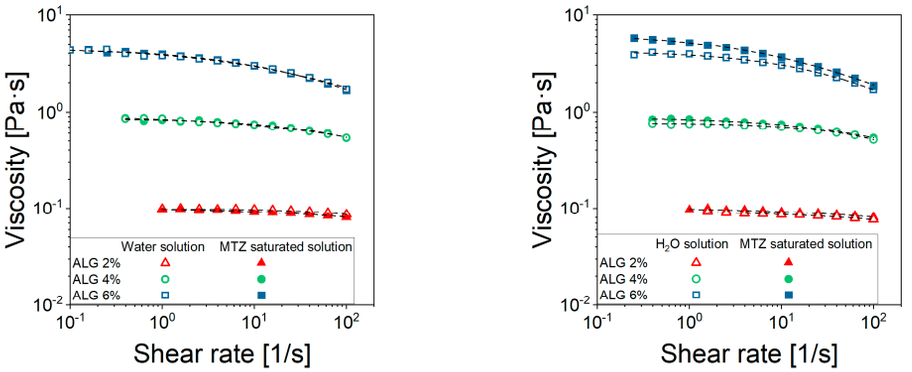

Figure 2. Viscosity curves of (**a**) ALG solutions and (**b**) $CaCO_3$-suspensions prepared using either water (□) or a saturated solution of MTZ (■). Each data point represents the average of at least 5 tests. For the sake of readability, standard deviations are omitted, being very limited. The excellent data reproducibility can be observed in the Supplementary Information, Figure S1.

Furthermore, there was no significant interaction between ALG and the selected drug, despite the ionic nature of both species (Figure 2a), as the viscosity seemed not to be affected by the presence of MTZ in solution. All viscosity data could be fitted using the Cross' model (Equation (5)) with the parameter reported in Table 1. Despite the 2% ALG solution, the determination of the m and l parameters is quite uncertain, given its quasi-Newtonian behavior. The most significant effect of ALG concentration, C_{ALG}, consisted of an increase in η_0 (Figure 3) according to Equation (1):

$$\eta_0 = A \times {C_{ALG}}^n \quad (1)$$

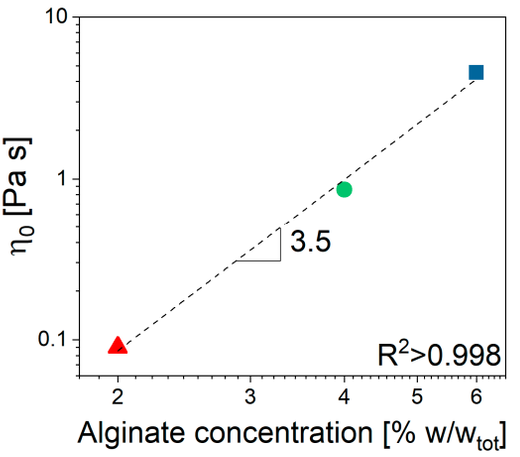

Figure 3. Unfilled alginate solution. Zero shear viscosity dependence on ALG concentration.

The value 3.5 of the power low index, n, indicated that in the given range of concentrations, the solution was in the entangled regime, according to Takahashi [26]. When $CaCO_3$ is dispersed in the solution containing 6% ALG (NA_C.0), a slight increase in viscosity at fixed shear rate can be observed, while no effect can be detected for solutions containing 2% and 4% ALG (Figure 2b).

Table 1. Cross' model (Equation (5)) parameters of formulation containing different amounts of ALG and $CaCO_3$, prepared starting from a saturated solution of MTZ.

ALG (%w/w_{tot})	$CaCO_3$ (%w/w_{tot})	η_0 (Pa·s)	m	λ (s)
2	0	0.100 ± 0.003	0.4 ± 0.1	n.d.
	0.17	0.101 ± 0.003	0.4 ± 0.1	n.d.
4	0	0.86 ± 0.01	0.60 ± 0.07	n.d.
	0.34	0.88 ± 0.01	0.52 ± 0.04	0.0043 ± 0.0003
6	0	4.52 ± 0.06	0.50 ± 0.02	0.028 ± 0.002
	0.51	6.63 ± 0.05	0.470 ± 0.007	0.07 ± 0.003

2.3. MTZ Suspensions Flow Behavior

The effects of adding MTZ powder above the limit of its solubility were manifold, and their impact depended also on the ALG concentration (Figure 4).

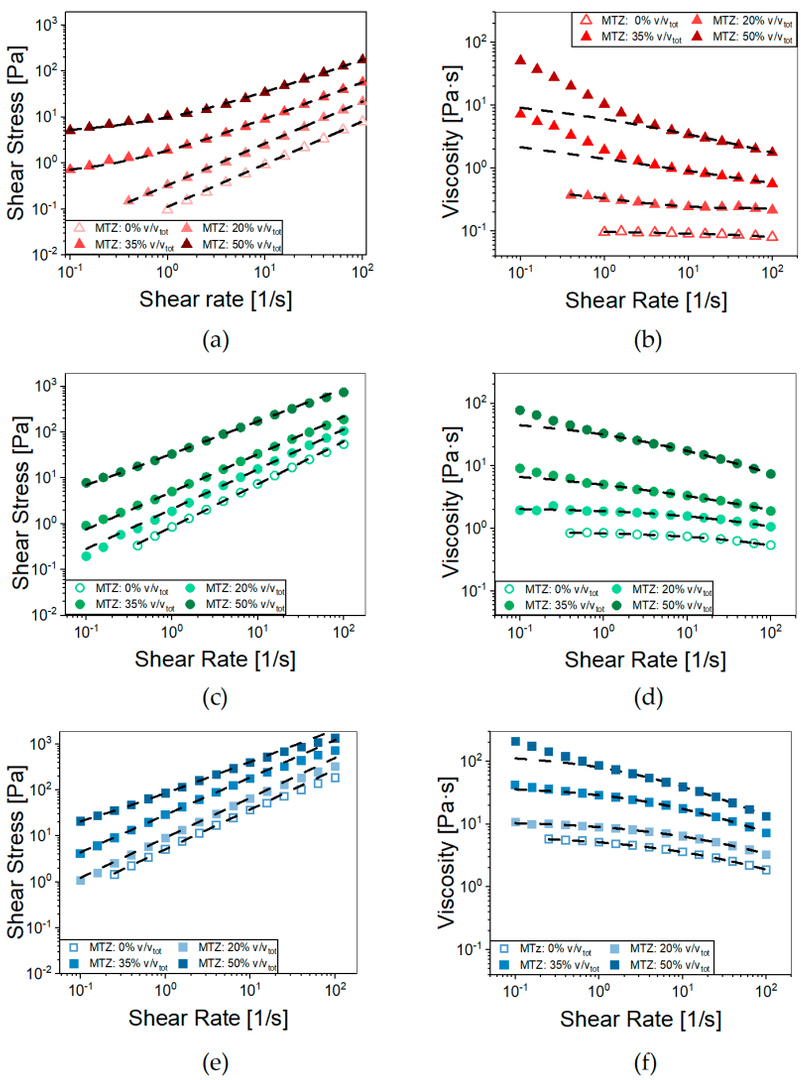

Figure 4. Flow curves of (**a**) NA_A, (**c**) NA_B, and (**e**) NA_C containing increasing volumetric fractions of MTZ powder (0–50%). Dashed lines represent the fitting with the Herschel–Bulkley model (Equation (6)). Viscosity curves of (**b**) NA_A, (**d**) NA_B, and (**f**) NA_C containing increasing amounts of MTZ powder (0–50%); dashed lines represent their fitting with the Cross' Model (Equation (5)). Each data point represents the average of at least 5 tests. For the sake of readability, standard deviations are omitted.

For all the ALG concentrations, when increasing the MTZ content, there was an upward shift in the viscosity curves at medium-to-high shear rate. In this range, the Cross' model fits the data with the parameters reported in Table 2. A second effect was the rise in the viscosity with decreasing shear rates in the presence of high MTZ volume fractions. Indeed, the substructures, due to particle interactions present in quiescent conditions, required the application of a shear stress above a certain threshold to be disaggregated, so that flow can occur. This effect was present in all formulations but was particularly evident for the A suspensions (NA_A.X—Section 4.2.2 Hydrogel preparation introduces the code adopted to designate the materials) where the Herschel–Bulkley model (Equation (6)) accurately fitted the stress–shear rate curves ($R^2 > 0.999$) over the entire shear rate range considered (Figure 4b, Table 3).

Table 2. Cross' model parameters of formulations containing different amounts of MTZ.

NA_	MTZ Powder, X (%V/V$_{tot}$)	η_0 (Pa·s)	m	λ (s)
A	20	0.44 ± 0.05	1 ± 0.2	1 ± 0.5
B	20	0.88 ± 0.02	0.5 ± 0.2	n.d.
	35	10 ± 1	0.30 ± 0.03	n.d.
	50	57 ± 4	0.45 ± 0.01	0.6 ± 0.2
C	20	11.3 ± 0.4	0.48 ± 0.09	0.06 ± 0.03
	35	40 ± 2	0.53 ± 0.04	0.16 ± 0.01
	50	130 ± 9	0.56 ± 0.02	0.4 ± 0.1

Table 3. Herschel–Bulkley parameters for NA_A dispersion containing different amounts of MTZ powder (0–50%).

MTZ Volume Fraction, (%V/V$_{tot}$)	τ_y (Pa)	k (Pa·s^n)	n
0	0 ± 0.02	0.11 ± 0.01	0.93 ± 0.01
20	0 ± 0.09	0.33 ± 0.03	0.91 ± 0.02
35	0.5 ± 0.1	1.36 ± 0.06	0.81 ± 0.01
50	4.3 ± 0.4	5.7 ± 0.2	0.74 ± 0.01

Besides increasing the suspension consistency coefficient, (k), and the yield stress threshold value, τ_y, raising the content of MTZ solid particles led to a more pronounced shear thinning, as suggested by the viscosity index (n) trend. This behavior can be due to particle orientation in the flow direction under intense shear, which is typical of suspensions characterized by limited interactions between the solid particles and the liquid phase [27]. A further mechanism favoring shear thinning is the breakdown of agglomerates; however, in this specific case, no clear sign of agglomeration was observed for the samples (see Figure S2). In any case, the contribution to shear thinning of some (hindered) interaction between the particles at high filler volume fraction cannot be excluded. From the extrudability standpoint, the presence of a yield stress threshold may imply exceedingly high extrusion pressures, especially in the case of long or thin nozzles/needles, as discussed in the following. On the other hand, it may be useful when the extrusion process is performed in the direction of gravitational forces, such as in 3D printing, because it prevents dripping.

The effect of MTZ volume fraction, ϕ, on the viscosity of NA_suspensions was apparent from Figure 5, in which an increase of over 40 times the viscosity of unfilled precursor solution was observed for the 2% ALG. The effect was lower, but still very important for the 4% ALG and 6% ALG solution.

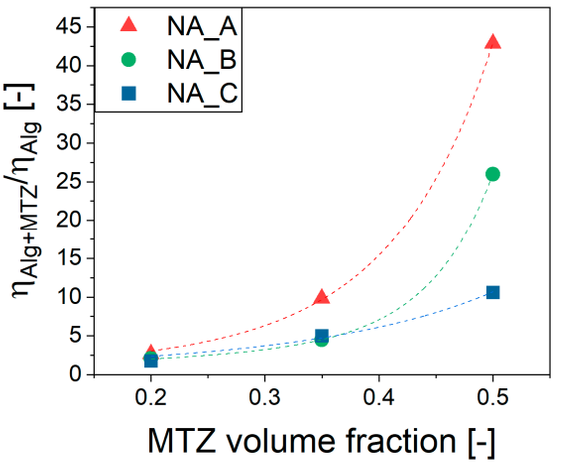

Figure 5. Viscosity dependence on MTZ volume fraction of ALG suspensions. Dashed lines are the Thomas' equation (Equation (2)) fitting. The viscosity data considered is that measured at 10 s^{-1}.

This highly non-linear effect was well captured by the Thomas equation (Equation (2)) [28]:

$$\eta_{NA_A.X}\left(\dot{\gamma} = 10s^{\cdot 1}\right) = \eta_{NA_A.0}\left(\dot{\gamma} = 10s^{\cdot 1}\right) \times \left(1 + 2.5\,\phi + 10.05\phi^2 + A^{B\phi}\right) \quad (2)$$

where ϕ is the MTZ volume fraction, and A and B are empirical coefficients (Table 4).

Table 4. Thomas equation coefficients.

Formulation	*A*	*B*
NA_A	0.11 ± 0.02	11.7 ± 0.4
NA_B	0.0025 ± 0.0007	18.1 ± 0.5
NA_C	0.08 ± 0.09	9 ± 2

2.4. Extrudability

The material ability to flow through a small opening under the application of pressure is defined here as extrudability. This parameter is strictly related to the viscosity which, in the case of non-Newtonian fluids, depends on the shear rate applied. Generally, in an extrusion process, the shear rates could range between 100 and 10,000 s^{-1}, which is definitely higher than the typical range explored through rotational rheometer experiments [29]. To properly estimate the viscosity in the above-mentioned range, it is possible to extrapolate a suitable rheological model to the shear rates of interest. This procedure may, however, be a source of errors. A more appropriate approach would be to experimentally extend the measurement range, adopting other rheological techniques. In this work, we propose the use of a 3D bioprinter as a capillary rheometer, following the procedure described in Section 4.2.4. By way of example, Figure 6a reports the flow rate's dependence on extrusion pressure and nozzle diameter for the most filled NA_suspension (NA_C.50). Figure 6b instead highlights the effect of the MTZ content at fixed nozzle diameter. It can be noted that at all imposed pressures the flow rate was higher for the NA_suspensions with lower viscosity. When considering NA_X.50 suspensions, a deviation from linearity could be observed due to the shear thinning behavior.

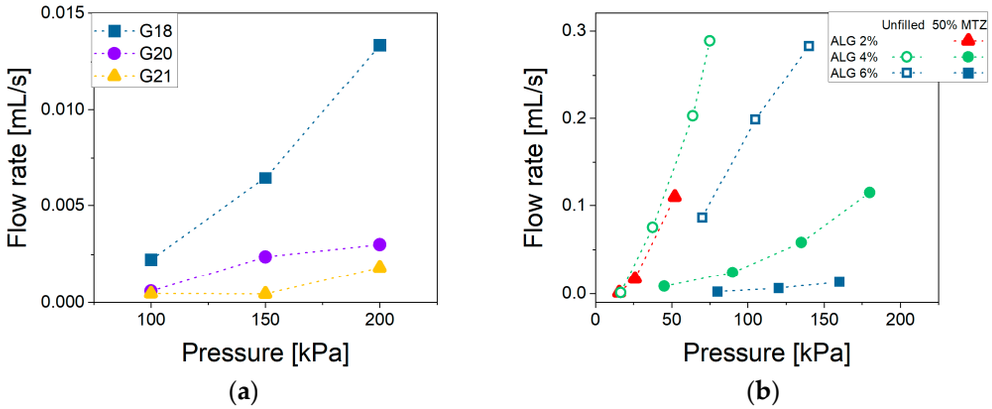

Figure 6. Flow rate vs. pressure for (**a**) NA_C.50 extruded through G18, G20, G21 nozzles and (**b**) NA_suspensions containing different MTZ amounts extruded through the G18 nozzle. Lines are intended as a visual aid. Data for the suspension containing ALG 2% are unavailable, as its low viscosity caused uncontrolled dripping from the cartridge even under atmospheric pressure.

Data of Figure 6b allowed us to estimate the viscosity at shear rates typical of the extrusion process by applying the method described in Section 4.2.4. For NA_C formulation, the data from rotational and capillary rheometry measured at the same shear rate overlap (Figure 7). The overlap confirmed the validity of the adopted method, including the procedures and assumptions adopted in data elaboration as reported in Section 4.2.4, at least for the case of NA_C suspensions. As for NA_A and NA_B, direct comparison between data at the same shear rate was not possible, and the agreement of experimental data and Cross' rheological model (Equation (5)) with parameters from Table 2 predictions is limited, even if still acceptable.

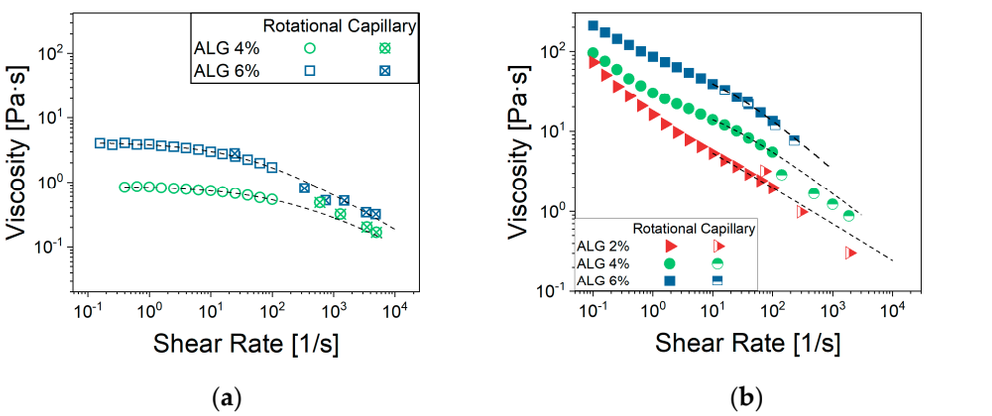

Figure 7. Flow curves for NA_suspensions (**a**) without MTZ-powder and (**b**) containing 50% of MTZ. For suspensions with 2% ALG, data could not be acquired due to spontaneous outflow from the cartridge.

Based on the proposed approach, once the rheological behavior of a suspension is known, its extrudability can be predicted, at least to an acceptable approximation, by the comparison of the estimated pressure/force required to extrude the material though a nozzle of any given diameter with the maximum pressure or force available for the extrusion process—as an example, about 80 N in the case of manual extrusion from a syringe. Furthermore, in case of automated extrusion processes, such as 3D bioprinting, the rational approach proposed allows us to select the appropriate pressure for the desired extrusion rate with a limited need to resort to time-consuming and expensive trial-and-error sessions. Obviously, the approach validity is limited to the cases in which no agglomeration

or nozzle clogging occurs. The second effect may be critical for clinical nozzles (<0.3 mm diameter) and suspension filled with particles with comparable dimensions.

2.5. Dynamic Mechanical Response ALG Based Hydrogels

The results of frequency sweep tests in Figure 8 confirm that, after GDL addition, a hydrogel was formed for any MTZ content, as confirmed by the limited dependence on frequency and the low level of the phase shift angle. Also, the crosslinking kinetics were practically unaffected by the filler: the gel point was reached after about 30 min from adding GDL, while the reaction ended after about 4 h (Figure S3).

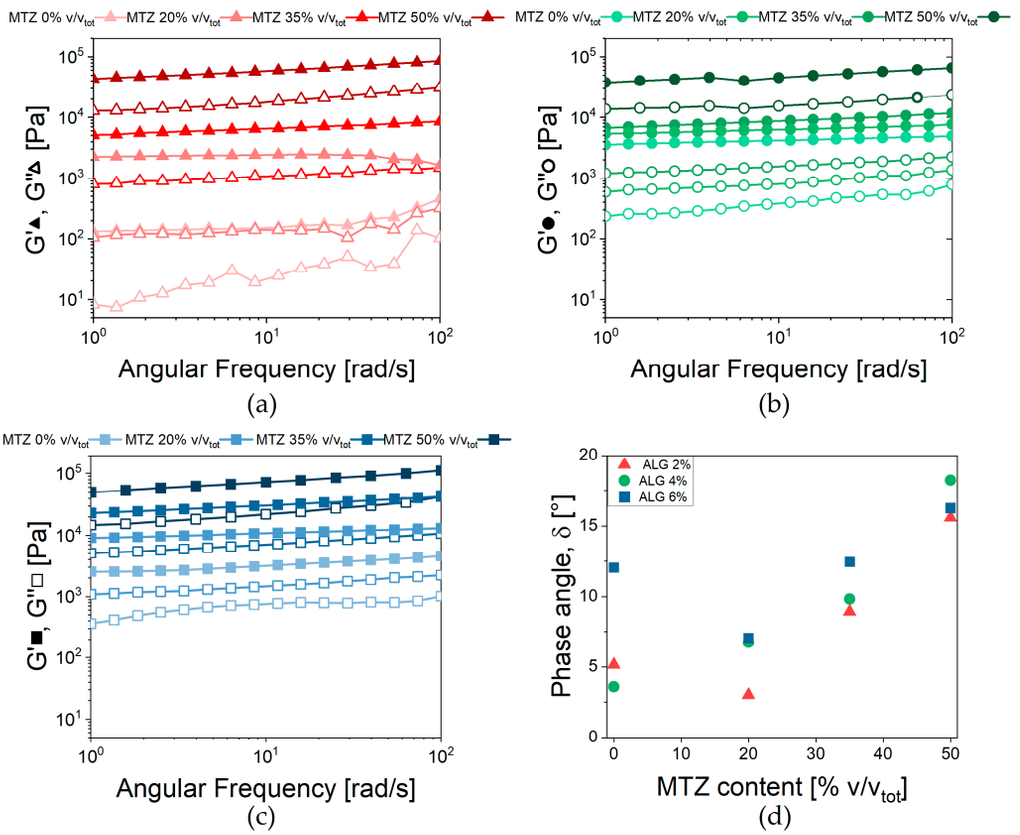

Figure 8. Viscoelastic behavior of ALG-based hydrogels. Storage (G′) and loss (G″) moduli vs. frequency for hydrogels containing (**a**) 2% Alginate, (**b**) 4% Alginate, and (**c**) 6% Alginate. (**d**) Phase shift angle measured at 2.5 rad/s for all the formulations tested.

Focusing on unfilled hydrogel, G′ and G″ increased with increasing ALG concentration, due to the increase in the Ca^{2+} links between alginate chains. To capture this effect, the average mesh size ξ [30,31] was obtained from Equation (3):

$$\zeta = \left(\frac{G_0 \cdot N_A}{RT}\right)^{-\frac{1}{3}} \quad (3)$$

where G_0, the fully relaxed hydrogel modulus, was approximated to G′, given the quasi-elastic behavior of the hydrogel, N_A is the Avogadro constant, R is the gas constant, and T is the absolute temperature, in this case 298.15 K. The parameter, inversely proportional to the distance between two crosslinks, is equal to 290 nm, 98 nm, and 110 nm for HA, HB, and HC unfilled hydrogels, respectively.

The same approach was not applied to the filled hydrogels, as the MTZ are not believed to directly affect the degree of crosslinking. Rather, based on the transient nature of the

ionic crosslinks, the limited dependence of the viscoelastic behavior on angular frequency, and the low phase angle, the Weak Gel model [32] (Equation (4)) was adopted:

$$G^*(\omega) = A_f \omega^{\frac{1}{z}} \quad (4)$$

This model describes the gel as constituted by flowing units—in the present case, the alginate polymeric chains—interacting with each other and the other components of the complex system. The parameter A_f is related to the strength of interaction between flowing units, and the scaling exponent z gives an indication of the number of interactions between them.

The parameters' dependence on MTZ concentration can be observed in Figure 9.

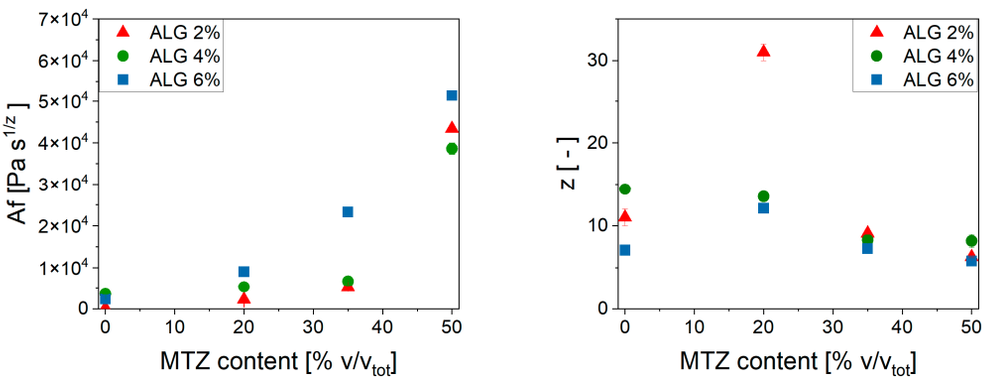

Figure 9. Weak gel model parameters' dependence on MTZ volume fraction. (**a**) Af; (**b**) z.

At each ALG concentration, the values of A_f increased with increasing MTZ content and reached a comparable value for all ALG concentration. On the other hand, the number of interactions between alginate chains, z, was, in general, reduced at increasing MTZ volumetric fractions. In general, MTZ appeared to dominate the rheological behavior of the hydrogel by stiffening it, probably due to the inherent stiffness of the MTZ particle, but also modifying the interactions between the macromolecules forming the hydrogel. This is also associated with an increase in the dissipative behavior of the filled hydrogel, as shown by the increase in the phase angle, δ (Figure 8d), whose cause is still to be identified.

2.6. Swelling Behavior and Stability

Figure 10 shows a fast buffer solution uptake occurring in the first hour, causing an increase in the mass of all the investigated hydrogels. This uptake magnitude is highlighted in Figure 11, showing the effects of ALG and MTZ contents. In unfilled hydrogels, the uptake is consistent with the mesh measurement, as expected. At each ALG concentration, the swelling ability decreased with the MTZ fraction, as the hydrogel volume might be gradually occupied by drug particles, which hindered the acetate buffer entrance.

After the maximum swelling ratios, Q was reached, and different behavior was observed based on the amount of MTZ powder. Unfilled hydrogels (HB.0 and HC.0) showed a limited deswelling followed by a plateau, corresponding to an equilibrium state for the whole experiment duration (650 h). HA.0 showed a significant reduction in the swelling ratio, which is not related to a loss of buffer solution mass, but to the disaggregation of the hydrogel sample, as also evident from images in Figure 12. This phenomenon is probably due to the presence of sodium ions in acetate buffer, which competed with calcium ions and led to a reduction in the crosslinking degree, followed by dissolution on the un-crosslinked alginate chains [33]. With increasing solid fraction content, all the hydrogels showed a reduction in the swelling ratio, to be interpreted in terms of ALG/MTZ mass loss. This

phenomenon was faster for hydrogels containing less ALG (at a fixed MTZ content), or more MTZ (at a fixed ALG concentration). On one hand, the lower stability of the ALG hydrogel may cause a combined MTZ release and filled gel disaggregation, but on the other, the solubilization of MTZ powder may generate cavities that weaken the structure and foster sample fragmentation.

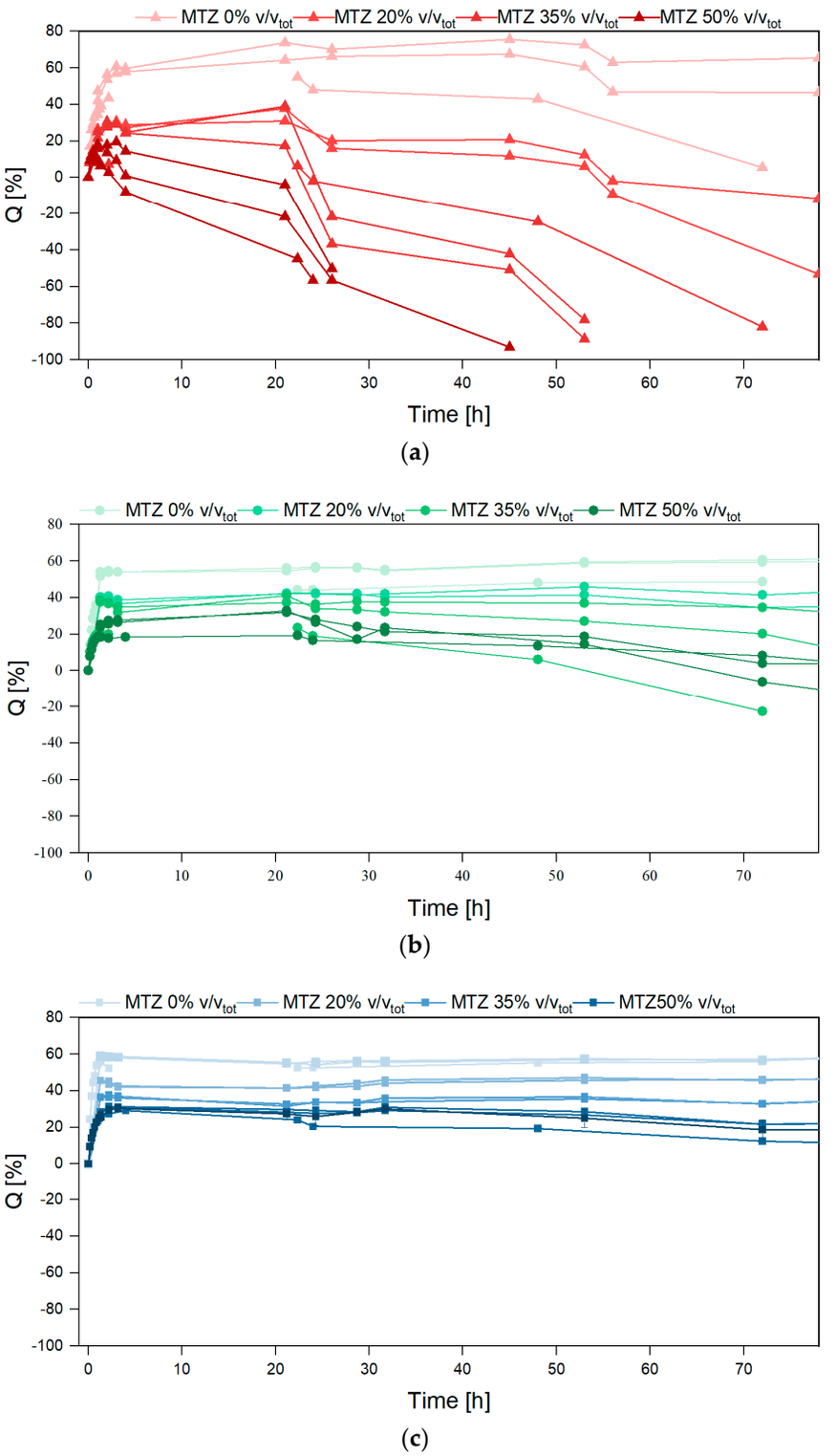

Figure 10. Swelling ratio vs. time for hydrogels containing (**a**) ALG 2%, (**b**) ALG 4%, and (**c**) ALG 6%.

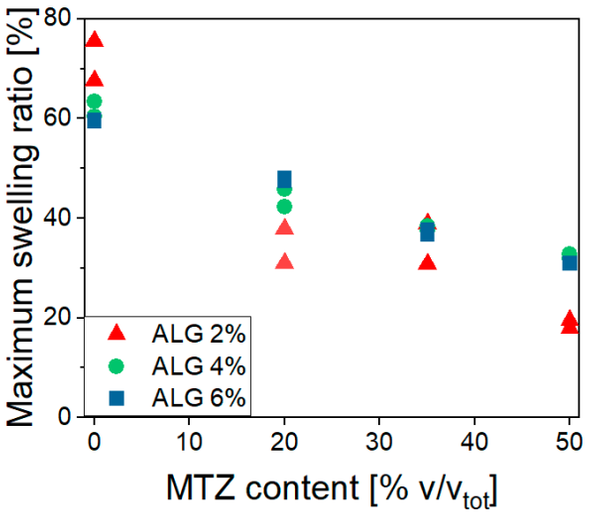

Figure 11. Maximum swelling ratio dependence on ALG and MTZ content.

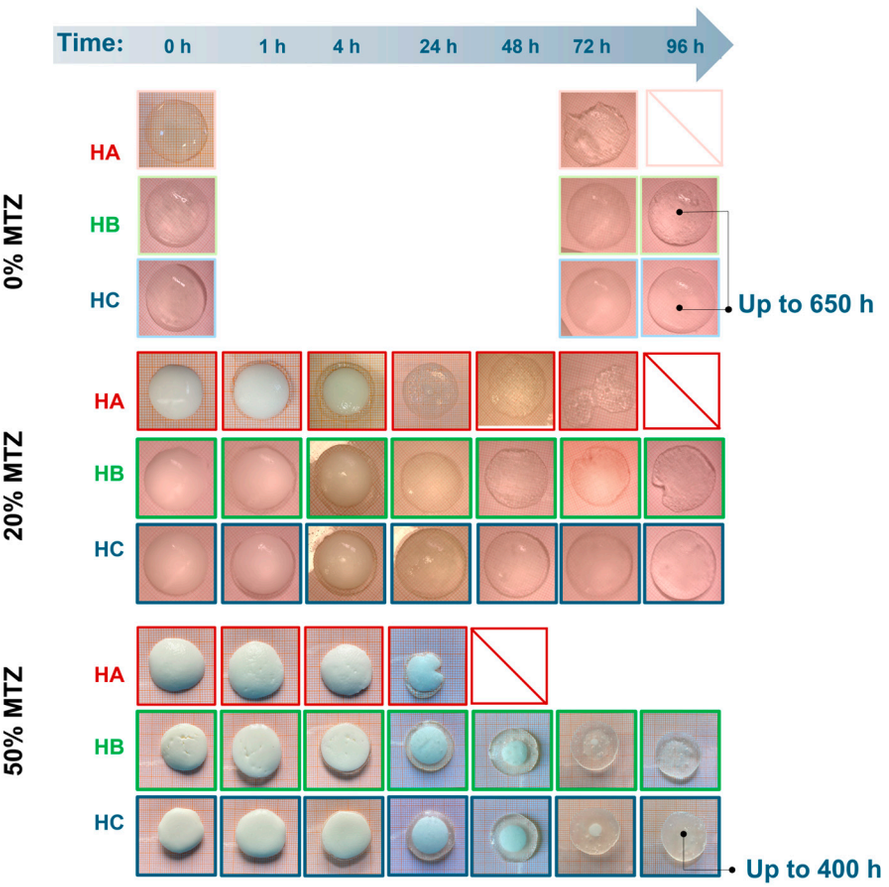

Figure 12. Images of samples extracted from the buffer solution at different time points of immersions.

This is made clearer from images of samples extracted from the buffer solution at different time points (Figure 12). The clearness of the hydrogel matrix allowed the direct observation of the MTZ dissolution, with the front moving towards the center of the sample. Indeed, HA.50 hydrogel MTZ dissolution also involved hydrogel fragmentation, whereas HB.50 and HC.50 remained intact while dissolution occurred, suggesting drug solubilization and diffusion through a swollen hydrogel layer mechanism. Comparing the last two, the presence of a small portion of MTZ powder in HC.50 at 72 h might indicate a slower dissolution when a higher alginate content was present, which is consistent with

the denser polymeric network for HC hydrogels. However, further investigation evidenced no differences in the dissolution profile of these hydrogels and demonstrated that the dissolution was governed by the solubility of the active ingredient which belongs to the BCS II class [34]. In all cases, for the investigated geometry, the MTZ dissolved completely after about 4 days of immersion in the buffer solutions. These results reflect the behavior of the hydrogels at pH 4.5, a reference value commonly [35] used in the context of bacterial vaginosis. However, since vaginal pH may vary between individuals, future studies should consider the impact of pH on drug release in the perspective of personalized therapy.

3. Conclusions

This study demonstrates that the addition of solid fillers impacts on the rheological behavior of hydrogels and their liquid precursors, on the hydrogel stability, and on the release of the filler, with implications for the design of extrusion-based drug delivery systems. Rather than developing a specific drug delivery system, we used a representative case to prove how filler incorporation affects hydrogel behavior, aiming to inform broader strategies for modeling and designing filled hydrogel systems.

This was explored through the specific case of alginate hydrogels filled with metronidazole (MTZ), a possible sustained release system for the first-line treatment for bacterial vaginosis. The addition of MTZ, up to a volumetric fraction of 0.5, significantly altered the flow behavior of the precursors of hydrogels. The effect is not only limited to a more-than-linear increase in shear viscosity at low shear rates but also involves a shift in the behavior of the complex system from (non-linear) viscous to Bingham-like, with a threshold shear stress required for flow. These changes have clear implications for both extrudability and shaping processes like extrusion or 3D printing.

Notably, extrudability is not determined only by hydrogel formulation, but also by boundary conditions such as nozzle geometry and applied pressure/driving force. A simple method was proposed to estimate the required extrusion pressure using basic fluid dynamics, with improved reliability when measurements reflect actual processing conditions.

Despite MTZ incorporation, the precursor suspension is extrudable even at the higher MTZ content. and the crosslinking reaction was not prevented. Through filler addition, the hydrogel properties can be tuned from those of a quite soft material to those of a stiff, self-standing one, indicating the possibility to modulate gel structure through filler addition.

While the findings are specific to the alginate–metronidazole system in a buffered solution, this work underscores the importance of systematically linking material formulation and flow behavior, setting up a framework for designing filled hydrogel-based delivery systems. This approach is particularly relevant in the context of personalized medicine, where no single formulation is likely to suit all clinical scenarios of bacterial vaginosis. Instead, different therapeutic needs may require tailored compositions with distinct rheological and release characteristics. Our study therefore provides formulation insights and practical tools to support the selection and design of systems best suited to individual requirements.

4. Materials and Methods

4.1. Materials

Sodium alginate (ALG; average Mw = 120,000–190,000 g/mol, M/G ratio = 1.56, Merk KGaA, Darmstadt, Germany); calcium carbonate, in the form of calcite ($CaCO_3$; Merk KGaA, Darmstadt, Germany); glucono-δ-lactone (GDL; Merk KGaA, Darmstadt, Germany); metronidazole (MTZ; Mw = 171.15 g/mol, density = 1.45 g/mL, Methapharmaceutical, Barcelona, Spain).

4.2. Methods

4.2.1. Metronidazole Preparation

MTZ particle size was reduced using a pin mill (Retsch ZM200, Retsch GmbH, Haan, Germany) equipped with a 250 µm mesh filtering-screen and by setting the rotation speed at 6000 rpm for 5 s.

The <180 µm fraction was selected. The particle size distribution of MTZ was assessed (Mastersizer 3000, Malvern Panalytical, Worcestershire, UK) before and after the milling process. Images of pristine and processed MTZ were acquired using an optical microscope (5× and 20× magnification, Olympus BX 60, Olympus Global, Tokyo, Japan).

4.2.2. Hydrogel Preparation

The hydrogel was attained by using a previously set-up protocol entailing an internal gelation process [34,36]. The developed procedure required addition of previously weighted (E50S/3, Gibertini Elettronica, Milano, Italy) amounts of $CaCO_3$ and ALG in a saturated solution of MTZ in distilled water with the formation, under magnetic stirring (300 rpm for about 30 min at room temperature), of a suspension, here referred to as $CaCO_3$-suspensions. When needed, MTZ powder was added in different volume fractions (20, 35, 50% V/V_{tot}) to the $CaCO_3$ suspension and manually mixed for 2 min, producing the drug-loaded suspension. During preparation the mechanical stirring was carried out so as to avoid particle aggregation phenomena. Figure S2 shows a micrograph of the particles incorporated in the hydrogel, whose dimensions are comparable to those of dry particles after milling and sieving. Ca^{2+} ions were made slowly available by adding the selected acidifying agent (i.e., GDL 3.6% w/w_{tot}) dissolved in an MTZ-saturated solution to the drug-loaded suspension, resulting in the formation of a GDL-activated suspension. The solution containing the acidifying agent was added in a 1:2 volume ratio with respect to the previously prepared $CaCO_3$-suspension, thus diluting its ingredients. This way, the hydrogel precursor formulation remained in the liquid state for approximately 30 min, while the complete crosslinking of the hydrogel required about 4 h.

When still extrudable (not less than 1 h and not more than 2 h from preparation), the hydrogel precursor formulations were extruded using either a 5 mL syringe equipped with G18 gauge (internal diameter = 0.84 mm) needles, attaining dome-shape samples, or an extrusion-based bioprinter (BIO X, CELLINK, Gothenburg, Sweden) equipped with a 3 mL cartridge and with G18 gauges to obtain 3D printed samples.

The final composition of all the hydrogels evaluated in this work, differing for the content of ALG, $CaCO_3$, and MTZ, is summarized in Table 5. Instead of testing the GDL-activated suspensions, which have time-dependent properties, not-activated suspensions (indicated with the prefix tag "NA_") having the same composition except for the presence of GDL were considered when needed.

Table 5. Hydrogel formulations overview. Solutions and suspensions were prepared starting from an MTZ saturated solution.

ALG (% w/w_{tot})	$CaCO_3$ (% w/w_{tot})	$CaCO_3$ Suspension Code	MTZ (% V/V_{tot})	Drug-Loaded Suspension Code	Hydrogel Code
2	0.17	A	0	A.0	HA.0
			20	A.20	HA.20
			35	A.35	HA.35
			50	A.50	HA.50

Table 5. *Cont.*

ALG (% w/w_{tot})	$CaCO_3$ (% w/w_{tot})	$CaCO_3$ Suspension Code	MTZ (% V/V_{tot})	Drug-Loaded Suspension Code	Hydrogel Code
4	0.34	B	0	B.0	HB.0
			20	B.20	HB.20
			35	B.35	HB.35
			50	B.50	HB.50
6	0.51	C	0	C.0	HC.0
			20	C.20	HC.20
			35	C.35	HC.35
			50	C.50	HC.50

Note: GDL was kept constant, at 1.2 w/$w_{tot.}$

4.2.3. Rotational Rheological Measurement on Solutions and Suspensions

Shear viscosity curves were measured using a Modular Compact Rheometer MCR 502 (Anton Paar, Graz, Austria) in a parallel plate configuration (25 mm or 50 mm diameter plates, 1.5 mm gap). Steady shear test measurements were performed by imposing a shear rate logarithmic ramp from 0.1 s^{-1} to 100 s^{-1} for each formulation. The test temperature was 25 °C.

The shear-thinning behavior of tested samples was fitted by Cross' model (Equation (5)).

$$\tau(\dot{\gamma}) = \eta(\dot{\gamma}) \times \dot{\gamma} \frac{\eta(\dot{\gamma}) - \eta_\infty}{\eta_0 - \eta_\infty} = \frac{1}{1 + (\lambda\dot{\gamma})^m} \quad (5)$$

where τ is the shear stress, $\eta(\dot{\gamma})$ is the shear rate dependent viscosity, $\dot{\gamma}$ the shear rate, η_0 and η_∞ are the viscosities at zero and infinite shear rate, respectively, λ is characteristic relaxation time, and m is the power law index.

In this work, η_∞ was assumed to be equal to zero. For some suspensions, yielding phenomena occurred and the relevant shear stress and shear rate curves were fitted by the Herschel–Bulkley model (Equation (6)).

$$\tau(\dot{\gamma}) = \tau_y + k\dot{\gamma}^n \quad (6)$$

where τ_y is the yield stress, k the fluid consistency, and n the viscosity index.

4.2.4. Extrudability/3D Printability

The possibility of extruding/3D printing the MTZ-filled hydrogel precursor formulations was evaluated with an extrusion-based bioprinter (BIO X, CELLINK, Gothenburg, Sweden) equipped with a 3 mL cartridge. This device is a pressure-controlled 3D printer and could be used to assess the minimum pressure required to extrude the considered NA_suspensions through 19 mm long G18, G20, and G21 needles, having an internal diameter of 0.84 mm, 0.61 mm, and 0.51 mm, respectively.

Furthermore, the device was also used as a capillary rheometer to estimate the rheological behavior of the hydrogel precursor formulations at extrusion-relevant shear rates [37]

The apparent shear stress at the wall τ_w was related to the pressure drop through the bioprinter needle, P_c:

$$\tau_w = \frac{R_c P_c}{2L_c} \quad (7)$$

where R_c and L_c are, respectively, the radius and the length of the needle.

The pressure drop in the capillary was calculated from the pressure imposed on the bioprinter piston, P_b, as:

$$P_c = P_b - P_e \quad (8)$$

where P_e is the pressure drop due to converging flow at the needle entrance, estimated in independent extrusion experiments performed without needles. P_e was assumed to be shear rate independent. The pressure drops along the reservoir/cartridge was neglected, given a ratio between nozzle and reservoir diameter of order 3.

Assuming the parabolic velocity field typical of Newtonian fluids in a cylindrical channel, the shear rate at wall, $\dot{\gamma}_{w,Newt}$, is related to the flow rate Q by Equation (9).

$$\dot{\gamma}_{w,Newt} = \frac{4Q}{\pi R_c^3} \quad (9)$$

For non-Newtonian fluids, this value represents the apparent shear rate, a lower estimation of the true value. An apparent shear viscosity η_{app} can be then calculated (Equation (10)):

$$\eta_{app} = \frac{\tau_w}{\dot{\gamma}_{w,Newt}} \quad (10)$$

In the case of Newtonian fluids, $\eta_{app} = \eta_{true}$.

Capillary rheometry was carried out using a G18 needle as the capillary. The test was performed applying 5 different pressure levels for a maximum of 30 s: (i) the minimum pressure required by each sample to flow, (ii) 50 kPa (if enough to flow), (iii) 100 kPa, (iv) 150 kPa, and (v) 200 kPa (the maximum pressure provided by the printer). During this time, at least 4 samples were collected and weighed. Also, the time needed to attain the sample was measured with a stopwatch (iPhone 11, Apple, Cupertino, CA, USA). The mass flow rate was then measured as the slope of the line interpolating the extruded mass vs. time data. The volume flow rate was estimated by dividing it by the density of each suspension.

To avoid any influence of the crosslinking reaction and to obtain a better reproducibility, NA_suspensions both with a higher amount of MTZ and without it, were used, with the assumption that the liquid response before crosslinking is independent of the presence of GDL. Tests were performed at 25 °C.

4.2.5. Dynamic Mechanical Analysis

Dynamic mechanical analysis was performed on unfilled and MTZ-filled hydrogels using a Modular Compact Rheometer MCR 502 (Anton Paar, Graz, Austria) in a parallel plate configuration (25 mm diameter plates, 1–2 mm gap depending on the height of hydrogel). The methods adopted were consistent with the recommendations of ASTM D4440-23 "Standard test method for plastics: dynamic mechanical properties Melts rheology" [38]. Oscillatory measurements on hydrogels were performed 24 h after GDL addition to ensure complete crosslinking. During that time, they were kept at room temperature in sealed Petri dishes.

Amplitude sweep tests were carried out in the shear amplitude range 0.01–1% at the constant frequency of 10 rad/s to determine the limit of the linear viscoelastic region (LVR), which was about 0.05%. Based on shear strain amplitude sweeps, frequency sweep measurements were performed from 1 rad/s to 100 rad/s and back to 1 rad/s for all samples at 0.01% shear strain amplitude.

The testing conditions were selected to obtain the appropriate information about structure and composition-to-mechanical property correlations, rather than to investigate the behavior of the hydrogel in mechanical conditions similar to those of the specific case of the vaginal environment.

4.2.6. Samples Preparation

The hydrogel precursors were cast in:

- custom made cylindric mold (radius = 12.5 mm, high = 1 mm) to provide samples suitable for dynamical mechanical test.
- silicon multi-portion mold with dome-shaped geometry (design shown in Figure 13) to supply samples for the swelling test. This geometry could in principle allow the estimation of both swelling and MTZ mass and volume release. The former can be obtained by mass measurement, as described below, while the latter from the optical observation of the dissolution front, exploiting the sample spherical symmetry and under the hypothesis of isotropic dissolution.

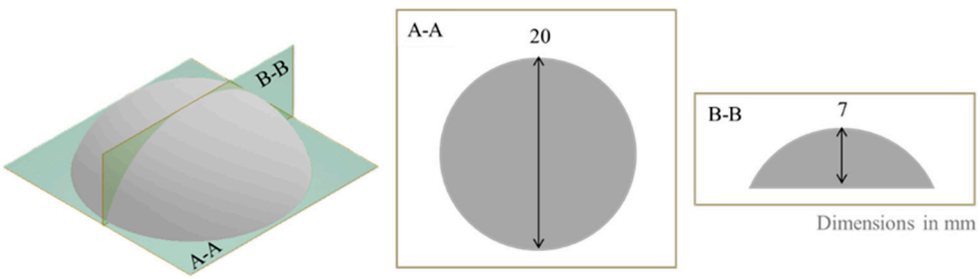

Figure 13. Design of dome-shaped cast sample.

The precursor solutions were cast in the molds immediately after the addition of the GDL solution. Before using dome-shaped hydrogels for further tests, they were kept overnight at room temperature in sealed Petri dishes containing wet paper towels to keep a humid environment.

4.2.7. Swelling and Stability Tests

Hydrogel samples based on all the formulations considered were cast in dedicated molds. They were submerged in 250 mL of acetate buffer at pH 4.5 (EUROPEAN PHARMACOPOEIA—4.1.3. Buffer solutions) and kept at 37 °C.

At pre-established times, the samples were removed from the buffer and weighed (E50S/3, Gibertini, Elettronica, Milano, Italy) to evaluate their stability and MTZ dissolution over time. The experiment lasted one month, during which the samples were also photographed (iPhone 11, Apple, Cupertino, CA, USA).

The mass data were used to calculate the swelling ratio Q, which helps quantify the medium absorption as:

$$Q(t) = \frac{W_0 - W_{(t)}}{W_0} \tag{11}$$

Supplementary Materials: The following supporting information can be downloaded at: https://www.mdpi.com/article/10.3390/gels11070510/s1, Figure S1: (a) An example of viscosity curves for MTZ-saturated solution containing 4% ALG and 50% MTZ (b) the relevant average viscosity curve. Error bars represent the standard deviation.; Figure S2: Micrograph of a filled hydrogel HB.50 sample. The filler dimensions are comparable to those of the dry filler after grinding and sieving (see Figure 1a of the manuscript); Figure S3: Loss factor, tan(δ) evolution in time for HB.50. The apparent gel point can be observed for tan(δ) = 1 at about 30 minutes from non activated precursor mixing with GDL.

Author Contributions: Conceptualization, A.M., P.P., and F.B.V.; methodology, A.C., A.M., and F.B.V.; formal analysis, A.F.; investigation, A.C., A.F., M.U., and F.C.; resources, F.B.V., P.P., and L.Z.; data curation, A.C. and A.F.; writing—original draft preparation, A.C.; writing—review and editing, P.P., L.Z., A.M., and F.B.V.; supervision, A.M., F.B.V. All authors have read and agreed to the published version of the manuscript.

Funding: This research received no external funding.

Institutional Review Board Statement: Not applicable.

Informed Consent Statement: Not applicable.

Data Availability Statement: The data supporting the discussion and conclusions of this study are presented in the manuscript, and are available from the corresponding author upon reasonable request.

Conflicts of Interest: The authors declare no conflicts of interest.

References

1. Malkin, A.Y.; Kulichikhin, V.G.; Khashirova, S.Y.; Simonov-Emelyanov, I.D.; Mityukov, A.V. Rheology of Highly Filled Polymer Compositions-Limits of Filling, Structure, and Transport Phenomena. *Polymers* **2024**, *16*, 442. [CrossRef] [PubMed]
2. Cui, J.; Shi, J.; Liu, Y.; Shi, X.; Sun, J.; He, Z.; Luo, C.; Zhang, S. Engineered hydrogel platform for diabetic wound healing. *Chem. Eng. J.* **2025**, *507*, 160379.
3. Lee, K.K.; Go, K.; Lee, E.; Kim, H.; Kim, S.; Kim, J.-H.; Chae, M.S.; Jeong, J.-O. Multifunctional hydrogels for advanced cancer treatment: Diagnostic imaging and therapeutic modalities. *Gels* **2025**, *11*, 426. [CrossRef] [PubMed]
4. Zhang, M.; Huang, Y.; Pan, W.; Tong, X.; Zeng, Q.; Su, T.; Qi, X.; Shen, J. Polydopamine-incorporated dextran hydrogel drug carrier with tailorable structure for wound healing. *Carbohydr. Polym.* **2021**, *253*, 117213. [CrossRef]
5. Gu, Z.; Chen, L.; Xu, Y.; Liu, Y.; Zhao, Z.; Zhao, C.; Lei, W.; Rong, Q.; Fang, R.; Zhao, T.; et al. General strategy to fabricate highly filled microcomposite hydrogels with high mechanical strength and stiffness. *ACS Appl. Mater. Interfaces* **2018**, *10*, 4161–4167. [CrossRef]
6. Ezike, T.C.; Okpala, U.S.; Onoja, U.L.; Nwike, C.P.; Ezeako, E.C.; Okpara, O.J.; Okoroafor, C.C.; Eze, S.C.; Kalu, O.L.; Odoh, E.C.; et al. Advances in drug delivery systems, challenges and future directions. *Heliyon* **2023**, *9*, e17488. [CrossRef]
7. Bordbar-Khiabani, A.; Gasik, M. Smart hydrogels for advanced drug delivery systems. *Int. J. Mol. Sci.* **2022**, *23*, 3665. [CrossRef]
8. Narayanaswamy, R.; Torchilin, V.P. Hydrogels and their applications in targeted drug delivery. *Molecules* **2019**, *24*, 603. [CrossRef]
9. Alshemary, A.Z.; Bilgin, S.; Işık, G.; Motameni, A.; Tezcaner, A.; Evis, Z. Biomechanical evaluation of an injectable alginate/dicalcium phosphate cement composites for bone tissue engineering. *J. Mech. Behav. Biomed. Mater.* **2021**, *118*, 104439. [CrossRef]
10. Chen, M.H.; Wang, L.L.; Chung, J.J.; Kim, Y.-H.; Atluri, P.; Burdick, J.A. Methods to assess shear-thinning hydrogels for application as injectable biomaterials. *ACS Biomater. Sci. Eng.* **2017**, *3*, 3146–3160. [CrossRef]
11. Alasvandian, S.; Shahgholi, M.; Karimipour, A. Investigating the effects of chitosan atomic ratio and drug type on mechanical properties of silica aerogel/chitosan nanocomposites using molecular dynamics approach. *J. Mol. Liq.* **2024**, *401*, 124639. [CrossRef]
12. Ahmed, E.M. Hydrogel: Preparation, characterization, and applications: A review. *J. Adv. Res.* **2015**, *6*, 105–121. [CrossRef] [PubMed]
13. Ahmed, E.M.; Aggor, F.S.; Awad, A.M.; El-Aref, A.T. An innovative method for preparation of nanometal hydroxide superabsorbent hydrogel. *Carbohydr. Polym.* **2012**, *91*, 693–698. [CrossRef]
14. Lohani, A.; Saxena, R.; Duarte, J.G.; Khan, S.; Figueiras, A.; Mascarenhas-Melo, F. Tailored polymeric hydrogels for regenerative medicine and drug delivery: From material design to clinical applications. *Int. J. Pharm.* **2025**, *681*, 125818. [CrossRef]
15. Mathew, A.P.; Uthaman, S.; Cho, K.-H.; Cho, C.-S.; Park, K.-K. Injectable hydrogels for delivering biotherapeutic molecules. *Int. J. Biol. Macromol.* **2018**, *110*, 17–29. [CrossRef]
16. Bakhrushina, E.O.; Mikhel, I.B.; Buraya, L.M.; Moiseev, E.D.; Zubareva, I.M.; Belyatskaya, A.V.; Evzikov, G.Y.; Bondarenko, A.P.; Krasnyuk, I.I., Jr.; Krasnyuk, I.I. Implantation of in situ gelling systems for the delivery of chemotherapeutic agents. *Gels* **2024**, *10*, 44. [CrossRef] [PubMed]
17. Tong, X.; Pan, W.; Su, T.; Zhang, M.; Dong, W.; Qi, X. Recent advances in natural polymer-based drug delivery systems. *React. Funct. Polym.* **2020**, *148*, 104501. [CrossRef]
18. Zhang, M.; Zhao, X. Alginate hydrogel dressings for advanced wound management. *Int. J. Biol. Macromol.* **2020**, *162*, 1414–1428. [CrossRef]

19. Besiri, I.N.; Goudoulas, T.B.; Fattahi, E.; Becker, T. Experimental advances in the real-time recording of cross-linking alginate in situ gelation: A review. *Polymers* **2023**, *15*, 2875. [CrossRef]
20. Zeng, H.; Tang, L.; Huang, L.; Yang, N.; Chen, X.; Peng, X.; Chen, Z.; Guo, J.; Weng, J.; Guo, T. A novel multi-functional PVA-alginate hydrogel with dynamic bond crosslinking for infected wound repair. *Carbohydr. Polym.* **2025**, *362*, 123636. [CrossRef]
21. Guagliano, G.; Volpini, C.; Sardelli, L.; Bloise, N.; Briatico-Vangosa, F.; Icaro Cornaglia, A.; Dotti, S.; Villa, R.; Visai, L.; Petrini, P. Hep3Gel: A shape-shifting extracellular matrix-based, three-dimensional liver model adaptable to different culture systems. *ACS Biomater. Sci. Eng.* **2023**, *9*, 211–229. [CrossRef] [PubMed]
22. Lopes, M.; Abrahim, B.; Veiga, F.; Seiça, R.; Cabral, L.M.; Arnaud, P.; Andrade, J.C.; Ribeiro, A.J. Preparation methods and applications behind alginate-based particles. *Expert Opin. Drug Deliv.* **2017**, *14*, 769–782. [CrossRef] [PubMed]
23. Ferreira, N.N.; Perez, T.A.; Pedreiro, L.N.; Prezotti, F.G.; Boni, F.I.; Cardoso, V.M.O.; Venâncio, T.; Gremião, M.P.D. A novel pH-responsive hydrogel-based on calcium alginate engineered by the previous formation of polyelectrolyte complexes (PECs) intended to vaginal administration. *Drug Dev. Ind. Pharm.* **2017**, *43*, 1656–1668. [CrossRef]
24. Shaaban, O.M.; Youssef, A.E.A.; Khodry, M.M.; Mostafa, S.A. Vaginal douching by women with vulvovaginitis and relation to reproductive health hazards. *BMC Womens Health* **2013**, *13*, 23. [CrossRef] [PubMed]
25. Cirri, M.; Maestrelli, F.; Scuota, S.; Bazzucchi, V.; Mura, P. Development and microbiological evaluation of chitosan and chitosan-alginate microspheres for vaginal administration of metronidazole. *Int. J. Pharm.* **2021**, *598*, 120375. [CrossRef]
26. Takahashi, Y.; Noda, I.; Nagasawa, M. Zero-shear viscosity of linear polymer solutions over a wide range of concentration. *Macromolecules* **1985**, *18*, 1002–1008. [CrossRef]
27. Wilms, P.; Hinrichs, J.; Kohlus, R. Macroscopic rheology of non-Brownian suspensions at high shear rates: The influence of solid volume fraction and non-Newtonian behaviour of the liquid phase. *Rheol. Acta* **2022**, *61*, 123–138. [CrossRef]
28. Thomas, D.G. Transport characteristics of suspension: VIII. A note on the viscosity of Newtonian suspensions of uniform spherical particles. *J. Colloid Sci.* **1965**, *20*, 267–277. [CrossRef]
29. Acierno, D.; Patti, A. Fused deposition modelling (FDM) of thermoplastic-based filaments: Process and rheological properties—An overview. *Materials* **2023**, *16*, 7664. [CrossRef]
30. Turco, G.; Donati, I.; Grassi, M.; Marchioli, G.; Lapasin, R.; Paoletti, S. Mechanical spectroscopy and relaxometry on alginate hydrogels: A comparative analysis for structural characterization and network mesh size determination. *Biomacromolecules* **2011**, *12*, 1272–1282. [CrossRef]
31. Karvinen, J.; Kellomäki, M. Characterization of self-healing hydrogels for biomedical applications. *Eur. Polym. J.* **2022**, *181*, 111641. [CrossRef]
32. Gabriele, D.; de Cindio, B.; D'Antona, P. A weak gel model for foods. *Rheol. Acta* **2001**, *40*, 120–127. [CrossRef]
33. Ito, F.; Usui, K.; Kawahara, D.; Suenaga, A.; Maki, T.; Kidoaki, S.; Suzuki, H.; Taiji, M.; Itoh, M.; Hayashizaki, Y.; et al. Reversible hydrogel formation driven by protein–peptide–specific interaction and chondrocyte entrapment. *Biomaterials* **2010**, *31*, 58–66. [CrossRef] [PubMed]
34. Chiappa, A.; Fusari, A.; Uboldi, M.; Petrini, P.; Melocchi, A.; Briatico Vangosa, F.; Zema, L. 3D printed reservoir-like vaginal rings for antibiotic delivery. *Int. J. Pharm.* **2025**, *671*, 125217. [CrossRef] [PubMed]
35. Boyd, P.; Variano, B.; Spence, P.; McCoy, C.F.; Murphy, D.J.; Dallal Bashi, Y.H.; Malcolm, R.K. In vitro release testing methods for drug-releasing vaginal rings. *J. Control Release* **2019**, *313*, 54–69. [CrossRef] [PubMed]
36. Guagliano, G.; Volpini, C.; Camilletti, J.; Donnaloja, F.; Briatico-Vangosa, F.; Visai, L.; Petrini, P. Internally crosslinked alginate-based bioinks for the fabrication of in vitro hepatic tissue models. *Biofabrication* **2023**, *15*, 035018. [CrossRef]
37. Maacosko, C.W. 6.2 Capillary Rheometer. In *Rheology: Principles, Measurements, and Applications*; Wiley-VCH: Weinheim, Germany, 1994.
38. *ASTM D4440-23*; Standard Test Method for Plastics: Dynamic Mechanical Properties Melts Rheology. ASTM International: West Conshohocken, PA, USA, 2023.

Formulation-dependent Extrudability of Highly-filled Alginate System for Vaginal Drug Delivery

Supplementary Information

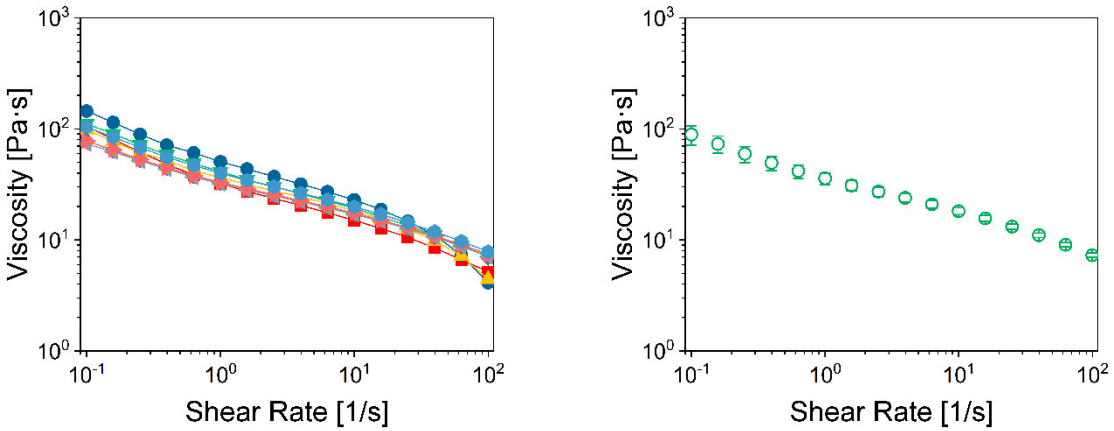

a b

Figure S1. a) An example of viscosity curves for saturated solution containing 4% ALG and 50% MTZ b) the relevant average viscosity curves. Error bars represent the standard deviation.

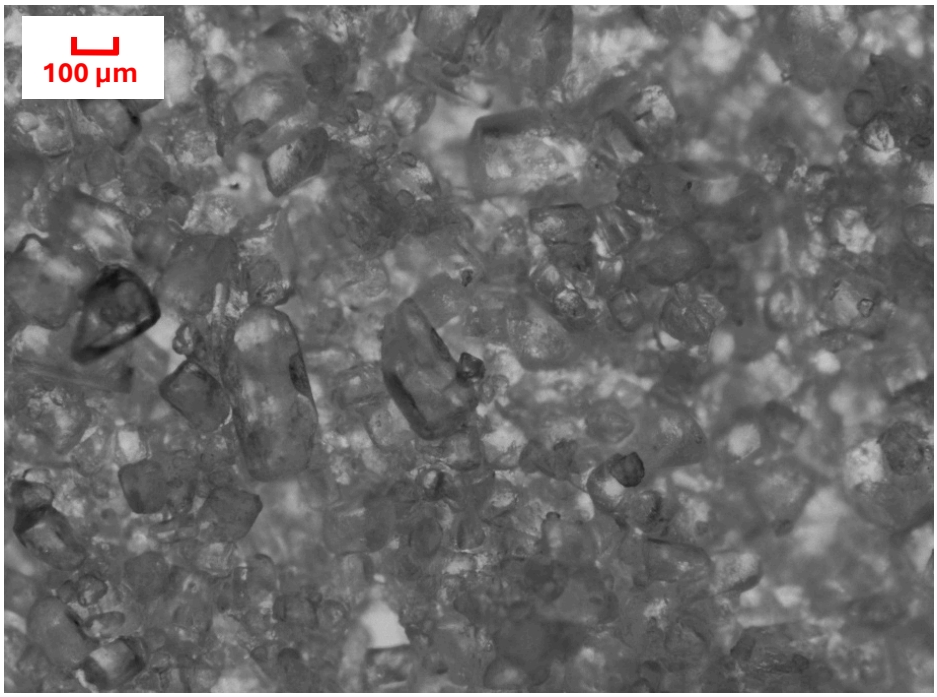

Figure S2: Micrograph of a filled hydrogel HB.50 sample. The filler dimensions are comparable to those of the dry filler after grinding and sieving (see Figure 1a)

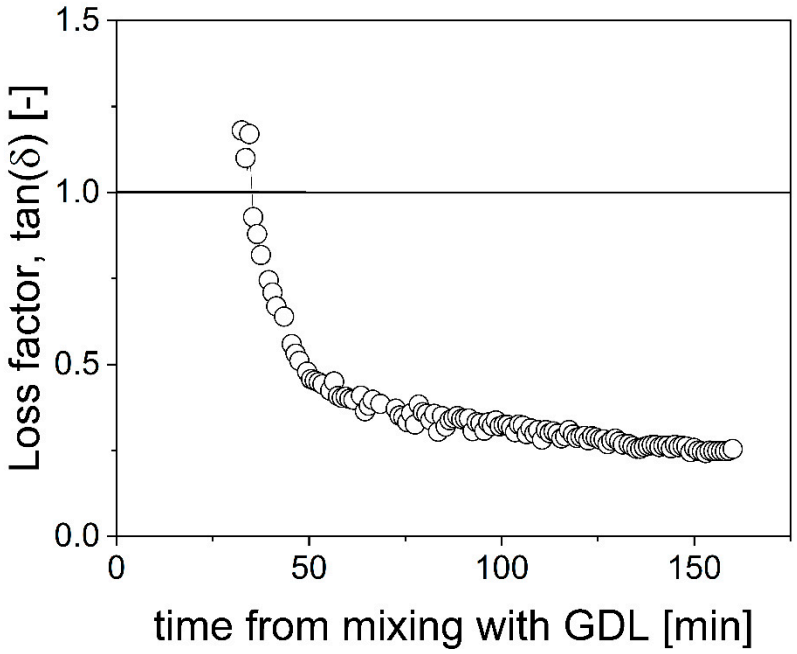

Figure S3. Loss factor, tan(δ) evolution in time for HB.50 The apparent gel point can be observed for tan(δ)=1 at about 30 minutes from non activated precursor mixing with GDL.

Appendix

Granules and pellets

1. Materials

Naproxen (**NPX**; batch 236102267, Zhejiang charioteer pharmaceutical Co., China); Croscarmellose Sodium, Ac-Di-Sol® (**AcDiSol**; Lot. T1431C, JRS Pharma, Germany); N-vinylpyrrolidone, Vivapharm® PVP K30 (**PVP**; Lot.010622012, JRS Pharma, Germany); Microcrystalline Cellulose, Avicel® (**MCC**; lot. 4574069598, Dupont, Ireland); cellets 250-355 µm (Lot-No.: 23A1007, process-center Gmbh & Co. KG, Germany).

2. Methods

2.1 Granulation

MCC, AcDiSol and NPX were accurately weighed (XSR8001S, Mettler-Toledo spa, D) to obtain, in final dry product, the weight ratio reported in Table 1. The materials were mixed manually in a plastic bag and loaded into the chamber of the fluidized bed (Mini-Glatt, Glatt GmbH, Germany), equipped with a top spray configuration (nozzle diameter = 0.5 mm). The binding solution was prepared dissolving PVP (10.7 % w/w) in distilled water. The granulation process started with a preheating phase, followed by a spraying and drying phase. The total process time was approximately 50 min. Based on preliminary studies, the final process parameters set are summarized in Table 2.

Table 1: theoretical composition (% w/w) of the resulting granules

	% w/w
AcDiSol	25
MCC	12.5
NPX	50
PVP	12.5

Table 2: granulation parameters set

	Tube diameter (mm)	1.6
Pre-heating phase	Inlet Air temperature (°C)	55
	Product temperature (°C)	28
	Time (min)	1
Spraying phase	Inlet air volume (m^3/h)	10 - 20
	Inlet air temperature (°C)	55
	Product temperature (°C)	24 - 28
	Atomization air pressure (bar)	0.6
	Spray rate (g/min)	1.4-4.5
	Total spraying time (min)	42
	Time to reach steady state spray conditions (min)	15
Drying phase	Inlet air volume (m^3/h)	10
	Inlet air temperature (°C)	55
	Product temperature	29
	Time (min)	8

2.2. Drug layering

Cellets™ (255-350 μm particle size range) were used as starter cores for the drug layering process. The latter was performed in fluidized bed (Mini-Glatt, Glatt GmbH, Germany) equipped with the Wurster insert (nozzle diameter = 0.5 mm). The drug containing suspension was prepared by dispersing the previously weighed amounts of both NPX (5.3 % w/w) and PVP (12.3 % w/w) in distilled water. The theoretical percentage composition of the resulting drug-coated dried cellets (*i.e.* pellets) is highlighted in Table 3. The process lasted about 105 min and the final process parameters set, which were selected based on initial feasibility trials, are shown in Table 4.

Table 3: theoretical composition (% w/w) of the resulting pellets

	% w/w
Cellets	66.7
NPX	10
PVP	23.3

Table 4: drug-layering parameters set

	Tube diameter (mm)	1.6
Preheating phase	Inlet Air temperature (°C)	60
	Product temperature (°C)	30
	Time (min)	1
Spraying phase	Inlet air volume (m^3/h)	19-21
	Inlet air temperature (°C)	60
	Product temperature (°C)	24 - 28
	Atomization air pressure (bar)	0.6
	Spray rate (g/min)	1.4-4.5
	Total spraying time (min)	42
	Time to reach steady state spray conditions (min)	15
Drying phase	Inlet air volume (m^3/h)	10
	Inlet air temperature (°C)	55
	Product temperature	29
	Time (min)	8

2.3 Characterizations

2.3.1 Practical yield

The resulting batches were weighed to evaluate the practical yield as the ratio, expressed in percentage, between the actual total weight of the batch and the theoretical one. Data reported in Table 5 indicate a highly efficient manufacturing process with limited material loss during handling and processing steps. These values are consistent with the high yields generally targeted in batch pharmaceutical production, where percent yield is used as a key indicator of process robustness and material accountability.

Table 5: Practical yield for granules and pellets.

	Practical yield (%)
Granules	98.4
Pellets	93.5

2.3.2 Sieves analysis

20 g of granules/pellets were sampled and checked for particle size using a vibrating screen (Retsch, Mettler-Toledo, Milan) equipped with 10 sieves ranging from 1400 to 63 μm. After sieving for 5 min at 1.5 mm amplitude, the product fraction in each sieve was evaluated. The resulting size distribution curves are reported in Figure 1a and 1b for granules and pellets, respectively. Both granules and pellets exhibited narrow particle size distributions, indicating good control of the manufacturing process and limited presence of fines or oversized particles.

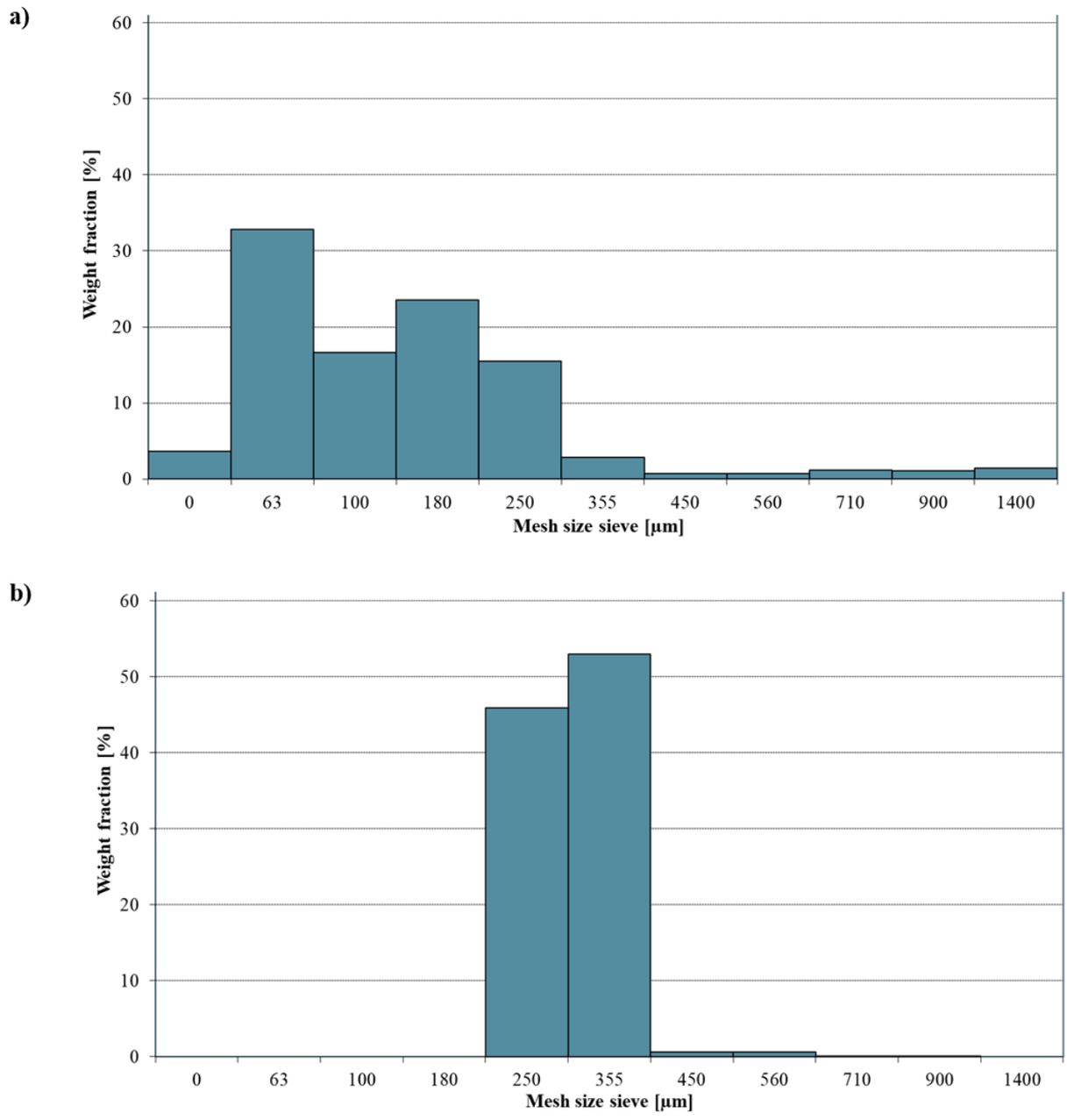

Figure 1: size distribution curves of (a) granules and (b) pellets.

2.3.3 Optical microscopy

Images of granules and pellets were taken using an optical microscope (Zeiss, Nosch, Germany) equipped with a camera (MikrOkularFull HD, Bresser GmbH, Germany) and connected to a computer (Figure 2 a,b). Optical microscopy revealed distinct morphological differences between granules and drug layered pellets, with granules showing irregular, porous shapes typical of wet granulation processes, while pellets exhibited smoother, pseudo-spherical geometries indicative of effective

coating uniformity. These visual characteristics align with expectations for the respective manufacturing routes and support the observed differences in particle size distributions and downstream processability.

a)

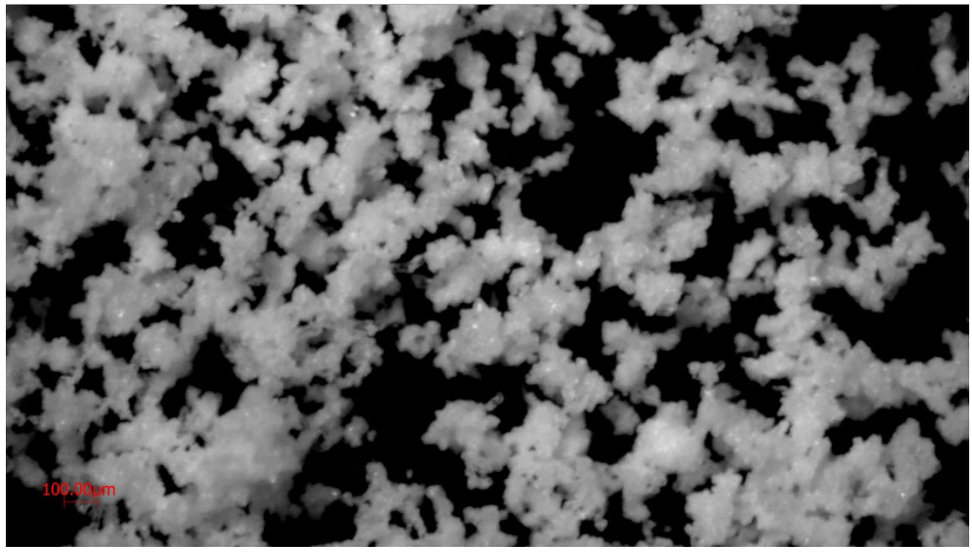

b)

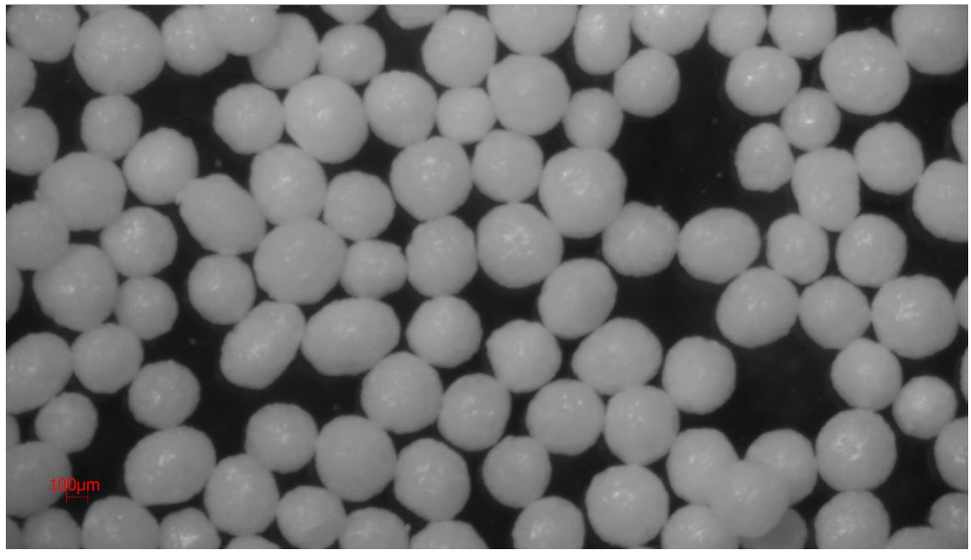

Figure 2: optical photographs of (a) granules and (b) pellets.

2.3.4 Loss on drying (LOD)

The residual water content in both granules and pellets was quantified using a thermobalance (VWR, Italy) (5 g samples, 110°C for 30 min). Data collected are reported in Table 6. Both granules and drug layered pellets showed low residual moisture levels, with LOD values below 3%, indicating adequate drying and suitability for subsequent handling and processing steps. The slightly higher water content measured for granules compared with pellets is still within typical ranges reported for dried granules. The relatively low coefficients of variation (x=3) further suggest good uniformity of moisture content within each batch.

Table 6: LOD results for granules and pellets.

	LOD ± CV (%)
Granules	2.59 ± 9.0
Pellets	1.86 ± 7.0

2.3.5 Bulk density (ρ_{bulk})

The density of both granules and pellets was calculated according to the USP - Method I procedure in *Bulk Density and Tapped Density of Powders*. By gently introducing approximately 30 mL of granules or pellets into a graduated cylinder, ρ_{bulk} was determined as the ratio of the mass of products to the volume occupied, respectively (Table 7). Bulk density measurements highlighted a marked difference between the two systems, with granules showing a very low bulk density (0.19 g/mL) typical of light, highly aerated powders, whereas pellets exhibited a much higher bulk density (0.74 g/mL), consistent with their more compact, spherical structure.

Table 7: ρ_{bulk} relevant to granules and pellets.

	ρ_{bulk} (g/mL)
Granules	0.19
Pellets	0.74

2.3.6 Drug content

The drug content analyses were performed by the analytical laboratory of Glatt Pharmaceutical Services GmbH Co. KG, with a confidential method. Results attained are summarized in Table 8 and confirmed that both granules and drug layered pellets achieved drug contents close to their respective theoretical values.

Table 8: Drug content of granules and pellets.

	Theoretical drug content (%)	**Actual drug content (%)**
Granules	50	49.90
Pellets	10	9.36